

# Energy Transfer in Heterogeneous Organic Material Systems

by

Xiao Liu

A dissertation submitted in partial fulfillment  
of the requirements for the degree of  
Doctor of Philosophy  
(Electrical Engineering)  
in The University of Michigan  
2019

Doctoral Committee:

Professor Stephen Forrest, Chair  
Professor L. Jay Guo  
Professor Jennifer Ogilvie  
Professor Max Shtein

Xiao Liu

sourceix@umich.edu

ORCID iD: 0000-0002-5397-6694

© Xiao Liu 2019

“How could a pond be so cool and clean?  
Because fresh water from the source flows in.”

- Xi Zhu, Chinese philosopher

## ACKNOWLEDGEMENTS

I owe thanks to the people who made this dissertation possible. First and foremost, I would like to express my sincere gratitude to my advisor, Prof. Stephen Forrest. His propound insight in science and dedication to high quality work have inspired me during this incredible PhD journey. He has challenged me to have critical thinking, broad vision, and prompt action to the research problems, and also influenced me by his business acumen beyond the scientific world, curiosity to art, and a keen sense of humor in daily life. I deeply appreciate his mentorship to me and treasure the memorable experience of working with him.

I am truly grateful to the support from my mentors and collaborators in the OCM group: Yifan Zhang and Michael Sloatsky, who have helped me initiate the PhD studies and trained me important experimental techniques and theoretical analyzing skills; Xiaozhou Che, Anurag Panda, Yue Qu, Dejiu Fan, Kan Ding, Quinn Burlingame, Caleb Coburn, who have overlapped with me throughout the most of my PhD journey and have been both my dearest friends and supportive colleagues; Jeremy Zimmerman, Cedric Rolin, Greg McGraw, Brian Lassiter, Kyle Renshaw, Xiaoran Tong, Xin Xiao, Jaesang Lee, Nana Wang, Shota Nunomura, who have offered valuable advice to my research in the early years; Olga Griffith, Kyusang Lee, Kevin Bergemann, Yongxi Li, Shaocong Hou, who have kindly involved me in their projects and shared their knowledge with me; our administrative staff, Eva Ruff, who has been an irreplaceable member of our group and provided me administrative supports; All other members including Jongchan Kim, Byungjun Lee, Chanhoh Soh, Clarence

Chan, Xiaoheng Huang, Xinjing Huang, Boning Qu, Hafiz Sheriff, Jeffrey Horowitz, John Tortorello, and ones I forget to mention.

I acknowledge the contributions from the excellent scientists outside the group. Jie Gu and Prof. Vinod Menon at the City University of New York have helped me in the 2D material projects; Yin Song and Prof. Jennifer Ogilvie at the University of Michigan have collaborated with me in the multidimensional spectroscopic projects. Kai Sun at University of Michigan has helped me with the transmission electron microscopy. I have been lucky to be involved in the MURI polariton project and work with Long Zhang, Timothy Zhou, Jason Horng, Prof. Hui Deng, Zheng Sun, and Prof. David Snoke. I also acknowledge my thesis committee members, Jay Guo, Jennifer Ogilvie, Max Shtein, who have provided important feedback to this dissertation.

I want to express special thanks to the friends, with whom I have spent joyful time to refresh myself after work. Chief among them are my previous roommates Shanghua Yang, Zhennan Shi, Eric Lin, Wenchi Lin, Yang Wang, Jiangyi Luo, Jiajian Zhou. I also acknowledge Yue Qu, Caleb Coburn, Wenxiong Li, and in particular Anurag Panda, who have been the groomsmen in my wedding.

Last, but not least, I thank my wife, Xin Tong. Her constant love and care have helped me through the most difficult time of my PhD. This thesis would have not been possible without her support. Above all, I am forever indebted to my parents for their love and sacrifice. It has been their support that made this six-year world-class educational opportunity possible.

Xiao Liu  
Ann Arbor, Michigan, USA  
November, 2018

# TABLE OF CONTENTS

DEDICATION . . . . .	ii
ACKNOWLEDGEMENTS . . . . .	iii
LIST OF FIGURES . . . . .	viii
LIST OF TABLES . . . . .	xi
LIST OF APPENDICES . . . . .	xii
LIST OF ABBREVIATIONS . . . . .	xiii
ABSTRACT . . . . .	xvii
<b>PART I: Energy Transfer at Organic Heterojunctions . . . . .</b>	<b>1</b>
<b>CHAPTER</b>	
<b>I. Introduction . . . . .</b>	<b>2</b>
1.1 Overview . . . . .	2
1.2 Properties of Organic Semiconductors . . . . .	5
1.2.1 Intermolecular Interactions . . . . .	6
1.2.2 Intramolecular Bonding and Molecular Orbitals . . . . .	7
1.3 Excitons in Organic Semiconductors . . . . .	10
1.3.1 Molecular Wavefunction and Exciton States . . . . .	10
1.3.2 Optical Transitions . . . . .	15
1.3.3 Exciton Energy Transfer . . . . .	18
1.4 Process and Deposition Methods for Organic Semiconductors . . . . .	20
1.4.1 Material Purification . . . . .	20
1.4.2 Organic Thin Film Deposition . . . . .	22
1.5 Fundamentals of Organic Donor-Acceptor Heterojunctions . . . . .	24
1.5.1 Heterojunctions: Types and Structures . . . . .	24
1.5.2 Photocurrent Generation at Type-II Donor-Acceptor Heterojunctions . . . . .	26
1.5.3 Charge Transfer Excitons and Theories of Exciton Dissociation . . . . .	29

1.5.4	Charge Transport and Mobility . . . . .	33
1.5.5	Applications: Organic Photovoltaics . . . . .	36
<b>II.</b>	<b>Morphological Properties of Organic Donor-Acceptor Heterojunctions . . . . .</b>	<b>39</b>
2.1	Experimental Section . . . . .	39
2.2	Nanostructures in the Blended DBP/C <sub>70</sub> Heterojunctions . . . . .	41
2.3	Percolation and Efficient Charge Collection . . . . .	45
<b>III.</b>	<b>Charge Transfer States in Dilute Donor-Acceptor Blend Organic Heterojunctions . . . . .</b>	<b>47</b>
3.1	Introduction . . . . .	47
3.2	Experimental Section . . . . .	49
3.3	Charge Transfer Excitons at Blended DBP/C <sub>70</sub> Heterojunctions . . . . .	50
3.4	Delocalization of Charge Transfer Exciton and Quantum Confinement Modeling . . . . .	55
3.5	Charge Transfer Exciton in a DBP/C <sub>70</sub> Multi-Quantum Well Structure . . . . .	59
3.6	Dissociation Efficiency of Charge Transfer Excitons in DBP/C <sub>70</sub> Heterojunctions . . . . .	61
<b>IV.</b>	<b>Energy Losses in Organic Photovoltaics . . . . .</b>	<b>64</b>
4.1	Introduction . . . . .	64
4.2	Theory and Modeling . . . . .	66
4.3	Experimental Section . . . . .	70
4.4	Results . . . . .	71
4.5	Discussion . . . . .	78
4.6	Designing Strategies for Low Energy Loss . . . . .	81
<b>V.</b>	<b>Exciton Dynamics in an Organic Type-I Guest-Host Heterojunction . . . . .</b>	<b>84</b>
5.1	Introduction . . . . .	84
5.2	Theory . . . . .	85
5.3	Experimental Section . . . . .	87
5.4	Results . . . . .	89
5.5	Discussion . . . . .	94
<b>PART II:</b>	<b>Energy Transfer in van der Waals Bonded Organic-Inorganic Heterojunctions . . . . .</b>	<b>100</b>
<b>CHAPTER</b>		
<b>VI.</b>	<b>Introduction to Organic-Inorganic Heterojunctions . . . . .</b>	<b>101</b>
6.1	Why Use an Organic-Inorganic Heterojunction . . . . .	101

6.2	Fundamentals of Organic-Inorganic Heterojunctions . . . . .	103
6.3	Hybrid Heterojunction Employing Two-Dimensional Transition Metal Dichalcogenides . . . . .	107
6.3.1	Two-Dimensional Transition Metal Dichalcogenides . . . . .	107
6.3.2	Synthesis and Transfer Techniques . . . . .	111
6.3.3	Two-Dimensional Organic/Transition Metal Dichalcogenide Heterojunctions . . . . .	113
<b>VII.</b>	<b>Dipole Aligned Energy Transfer Between Excitons in a Two-dimensional Transition Metal Dichalcogenide and an Organic Semiconductor . . . . .</b>	<b>116</b>
7.1	Introduction . . . . .	116
7.2	Experimental Section . . . . .	117
7.3	Dipole Aligned Förster Transfer at PTCDA/MoSe <sub>2</sub> Heterojunction . . . . .	118
<b>VIII.</b>	<b>Photoresponse of an Organic Semiconductor/Two-Dimensional Transition Metal Dichalcogenide Heterojunction . . . . .</b>	<b>124</b>
8.1	Introduction . . . . .	124
8.2	Theoretical Calculations of 2D Hybrid Charge Transfer State . . . . .	125
8.3	Experimental Section . . . . .	127
8.4	Photoresponse of PTCDA/WS <sub>2</sub> Heterojunction . . . . .	129
8.5	Discussion . . . . .	132
<b>IX.</b>	<b>Outlook . . . . .</b>	<b>136</b>
9.1	Prospects for Organic Photovoltaics . . . . .	136
9.2	Future Work on 2D Organic/Transition Metal Dichalcogenide Heterojunctions . . . . .	140
	<b>APPENDICES . . . . .</b>	<b>146</b>
	<b>BIBLIOGRAPHY . . . . .</b>	<b>154</b>



## LIST OF FIGURES

### Figure

1.1	Organic optoelectronic products . . . . .	3
1.2	Energy transfer processes in the organic optoelectronic devices . . .	4
1.3	Chemical structures of small molecule, DBP and polymer, P3HT . .	5
1.4	Crystal structures of Si and C <sub>60</sub> . . . . .	7
1.5	The $\sigma$ and $\pi$ bonds between hybridized carbon atoms . . . . .	8
1.6	Six $p$ orbitals of carbons in benzene produce the molecular frontier orbitals . . . . .	9
1.7	The orbital and state diagrams of $S_0$ and $S_1$ states . . . . .	11
1.8	Three types of excitons and their different characteristics . . . . .	14
1.9	Optical spectra and the corresponding energy diagram of DBP . . .	16
1.10	Three exciton energy transfer approaches between molecules . . . .	19
1.11	The apparatus for thermal gradient sublimation purification . . . .	21
1.12	Schematic of the vacuum thermal evaporation system . . . . .	23
1.13	Three types of organic HJs . . . . .	24
1.14	Structures of type-II donor/acceptor HJs . . . . .	26
1.15	Schematic of photogeneration processes in the donor-acceptor HJ . .	27
1.16	Schematic of J-V characteristic of an ideal photodiode . . . . .	28
1.17	Energy diagram of exciton dissociation mechanisms at the donor-acceptor HJ . . . . .	32
1.18	Gaussian distribution of density of states around energy level $E_0$ . .	33
1.19	Energy diagram of the classical Marcus transfer theory . . . . .	35
1.20	The device structure of a single junction OPV . . . . .	37
2.1	Intensity of the C <sub>70</sub> X-ray diffraction peak of DBP/C <sub>70</sub> blends . . .	41
2.2	TEM images of DBP/C <sub>70</sub> blends . . . . .	42
2.3	3D simulation of the morphology of DBP/C <sub>70</sub> blends . . . . .	43
2.4	Average C <sub>70</sub> cluster radius vs. C <sub>70</sub> concentration in the blends . . .	44
2.5	3D simulation of the DBP percolating paths . . . . .	46
3.1	EL spectra of OPV with different C <sub>70</sub> concentrations in the blends .	51
3.2	Steady-state PL spectra and CT states energies of DBP/C <sub>70</sub> blends	52
3.3	Calculated singlet energies of different combinations of DBP and C <sub>70</sub> and charge density distribution of the CT states . . . . .	53
3.4	Time-resolved PL for DBP/C <sub>70</sub> blends at different temperatures . .	54

3.5	Measured and calculated energies and recombination rate of CT2 states as functions of $C_{70}$ domain radius . . . . .	57
3.6	STEM image of DBP/ $C_{70}$ multi-quantum well structure . . . . .	59
3.7	PL of DBP/ $C_{70}$ multi-quantum well structures . . . . .	60
3.8	EQE at reverse bias for OPVs with different $C_{70}$ concentration . . .	62
4.1	Energy diagrams of charge transfer and non-radiative recombination processes . . . . .	66
4.2	Charge transfer and non-radiative recombination rates vs. the energy loss as a function of electron-phonon coupling . . . . .	69
4.3	The molecular structures and charge density distributions of NFAs .	72
4.4	Exciton binding energy and static polarizability vs. the size of acceptor molecules . . . . .	73
4.5	Measured charge transfer rate vs. the energy offset at the HJs comprising fullerene and NFAs . . . . .	75
4.6	Measured charge transfer rate vs. temperature at NFA based HJs .	76
4.7	EQE of CT states EL from OPVs using fullerene and NFAs . . . . .	77
4.8	EL and EQE spectra of OPVs using fullerene and NFAs . . . . .	77
5.1	An archetypical fluorescent guest-host system . . . . .	86
5.2	Schematic of the pump-probe triplet absorption measurement . . . . .	88
5.3	PL turn-on transient for a DCM2:Alq <sub>3</sub> film . . . . .	89
5.4	Temperature dependence of the rates of singlet-triplet annihilation .	90
5.5	Time resolved PL response of the DCM2:Alq <sub>3</sub> film to the 1.5 ns pump pulse . . . . .	90
5.6	The edge emission obtained in the guest triplet absorption measurement of a 3% vol. DCM2 in Alq <sub>3</sub> film . . . . .	92
5.7	Transient response of the guest triplet density vs. temperature of a 3% vol. DCM2 in Alq <sub>3</sub> film . . . . .	93
5.8	Arrhenius plots of the TTA rate obtained for DCM2:Alq <sub>3</sub> films . . .	96
6.1	Schematic of photogeneration processes at the hybrid type-II HJ . .	104
6.2	EL spectra of HCTE at the ZnO/CBP HJ vs. temperature . . . . .	106
6.3	A 2D device structure and crystalline structure of TMDC . . . . .	108
6.4	The simplified band diagram and optical spectra of a monolayer of MoSe <sub>2</sub> . . . . .	110
6.5	2D materials processing techniques . . . . .	112
7.1	Schematic of PTCDA, MoSe <sub>2</sub> , and the Fourier space imaging setup	118
7.2	Fourier space images of MoSe <sub>2</sub> , PTCDA and calculated emission patterns of in-plane and out-of-plane dipoles . . . . .	119
7.3	Differential reflectivity and PL of PTCDA, MoSe <sub>2</sub> , and their HJ . .	120
7.4	Time-resolved PL of PTCDA, MoSe <sub>2</sub> , and their HJ . . . . .	121
7.5	Photoluminescence excitation spectral intensity of MoSe <sub>2</sub> . . . . .	122
8.1	Energy level diagram and illustration of PTCDA/WS <sub>2</sub> HJ and the energy eigenvalues of HCTE . . . . .	127
8.2	PL and time-resolved PL of PTCDA, WS <sub>2</sub> , and their HJ . . . . .	129
8.3	Absorbed power distribution and absorption coefficients of WS <sub>2</sub> and PTCDA in the hybrid cell . . . . .	131

8.4	EQE and IQE of the PTCDA/WS <sub>2</sub> hybrid cell . . . . .	132
8.5	Photocurrent density and EQE vs. electric field in a PTCDA photoconductor . . . . .	133
9.1	The narrow absorption bands of a-d-a-type NFAs at different wavelength . . . . .	137
9.2	Schematic of the transfer process at the HJ and low temperature PL of the singlet and triplet states of IT-IC . . . . .	139
9.3	Photoluminescence of exfoliated and CVD-grown 2D WS <sub>2</sub> . . . . .	141
9.4	Unsuccessful examples of 2D TMDC transfer . . . . .	142

## LIST OF TABLES

### Table

4.1	The intramolecular reorganization energy due to electron transfer of archetypical fullerenes and NFAs. . . . .	74
5.1	Singlet lifetime of a 3% vol. DCM2 in Alq <sub>3</sub> film vs. temperature . .	91
5.2	Triplet-triplet annihilation rate vs. temperature for Alq <sub>3</sub> . . . . .	94
5.3	Guest triplet natural lifetime vs. temperature in DCM2:Alq <sub>3</sub> films .	95
6.1	Comparison of the physical properties of organic and inorganic semi-conductors . . . . .	102
A.1	Chemical structures and short names of molecules used in Ch. IV. .	148
B.1	The static polarizability tensor of fullerene and NFAs calculated by DFT . . . . .	153

## LIST OF APPENDICES

### Appendix

- A. Chemical structures and short names of molecules used in Chapter IV. 147
- B. Polarizability of Fullerene and Nonfullerene Acceptors . . . . . 152

## LIST OF ABBREVIATIONS

### Acronyms

<b>2D</b>	two-dimensional
<b>3D</b>	three-dimensional
<b>ALD</b>	atomic layer deposition
<b>BIPV</b>	building integrated photovoltaics
<b>CB</b>	conduction band
<b>CCD</b>	charge-coupled device
<b>CT</b>	charge transfer
<b>CVD</b>	chemical vapor deposition
<b>DFT</b>	density functional theory
<b>DOS</b>	density of states
<b>DSSC</b>	dye-sensitized solar cell
<b>EL</b>	electroluminescence
<b><i>EQE</i></b>	external quantum efficiency
<b><i>FC</i></b>	Franck-Condon
<b>FCC</b>	face-centered cubic
<b>FET</b>	field-effect transistor
<b>FIB</b>	focused ion beam
<b>FRET</b>	Förster resonant energy transfer
<b>FWHM</b>	full width at half maximum
<b>GDM</b>	Gaussian disorder model

<b>HCTE</b>	hybrid charge transfer exciton
<b>HJ</b>	heterojunction
<b>HOMO</b>	highest occupied molecular orbital
<b>ICT</b>	intramolecular charge transfer
<b><i>IQE</i></b>	internal quantum efficiency
<b>IRF</b>	instrument response function
<b>ITO</b>	indium tin oxide
<b>J-V</b>	current density-voltage
<b><i>J<sub>sc</sub></i></b>	short-circuit current
<b>KMC</b>	kinetic Monte Carlo
<b>LUMO</b>	lowest unoccupied molecular orbital
<b>NFA</b>	nonfullerene acceptor
<b>NIR</b>	near infrared
<b>OI</b>	organic-inorganic
<b>OLED</b>	organic light emitting diode
<b>OPV</b>	organic photovoltaic
<b>OVJP</b>	organic vapor jet printing
<b>OVPD</b>	organic vapor phase deposition
<b><i>PCE</i></b>	power conversion efficiency
<b>PDI</b>	perylene diimide
<b>PL</b>	photoluminescence
<b>PLE</b>	photoluminescence excitation
<b>QD</b>	quantum dot
<b>R2R</b>	roll-to-roll
<b>SSA</b>	singlet-singlet annihilation
<b>SPA</b>	singlet-polaron annihilation
<b>STA</b>	singlet-triplet annihilation

<b>STEM</b>	scanning transmission electron microscope
<b>TADF</b>	thermally activated delayed fluorescence
<b>TDDFT</b>	time dependent density functional theory
<b>TEM</b>	transmission electron microscope
<b>TPA</b>	triplet-polaron annihilation
<b>TTA</b>	triplet-triplet annihilation
<b>UV</b>	ultraviolet
<b>VB</b>	valence band
<b><math>V_{oc}</math></b>	open-circuit voltage
<b>VTE</b>	vacuum thermal evaporation

## Chemical Names

<b>Alq<sub>3</sub></b>	tris(8-hydroxyquinolato) aluminum
<b>Bphen</b>	bathophrenanthroline
<b>Br<sub>2</sub>-DBP</b>	dibenzo([f,f']-4,7'-di[4bromophenyl]-4',7'-diphenyl)diindeno[1,2,3-cd:1',2',3'-lm]-perylene
<b>CBP</b>	4,4-bis(N-carbazolyl)-1,1-biphenyl
<b>DBP</b>	tetraphenyldibenzoperiflanthene
<b>DCM2</b>	4-(dicyanomethylene)-2-methyl-6-julolidyl-9-enyl-4H-pyran
<b>F4TCNQ</b>	2,3,5,6-tetrafluoro-7,7,8,8-tetracyanoquinodimethane
<b>MDMO-PPV</b>	poly[2-methoxy-5-(30,70-dimethyloctyloxy)-1,4-phenylenevinylene]
<b>MPS</b>	(3-mercaptopropyl) trimethoxysilane
<b>NPD</b>	N,N'-Di(1-naphthyl)-N,N'-diphenyl-(1,1'-biphenyl)-4,4'-diamine
<b>NTCDA</b>	3,4,7,8-naphthalene tetracarboxylic dianhydride
<b>P3HT</b>	Poly(3-hexylthiophene-2,5-diyl)
<b>PBPMSi</b>	poly[biphenyl(methyl)silylene]
<b>PC<sub>61</sub>BM</b>	[6,6]-phenyl-C61-butyric acid methyl ester



<b>PC<sub>71</sub>BM</b>	[6,6]-phenyl-C71-butyric acid methyl ester
<b>PDMS</b>	polydimethylsiloxane
<b>PF2/6</b>	poly(2,7-(9,9-bis(2-ethylhexyl)fluorene))
<b>PMMA</b>	poly(methylmethacrylate)
<b>PTCDA</b>	3,4,9,10-perylene tetracarboxylic dianhydride
<b>TDBC</b>	5,5',6,6'- tetrachloro-1,1'- diethyl-3,3'- di(4-sulfobutyl)- benzimidazolocarboaniline
<b>TMDC</b>	transition metal dichalcogenide
<b>TCNQ</b>	7,7,8,8-tetracyanoquinodimethane
<b>TTF</b>	tetrathiafulvalene
<b>TFSI</b>	bis(trifluoromethane)

## ABSTRACT

Rapid technological developments of photodiodes using organic semiconductors have gained significant attention over the past years. Innovative molecular and thin-film morphological designs of organic heterojunctions (HJs) are still required to enable devices such as organic photovoltaics (OPVs) approaching the market-entry-level performance. This thesis explores energy transfer properties of HJs as functions of molecular geometry, blend HJ structures, and material combinations, providing guidelines for future designs of organic optoelectronic material systems.

In the first part of this thesis, we investigate the charge transfer (CT) properties in small-molecule blend HJs comprising the nonpolar donor, tetraphenyldibenzoperiflanthene (DBP), and the acceptor, C<sub>70</sub>. A kinetic Monte Carlo model along with transmission electron microscopy and X-ray diffraction are used to quantitatively evaluate the crystallinity and percolation of the donor and acceptor at various blend ratios. A quantum confinement model is used to describe the dependence of both CT state energy and lifetime on the C<sub>70</sub> or DBP crystalline size. We identify that the delocalized CT2 state at the crystalline phase having >90% dissociation efficiency significantly contributes to efficient photogeneration in highly dilute (>80% C<sub>70</sub>) DBP/C<sub>70</sub> HJs.

We also explore the loss mechanisms of OPVs during the transition from the photo-generated exciton energy of donor or acceptor ( $E_{ex}$ ) to the open circuit energy ( $qV_{oc}$ ). We derive universal relationships connecting the polarizabilities and exciton binding

energies ( $E_B$ ) to molecular geometry. The design of large conjugated volumes along with the juxtaposition of electron donating and withdrawing groups characteristic of thiophene-based nonfullerene acceptors significantly decreases their  $E_B$  and electron-phonon couplings, compared to more compact and symmetric fullerenes, leading to the decrease of energy loss by  $>0.2$  eV and increase of efficiency for OPVs.

Furthermore, we explore the exciton energy transfer and annihilation at the high-exciton-density regime of an organic type-I HJ comprising 4-(dicyanomethylene)-2-methyl-6-julolidyl-9-enyl-4H-pyran (DCM2) and tris(8-hydroxyquinolato) aluminum ( $\text{Alq}_3$ ). Interactions of singlet and triplet excitons show significantly different temperature dependence, suggesting their different energy transfer mechanisms, and eventually allowing for a separate management of singlet and triplet energy transport in organic material systems.

Second part of this thesis presents optoelectronic properties and applications of a new class of organic-inorganic HJs comprising a monolayer of transition metal dichalcogenide (TMDC) and a thin film of organic semiconductor. Both theoretical and experimental investigations of a HJ employing  $\text{WS}_2$  and 3,4,9,10-perylene tetracarboxylic dianhydride (PTCDA) indicate that Frenkel states in PTCDA and two-dimensional (2D) Wannier-Mott states in the  $\text{WS}_2$  dissociate to form hybrid CT excitons at the interface that subsequently dissociate into free charges that are collected at opposing electrodes. Approximately 30% Förster resonant energy transfer is observed between excitons in the PTCDA and a monolayer  $\text{MoSe}_2$ . This energy transfer from low mobility organic materials to higher mobility 2D semiconductors along with their extremely large oscillator strengths presents an attractive platform for developing new types of photodetection and energy harvesting systems.

## PART I

# Energy Transfer at Organic Heterojunctions

# CHAPTER I

## Introduction

### 1.1 Overview

Optoelectronic semiconductor devices have been influential in shaping the development of our society in many ways: light emitting diodes in displays and lighting; photovoltaics in renewable energy generation; photodetectors in imaging and sensing. Organic semiconductor is an important material category for optoelectronic applications that has been developed and implemented over the past decades. While organic photovoltaics (OPVs) and organic photodetectors are still transitioning from the laboratory to broadly commercialized products, organic light emitting diodes (OLEDs) have made significant progress into the market and have found wide acceptance in the areas of information display and solid-state lighting. Figure 1.1 shows an example of a commercially available curved OLED wallpaper display (left) and a demonstration of curved organic solar panels installed on a bus shelter in San Francisco (right).

The continuous technological developments of organic optoelectronics have been driven by a fundamental understanding of the nature of excitonic energy transfer and charge transport phenomena in organic semiconductors. Optoelectronic devices transfer energy and information from photons to electrons, or vice versa. Control over every aspect of the energy transfer process at both macroscopic and microscopic scales is essential for successful organic device design. Figure 1.2 summarizes the



Figure 1.1: Organic optoelectronic products: (left) an example of a commercially available curved OLED wallpaper display; (right) the curved organic solar panels installed on a bus shelter in San Francisco. Images from the news (<https://www.commercialintegrator.com/digital-signage/digital-signage-hardware/lg-oled-wallpaper-video-wall-dse/> and <https://inhabitat.com/solar-powered-bus-shelter-unveiled-in-san-francisco/>)

major energy transfer processes that occur in a light emitting diode, i.e. electrical to optical transfer from left to right, and a photodiode, i.e. optical to electronic transfer from right to left. Electrons and holes at metal-organic interfaces of the light emitting diode are injected from the electrodes into the lowest unoccupied molecular orbital (LUMO) and highest occupied molecular orbital (HOMO) of the organic layers, respectively. They drift in opposite directions under the influence of the static electric field generated by the forward bias, and subsequently, capture one another to recombine at the active layer, leading to the formation of excitons. During their characteristic lifetimes, excitons can hop among molecules and interact with each other via an energy-transfer processes. Excitons radiatively decay and generate photons that are coupled out of the devices. The organic photodiode, however, operates in the opposite direction, as illustrated in the bottom of Fig. 1.2. The photons are absorbed in the organic layers and generate excitons that diffuse towards the heterojunction (HJ), where they can dissociate into free charges as a result of a charge transfer process

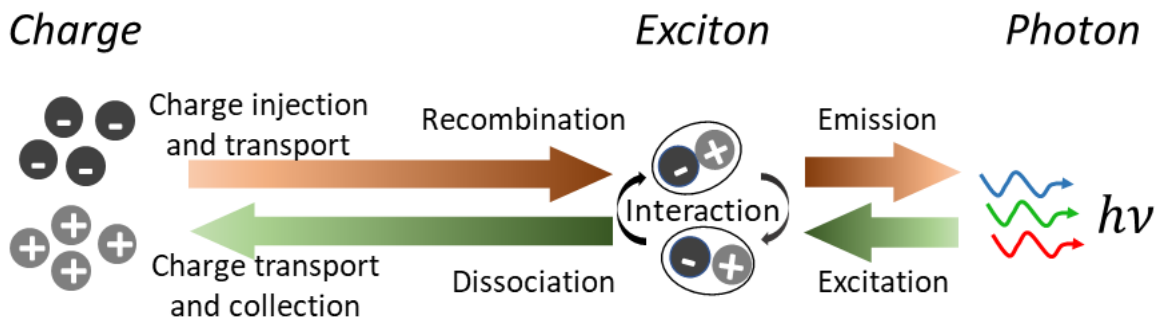


Figure 1.2: Energy transfer processes in the organic optoelectronic devices.

between the electron donor and acceptor molecular layers. The charges that remain separated drift in the organic layers under the influence of a superimposed electric field generated by the voltage bias and the built-in potential between two electrodes, and ultimately are collected at the electrodes.

This thesis focuses on the photocurrent generation process in the organic photodiode and presents recent works and understanding of exciton physics and the energy transfer process at organic HJs. The thesis is divided into nine Chapters. We begin by reviewing the unique characteristics of organic semiconductors and introducing important concepts of optical transitions, excitonic properties and operational principles of organic donor-acceptor HJs. Chapter II examines the morphology of organic bulk HJs and its dependence on the donor/acceptor blend ratio. Chapters III and IV present studies on the energy and dynamics of charge transfer (CT) excitons, charge transfer efficiency, and energy loss vs. morphologies of HJs and molecular structures of acceptors. Chapter V explores exciton energy transfer and annihilation dynamics in the presence of high excitation intensity at an organic type-I HJ. In Chapters VI to VIII, we explore emerging organic-inorganic HJs and construct van der Waals bonded HJs by combining organic semiconductors with two-dimensional (2D) transition metal dichalcogenide (TMDCs). Chapter IX presents conclusions and a future outlook.

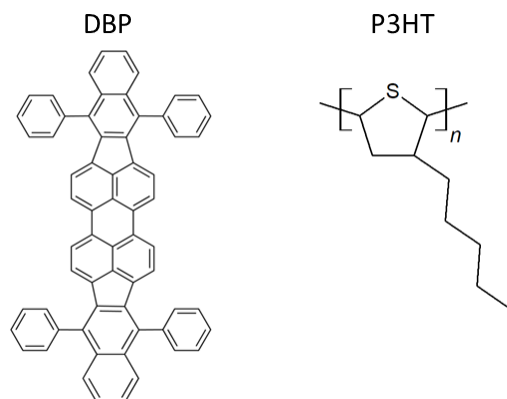


Figure 1.3: Chemical structures of small molecule, DBP and polymer, P3HT.

## 1.2 Properties of Organic Semiconductors

Organic semiconductors are a class of materials that are based on carbon and hydrogen atoms, with a few heteroatoms such as oxygen, nitrogen, or sulfur. In the field of organic optoelectronics, organic semiconductors are generally classified into two types: small molecule and polymer. Small molecules have well-defined structures and molecular weights, e.g. tetraphenyldibenzoperiflanthene (DBP) as illustrated in Fig. 1.3 (left). Polymers consist of variable chain lengths of repeating monomers with indefinite molecular weight, such as Poly(3-hexylthiophene-2,5-diyl) (P3HT) shown in Fig. 1.3 (right). In contrast to well-established inorganic semiconductors, such as Si, GaAs, InP that are highly crystalline with strong covalent bonds between atomic constituents (see Fig. 1.4 (left)), organic semiconductors consist of covalently bonded molecular constituents held together by van der Waals bonds. The unique bonding characteristics of organic materials directly lead to their distinct optical properties, mechanical versatility, unlimited synthetic and processing potential, and hence extraordinary device applications compared to their inorganic counterparts.



### 1.2.1 Intermolecular Interactions

Van der Waals bonds between molecules arise from the interactions between fixed or induced dipoles of the molecules. In non-polar molecules, instantaneous fluctuations in their equilibrium electron distributions induce a dipole that subsequently produces a counter-polarized dipole in the neighboring molecules. The net attraction between two induced dipoles follows the *London relationship*,<sup>[1]</sup> where the interaction potential decreases as  $r^{-6}$ . Here,  $r$  is the relative distance between two molecular dipoles. A similar relationship exists for the attraction of fixed dipoles and fixed-induced dipoles between molecules that have ground state dipole moments. The total attraction potential is, therefore, the superposition of the potentials of all interactions. The attraction force is counteracted by repulsion of the electronic orbital due to the *Pauli Exclusion Principle*. Generally, a *Lennard-Jones 6-12 potential* is used to approximate the intermolecular interaction:

$$U(r) = 4\epsilon\left[\left(\frac{\sigma}{r}\right)^{12} - \left(\frac{\sigma}{r}\right)^6\right], \quad (1.1)$$

where  $\epsilon$  and  $\sigma$  are empirical parameters that correspond to the strength of attraction and the inter-particle distance at which the potential is zero, respectively.

In principle, the optimum separation between two molecules in the solid is obtained by taking the first derivative of  $U(r)$  with respect to  $r$  and set the derivative to zero. The minimum energy and crystal structure of the molecular solid is determined by iterating the calculation for each molecule with respect to all neighboring molecules. In practice, other factors such as the molecular shape and internal degrees of freedom for non-rigid molecules may deviate from this analysis. More sophisticated molecular dynamics calculations, including all pairwise interactions between atoms comprising the separate molecules, are then necessary.

Figure 1.4 (right) shows an example of the ideal face-centered cubic (FCC) crys-

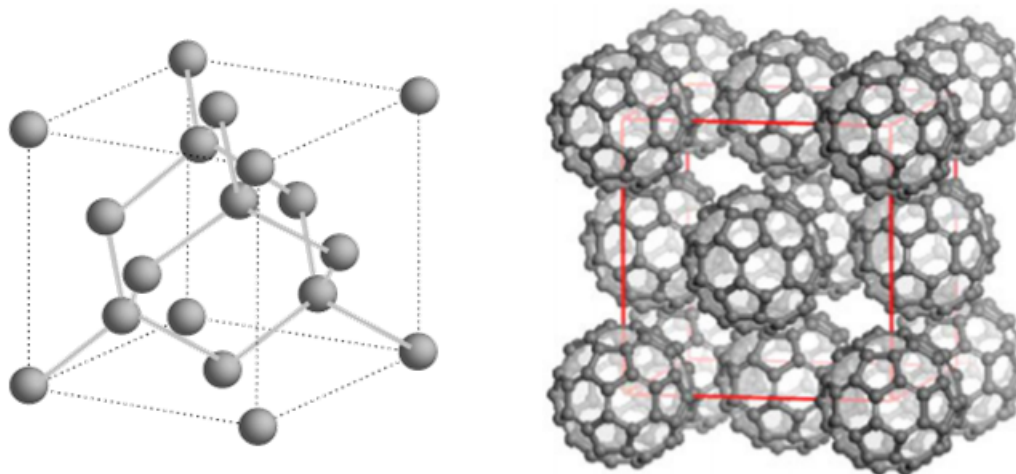


Figure 1.4: Crystal structures of Si and C<sub>60</sub>. Image adapted from ref. [2] and [3]

tal structure of fullerene C<sub>60</sub> obtained by calculation. In practical cases, however, instead of forming a perfect single crystalline structure, organic solids form at a local energy minimum, and they have a variety of morphology ranging from amorphous to polycrystalline. Depending on the magnitude of external driving forces that perturb the structure from its local energy minimum, the morphology of the organic thin film and its corresponding electronic and optical properties can be further adjusted.

### 1.2.2 Intramolecular Bonding and Molecular Orbitals

#### *Atomic orbitals*

Atomic constituents within the molecule form strong covalent bonds (bond energies of several eV) between their unpaired valence electrons. Carbon atoms are the major building blocks of organic molecules with four valence electrons distributed over four outer-shell orbitals,  $2s2p_x2p_y2p_z$ . A linear superposition (also known as hybridization) of  $2s$  and  $2p$  orbitals yields  $sp^n$  orbitals, where  $n=1, 2,$  or  $3$  depending on the number of  $p$  orbitals participating in the hybridization. (See Fig. 1.5) Generally, two types of covalent bonds exist between carbon atoms: the  $\sigma$  bond through the

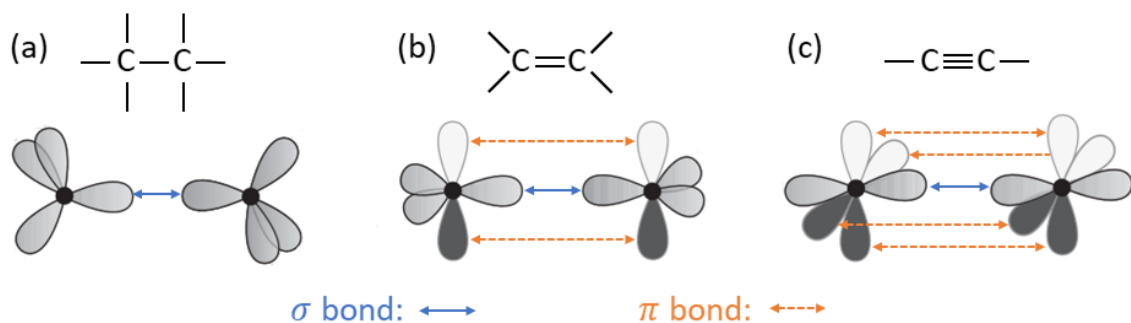


Figure 1.5: The  $\sigma$  and  $\pi$  bonds between (a)  $sp^3$ , (b)  $sp^2$ , and (c)  $sp$  hybridized carbon atoms. Figure adapted from ref. [4]

overlap of two  $sp^n$  hybridized orbitals, and the  $\pi$  bond between lone  $p$  orbitals. All bonding schemes are shown in Fig. 1.5. Due to the axial symmetry of  $\sigma$  bonds, two carbon atoms are free to rotate with respect to the bonding axis, unless a  $\pi$  bond is present. The  $sp^2$  hybridization shown in Fig. 1.5(b) is the dominant bonding configuration in conjugated organic molecules, where carbon atoms are connected by  $\sigma$  bonds within the plane of  $sp^2$  orbitals and the lone electrons in the  $p$  orbitals are shared through the  $\pi$  bonds by the conjugated group of atoms, which creates a delocalized electron cloud over the entire conjugated backbone.

#### *Atomic-to-molecular orbitals*

The total number of molecular orbitals is equal to the number of atomic orbitals that participate in bonding. The mutual interactions of atomic orbitals through  $\sigma$  or  $\pi$  bonds incur an energy splitting of bonding and anti-bonding molecular orbitals and, hence, determines the energy structure of the molecules. Figure 1.6 depicts the schematic of *frontier  $\pi$  orbitals*, in particular, the highest occupied molecular orbital (HOMO) and lowest unoccupied molecular orbital (LUMO) in benzene that are generated by the overlap of six lone  $p$  orbitals in  $sp^2$  hybridized carbon. The bonding and anti-bonding  $\pi$  orbitals are denoted as  $\pi$  and  $\pi^*$ , respectively. Note that there are two pairs of degenerate orbitals,  $\pi_2$  and  $\pi_3$ , and  $\pi_4^*$  and  $\pi_5^*$ . According to the *Auf-*

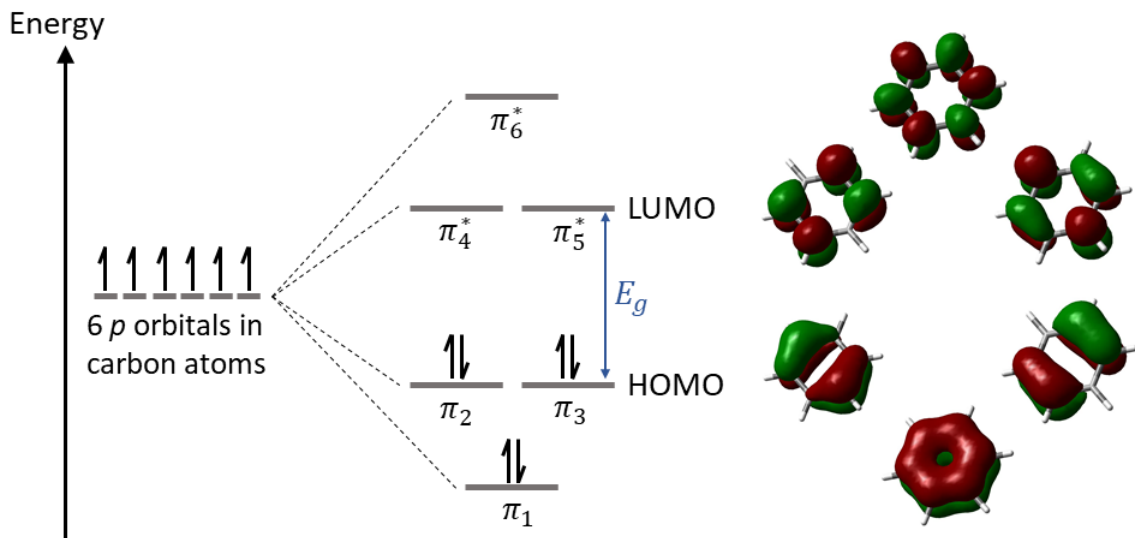


Figure 1.6: Six  $p$  orbitals of carbons of benzene produce bonding and anti-bonding molecular frontier orbitals. The six valence electrons fill the orbitals pairwise, resulting in HOMO and LUMO. The energy gap of a molecule between HOMO and LUMO is denoted as  $E_g$ . The molecular orbitals of benzene shown on the right are calculated using the density functional theory (DFT).

*bau* and *Pauli Exclusion Principles*, electrons with opposite spins fill each molecular orbital pairwise until reaching the HOMO level in the ground state configuration, leaving the anti-bonding orbitals empty.

There are many approaches for calculating molecular orbitals, ranging from *semi-empirical* to *ab initio* methods depending on the level of approximation. Density functional theory (DFT)<sup>[5]</sup>, an increasingly popular approach, is used in this thesis. Generally, six primitive Gaussians are employed to construct each core atomic orbital basis function. The valence orbitals are composed of two basis functions each: one is a linear combination of 3 primitive Gaussian functions; the other is a single primitive Gaussian function. The overall basis set is hence denoted as 6-31G. In DFT, the  $n$ -body problem based on an electronic wavefunction  $\psi$  with  $3n$  degrees of freedom is reduced to a single-body problem focusing on electron density that has only 3 spatial variables. In this approximation, the density  $\rho(\mathbf{r})$  is constructed by a superposition

of “Kohn-Sham” orbitals  $\phi(\mathbf{r})$  for  $n$  electrons in the molecule:

$$\rho(\mathbf{r}) = \sum_i^n |\phi_i(\mathbf{r})|^2. \quad (1.2)$$

The orbitals and, hence, electron density are solved iteratively and self-consistently using a one-particle Schrödinger-like equation, known as the Kohn-Sham equation:

$$\left( -\frac{\hbar^2}{2m} \nabla^2 + v_{\text{eff}}(\mathbf{r}) \right) \phi_i(\mathbf{r}) = \varepsilon_i \phi_i(\mathbf{r}), \quad (1.3)$$

where  $\hbar$  is the Planck constant divided by  $2\pi$ ,  $m$  is the electron mass,  $\varepsilon_i$  is the energy that corresponds to  $\phi_i$ , and  $v_{\text{eff}}$  is the Kohn-Sham potential which is the sum of external  $v_{\text{ext}}$ , Coulomb  $v_c$ , and exchange-correlation  $v_{\text{xc}}$  potentials. More in-depth detail of DFT can be found in ref. [5].

## 1.3 Excitons in Organic Semiconductors

### 1.3.1 Molecular Wavefunction and Exciton States

Previous discussions of molecular orbitals have considered stationary atomic nuclei in the molecule. It provides the possible configurations of electron distributions over the molecular orbitals. Shown in Fig. 1.7 (left) are two most common configurations: (i) all electrons fill up to the HOMO, known as the ground state,  $S_0$ ; (ii) one of the electrons excited to the LUMO leaves the other with the opposite spin in the HOMO, known as the first singlet excited state,  $S_1$ . The corresponding *state diagram* is illustrated on the right. To accurately describe the properties of these electronic states, interactions between electrons, or electrons and nuclear vibrations cannot be ignored. A full molecular wavefunction is written as:

$$\Psi = \psi(\{\mathbf{r}_i\}, \{\mathbf{R}_I\}) \chi(\{\mathbf{R}_I\}) \sigma(\{S_i\}, \{m_{si}\}), \quad (1.4)$$

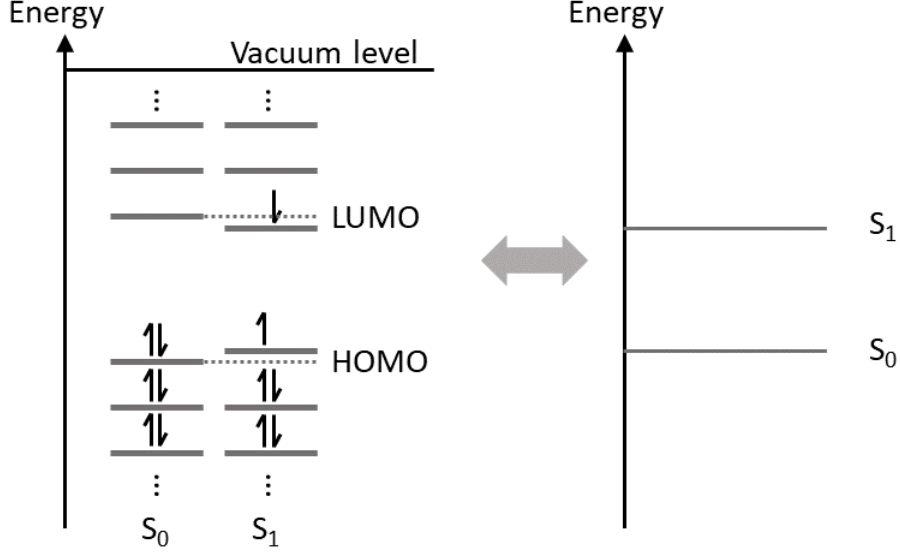


Figure 1.7: The orbital (left) and state (right) diagrams of singlet  $S_0$  and  $S_1$  states. In the orbital diagram, the energy levels of HOMO and LUMO at  $S_1$  state are shifted due to the Coulomb interaction between the electron and the hole. Image is adapted from ref.<sup>[4]</sup>

where the total wavefunction is divided into the electronic spatial ( $\psi$ ), nucleus vibrational ( $\chi$ ) and electronic spin ( $\sigma$ ) components, and  $\{\mathbf{r}_i\}$  is the  $i^{th}$  spatial vector of  $n$  electrons in the molecule,  $\{\mathbf{R}_I\}$  is the  $I^{th}$  nuclear coordinate vector of  $N$  nuclei,  $\{S_i\}$  is the total spin quantum number, and  $\{m_{si}\}$  the projected spin quantum number.

The vibrational motions of the nuclei in a molecule are described by  $\chi(\{\mathbf{R}_I\})$ . Generally, the interatomic interaction is approximated by an infinite potential of the simple harmonic oscillator:

$$V = \frac{1}{2}m\omega^2\Delta Q^2, \quad (1.5)$$

where  $m$  is the reduced mass of the nucleus,  $\omega$  is the vibrational frequency, and  $\Delta Q = \sum_I^N(\Delta\mathbf{R}_I)$  is an integrated nuclear displacement. The vibrational energy,  $E = (n + \frac{1}{2})\hbar\omega$ , is quantized, where  $n$  is the excited quanta. Alternatively, a more accurate asymmetric *Morse potential* can be employed:<sup>[6]</sup>

$$V = D_e(1 - e^{-a\Delta Q})^2, \quad (1.6)$$

where  $D_e$  is the potential well depth from the minimum to the dissociation energy, and  $a = \sqrt{k/2D_e}$ . Here,  $k$  is the force constant of oscillation. Near the minimum, the *Morse potential* surface is approximately harmonic.

Different atoms comprising the molecule oscillate at a different frequency  $\omega_i$  and form a set of coupled oscillators. For example, the stretching mode of a carbon-carbon double bond has a frequency of  $\sim 1600 \text{ cm}^{-1}$ , the torsion mode of phenyl rings has a frequency of  $\sim 70 \text{ cm}^{-1}$  and the stretching mode of a carbon-hydrogen bond has a frequency of  $\sim 3000 \text{ cm}^{-1}$ .<sup>[4]</sup> The vibronic progression of optical spectra is often broadened, and only the effective mode (dominantly carbon-carbon stretching) and a mean energy of quanta can be seen. An example will be shown in Fig. 1.9 in section 1.3.2. Due to the interaction between electrons and nuclei, the vibrational energy levels are added to the electronic energy levels to fully describe the property of each electronic state.

When considering the spin wavefunction  $\sigma$ , the two pairwise outermost valence electrons at  $\mathbf{r}_1$  and  $\mathbf{r}_2$  in the molecular orbitals are of particular interest. Their total spin wavefunctions have four possible configurations:

$$\sigma(0, 0) = \frac{1}{\sqrt{2}} [|\uparrow\downarrow\rangle - |\downarrow\uparrow\rangle], \quad (1.7)$$

$$\begin{cases} \sigma(1, +1) = [|\uparrow\uparrow\rangle] \\ \sigma(1, 0) = \frac{1}{\sqrt{2}} [|\uparrow\downarrow\rangle + |\downarrow\uparrow\rangle] \\ \sigma(1, -1) = [|\downarrow\downarrow\rangle] \end{cases} \quad (1.8)$$

Here,  $|\uparrow\rangle$  and  $|\downarrow\rangle$  denote two different spins for each electron, i.e.  $m_s = \frac{1}{2}$  and  $-\frac{1}{2}$ , respectively. The anti-symmetric spin state  $\sigma(0, 0)$  is known as the singlet state, while three symmetric spin states  $\sigma(1, +1)$ ,  $\sigma(1, 0)$ ,  $\sigma(1, -1)$  are the triplet states. According to the *Pauli exclusion principle*, the total electronic wavefunction  $\psi(\mathbf{r}_1, \mathbf{r}_2)\sigma(S, m_s)$

of these two electrons must be asymmetric under particle exchange; that is to say, the spatial wavefunction of singlet ( $\psi_S$ ) and triplet states ( $\psi_T$ ) should be symmetric and asymmetric, respectively:

$$\begin{aligned}\psi_S(\mathbf{r}_1, \mathbf{r}_2) &= \frac{1}{\sqrt{2}}(\psi_a(\mathbf{r}_1)\psi_b(\mathbf{r}_2) + \psi_a(\mathbf{r}_2)\psi_b(\mathbf{r}_1)) \\ \psi_T(\mathbf{r}_1, \mathbf{r}_2) &= \frac{1}{\sqrt{2}}(\psi_a(\mathbf{r}_1)\psi_b(\mathbf{r}_2) - \psi_a(\mathbf{r}_2)\psi_b(\mathbf{r}_1))\end{aligned}\tag{1.9}$$

Here,  $\psi_a$  and  $\psi_b$  are the spatial functions of molecular orbitals where the two electrons are located. The energy of singlet and triplet states can then be calculated:

$$\begin{aligned}E_S &= \frac{e^2}{8\pi\epsilon_0} \langle \psi_a(\mathbf{r}_1)\psi_b(\mathbf{r}_2) + \psi_a(\mathbf{r}_2)\psi_b(\mathbf{r}_1) | \frac{1}{r_{1-2}} | \psi_a(\mathbf{r}_1)\psi_b(\mathbf{r}_2) + \psi_a(\mathbf{r}_2)\psi_b(\mathbf{r}_1) \rangle \\ E_T &= \frac{e^2}{8\pi\epsilon_0} \langle \psi_a(\mathbf{r}_1)\psi_b(\mathbf{r}_2) - \psi_a(\mathbf{r}_2)\psi_b(\mathbf{r}_1) | \frac{1}{r_{1-2}} | \psi_a(\mathbf{r}_1)\psi_b(\mathbf{r}_2) - \psi_a(\mathbf{r}_2)\psi_b(\mathbf{r}_1) \rangle\end{aligned}\tag{1.10}$$

where  $e$  is the unit charge and  $\epsilon_0$  is the vacuum dielectric constant. This yields:

$$\begin{aligned}E_S &= K + J \\ E_T &= K - J\end{aligned}\tag{1.11}$$

Here  $K$  is called the Coulomb repulsion energy and  $J$  is the exchange energy, where:

$$\begin{aligned}K &= \frac{e^2}{4\pi\epsilon_0} \langle \psi_a(\mathbf{r}_1)\psi_b(\mathbf{r}_2) | \frac{1}{r_{1-2}} | \psi_a(\mathbf{r}_1)\psi_b(\mathbf{r}_2) \rangle \\ J &= \frac{e^2}{4\pi\epsilon_0} \langle \psi_a(\mathbf{r}_1)\psi_b(\mathbf{r}_2) | \frac{1}{r_{1-2}} | \psi_b(\mathbf{r}_1)\psi_a(\mathbf{r}_2) \rangle\end{aligned}\tag{1.12}$$

Therefore, the excited triplet state has  $2J$  lower energy than the singlet state. This energy difference is governed by the overlap between  $\psi_a$  and  $\psi_b$ , e.g. HOMO and LUMO, which varies with the molecular structure.



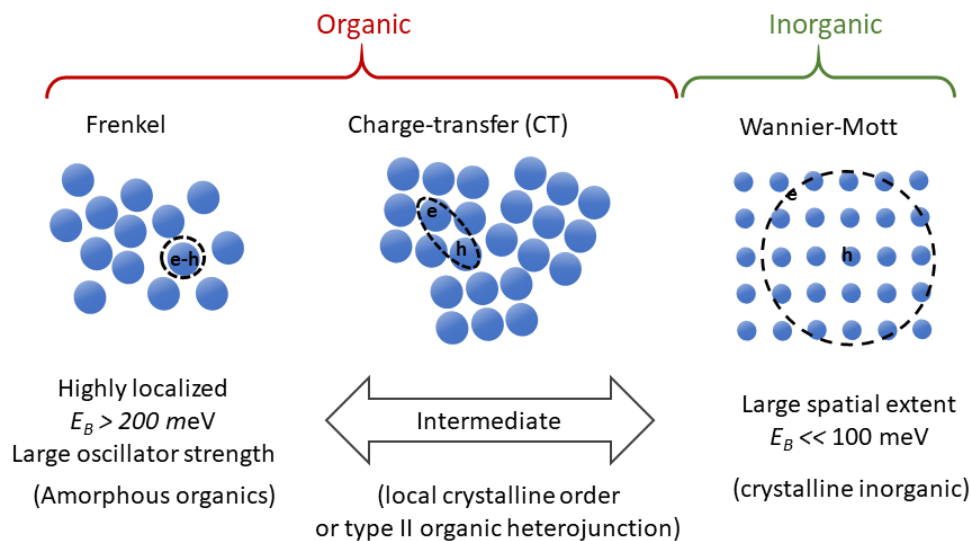


Figure 1.8: Three types of excitons and their different characteristics

At the excited state, e.g.  $S_1$  (see Fig. 1.7(left)), the vacancy in the HOMO is generally considered as a hole that mirrors the behaviour of the remaining electron. The coulombically correlated electron-hole pair is treated as a quasi-particle, known as an *exciton*. The interaction between the electron and hole typically reduces the energy of the exciton state from the theoretical energy gap between the HOMO and LUMO. This energy difference is indicated by the solid and dashed lines in Fig. 1.7(left) and is generally referred to as the exciton binding energy,  $E_B$ . The excitons are divided into three different types, depending on their spatial extent and binding energy: Frenkel excitons, charge transfer (CT) excitons, and Wannier-Mott excitons as shown in Fig. 1.8. The most common excitons in amorphous organic materials are of the Frenkel type which has the most localized wavefunction (usually confined to a single molecule) and the highest binding energy ( $> 200 \text{ meV}$ ) among the three. Charge transfer excitons have broader spatial extent and occur when the intermolecular coupling between neighboring molecules is sufficient, and are often seen in organics with local crystalline order.<sup>[7]</sup> The delocalized Wannier-Mott exciton has a small binding energy of  $\ll 100 \text{ meV}$ . It is observed in high dielectric constant

crystalline inorganic semiconductors and is generally not stable at room temperature.

### 1.3.2 Optical Transitions

The optical transitions, i.e. absorption and emission, between excitonic states  $S_0$  and  $S_1$  occur vertically between their vibrational sub-levels, as shown in Fig. 1.9. This is based on the *Franck-Condon (FC) principle*, a manifestation of the *Born-Oppenheimer approximation*, that states the fast oscillating electromagnetic field of light interacts with the electrons in such a short time scale that the nuclei do not respond. During the characteristic lifetime  $\tau$  ( $\sim ns$ ) of the excited state  $S_1$ , the molecules relax from the configuration  $Q_0$  to the new equilibrium configuration  $Q_1$  on the order of  $10^{-13}s$ . The subsequent transition, therefore, preferentially occurs from the lowest vibrational sub-levels. This is also known as *Kasha's rule*,<sup>[8]</sup> resulting in mirror-symmetric absorption-emission spectra as shown in Fig. 1.9. The energy separation between the absorption and emission spectra is termed the *FC shift*. In solution or solid, the 0-0 emission peak is further shifted from the 0-0 absorption peak due to the solvation effect from the surrounding medium.

The optical transition rate can be calculated by *Fermi's Golden Rule*:<sup>[9]</sup>

$$k_{if} = \frac{2\pi}{\hbar} | \langle \Psi_f | H | \Psi_i \rangle |^2 \rho_f, \tag{1.13}$$

where the subscripts  $i$  and  $f$  indicate the initial and final state,  $\Psi$  is the total molecular wavefunction from Eq. 1.4,  $\rho_f$  is the density of the final states, and  $H$  is the perturbing Hamiltonian. To a first order approximation  $H = -e\mathbf{r} \cdot \mathbf{F}$ ,<sup>[10]</sup> where  $e\mathbf{r}$  is the electric dipole moment of molecular charge distribution,  $\mathbf{F}$  is the optical electric field. Generally, the dipole operator only acts on the electronic spatial wavefunction  $\psi$ , since the nuclei are too slow to respond and the spin of the electron is unchanged

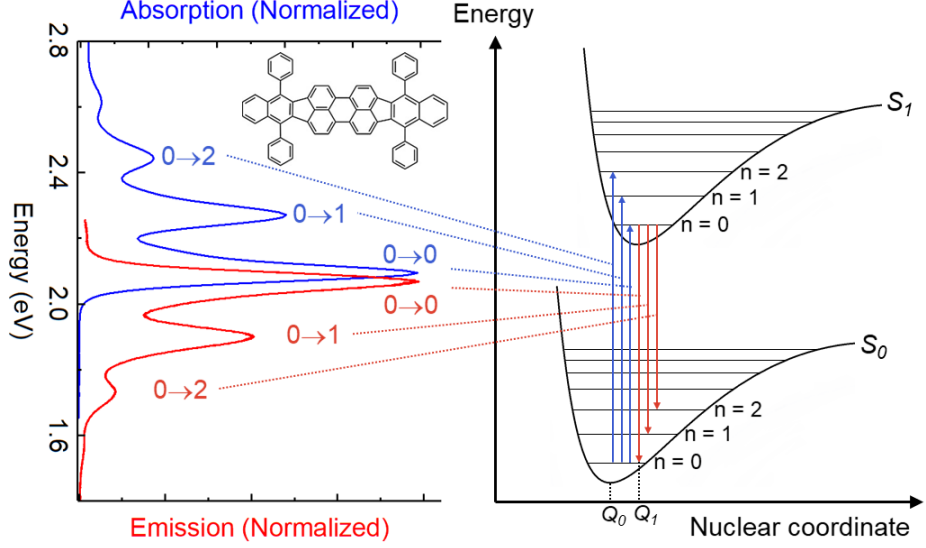


Figure 1.9: (Left) Emission and absorption spectra of DBP (the chemical structure is shown in the inset) dissolved in chlorobenzene, and (right) the corresponding energy diagram of the ground singlet state  $S_0$  and first excited singlet state  $S_1$ . The vibrational energy levels are added to the electronic energy levels. The potential surface is described by Eq. 1.6. The vibrational sub-levels of both states are indicated by  $n = \{1, 2, 3, \dots\}$ . The transition occurs between lowest vibrational state of one electronic state to the  $n^{\text{th}}$  of the other, i.e.  $0 \rightarrow 0$ ,  $0 \rightarrow 1$ ,  $0 \rightarrow 2$ , etc. The equilibrium coordinates of ground and excited states are denoted as  $Q_0$  and  $Q_1$ , respectively.

in the absence of strong spin-orbit coupling. This gives:

$$k_{if} = \frac{2\pi}{\hbar} \mathbf{F}^2 \rho_f |\langle \psi_f | -e\mathbf{r} | \psi_i \rangle|^2 |\langle \chi_f | \chi_i \rangle|^2 |\langle \sigma_f | \sigma_i \rangle|^2. \quad (1.14)$$

The term,  $|\langle \psi_f | -e\mathbf{r} | \psi_i \rangle|^2$ , is known as the transition dipole moment, which determines the oscillator strength,  $f$ :

$$f = \frac{2m_e}{3\hbar} (E_f - E_i) |\langle \psi_f | \mathbf{r} | \psi_i \rangle|^2, \quad (1.15)$$

where  $m_e$  is the electron mass, and  $E_f$  and  $E_i$  are the final and initial state energies, respectively. The absorption and emission intensities, hence, scale with the value of

dipole moment ( $-\epsilon\mathbf{r}$ ) and the electronic orbital overlap.

The second term,  $|\langle\chi_f|\chi_i\rangle|^2$ , is the *FC factor*. This overlap integral of vibrational wavefunctions determines the probabilities, i.e. relative intensities, of the transitions from  $0^{th}$  vibrational level of one electronic state to the  $n^{th}$  of the other. Since the dominant normal modes in organic molecules have energies much larger than the thermal energy,  $\hbar\omega \gg k_B T$ , e.g.  $\hbar\omega \approx 0.17\text{eV}$  for carbon-carbon stretching, the *FC factor* can be approximated by a Poisson distribution:<sup>[11,12]</sup>

$$|\langle\chi_f|\chi_i\rangle|^2 = \frac{S^n}{n!} e^{-S}, \quad (1.16)$$

$$S = \frac{\frac{1}{2}m\omega^2\Delta Q^2}{\hbar\omega} = \frac{1}{2} \frac{m\omega}{\hbar} \Delta Q^2. \quad (1.17)$$

Here  $S$  is known as the *Huang-Rhys factor*. The oscillation of the vibrational mode for Eq. 1.17 is treated as a simple harmonic oscillator. (see Eq. 1.5).

The last term,  $|\langle\sigma_f|\sigma_i\rangle|^2$ , is the spin factor. The initial and final states must have the same parity to ensure a non-zero transition rate; that is, the transition between two singlet states is spin-allowed, while that between a triplet and a singlet state is forbidden. In reality, the phosphorescent process from  $T_1$  to  $S_0$  still occurs at an extremely low rate due to the spin-orbital coupling<sup>[13]</sup> that produces the singlet-triplet mixing. This effect can be greatly enhanced by employing heavy metal atoms in the molecules. The highly efficient phosphorescent OLED is therefore achieved based on this design.<sup>[14]</sup>

Note that all the discussions above describe radiative transitions based on the assumption of a separable wavefunction written in Eq. 1.4. In a non-radiative transition process, however, the electronic state significantly couples with the vibrational modes, and the *Born-Oppenheimer approximation* no longer applies. The potential energy surfaces of the excited,  $S_1$ , and ground state,  $S_0$ , shown in Fig. 1.9 will cross. The transitions between two electronic states are no longer vertical. The molecule

is therefore de-excited through the conversion of electronic energy into lattice vibrational energy, i.e. phonon energy. The non-radiative transition rate,  $k_{nr}$ , competes with that for radiative transitions,  $k_r$ , resulting in a luminescent quantum yield of:

$$\eta = \frac{k_r}{k_r + k_{nr}}. \quad (1.18)$$

The characteristic exciton lifetime is defined as:  $\tau = \frac{1}{k_r + k_{nr}}$ . More details of the non-radiative transition will be discussed in Chapter IV.

### 1.3.3 Exciton Energy Transfer

We have considered the dynamics of excitons within the molecule. In the organic solid, the exciton energy transfer between molecules also plays an essential role in the exciton dynamics. Exciton energy transfer is governed by three principle mechanisms depending on the distance between an excited state donor and ground state acceptor molecule: (i) near-field exchange energy transfer, known as Dexter transfer;<sup>[15]</sup> (ii) dipole-dipole interactions, known as Förster resonant energy transfer (FRET);<sup>[16]</sup> and (iii) far-field radiative transfer.

The Dexter transfer, as shown in Fig. 1.10, occurs by electron exchange between donor and acceptor in close contact, and is allowed for either the same or different spin multiplicities of two states. The transfer rate as a function of intermolecular distance  $R_{DA}$  is given by:<sup>[15]</sup>

$$k_D \propto \frac{J}{R_{DA}^2} \exp(-2R_{DA}/L), \quad (1.19)$$

where  $J = \int f_D(\lambda)\sigma_A(\lambda)d\lambda$  is the spectral overlap integral between the normalized spectrum of the donor,  $f_D(\lambda)$ , and the absorption spectrum of acceptor,  $\sigma_A(\lambda)$ , and  $L$  is the exciton radius. The typical Dexter interaction range is less than 1 nm.

Another near-field energy transfer, FRET, originates from non-radiative resonant

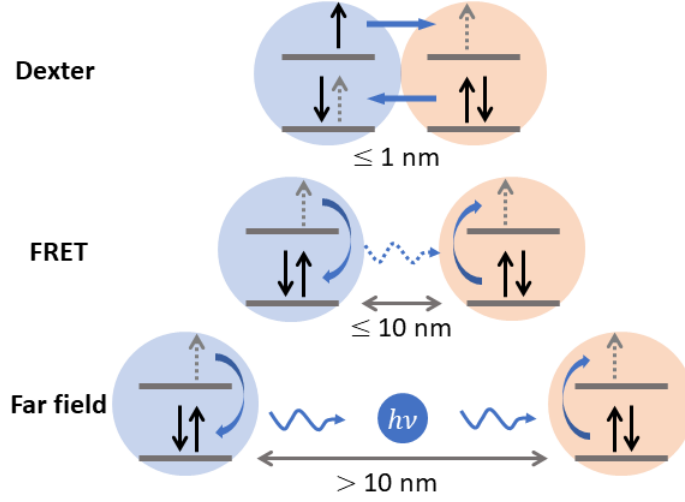


Figure 1.10: Three exciton energy transfer approaches between molecules: near-field Dexter transfer between excitons  $\leq 1\text{nm}$  apart, Förster resonant energy transfer (FRET) between excitons  $\leq 10\text{nm}$  apart, and far-field radiative transfer between excitons  $> 10\text{nm}$  apart.

dipole-dipole coupling. The transfer rate derived from Fermi's Golden rule with dipole-dipole perturbation is:<sup>[16]</sup>

$$k_F = \frac{1}{\tau_D} \left( \frac{R_F}{R_{DA}} \right)^6. \quad (1.20)$$

The rate is determined by the donor exciton lifetime  $\tau_D$ , donor-to-acceptor distance  $R_{DA}$ , and  $R_F$  is known as the Förster radius,

$$R_F^6 = \frac{9\kappa^2\eta_D}{128\pi^5n^4} \int f_D(\lambda)\sigma_D(\lambda)\lambda^4d\lambda, \quad (1.21)$$

where  $\kappa$  is the relative molecular orientation factor of donor and acceptor,  $\eta_D$  is the donor emission quantum yield, and  $n$  is the refractive index. Efficient FRET occurs when  $R_{DA}$  is comparable to the Förster radius which is typically in the range of  $\leq 10 \text{ nm}$ .

Far-field radiative transfer is dominant between molecules that are  $> 10\text{nm}$  apart

where near-field Dexter transfer and FRET are no longer active. The donor molecule emits a photon that is subsequently absorbed by the acceptor molecule. The radiative transfer rate scales with  $R_{DA}^{-2}$ .<sup>[17]</sup>

The total energy transfer rate is the sum of all active processes. A collective random motion of incoherent exciton transport over macroscopic distances in the organic solid results in the energy transfer across a characteristic length,  $L_D$ , known as the exciton diffusion length. The diffusivity  $D$  of the material is hence defined as the exciton diffusion length within its lifetime  $\tau$ , that is,  $D = L_D^2/\tau$ . The rate equation that describes the exciton dynamics is written as:

$$\frac{\partial N(\mathbf{r}, t)}{\partial t} = G(\mathbf{r}, t) - \frac{N(\mathbf{r}, t)}{\tau} + D\nabla^2 N(\mathbf{r}, t), \quad (1.22)$$

where  $N(\mathbf{r}, t)$  is the local exciton density as a function of position and time,  $G(\mathbf{r}, t)$  is the local exciton generation rate, and  $\nabla^2 N(\mathbf{r}, t)$  represents the local exciton flow rate.

## 1.4 Process and Deposition Methods for Organic Semiconductors

### 1.4.1 Material Purification

High purity of an organic semiconductor is essential for achieving optimal optical and electrical device performance, and a reproducible, comprehensible physical characterization of the organic material system. The intrinsic properties of the material system can only be accurately studied without extrinsic behaviors introduced from foreign species. Chemical impurities have invariably different HOMO and LUMO levels than the major constituents, and may form traps that result in a decrease of charge mobility and exciton diffusion length.<sup>[18,19]</sup> The impurities may also diminish

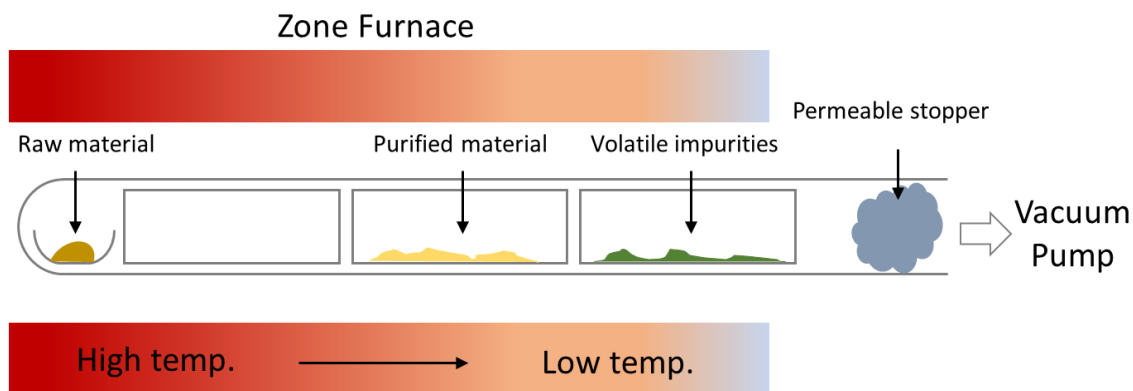


Figure 1.11: The apparatus for thermal gradient sublimation purification.

luminescence efficiency due to exciton quenching or introduce parasitic luminescence at an undesired wavelength.

A variety of solution-based purification techniques compatible with both polymer and small molecule organics is available including fractional crystallization,<sup>[20]</sup> chromatography,<sup>[21]</sup> centrifugation,<sup>[22]</sup> etc. Effective separation of the organic compound from impurities relies on their difference in solubility, molecular size, and weight. These methods are usually the first purification steps following synthesis, and yet the purity level is still unacceptable although labeled as  $> 98\%$  by the manufacturer.

Thermal gradient sublimation is the widely adopted method for small molecule organics to refine the purity level.<sup>[23]</sup> As illustrated in Fig. 1.11, a horizontal three-zone furnace is used to maintain a thermal gradient along a quartz tube, where the raw organic material is loaded in a quartz boat at the hot end. The tube is evacuated to  $10^{-6}$  Torr vacuum using a combination of dry mechanical and turbo pumps. The temperature is gradually ramped up until slow sublimation of the raw material is observed. Organic compounds with different volatility diffuse along the thermal gradient and condense at different catching sleeves in the tube, allowing for spatial separation and collecting the purified material from impurities. A permeable stopper, e.g. quartz wool, is placed near the tube open end to stop the organic



vapor from contaminating the pump system. Each cycle of purification process lasts approximately one week. Several iterations are sometimes needed to reach acceptable purity levels.

### 1.4.2 Organic Thin Film Deposition

The intermolecular van der Waals bond of organic materials enables a wide range of deposition methods, free from the requirement of lattice matching characteristic of inorganic semiconductors. An even larger variety of material combination, thin film morphologies, and device geometries on various substrates can therefore be achieved. This section provides a brief introduction of widely used organic deposition techniques, in particular, those used in the subsequent chapters.

The most common organic deposition method for both research and large scale manufacturing purposes is vacuum thermal evaporation (VTE).<sup>[23,24]</sup> The configuration of VTE is illustrated in Fig. 1.12. The source material is placed in a baffled metal boat made of tungsten or molybdenum that is resistively heated in vacuum by passing current through it. The evaporation is generally operated at  $10^{-6}$  to  $10^{-9}$  Torr vacuum, resulting in a ballistic and highly directional organic vapor stream towards the substrate. The shadow mask attached to the substrates as shown in Fig. 1.12 is used to pattern growth features and define the device area. The deposition rate is controlled in real time by a quartz crystal monitor and a feedback loop to the boat heating controller. Multiple organic sources can be simultaneously deposited, with the deposition rate and thus concentration of each source controlled by individual crystal monitors. Substrate rotation enables the uniformity of film thickness and composition.

A promising alternative to VTE is organic vapor phase deposition (OVPD),<sup>[26-28]</sup> whereby organic materials are thermally evaporated at a low pressure (0.1-10 Torr) into a heated carrier gas stream and transported through a hot wall reactor to a

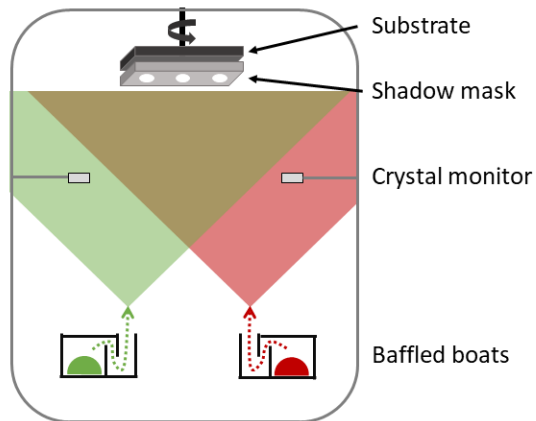


Figure 1.12: Schematic of the vacuum thermal evaporation (VTE) system. Image adapted from ref.<sup>[25]</sup>

cooled substrate. In OVPD, the process of evaporation and transport are essentially decoupled. Molecules evaporated from the sources undergo collisions with the gas molecules, resulting in a loss of kinetic energy. The molecules remain near the source region until being carried away by the gas stream. Control over the evaporation temperature and gas flow rate results in a shift between equilibrium and kinetically limited growth regime,<sup>[29]</sup> and therefore vastly different morphology of the film. One subclass of OVPD is organic vapor jet printing (OVJP),<sup>[30][31]</sup> where the vapor stream is passed through a heated nozzle towards the substrate with  $< 1$  mm substrate-to-nozzle distance. Instead of using a shadow mask for film patterning, OVJP is designed to directly pattern the features with  $< 10\mu\text{m}$  resolution.<sup>[31]</sup> Also note that OVJP offers a superior material utilization efficiency compared to VTE and OVPD.

Solution-based depositions are another major class of organic deposition techniques. They are applicable for processing large molecular weight or low decomposition temperature organic molecules. Most notable of these techniques include spin-, dip-, and blade-coating, inkjet printing<sup>[32]</sup> and screen-printing,<sup>[33]</sup> etc. Organic materials are dissolved or suspended in the solvent, and subsequently contact the substrate as the solvent evaporates. Post annealing by heat or solvent vapor can be used to

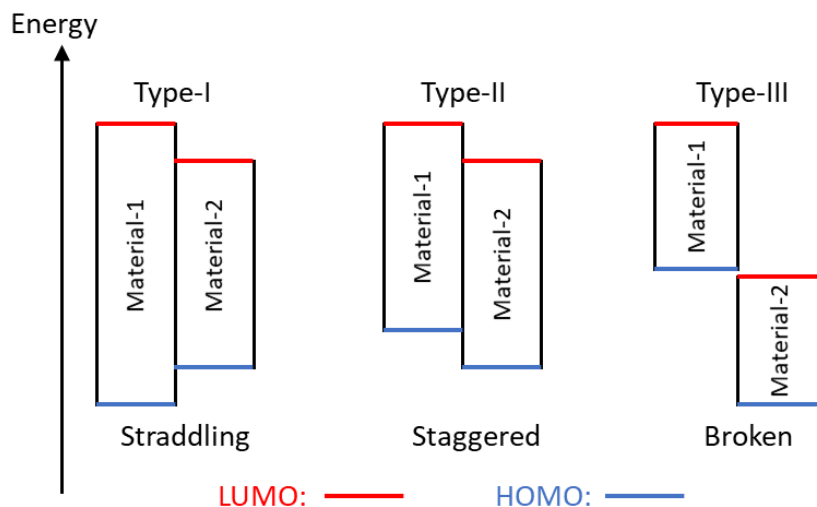


Figure 1.13: Three types of organic heterojunctions (HJs).

further alter film morphology. Solution processing has the advantage of very-high-speed deposition over large substrate areas, but has difficulty in growing complicated multi-layer structures and device patterning.

## 1.5 Fundamentals of Organic Donor-Acceptor Heterojunctions

### 1.5.1 Heterojunctions: Types and Structures

The HJ, i.e. the junction between two dissimilar semiconductors, is the essential building block for electronic devices. The energy gap alignment of constituting semiconductors at the interface governs the properties of HJs for different device applications. Similar to other semiconductor materials, organic materials at the interface can be organized into three types of HJs: type-I straddling junction, type-II staggered junction, and type-III broken junction.

The type-I HJ, shown in Fig. 1.13(left), has the energy gap of material-2 nested within that of material-1. The excitons generated on material-1 preferentially transfer

towards lower energy molecular sites in material-2, while those generated on material-2 are confined within the layer. Such a structure is commonly used in the organic host(material-1)-guest(material-2) system for light emitting devices, where the guest, e.g. organic light emitting dopant, is blended into a wide energy gap host at a dilute volume concentration of 1 - 10 %. Isolated guest molecular domains analogous to quantum dot structures enable high luminescent quantum yield. The type-I HJ is also applied in organic multi-quantum well structures<sup>[34]</sup>, or as an exciton blocking structure in OPVs.<sup>[35]</sup>

A type-II HJ, as illustrated in Fig. 1.13(middle), has both HOMO and LUMO of material-1 higher than that of material-2. This energy gap alignment facilitates electron transfer from material-1 (the electron donor) to material-2 (the electron acceptor) while leaving the hole behind. Organic donor-acceptor HJs are the crucial design elements in organic photodetectors and photovoltaics where the energy offset at the interface provides the driving force for the dissociation of tightly-bound electron-hole pairs. Due to the versatility of organic thin film growth techniques, various geometries of the organic HJ as shown in Fig. 1.14 can be achieved. (i) Planar structure with one layer grown on top of the other; (ii) finger-like donor-acceptor interpenetrating structures that can be grown by OVPD in the equilibrium growth regime;<sup>[36]</sup> or (iii) blended bulk HJs with donor and acceptor materials intermixed with each other.

The type-III HJ shown in Fig. 1.13(right) is an extreme case of type-II HJ where the energy offset is larger than the energy gaps of the two materials and the HOMO of material-1 partially overlaps the LUMO of material-2. This type of structure is applied in devices, such as Esaki tunnel diode.<sup>[37]</sup>

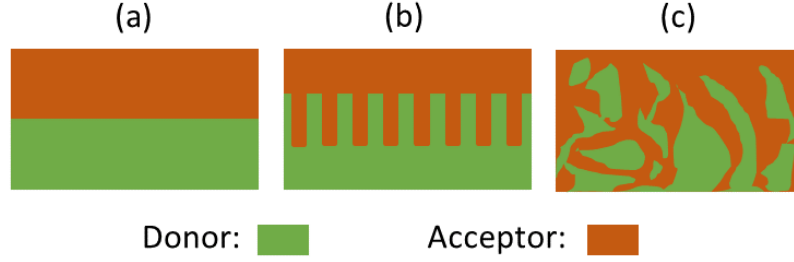


Figure 1.14: Structures of type-II donor/acceptor HJ: (a) planar, (b) finger-like interpenetrating, and (c) blended HJs.

### 1.5.2 Photocurrent Generation at Type-II Donor-Acceptor Heterojunctions

The energy transfer process at the type-II donor-acceptor HJ are the main focus of this thesis. As depicted in Fig. 1.15, a photon is absorbed by either the donor or acceptor layer and generates an exciton that diffuses to the HJ interface where charge transfer occurs. Here, a blended heterojunction (see Fig. 1.14 (c)) is usually applied to circumvent the trade-off between a short exciton diffusion length ( $L_D$ ) and a considerably longer optical absorption length. Subsequently, an intermediate CT exciton is formed at the interface and dissociated into free charges that are collected at the electrode. The external quantum efficiency ( $EQE$ ) of charge generation at the organic HJ is:

$$\eta_{EQE}(V, \lambda) = \eta_A(\lambda) \cdot \eta_{diff} \cdot \eta_{diss}(\lambda, V) \cdot \eta_{CC}(V), \quad (1.23)$$

where  $\eta_A$  is the absorption efficiency,  $\eta_{diff}$  is the exciton diffusion efficiency,  $\eta_{diss}$  is the exciton dissociation efficiency at HJ, and  $\eta_{CC}$  is the charge collection efficiency. The  $\eta_A$  and  $\eta_{diss}$  vary with wavelength  $\lambda$  of the incident photons, and  $\eta_{diss}$  and  $\eta_{CC}$  are dependent on the applied voltage  $V$ . These dependences will be further discussed in Chapter III. Figure 1.15(right) shows the transfer rate of each process. Excitons at the donor or acceptor layer diffuse towards the interface at a rate of  $J_x/a_0$ , where  $J_x$  is

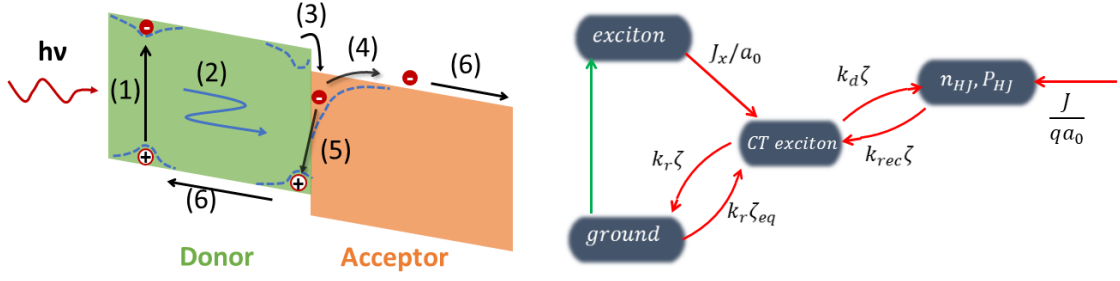


Figure 1.15: (Left) Schematic of photogeneration processes in the type-II organic donor-acceptor HJ. (1) Exciton generation in the organic upon photon absorption. The blue dashed line depicts the mutual Coulomb potential of electron-hole pair. (2) The exciton diffuse to the interface at a flux  $J_x$ . (3) Charge transfer occurs at the HJ interface in the region of width  $a_0$ . The charge transfer excitons (at a population of  $\zeta$ ) either (4) dissociate ( $k_d$ ) into free charge carriers ( $n_{HJ}$  and  $p_{HJ}$ ) or (5) recombine ( $k_r$ ). Charge carriers near the interface can also recombine at a rate of  $k_{rec}$  to form CT excitons. (6) Charge extraction at a rate of  $\frac{J}{qa_0}$ . (Right) State diagram of all processes.

the exciton flux and  $a_0$  is the average electron-hole separation at HJ. The dissociate rate ( $k_d$ ) of the CT excitons (whose population is  $\zeta$ ) competes with the CT exciton recombination rate ( $k_r$ ) and the geminate charge recombination rate ( $k_{rec}$ ). The rate of charge extraction from the HJ is  $J/(qa_0)$ . The steady state rate equations of the CT excitons and charge carriers ( $n_{HJ}$  and  $p_{HJ}$ ) are written as:<sup>[38]</sup>

$$\begin{cases} \frac{J_x}{a_0} - k_r(\zeta - \zeta_{eq}) - k_d\zeta + k_{rec}n_{HJ}p_{HJ} = 0 \\ k_d\zeta - k_{rec}n_{HJ}p_{HJ} + \frac{J}{qa_0} = 0 \end{cases} . \quad (1.24)$$

Here,  $\zeta_{eq}$  is the thermal equilibrium population of the CT state in the absence of bias and illumination determined by detailed balance, finding  $\zeta_{eq} = k_{rec}n_{eq}p_{eq}/k_{d,eq}$ .<sup>[39]</sup>

Solving Eq. 1.24 yields the current going through the HJ as:<sup>[38]</sup>

$$J = qa_0k_{rec}(1 - \eta_d) \left( n_{HJ}p_{HJ} - \frac{k_d}{k_{d,eq}}n_{eq}p_{eq} \right) - qJ_x\eta_d, \quad (1.25)$$

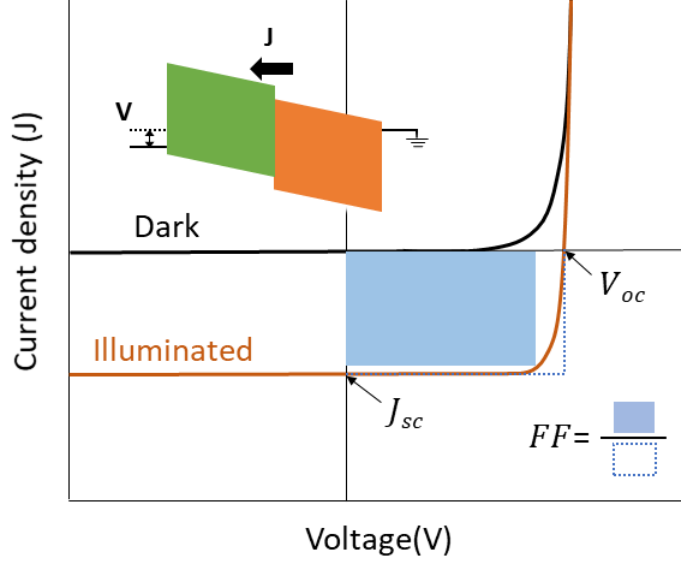


Figure 1.16: Schematic of J-V characteristic of an ideal photodiode. Three major parameters,  $J_{sc}$ ,  $V_{oc}$ ,  $FF$  are shown. The  $FF$  is the area ratio of the blue and dashed rectangles. Inset: illustration of voltage and current flow from the photodiode based on a donor-acceptor type-II heterojunction.

where  $\eta_d = \frac{k_d}{(k_d + k_r)}$  is the dissociation efficiency of the CT exciton. Assuming quasi-equilibrium, the carrier density at the HJ ( $n_{HJ}$ ,  $p_{HJ}$ ) can be related to that at the contact ( $n_C$ ,  $p_C$ ) via<sup>[40]</sup>  $n_{HJ}p_{HJ} = n_Cp_C \exp(\frac{q(V_a - V_{bi})}{k_B T})$ , where  $V_a$  is the applied bias,  $V_{bi}$  is the built-in voltage of the HJ,  $k_B$  is the Boltzmann constant, and  $T$  is the temperature. Furthermore, assuming detailed balance of the charge density adjacent to an injecting contact, the ideal current density-voltage (J-V) characteristic of the organic donor-acceptor HJ can thus be derived as:<sup>[38]</sup>

$$J = J_{s0} \left[ \exp(qV_a/k_B T) - \frac{k_d}{k_{d,eq}} \right] - q\eta_d J_x, \quad (1.26)$$

where  $J_{s0}$  is the dark current prefactor that is a function of  $n_C$ ,  $p_C$ ,  $V_{bi}$ , contact barriers etc. A more detailed derivation is described in ref.<sup>[38]</sup>. At forward bias,  $\frac{k_d}{k_{d,eq}} \approx 1$ . The term on the right is the photocurrent. Inserting  $J_x=0$  gives the dark J-V characteristics.

Equation 1.26 yields the dark and illuminated J-V curve of an ideal photodiode employing the type-II donor-acceptor HJ, as shown in Fig. 1.16. The three main characteristic parameters of an illuminated J-V curve are short circuit current ( $J_{sc}$ ) at  $V = 0$ , open circuit voltage ( $V_{oc}$ ) at  $J = 0$ , and fill factor  $FF$  ( $= \frac{P_{max}}{J_{sc}V_{oc}}$ ). The maximum power output  $P_{max}$  is the area of blue square shown in Fig. 1.16. Generally, photovoltaics operate in the fourth quadrant to generate power while photodetectors work in the third quadrant under reverse voltage bias to maximize the current output. In the context of OPV characterization,  $J_{sc}$ ,  $V_{oc}$ , and  $FF$  under the illumination of AM 1.5 solar spectrum are usually reported. The power conversion efficiency ( $PCE$ ) equals  $\frac{P_{max}}{P_{incident}} = \frac{J_{sc}V_{oc}FF}{P_{incident}}$ . Under AM 1.5G solar irradiation, the incident power density  $P_{incident} = 100mW/cm^2$ .

### 1.5.3 Charge Transfer Excitons and Theories of Exciton Dissociation

Exciton dissociation at the interface gives rise to the formation of a CT exciton, where the hole and the electron of the exciton reside on molecules of different materials at the HJ but are still weakly bound across the interface. Charge transfer excitons play a crucial role in photogeneration of charges and thus determine the OPV open-circuit voltage and short-circuit current. A considerable body of research has studied the interfacial CT states whose existence has been confirmed by the observation of the distinct absorption or luminescence features of organic HJs. Photoluminescence peaks with energies less than the lowest Frenkel exciton energy in the comprising materials have been attributed to radiative recombination of CT complexes.<sup>[41–43]</sup> Other methods, including transient absorption,<sup>[44]</sup> time-resolved photoluminescence (PL),<sup>[45]</sup> electroabsorption,<sup>[42,46]</sup> time-resolved two photon photoemission,<sup>[47,48]</sup> time-resolved second harmonic generation,<sup>[49]</sup> and theoretical quantum chemical calculations,<sup>[47,50]</sup> have been applied to understand the characteristics of CT states.



With a decreased overlap between the electron and the hole wavefunctions, the CT exciton has a lower binding energy and smaller energy splitting (see Eq. 1.11) between its singlet and triplet spin states as compared to Frenkel excitons. However, a typical CT exciton binding energy at the organic HJ ( $\sim 200meV$ ) is still much larger than thermal energy, making mechanisms of CT exciton dissociation an open question. Onsager<sup>[51]</sup> considered a Coulombically bound electron-hole pair with separation,  $r_0$ , in a dielectric medium with relative dielectric constant,  $\epsilon_r$ . The general Smoluchowski model is used to describe the Brownian motion of charge within the Coulomb potential that is superimposed with the applied external field  $F$ . Since both recombination and dissociation are diffusion controlled, the trade-off of both processes is independent of the diffusion constant. As a result, the dissociation probability as a function of  $r_0$ ,  $F$ ,  $\epsilon_r$ , temperature  $T$  and the angle  $\theta$  between the dipole moment of the electron-hole pair and the applied field is given by:<sup>[51,52]</sup>

$$\Phi(F) = \exp\left(-\frac{r_{coul}}{r_0}\right) \left(1 + \frac{e^3 F}{8\pi\epsilon_r\epsilon_0(k_B T)^2}(1 + \cos\theta)\right), \quad (1.27)$$

where  $r_{coul} = \frac{e^2}{4\pi\epsilon_r\epsilon_0 k_B T}$  is the Coulombic capture radius. Braun et al. furthered Onsager Theory and introduced a finite lifetime of CT exciton to correct the “infinite sink approximation” that the electron and the hole directly recombine on encounter.<sup>[53]</sup> The dissociation probability is thus determined from the trade-off between the dissociation rate  $k_d(F)$  and CT recombination rate  $k_r$ :

$$\Phi(F) = \frac{k_d(F)}{k_d(F) + k_r} = \frac{k_d(F)}{\tau}. \quad (1.28)$$

Here, the CT exciton lifetime  $\tau$  is determined by both  $k_d(F)$  and  $k_r$ . The field and temperature dependent dissociation rate  $k_d(F)$  is given by:

$$k_d(F) = A_{CT} k_{rec} \exp\left(-\frac{\Delta E}{k_B T}\right) \frac{J_1(2\sqrt{-2b})}{\sqrt{-2b}}, \quad (1.29)$$

where  $J_1$  is the Bessel function of order one, and  $b = \frac{e^3 F}{8\pi\epsilon_r\epsilon_0(k_B T)^2}$ ,  $\Delta E$  is the Coulomb binding energy of the CT exciton. The prefactor  $A_{CT}$  is the reciprocal of the CT exciton volume. Assuming a classical ion pair bound in a sphere of radius  $r_0$ ,  $A_{CT} = \frac{3}{4\pi}r_0^{-3}$ . In the case where the CT exciton has a Wannier character,  $A_{CT} = (m^*k_B T/3\pi\hbar^2)^{3/2}$ , where  $m^*$  is the effective mass of electron. In disordered organic solids, the charge recombination rate is diffusion limited and follows *Langevin recombination* statistics of  $k_{rec} = \frac{q\langle\mu\rangle}{\epsilon_0\epsilon_r}$ , where  $\langle\mu\rangle = \mu_e + \mu_h$  is the effective mobility of the electron and hole.

Although successful applications of Onsager-Braun model have been made to describe charge photogeneration of donor-acceptor systems,<sup>[54,55]</sup> the model often overestimates field and temperature dependence of the dissociation yield in practice.<sup>[56,57]</sup> Due to the complex energy structure of the CT states and contributions of excess energy upon exothermic charge transfer at the interface, the CT exciton dissociation mechanisms vary case-by-case. Figure 1.17 depicts three prevalent ones. The first possibility (Fig. 1.17(1)) is that the excess energy upon charge transfer is converted into the kinetic energy of the electron and hole. The hot carriers rapidly dissipate their energy to the local heat bath by inelastic scattering, which creates thermalized yet loosely bound electron-hole pairs and also increases the Boltzmann factor,  $\exp(\frac{\Delta E}{k_B T})$  that enhances the dissociation yield.<sup>[52,58,59]</sup> In such a scheme, however, charge transfer has to be fast enough to outcompete the relaxation of the CT exciton to its low energy configuration. Another possible dissociation pathway is through a higher electronic CT state that couples to the charge separated state more efficiently as compared to the lowest CT state(Fig. 1.17(2)). The dissociation yield, therefore, varies with the energy structure of CT states which is dependent on HOMO and LUMO energy levels and local morphology of the donor-acceptor HJ. The third dissociation theory (Fig. 1.17(3)) argues that efficient charge generation can occur through the relaxed CT state (CT1). It does not matter if the excess energy exists,

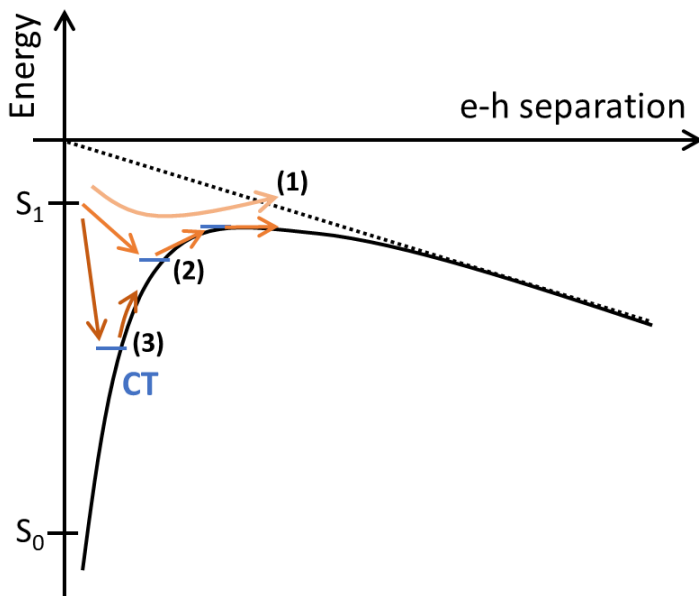


Figure 1.17: Energy diagram of three possible exciton dissociation mechanisms at the donor-acceptor HJ: (1) hot CT exciton dissociation, (2) dissociation via higher electronic CT manifold, and (3) relaxed CT dissociation. Image adapted from ref. <sup>[52]</sup>

or if the higher electronic CT states are accessed. This notion is supported by the work of Vandewal et al. <sup>[60]</sup>, where the quantum yield of charge generation through the selectively excited CT1 state is found to be equal to that through optical excitation of the bulk donor and acceptor states in an OPV.

Research on the mechanisms of CT exciton dissociation has not yielded conclusive answers. Indeed, due to a variance of molecular structure and morphological characteristics for each organic system, investigations have yet to proceed on a case-by-case basis. Scientists have also been highly interested in the roles played by other parameters such as electrostatic screening due to the interfacial dipoles, <sup>[61–63]</sup> entropy, <sup>[64,65]</sup> and local morphology. <sup>[42,66–69]</sup> Of these parameters, the local morphology of donor-acceptor HJs has been gaining considerable attention. Charge transfer state energies and dissociation dynamics can be dramatically altered by varying the morphology at the interface. The origins of these excitonic property changes and their resulting

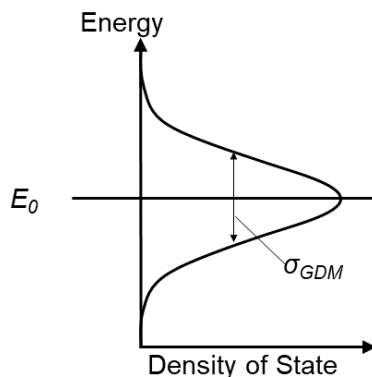


Figure 1.18: Gaussian distribution of density of states around energy level  $E_0$  and with width  $\sigma_{GDM}$ .

implications on device performance will be the main topic in Chapters II and III.

#### 1.5.4 Charge Transport and Mobility

After charge separation, electrons and holes transport in the LUMO and HOMO levels, respectively. Due to weak intermolecular electronic coupling, the intramolecular electron-phonon coupling and consequent nuclear configuration relaxation in the presence of a charge carrier occurs faster than the charge transport process. The surrounding molecules are also rapidly polarized by the charge, and lower their energy. The electron and local nuclear distortion and polarization are treated as a composite quasi-particle, called a polaron. The total molecular reorganization energy is known as the polaron binding energy.

The polaron travels through the organic film by incoherent stochastic hopping. In the presence of disorder, the density of states  $g(E_i)$  around the energy level  $E_0$ , i.e. HOMO and LUMO, is approximated by the Gaussian disorder model (GDM) for convenience:<sup>[70]</sup>

$$g(E_i) = \frac{1}{\sqrt{2\pi\sigma_{GDM}^2}} \exp\left(-\frac{(E_i - E_0)^2}{2\sigma_{GDM}^2}\right). \quad (1.30)$$

The Gaussian distribution with width  $\sigma_{GDM}$  is shown in Fig. 1.18. The polaron

hopping in organic films can be described by two models: Miller-Abrahams<sup>[71]</sup> and Marcus transfer models.<sup>[72]</sup> The hopping rate of Miller-Abrahams transfer is given as:

$$k_{CT} = \nu \exp(-2\gamma R) \begin{cases} \exp(-\frac{\Delta E}{k_B T}) & \Delta E > 0 \\ 1 & \Delta E < 0 \end{cases}, \quad (1.31)$$

where  $\nu$  is the transfer attempt frequency,  $R$  is the distance between two sites,  $\gamma$  is the spatial wavefunction overlap factor, and  $\Delta E = E_f - E_i$  is the energy difference between final ( $E_f$ ) and initial ( $E_i$ ) sites. If the energy of the final site is higher than the initial site ( $\Delta E > 0$ ), the transfer rate is thermally activated, otherwise the transfer is exothermic with a unity probability times the prefactor that describes the overlap decay. Alternatively, classical Marcus transfer can be used to describe the hopping rate as:

$$k_{CT} = A \exp\left(-\frac{(\Delta G + \lambda)^2}{4\lambda k_B T}\right), \quad (1.32)$$

where  $A$  is the prefactor that depends on the electronic coupling between the initial and final states,  $\Delta G$  is the change in the Gibbs free energy, and  $\lambda$  is the reorganization energy upon charge transfer. A schematic of non-adiabatic Marcus charge transfer is shown in Fig. 1.19. Potential energy surfaces of two molecular states are described by the simple harmonic oscillator model (see Eq. 1.5). If assuming the same and symmetric parabolic potential surfaces of two molecules, we get  $\lambda = \frac{1}{2}k(Q_i - Q_f)^2$ , where  $k$  is the force constant of nuclear vibration,  $Q_i$  and  $Q_f$  are the equilibrium nuclear coordinates of the initial and final states, as labeled in Fig. 1.19. The thermal activation barrier is  $E_a = \frac{(\Delta G + \lambda)^2}{4\lambda}$ .

The mobility of the charge in the solid can thus be obtained by employing either Miller-Abrahams or Marcus transfer theory in the three-dimensional (3D) solid. As an example, we proceed with Miller-Abrahams transfer. The charge mobility ( $\mu$ ) in the presence of the field  $F$  is determined by the effective charge carrier hopping in

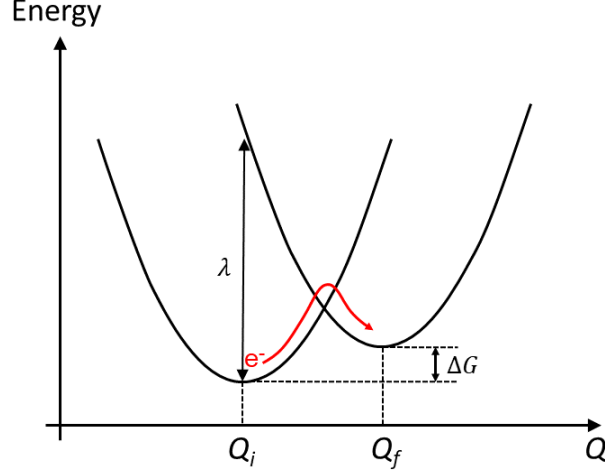


Figure 1.19: Energy diagram of the classical Marcus transfer theory. The change in Gibbs free energy between the initial and final sites,  $\Delta G$ , and the reorganization energy,  $\lambda$ , are the key parameters that governs the transfer rate. The equilibrium coordinates of the initial and final states are indicated by  $Q_i$  and  $Q_f$ , respectively.

the direction along and against the electrical field  $W_e^+$  and  $W_e^-$ :<sup>[73]</sup>

$$\mu = a \frac{W_e^+ - W_e^-}{F}, \quad (1.33)$$

where  $a$  is the distance between two hopping sites and

$$\begin{cases} W_e^+ = \nu \exp(-2\gamma_{if}a) \exp\left(-\frac{|E_f - E_i - qaF| + (E_f - E_i - qaF)}{2k_B T}\right) \\ W_e^- = \nu \exp(-2\gamma_{if}a) \exp\left(-\frac{|E_i - E_f + qaF| + (E_i - E_f + qaF)}{2k_B T}\right) \end{cases}, \quad (1.34)$$

where  $q$  is electron charge. In the organic solid, energetic configurational averaging over the Gaussian distributed density of states using Eq. 1.30 and 1.34 yields the hopping probability in the solid:<sup>[73]</sup>

$$Y_e^\pm = \nu \exp(-2\gamma a) \cdot \frac{1}{2} \left\{ \exp\left(-\frac{1}{2}x^2 \pm xf\right) \left[ 1 - \operatorname{erf}\left(\frac{\pm f}{\sqrt{2}}\right) \right] + \left[ 1 - \operatorname{erf}\left(\frac{x \mp f}{\sqrt{2}}\right) \right] \right\}, \quad (1.35)$$

where  $x = \sigma_{GDM}/k_B T$ ,  $f = qaF/\sigma_{GDM}$ , and  $\text{erf}(z) = (2/\sqrt{\pi}) \int_0^z dt \exp(-t^2)$  is the error function. If assuming  $1/x \ll f \ll x$ , combining Eq. 1.35 and 1.33 yields:

$$\mu_e = \mu_1 \exp \left[ -\frac{1}{2} \left( \frac{\sigma_{GDM}}{k_B T} \right)^2 + \frac{\sigma_{GDM}}{k_B T} \frac{qaF}{\sigma_{GDM}} - \frac{1}{2} \left( \frac{qaF}{\sigma_{GDM}} \right)^2 \right], \quad (1.36)$$

where  $\mu_1 = \mu_0/(\sqrt{2\pi} x f^2)$ ,  $\mu_0 = (qa^2 \nu/k_B T) \exp(-2\gamma a)$ . Considering the correlation that  $\frac{qaF}{\sigma_{GDM}} \approx \sqrt{\frac{\sigma_{GDM}}{2k_B T}} \sqrt{\frac{qaF}{\sigma_{GDM}}}$ ,<sup>[74]</sup> Eq. 1.36 can be extrapolated to arrive at the following expression:<sup>[73]</sup>

$$\mu_e = \mu_1 \exp \left\{ -\frac{1}{2} \left( \frac{\sigma_{GDM}}{k_B T} \right)^2 + \frac{1}{\sqrt{2}} \left[ \left( \frac{\sigma_{GDM}}{k_B T} \right)^{1.5} - \left( \frac{\sigma_{GDM}}{k_B T} \right)^{0.5} \right] \sqrt{\frac{qaF}{\sigma_{GDM}}} \right\}, \quad (1.37)$$

As a result, Eq. 1.37 predicts the well-known *Frenkel-Poole* type electric field dependence of the mobility that  $\mu_e \sim \exp(-A\sqrt{F})$ . Also note that the temperature dependence of drift mobility  $\ln(\mu_e) \propto \frac{1}{T^2}$  is different from the conventional first order thermal activation relation.

### 1.5.5 Applications: Organic Photovoltaics

As illustrated in Fig. 1.20, the basic structure of a single junction OPV includes a donor-acceptor HJ that is sandwiched between the buffer/transport layers followed by electrodes on two sides. The buffer/transport layers selectively conduct only one type of charge carrier (either electron or hole) and block the other. Lab-made OPVs often use a bottom-illuminated structure where the photons come in from the glass substrate and pass through a transparent anode, e.g. indium tin oxide (ITO) or a thin layer of metal ( $\sim 20$  nm), such as Ag or Al. Thick metal cathodes are usually deposited on the opposite side of the device. It can be replaced by a transparent electrode top illumination or semi-transparency. The choice of electrode material and thickness crucially depends on the trade-off between low sheet resistance and high optical transparency. A considerable amount of research has focused on the

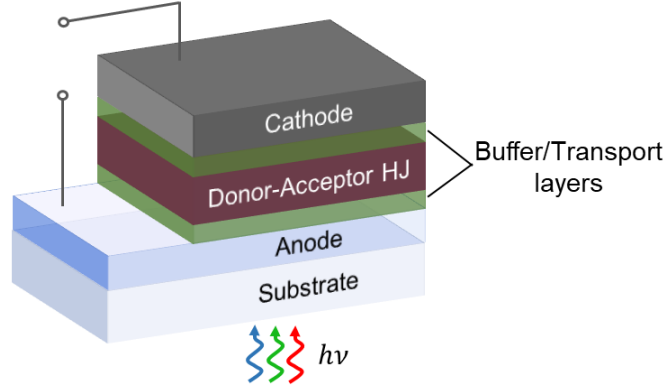


Figure 1.20: The device structure of a single junction OPV.

alternative electrode materials including thin metal alloys,<sup>[75]</sup> carbon nanotubes,<sup>[76,77]</sup> graphene<sup>[78,79]</sup>, etc. A successful device architecture requires a balanced design of each layer thickness. The transfer matrix model<sup>[80]</sup> is usually applied to analyze how the interaction of electromagnetic radiation with the photoactive materials is modified by optical interference for the purpose of achieving optimum absorption efficiency  $\eta_A$  at the HJ.

Organic photovoltaics provide unique features over the conventional bulk and thin film inorganic PVs. The low energy-cost deposition and non-epitaxial growth of organic semiconductors greatly reduces the substrate and the device fabrication cost. Due to the high optical density of organic materials, the thickness of organic HJs and, therefore, the material consumption per unit power absorption, is reduced. In addition, the benefit of light weight and the flexible characteristic make the OPV adaptable to the curved surface of everyday products such as windows, cars and electronic devices, and generates power without altering the product look and function. The narrow and tunable absorption band of organic semiconductors can alter the appearance of OPV from neutral to any saturated visible color for the purpose of transparency or decoration.

To approach a market-viable level of OPV performance, three critical elements



have to be achieved: high *PCE*, long device operational lifetime, and low-cost scalable production. Decades of research efforts result in a great leap of device *PCE* from  $\sim 1\%$  of first OPV demonstration in 1986 by C.W. Tang<sup>[81]</sup> to  $> 15\%$  in 2018.<sup>[82]</sup> An extrapolated device operational lifetime of post-burn-in  $T_{80}$ , i.e. 80% of the *PCE* drop, over 10 years has been reported.<sup>[83]</sup> In terms of low-cost scalable production, early lab-scale demonstrations of solution-processed<sup>[84,85]</sup> and vacuum-deposited<sup>[86]</sup> roll-to-roll (R2R) processing has been shown. Owing to this rapid progress in the area of organic material design and device fabrication techniques, OPV products are starting to appear in the emerging market of building integrated photovoltaics (BIPV)<sup>[87]</sup> and smart windows,<sup>[88]</sup> and eventually will become one of the competitive power generation technologies.

## CHAPTER II

# Morphological Properties of Organic Donor-Acceptor Heterojunctions

The donor-acceptor blend ratio and consequent morphology of organic bulk HJ determines the properties of exciton dissociation and the charge extraction process in OPVs. In this chapter, we present systematic morphological characterizations of an archetype small-molecule blend HJ comprising the donor DBP and the acceptor, C<sub>70</sub>,<sup>[66,69]</sup> needed to understand excitonic properties, charge transfer dynamics and charge collection.

### 2.1 Experimental Section

Prior to deposition via vacuum thermal evaporation in a system with a base pressure of  $\sim 2 \times 10^{-7}$  Torr, both C<sub>70</sub> and DBP were purified once via vacuum thermal gradient sublimation.<sup>[23]</sup> The 54 nm thick DBP/C<sub>70</sub> blend films (with C<sub>70</sub> volume concentrations of 0, 10, 25, 50, 65, 80, 90, 95, and 100%) were grown on quartz substrates. The sample morphology was characterized by grazing-incidence X-ray diffraction at a fixed incidence angle of 0.2° using Cu K $\alpha$  radiation in a Rigaku diffractometer. The nanostructure of the blend were visualized using a JEOL 2100F high-resolution transmission electron microscope (TEM) at an accelerating voltage

of 80 kV. The organic films for TEM measurement were deposited on Si substrates precoated with a 10 nm thick layer of MoO<sub>3</sub>, subsequently lifted off by dissolving the MoO<sub>3</sub> in deionized water, and then captured by a Cu TEM grid.

A kinetic Monte Carlo (KMC) simulation model was also applied to quantitatively simulate the nanomorphology. Following Peumans, et al.<sup>[89]</sup> and Yang, et al.,<sup>[90]</sup> molecules filled sites starting at the substrate surface in a FCC lattice with a lattice constant of 1.06 nm, consistent with the crystal structure of C<sub>70</sub>. Each DBP molecule had a length of 2.15 nm and could contact between 16 to 22 C<sub>70</sub> molecules. Given its large size compared with C<sub>70</sub>, each DBP molecule was allowed to occupy two adjacent FCC sites, resulting in a coordination number of 18. The intermolecular binding energies for molecules in various configurations were evaluated using the Forcite molecular dynamics module in Materials Studio<sup>®</sup>. To simulate the deposition dynamics, a two-step process was employed: single molecule deposition followed by full sample annealing. In the first step, a molecule normally incident to the substrate landed at a random location at the growth surface, and attempted to move to adjacent vacant sites. An attempt was accepted if the target site had a lower total energy than its initial site, otherwise the attempt was accepted with a reduced probability of  $P(\Delta E) = \exp(-\frac{\Delta E}{k_B T})$ , where  $\Delta E$  was the difference between the total binding energies of the target and initial sites,  $k_B$  was the Boltzmann constant and  $T = 300K$  was the temperature. The number of attempts a molecule allowed to make was used as a parameter to control the average sizes of the molecular aggregates. For DBP molecules, there was an extra rotational attempt where one end of the DBP molecule stayed in its original site while the other end attempted to move to an adjacent vacant site, or exchange with an adjacent C<sub>70</sub>. To account for the many-body dynamics during deposition, full sample annealing occurred after every 1,000 molecules were deposited. During this step, the 1,000 molecules were allowed to move to adjacent sites. The attempts followed the same rules as in the single molecule

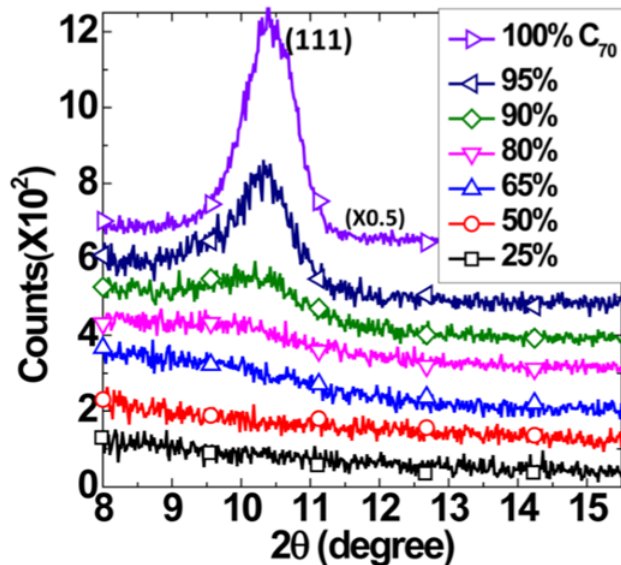


Figure 2.1: Intensity of the (111)  $C_{70}$  X-ray diffraction peak of several DBP/ $C_{70}$  blends whose  $C_{70}$  concentrations are provided in the legend.

deposition process. Full sample annealing significantly reduced the computational intensity compared with real-time simulations in which the dynamics of all molecules were simultaneously considered. This enabled the simulation of systems with a very large number of molecules ( $\sim 10^6$ ).

## 2.2 Nanostructures in the Blended DBP/ $C_{70}$ Heterojunctions

The nanostructures formed in DBP/ $C_{70}$  blends are examined using the X-ray diffraction patterns shown in Fig. 2.1. The peak at  $10.3 \pm 0.1^\circ$  corresponds to diffraction from the (111) crystal planes of the  $C_{70}$  FCC structure.<sup>[91]</sup> Blending with DBP results in broadened and less well-defined diffraction peaks. The average  $C_{70}$  nanocrystallite diameters calculated using the Scherrer equation<sup>[92]</sup> are  $11.6 \pm 0.1$ ,  $10.8 \pm 0.2$ ,  $5.6 \pm 0.3$ ,  $4.1 \pm 0.6$  nm,  $3.3 \pm 1.0$  nm for neat  $C_{70}$ , 95%, 90%, 80%, and 65%  $C_{70}$  blends, respectively. The diffraction patterns become structureless for

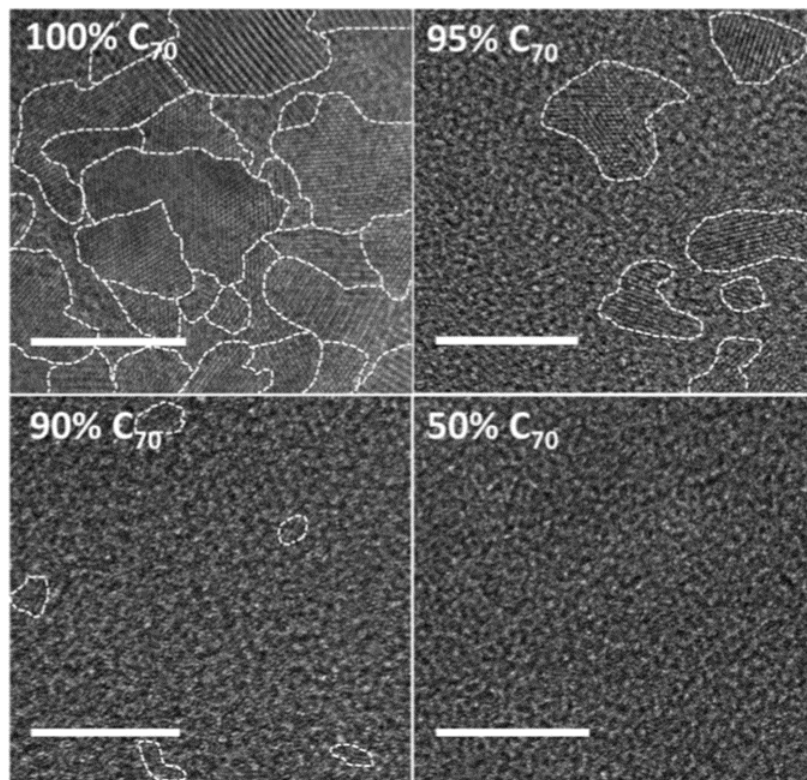


Figure 2.2: Transmission electron microscope (TEM) images of DBP/ $C_{70}$  blends with different  $C_{70}$  concentrations. Crystalline  $C_{70}$  domain boundaries are outlined in white. Scale bars in the lower left of each micrograph are 20 nm.

blends with  $C_{70}$  concentration  $< 65\%$ , indicating a lack of crystalline formation to the resolution of X-ray diffraction. No evidence for DBP crystallization is found at any blend concentration studied.

High resolution TEM images for four representative blended films are provided in Fig. 2.2. The neat  $C_{70}$  film has 10 to 20 nm diameter interconnected nanocrystalline domains, whereas 95%  $C_{70}$  in DBP results in  $\sim 10$  nm  $C_{70}$  nanocrystallites isolated by amorphous regions where DBP and  $C_{70}$  are mixed. For 90%  $C_{70}$ , the domain diameters are decreased yet further, and are increasingly isolated by amorphous regions. Finally, the 50%  $C_{70}$  blend shows no evidence for nanocrystallites at any scale.

Due to the low contrast between DBP and  $C_{70}$  (both are carbon-based) in the TEM

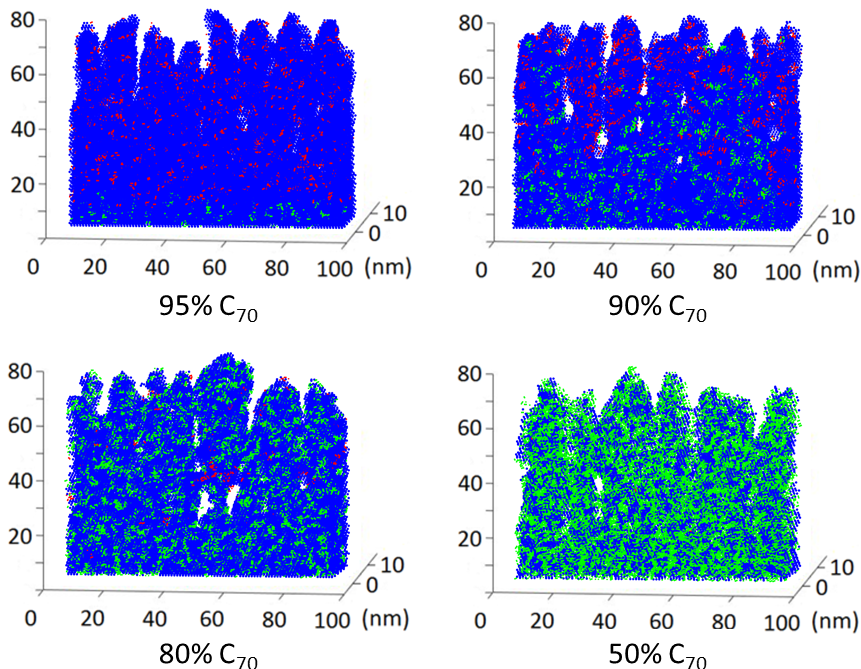


Figure 2.3: Three-dimensional simulation of the morphology of a 10 nm deep by 80 nm thick slice of 95%, 90%, 80%, and 50%  $C_{70}$  in the DBP/ $C_{70}$  blends. Growth is simulated by molecules arriving at the top of the surface starting the bottom surface. Blue areas are  $C_{70}$  molecules. Green (red) areas are DBP molecules that form (do not form) percolating paths to the bottom surface. Note the voids in the thin film. The simulation comprises 600,000 molecules.

image, the further details of the nanomorphology, in particular, those at amorphous regions are studied via the KMC simulation based on the van der Waals attraction between molecules. Figure 2.3 shows the 10 nm deep slice of simulated DBP/ $C_{70}$  blends with 95, 90, 80, 50 mol %  $C_{70}$ . The evaporated molecules are incident from the top and travel normal to the bottom surface of the film with the anode (ITO coated with  $MoO_3$ ) at the base. The 80 nm thick film has a rough surface and a modest density of voids. Here, the  $C_{70}$  regions are shown in blue, and the green areas are DBP molecules that form into percolating paths to the anode surface. The red areas are isolated islands of DBP disconnected from the anode. The isolated DBP islands remain in a substantial minority until  $> 90\%$   $C_{70}$  concentration.

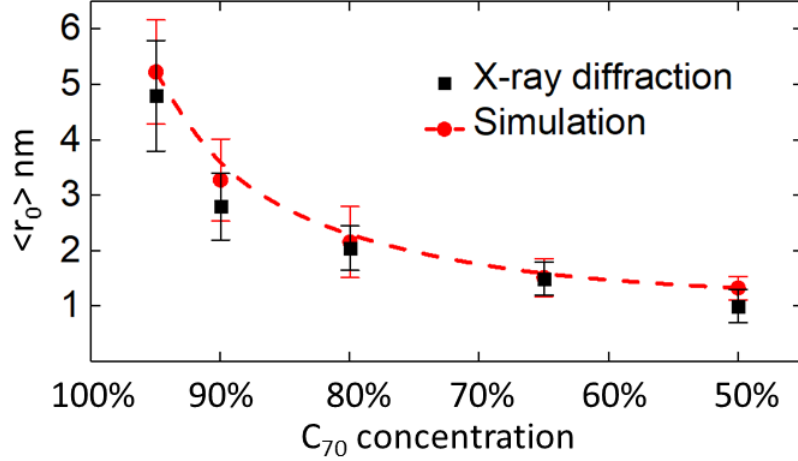


Figure 2.4: Average  $C_{70}$  cluster radius  $\langle r_0 \rangle$  vs.  $C_{70}$  concentration in DBP/ $C_{70}$  blends. The radii obtained from X-ray diffraction (squares) in Fig. 2.1 and KMC simulations (circles) are indicated. Error bars for the X-ray diffraction data arise from uncertainties in line widths at half maxima. Error bars are standard deviations of the simulated cluster size distributions.

The morphology of the simulated blend is evaluated by determining the  $C_{70}$  aggregate size. Spheres with increasing diameters are compared with the  $C_{70}$  cluster shape. The diameter of the largest sphere that can fit within the  $C_{70}$  cluster with a volume shape mismatch below 5% is used to characterize the  $C_{70}$  aggregate size. From X-ray diffraction data in Fig. 2.1, the diffracted intensity from a spherical cluster containing  $N$  molecules is proportional to  $N^2$ . Therefore, the average radius of a simulated blend is derived using an average with weight of  $r^6$ , and the standard deviation is given by the error bars in Fig. 2.4. The simulation results of the average nanocrystalline  $C_{70}$  cluster radius  $\langle r_0 \rangle$  is shown as circles, compared with values inferred from the Scherrer approximation of the X-ray diffraction pattern (squares). As the  $C_{70}$  concentration decreases from 95% to 50%,  $\langle r_0 \rangle$  decreases from  $5.2 \pm 0.9$  to  $1.3 \pm 0.2$  nm in the simulated mixed layer, which agrees with the experiment findings.

### 2.3 Percolation and Efficient Charge Collection

Figure 2.5(a) shows only those percolating paths of 10 mol % DBP in DBP/C<sub>70</sub> blends that extend from the anode into the active layer of a 50 nm deep by 80 nm thick slice. During deposition, the planar DBP molecules form continuous  $\pi-\pi$  stacks that exclude C<sub>70</sub> molecules from their interstices, thus minimizing the total energy of the blend. The stacks increase the probability of the formation of percolating paths to the anode even at very high dilutions (10%). We define the 2D density of paths using

$$\rho(z) = N_p(z)/A, \quad (2.1)$$

where  $N_p(z)$  is the number of DBP molecules forming into continuous regions in a single layer at a distance  $z$  from the anode, and  $A$  is the anode contact area. Figure 2.5(b) shows the 2D density of percolating paths in the substrate plane in a blend with 10% DBP versus the distance from the anode. The simulation follows:

$$\rho(z) = \rho_0(z) \exp\left(-\frac{z}{\zeta}\right), \quad (2.2)$$

shown by the line in Fig. 2.5(b). Here,  $\rho_0$  is the 2D density of percolating paths originating at the anode, and from the fit,  $\zeta = 33 \pm 5$  nm is the characteristic percolation length. At thickness  $d = 50$  nm, which is the typical active HJ layer thickness of an OPV cell, then  $\rho \approx 0.05 \text{ nm}^{-2}$ ,<sup>[35]</sup> corresponding to a mean distance between percolating paths of 4.5 nm. This is well below the C<sub>70</sub> exciton diffusion length ( $\sim 8$  nm),<sup>[93]</sup> suggesting that the holes can be extracted throughout the active layer with a DBP concentration of only 10 mol %.

Figure 2.3 also shows that a fraction of DBP clusters form isolated islands where holes can be trapped following exciton dissociation. Dissociation on islands is therefore limited by the recombination rate of the previously dissociated charges within a particular island. Due to the spatial separation and energetic barriers of the trapped



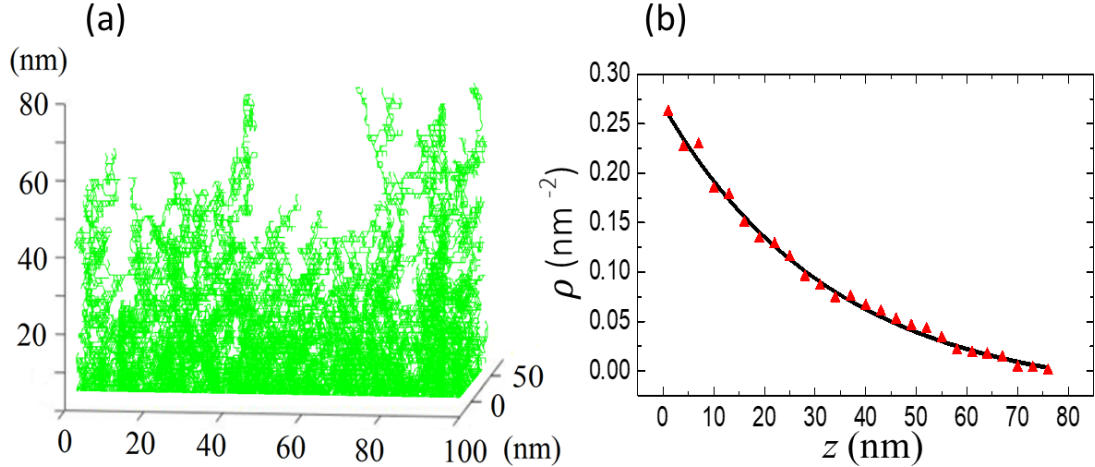


Figure 2.5: (a) Three-dimensional simulation of the DBP percolating paths of a 50 nm deep and 80 nm thick vertical slice of a blend with 10 mol % DBP in  $C_{70}$ . The  $C_{70}$  molecules are not shown. Percolating paths are identified by connecting adjacent DBP molecules with green lines. (b) Two-dimensional density of DBP percolating paths,  $\rho$ , in the substrate plane as a function of distance from the anode,  $z$  (triangles). An exponential fit to the data is shown by the line.

holes and free electrons delocalized among  $C_{70}$  molecules, the hole recombination rate in the blends with DBP concentration  $> 10\%$  is expected to be low compared with the charge extraction rate. In steady state, therefore, the exciton dissociation rate on isolated DBP islands is smaller than within the percolating paths. This is supported by the high peak internal quantum efficiencies of devices at donor concentrations of  $\sim 10\%$  in ref. [35].

In summary, we have studied nanomorphology of the blended HJ using a combination of experimental and computational methods. As shown in the TEM images in Fig. 2.2, the  $C_{70}$  crystalline phase coexists with the amorphous DBP/ $C_{70}$  mixed phase at high  $C_{70}$  concentrations. At low donor concentrations, the planar and high-aspect-ratio DBP molecules readily form continuous and extended percolating paths, allowing for the extraction of photogenerated charges at the opposing electrodes that are positioned at exceptionally large distances from their point of origin.

## CHAPTER III

# Charge Transfer States in Dilute Donor-Acceptor Blend Organic Heterojunctions

### 3.1 Introduction

Exciton dissociation at the donor-acceptor interface gives rise to the formation of a CT state that plays a crucial role in photogeneration of charges and thus determines the OPV open-circuit voltage and short-circuit current. A key to improving OPV performance is to optimize the donor-acceptor blend ratio in the photoactive HJs. While dilute donor and fullerene acceptor blends are commonly used,<sup>[35]</sup> the fundamental properties of CT states such as their energy levels and dynamics have yet to be fully clarified. Bernardo et al. explored CT states at N,N'-Di(1-naphthyl)-N,N'-diphenyl-(1,1'-biphenyl)-4,4'-diamine (NPD)/C<sub>60</sub> HJs with varying C<sub>60</sub> concentrations and found that the dependence of CT state energy on the dielectric constant is affected by the crystallinity of C<sub>60</sub> in the blend. Their results point to the importance of local crystallinity in enabling delocalization of electrons and/or holes of the CT state to facilitate the charge separation process. However, their luminescence spectra failed to cover energies <1.2 eV, giving incomplete data of the important CT spectral features at long wavelengths.<sup>[42]</sup> Arndt et al. studied the time-resolved and temperature-dependent PL of CT states in P3HT/[6,6]-phenyl-C61-butyric acid

methyl ester (PC<sub>61</sub>BM) blends. They showed that an excess amount of fullerene led to an increased probability of CT state formation, although the disruption of the polymer packing at high fullerene concentrations negatively influences charge separation.<sup>[45]</sup> Piersimoni et al. discussed the change of film morphology and energies of CT states in the blends consisting of poly[2-methoxy-5-(30,70-dimethyloctyloxy)-1,4-phenylenevinylene] (MDMO-PPV) as donor and fullerene molecules with different side chains as acceptors, where the CT energy decreases as fullerene concentration increases.<sup>[94]</sup>

In this chapter, we continue focusing on small-molecule blend HJs comprising the donor DBP and the acceptor, C<sub>70</sub>. When used in an OPV structure, the device performance is optimized at a surprisingly dilute donor volume ratio of 1:8 DBP/C<sub>70</sub> (~90% C<sub>70</sub>).<sup>[35]</sup> Charge transfer state properties at various blend ratios are studied by means of both steady-state and time-resolved PL, electroluminescence (EL), and reverse-biased OPV *EQE*, and analyzed based on DFT. We identify two CT states in blends where the amorphous DBP/C<sub>70</sub> mixed and nanocrystalline C<sub>70</sub> phases coexist: a localized, high binding energy CT1 state; and a delocalized, lower binding energy CT2 state. To confirm the proposed morphological origins of both CT states, we intentionally control the spatial confinement of them by growing multi-quantum well structures of C<sub>70</sub> and DBP with the degree of CT localization determined by the individual layer thicknesses.

In the blended DBP/C<sub>70</sub> HJ, the energy and lifetime of the CT states are functions of the size of the C<sub>70</sub> nanocrystallites, which is quantitatively understood in terms of a quantum confinement model. The ratio of the CT2-to-CT1 population increases as the relative volume of the C<sub>70</sub> crystalline phase increases. The delocalized C<sub>70</sub> state exhibits  $> 91 \pm 2\%$  dissociation efficiency in HJs with a 90% C<sub>70</sub> concentration. The contribution of CT2 dominates the charge generation in highly dilute DBP/C<sub>70</sub> HJs.

## 3.2 Experimental Section

Using the same purification and deposition methods described in Chapter II, 54nm blended DBP/C<sub>70</sub> HJs were grown on sapphire substrates. During the growth of multilayer DBP/C<sub>70</sub> quantum well structures, however, temperatures of both sources were adjusted to give a stable growth rate of 0.1 Å/s while two independently controlled source shutters were used to switch between DBP and C<sub>70</sub> after each layer growth was completed.

Samples for the scanning transmission electron microscope (STEM) measurements were capped with a C<sub>70</sub> layer with a thickness equal to the total multilayer stack thickness, and a 100 nm thick Ag protection layer. The sample was then cut into thin slices using focused ion beam (FIB) milling (FEI Nova 200 Nanolab SEM/FIB). The sample thicknesses were estimated to be tens of nanometers. The samples were then examined using a JEOL 2100F high-resolution transmission electron microscope at an accelerating voltage of 200 kV. The dibenzo([f,f']-4,7'-di[4bromophenyl]-4',7'-diphenyl)diindeno[1,2,3-cd:1',2',3'-lm]-perylene (Br<sub>2</sub>-DBP) molecules used in STEM samples were synthesized by Luminescence Technology Corp.<sup>[95]</sup>

Steady-state PL spectra were obtained by exciting the organic samples in vacuum at a wavelength of  $\lambda = 442$  nm using a continuous wave He-Cd laser. The EL from forward-biased OPVs was investigated using the device structure: ITO/10 nm MoO<sub>3</sub>/54 nm DBP/C<sub>70</sub>/8 nm bathophrenanthroline (Bphen)/100 nm Al. All spectra were collected normal to the substrate using a fiber-coupled monochromator (Princeton Instruments SP2300i) equipped with both a Si charge-coupled device (CCD) array (PIXIS:400) and an InGaAs photoreceiver with sensitivity from  $\lambda = 800$  to 1700 nm (Newport model 2153). Time-resolved PL measurements were performed using a time-correlated single photon counter (PicoHarp 300) coupled to a Si single photon avalanche detector (PDM Series). The samples were excited at  $\lambda = 480$  nm using 150 fs pulses at a 1 kHz repetition rate from a Ti:sapphire laser (ClarkMXR CPA-series)

pumped optical parametric amplifier (TOPAS-C). A  $\lambda = 800$  nm cutoff long-pass filter was used to remove DBP and C<sub>70</sub> emission to isolate the CT state spectra.

For reverse-biased *EQE* measurements, the OPVs were excited normal to the substrate by focused monochromated light from a Xe arc-discharge lamp chopped at 200 Hz. A current amplifier (Keithley 480) was used to provide a voltage bias and further amplify the photocurrent before measurement with a lock-in amplifier (Stanford Research Systems SR830). Under sufficiently high reverse bias, the CT exciton dissociation efficiency  $\eta_{diss}$  and charge collection efficiency  $\eta_{CC}$  approach unity, leading to  $\eta_{EQE} = \eta_A$  (See Eq. 1.23) in the blend HJ with 100% diffusion efficiency  $\eta_{diff}$ .<sup>[96]</sup> The internal quantum efficiency (*IQE*) can therefore be obtained from the ratio of  $\eta_{EQE}/\eta_A$ . Optical constants (i.e., the real and imaginary parts of the index of refraction) of the neat and blended films were measured by variable angle spectroscopic ellipsometry.

Quantum chemical calculations were carried out using DFT and time dependent density functional theory (TDDFT) in the Gaussian 09w package.<sup>[97]</sup> Calculations were performed on various monomer, dimer, and trimer combinations of the C<sub>70</sub> and DBP molecules. The geometries were optimized using the B3LYP functional and 6-31G(d) basis set. Based on the optimized structures, TDDFT was used to obtain the electron densities and energy levels of excited states based on the B3LYP functional and 6-31G(d) basis set.

### 3.3 Charge Transfer Excitons at Blended DBP/C<sub>70</sub> Heterojunctions

Figure 3.1(a) shows the EL spectra of OPVs with different DBP/C<sub>70</sub> blends at +3 V forward bias. The EL resulting from two CT states in the near-infrared ( $\lambda = 1.0 - 1.6$  eV) is easily distinguished from the singlet emission of neat C<sub>70</sub> and DBP at  $\lambda >$

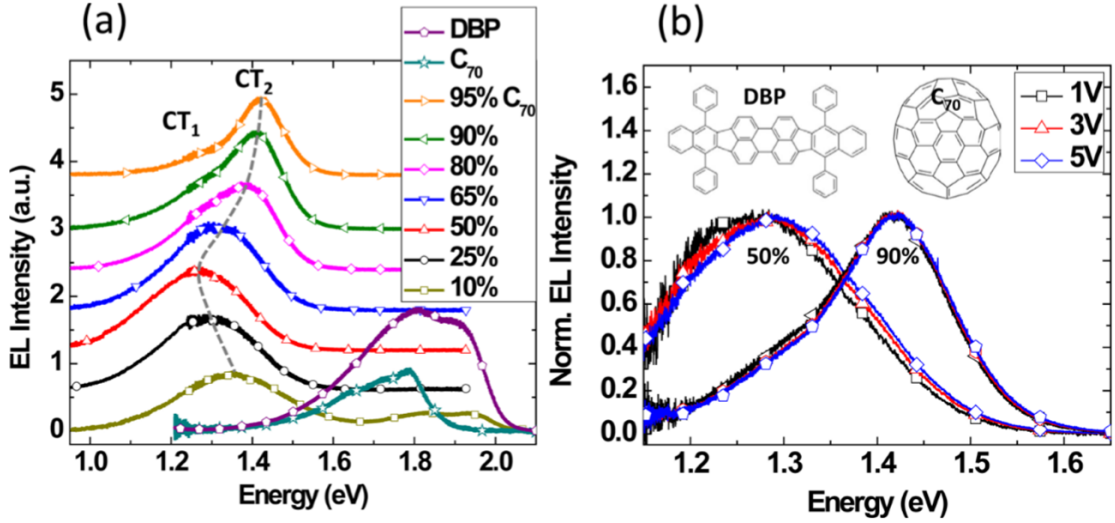


Figure 3.1: (a) EL spectra of OPV with different  $C_{70}$  concentrations in blends with DBP under  $\pm 3$  V forward bias. The spectra above and below 1.22 eV are detected by a Si CCD and an InGaAs photoreceiver, respectively. The spectra are offset for clarity. Two charge transfer excitons are labeled CT1 and CT2. The spectra from neat DBP and  $C_{70}$  are shown for comparison. (b) Voltage dependence of EL with 90 and 50%  $C_{70}$  concentrations in DBP. Inset: Molecular structures of DBP and  $C_{70}$ .

1.6 eV. We denote the low- and high-energy states as CT1 and CT2, respectively. The EL spectrum from the 50%  $C_{70}$  blend is relatively structureless. The CT state energy increases as the  $C_{70}$  concentration is either decreased or increased away from 50%, where the CT2 state becomes dominant for blends with  $>65\%$   $C_{70}$  concentration. The low-energy EL shoulder for  $>65\%$   $C_{70}$  blends is associated with the separate CT1 state. Surprisingly, insignificant DBP or  $C_{70}$  Frenkel exciton emission appears in the blends even with highly asymmetric blend concentrations (95 or 10%  $C_{70}$ ) due to the efficient recombination of injected negative and positive charges at the HJ. As the drive voltage increases from +1 to +5 V in Fig. 3.1(b), the low-energy EL shoulder from the device with 90%  $C_{70}$  slightly decreases in intensity, while the peak energy remains unchanged at  $1.41 \pm 0.01$  eV. The EL peak of the 50%  $C_{70}$  device has a minor blue shift of  $20 \pm 5$  meV as the voltage is increased from  $\pm 1$  to  $\pm 5$  V.

The PL spectra from various thin film blends at 20 K are shown in Fig. 3.2(a).

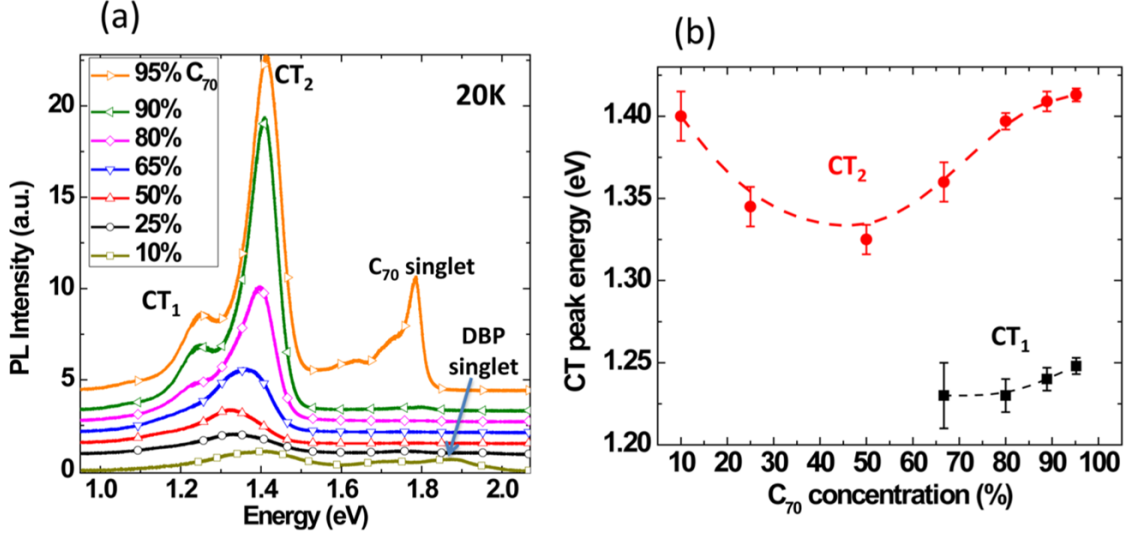


Figure 3.2: (a) Steady-state PL spectra of DBP/ $C_{70}$  blends excited by a  $\lambda = 442$  nm wavelength laser at 20 K. Both CT and monomer singlet emission spectra are noted. The spectra are offset for clarity. (b) Charge transfer exciton energies vs  $C_{70}$  concentration. The curves are a guide for the eye.

Charge transfer state emission appears in the same energy range as from EL for all blends tested, whereas the CT2-to-CT1 intensity ratio is larger than that in EL, with intensity ratios calculated based on Gaussian fits to the spectra of  $3.0 \pm 0.4$ ,  $2.7 \pm 0.5$ ,  $1.9 \pm 0.6$ , and  $1.3 \pm 0.6$  for 95, 90, 80, and 65%  $C_{70}$  concentration, respectively. At  $<65\%$  concentration, the PL spectra become structureless and it is no longer possible to resolve the two charge transfer features. The CT2-to-CT1 intensity ratio does not change as the excitation energy varies from 2.80 to 1.60 eV. No  $C_{70}$  or DBP Frenkel exciton emission is observed for blends with  $C_{70}$  concentrations between 90 and 25%, indicating  $\sim 100\%$  exciton diffusion to, and charge transfer efficiency at the interface. The CT state energies as a function of  $C_{70}$  concentration are provided in Fig. 3.2(b).

Calculations using TDDFT were employed to investigate the shift in CT energy, with the results of singlet Frenkel/CT exciton energies shown in Fig. 3.3(a). The  $C_{70}$  monomer has the lowest singlet energy of  $E_S = 2.04$  eV, while the DBP monomer has  $E_S = 2.18$  eV. Other high-energy singlet states are also shown. The singlet energies

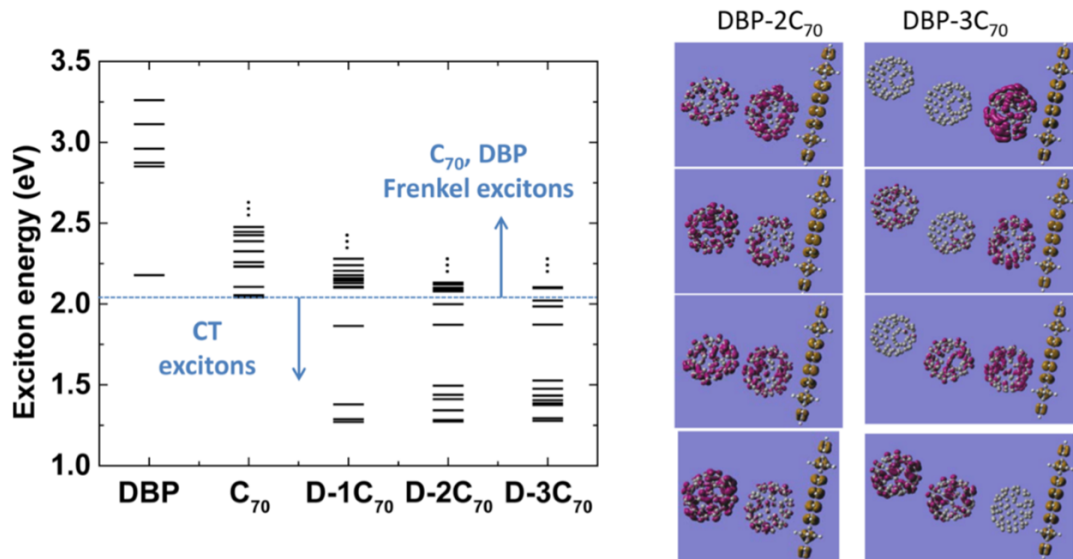


Figure 3.3: (a) Calculated singlet energies of different monomer, dimer, trimer, and tetramer combinations of DBP and  $C_{70}$  using TDDFT. On the abscissa, DBP is abbreviated as D. (b) Visualized charge density difference analysis of the first four CT states of the DBP/ $C_{70}$  dimer (left) and trimer (right) complexes. The electron (purple) and the hole (yellow) density distributions are located on the  $C_{70}$  and DBP molecules, respectively.

of the DBP- $C_{70}$  physical dimer, trimer (one DBP/two  $C_{70}$  molecules), and tetramer (one DBP/three  $C_{70}$  molecules) that lie below the DBP and  $C_{70}$  monomer states are CT states. We note that these calculations consider only a few of the many possible DBP- $C_{70}$  molecular configurations, with those provided here serving as examples. The charge density distribution of CT states shown in Fig. 3.3(b) indicates that the electron (purple) and hole (yellow) densities are on  $C_{70}$  and DBP, respectively. Including more  $C_{70}$  into the complex leads to moderate electron delocalization and creates several higher-energy CT states. This is also consistent with DFT results reported for  $PC_{61}BM$  clusters of varying sizes.<sup>[98]</sup> The calculated oscillator strengths of dimer CT states are in the range of  $10^{-4}$  to  $10^{-3}$ , which are  $10^2$  to  $10^3$  times lower than for the monomers but higher than for trimer and tetramer CT states.

The dynamics of CT state recombination were studied using time-resolved PL at



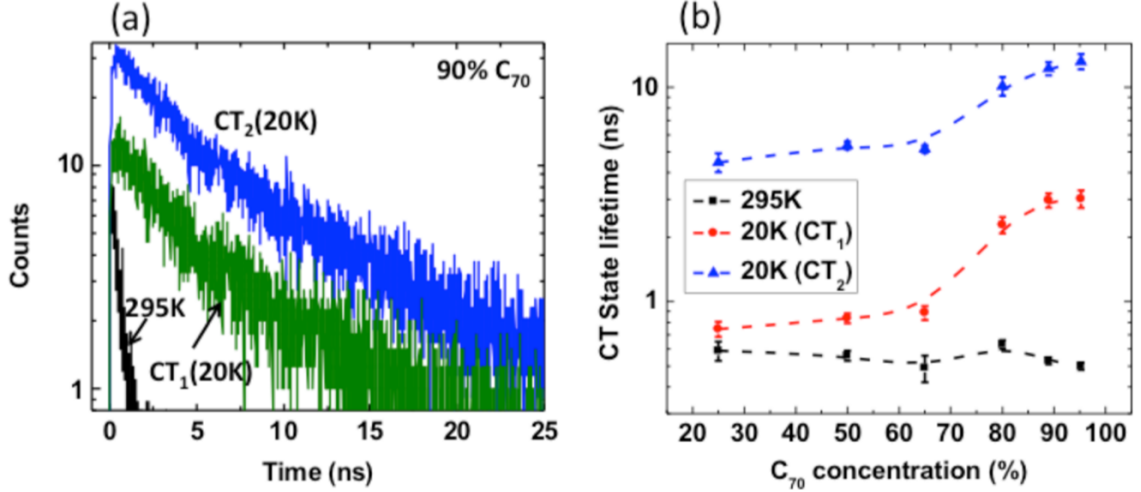


Figure 3.4: (a) Time-resolved PL for a DBP/C<sub>70</sub> blend with 90% C<sub>70</sub> at 295 K and 20 K. (b) CT state lifetime vs C<sub>70</sub> concentration at 295 and 20 K. The error bars are the 95% confidence intervals. The data points are connected by curves to guide the eye.

room temperature and 20 K, with results shown in Fig. 3.4. At room temperature, the transient is fit by a single lifetime of  $\tau = 0.55 \pm 0.05$  ns with no dependence on C<sub>70</sub> concentration (see Fig. 3.4(b)). At 20 K, nonradiative recombination is diminished, leading to an increase in CT lifetime that is dependent on concentration. The time-resolved PL of CT<sub>1</sub> and CT<sub>2</sub> are separately determined by illumination through  $\lambda = 950$  nm long-pass and 900 nm band-pass filters, respectively. The best fits are bi-exponential for both regions, yielding two similar characteristic lifetimes except that the slope intersection point for the transient at  $\lambda > 950$  nm region is lower than that near 900 nm due to the different intensities of the two CT states. The lifetimes of CT<sub>1</sub> and CT<sub>2</sub> versus C<sub>70</sub> concentration have similar trends, remaining relatively unchanged at  $< 65\%$  C<sub>70</sub> concentration and increased by a factor of 2 as concentration is increased from 65 to 95%.

### 3.4 Delocalization of Charge Transfer Exciton and Quantum Confinement Modeling

Luminescence spectra in Fig. 3.1 and 3.2 show that CT exciton energies,  $E_{CT}$ , in DBP/C<sub>70</sub> blends increase as the C<sub>70</sub> concentration is either increased or decreased away from 50%. This trend is strikingly different from that reported for other material combinations, where the  $E_{CT}$  decreases monotonically as the fullerene concentration increases. The change of dielectric constant for different blend ratios has typically been invoked to explain the shift in  $E_{CT}$ .<sup>[41,42,94]</sup> However, the optical dielectric constant ( $\epsilon_r$ ) of DBP/C<sub>70</sub> blend increases monotonically with C<sub>70</sub> concentration ( $x_{C_{70}}$ ), which fits to  $\epsilon_r = 3.88 \pm 0.0064 \cdot x_{C_{70}}$ . While this behavior may result in the spectral shift observed in CT1, it nevertheless fails to explain the trend of CT2 with an energy minimum at 50% C<sub>70</sub> and the change in slope toward an apparent asymptote at > 80% C<sub>70</sub> concentration. Furthermore, the shift cannot be explained by the solid-state solvation effect<sup>[99]</sup> since both DBP and C<sub>70</sub> are nonpolar molecules.<sup>[100]</sup>

Alternatively, the shift in CT2 energy can be attributed to the change in exciton binding energy as a result of CT delocalization and quantum confinement in the C<sub>70</sub> nanocrystals or DBP aggregates. As the C<sub>70</sub> concentration increases to >50%, the electron on a C<sub>70</sub> nanocrystal bound to the hole on DBP is delocalized over several C<sub>70</sub> molecules (cf. Fig. 3.3(b)), leading to a decrease in the binding energy and therefore an increase of CT state energy. Similarly, as the C<sub>70</sub> concentration decreases below 50%, the DBP aggregate size increases, allowing for increasing hole delocalization. To model the CT states at >50% C<sub>70</sub> concentration, we assume for simplicity that the C<sub>70</sub> domain is spherical with radius  $\langle r_0 \rangle$  estimated from X-ray diffraction data in Fig. 2.1 and is located tangent to the x-y plane. An electron within the domain is confined by a potential barrier  $\phi_b = 0.5$  eV on the boundary, which corresponds to the difference between the LUMO energies of DBP and C<sub>70</sub>.<sup>[35]</sup> The hole bound

to that electron is fixed on a DBP molecule at  $\mathbf{a} = (0, 0, -0.4 \text{ nm})$ , where 0.4 nm is the distance to the neighboring  $C_{70}$  obtained from DFT geometric optimization. We assume that the electron mobility in  $C_{70}$  is at least as large or larger than the hole in DBP and hence can occupy a greater volume, as noted by Peumans and Forrest.<sup>[55]</sup> The electron Hamiltonian is then

$$H = -\frac{\hbar}{2m^*}\nabla^2 + V(\mathbf{r})$$

$$V(\mathbf{r}) = \begin{cases} -\frac{q^2}{4\pi\epsilon_0\epsilon_r(C_{70})|\mathbf{r}-\mathbf{a}|} & (|\mathbf{r}-\mathbf{r}_0| < r_0) \\ -\frac{q^2}{4\pi\epsilon_0\epsilon_r(DBP)|\mathbf{r}-\mathbf{a}|} + \phi_b & (|\mathbf{r}-\mathbf{r}_0| > r_0) \end{cases} \quad (3.1)$$

where  $q$  is the electron charge,  $m^*$  is the electron effective mass,  $r_0$  is the  $C_{70}$  domain radius,  $\mathbf{r}_0$  is the coordinate of the center of  $C_{70}$  domain. and  $|\mathbf{r}-\mathbf{a}|$  is the distance between the hole and the electron. The relative dielectric constants are  $\epsilon_r(C_{70}) = 4.60$  and  $\epsilon_r(DBP) = 3.92$  at  $\lambda = 900 \text{ nm}$ .

We obtained the energy eigenvalues of the Hamiltonian with and without the potential  $V(\mathbf{r})$ , yielding the energy of the Coulombically bound and unbound electron states, respectively. The energy difference between them corresponds to the CT binding energy, shown in Fig. 3.5(a). The electron density of a Coulombically bound state for a  $C_{70}$  domain radius  $\langle r_0 \rangle = 2 \text{ nm}$  is shown in the inset of Fig. 3.5(a). The calculated binding energies fit reasonably well with the measured  $E_{CT}$  after including the 1.52 eV energy difference between the DBP HOMO and the  $C_{70}$  LUMO.<sup>[35]</sup>

We can apply the same approach to analyze the energy of holes located on DBP aggregates at  $C_{70}$  concentrations  $< 50\%$ . However, crystallographic data show no evidence for DBP nanocrystals at any concentration. Thus, our analysis assumes cofacial stacking<sup>[100]</sup> of only a few DBP molecules to a thickness,  $d$ , at the interface, with the bound electron fixed on the adjacent  $C_{70}$  molecule. Calculation of the eigenenergies for the hole using a Hamiltonian similar to Eq. 3.1 suggests that stacks of only  $4 \pm 1$

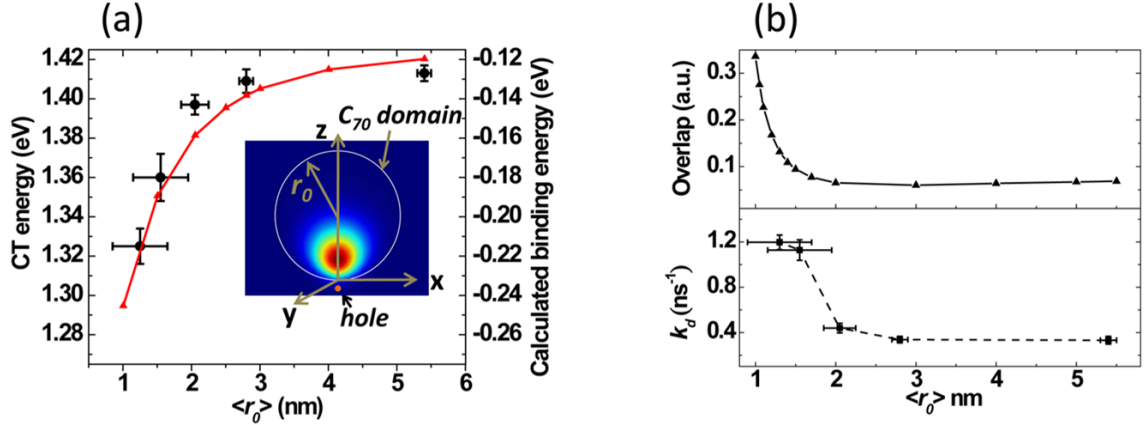


Figure 3.5: (a) Measured peak energies of CT2 states (data points) and calculated CT binding energies (red line) as functions of  $C_{70}$  domain radius,  $\langle r_0 \rangle$ . Inset: Calculated electron density distribution for a domain with  $\langle r_0 \rangle = 2$  nm. (b) (Top) Calculated probability density overlap  $J$  vs  $\langle r_0 \rangle$ . (Bottom) Measured recombination rate  $k_d$  for CT2 vs  $\langle r_0 \rangle$ .

DBP molecules can lead to the shifts in CT2 spectra in Fig. 3.2(b) observed at high DBP concentrations. Since most of the DBP region is highly disordered, the fits are not as convincing as for  $C_{70}$  nanocrystallites in Fig. 3.5(a).

As inferred from the TEM images in Fig. 2.2, the  $C_{70}$  crystalline phase coexists with the amorphous DBP/ $C_{70}$  mixed phase at high  $C_{70}$  concentrations. Charge transfer excitons in the amorphous regions are more localized than in the crystalline domains.<sup>[101]</sup> As a result, two discrete CT peaks are found in the PL spectra of thin film blends with  $>65\%$   $C_{70}$ , at which point  $C_{70}$  nanocrystallites with diameters  $>4$  nm appear. The population of CT2 excitons significantly decreases at  $C_{70}$  concentrations  $<65\%$  due to the decrease of  $C_{70}$  nanocrystallites, thereby resulting in a decrease in CT2 emission intensity.

The different lifetimes of CT1 and CT2 result in a bi-exponential PL decay at 20 K, as shown in Fig. 3.4(a). We find that the CT2 lifetime, as in the case of its binding energy, is also dependent on the  $C_{70}$  domain size, with the lifetime increasing with  $\langle r_0 \rangle$ , as shown in Fig. 3.5(b). Quantum confinement in the  $C_{70}$  domains leads

to an increase in the overlap of the electron and hole probability density as  $\langle r_0 \rangle$  decreases, resulting in a concomitant increase in the CT2 recombination rate. To model this dependence, we calculate the overlap of the probability density of the excited ( $|\psi_{CT}|^2$ ) and ground states ( $|\psi_G|^2$ ), that is,  $J = \int |\psi_{CT}|^2 |\psi_G|^2 dr^3$ , where  $\psi_G$  is the electron wave function at the DBP HOMO obtained from TDDFT calculations. The overlap integral,  $J$ , vs  $C_{70}$  domain radius is shown in Fig. 3.5(b), top panel, which qualitatively agrees with the trend observed for the decay rate of CT2, that is  $k_d (= 1/\tau)$ , in the bottom panel. A quantitative prediction of CT lifetime versus the domain size requires an accurate knowledge of the electron wavefunction phase which can only be obtained from a description of the actual  $C_{70}$  molecular configurations in the solid. This makes an accurate calculation of the transition oscillator strength as a function of  $\langle r_0 \rangle$  impossible using our current approach.

For the largest  $C_{70}$  nanocrystalline domains, the more delocalized CT states with lower binding energy may also suffer from a higher probability of exciton dissociation than for the localized CT1 states. Absent charge extraction, however, the dissociated electron eventually recombines with the hole to reform a CT exciton at the HJ, which further increases its lifetime. The CT1 lifetime versus  $C_{70}$  concentration in Fig. 3.5(b) is similar to that of CT2. Although spatially separated by different phases, some of the delocalized CT2 excitons may transfer via exchange interactions to CT1 or execute a diffusive random walk along the interface and relax to a strongly bound CT1 state.<sup>[102]</sup> Thus, a change in the CT2 lifetime may also result in changes in the observed CT1 lifetime.

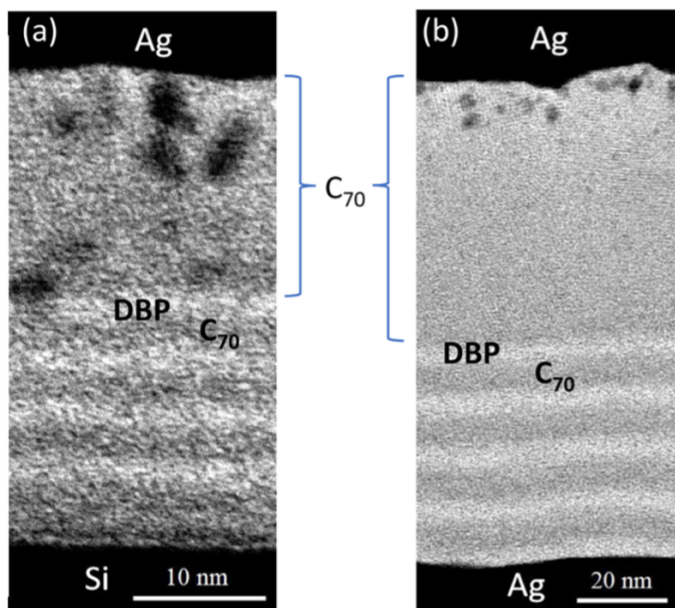


Figure 3.6: (a) Bright field cross-sectional STEM image of 5 pairs of 2 nm thick alternating layers capped by a 20 nm thick  $C_{70}$  layer and a 150 nm thick Ag protection layer. The dark spots are due to Ag diffusion from the contact. (b) Image of 5 pairs of 5 nm thick alternating layers capped by a 20 nm thick  $C_{70}$  layer and a 50 nm thick Ag layer.

### 3.5 Charge Transfer Exciton in a DBP/ $C_{70}$ Multi-Quantum Well Structure

To further confirm the proposed morphological origins of CT states and test the hypothesis of CT exciton delocalization, we systematically control the degree of CT exciton confinement by growing alternating multilayer quantum well structure of DBP/ $C_{70}$  to gain insights into the mechanisms affecting CT states in the blends of similar ratios of the two constituents. Figure 3.6 shows bright field cross-sectional STEM images of the multi-quantum well structure with alternating layer thicknesses of 2 and 5 nm. To increase the image contrast between  $C_{70}$  and DBP molecules,  $Br_2$ -DBP was substituted for DBP. Each sample contains 5 pairs of DBP and  $C_{70}$  layers capped by a  $C_{70}$  layer with the same thickness as the multilayer stack, and 100 nm of Ag. Individual layers as thin as 2 nm are clearly identified in the images in

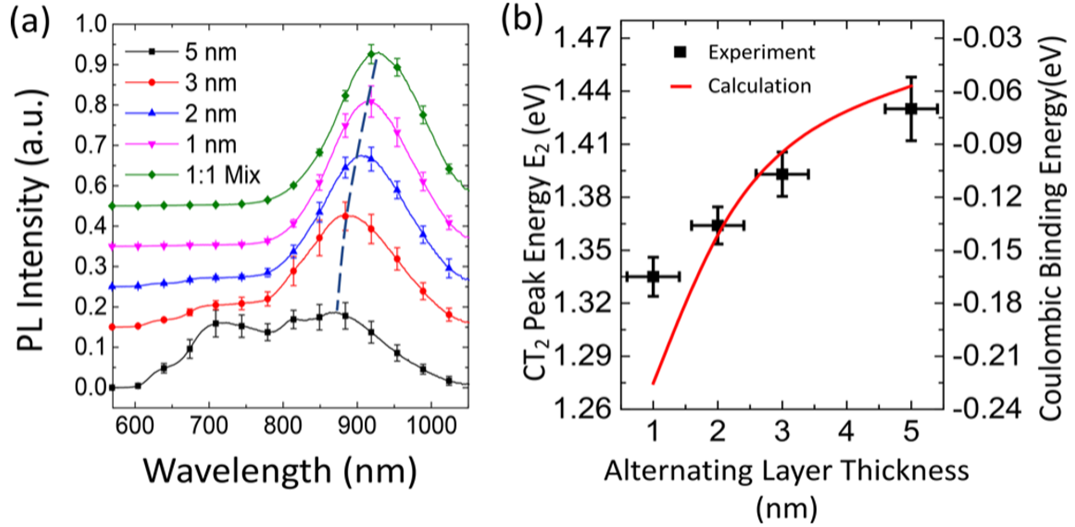


Figure 3.7: (a) Room temperature PL spectra of multi-quantum wells consisting of alternating layers of DBP and C<sub>70</sub> and a 1:1 blended sample. To achieve a total thickness of 40 nm, the multi-quantum well structures with alternating layer thicknesses of 1, 2, 3, and 5 nm contain 20, 10, 7, and 4 pairs of DBP and C<sub>70</sub> layers, respectively. The spectra are normalized to the same integrated intensity, and are offset for clarity. (b) Photoluminescence peak energies of CT<sub>2</sub> states,  $E_2$ , and calculated Coulombic binding energies vs layer thickness.

Fig. 3.6.

Figure 3.7(a) shows the normalized room temperature PL spectra from DBP and C<sub>70</sub> stacks with various layer thicknesses. All samples have a total thickness of 400 nm. The spectra are compared with that of a 1:1 DBP:C<sub>70</sub> blend HJ. The blend sample has a lowest CT<sub>2</sub> peak energy  $E_2 = 1.33 \pm 0.01$  eV. As the alternating layer thicknesses increase from 1 to 5 nm,  $E_2$  blue shifts to  $1.43 \pm 0.02$  eV.

The energy shift of CT exciton shown in Fig. 3.7(a) is consistent with the model described in the last section. Since the volume and ratio of materials in all the samples are equal, the energy shift of the CT<sub>2</sub> peak is attributed to quantum confinement as the individual layer thicknesses decrease. The quantum mechanical model developed in the last section is modified to calculate the binding energy between electron and hole of the CT<sub>2</sub> states with various alternating layer thicknesses. The experimental

and simulated results are shown in Figure 3.7(b). The calculated energy shift reasonably agrees with experiment except for the sample with 1 nm thick layers. This is possibly due to incomplete layer coverage for the thinnest sample, leading to reduced confinement.

### 3.6 Dissociation Efficiency of Charge Transfer Excitons in DBP/C<sub>70</sub> Heterojunctions

In the OPV comprising a DBP/C<sub>70</sub> blended HJ, as the volume containing the CT state decreases, an increased overlap between the electron and hole wavefunctions occurs, resulting in a larger recombination rate and a smaller dissociation efficiency compared with that of the delocalized CT states. To further study the dissociation efficiency of CT states at different blend ratios, the *EQE* of reverse-biased OPVs with 90 and 50% C<sub>70</sub> concentrations and their *IQE* versus photon energy are measured and calculated, as shown in Fig. 3.8. Both *EQE* spectra show a shoulder at  $<1.70 \pm 0.02$  eV that is absent in devices with either a neat C<sub>70</sub> or DBP photoactive layer. We attribute this feature to direct CT state absorption and exciton dissociation at the interface. At 90% C<sub>70</sub> concentration shown in Fig. 3.8(a), *IQE* remains constant at photon energies  $>1.55 \pm 0.02$  eV, while it substantially decreases from  $0.91 \pm 0.02$  to  $0.20 \pm 0.01$  as the photon energy decreases from 1.55 to 1.30 eV. At 50% C<sub>70</sub> concentration shown in Fig. 3.8(b), the *IQE* decreases from  $0.71 \pm 0.01$  to  $0.40 \pm 0.09$ .

The properties of different CT excitons are also apparent from the OPV *EQE* spectra at both 0 and -5V reverse bias. The ratio of the *EQE* at these two voltages is

$$\begin{aligned} \frac{\eta_{EQE}(0V)}{\eta_{EQE}(-5V)} &\approx \frac{\eta_A(E_{ph}) \cdot \eta_{diff} \cdot \eta_{diss}(E_{ph}, 0V) \cdot \eta_{CC}(0V)}{\eta_A(E_{ph}) \cdot \eta_{diff}} \\ &= \eta_{diss}(E_{ph}, 0V) \cdot \eta_{CC}(0V) = \eta_{IQE} \end{aligned} \quad (3.2)$$



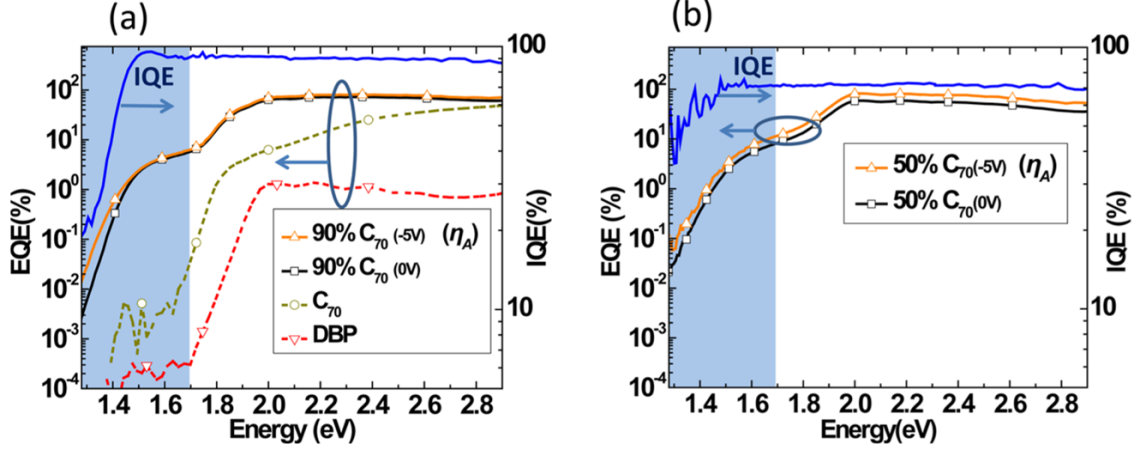


Figure 3.8: External quantum efficiency at 0 and  $-5$  V reverse bias for OPVs with (a) 90%  $C_{70}$  concentration in DBP, neat  $C_{70}$ , and neat DBP; (b) 50%  $C_{70}$  concentration in DBP. The  $EQE$  at  $-5$  V is equal to  $\eta_A$ . The internal quantum efficiency spectra for two blends are shown with blue lines.

where  $\eta_A$  is the absorption efficiency,  $\eta_{diff}$  is the exciton diffusion efficiency,  $\eta_{diss}$  is the CT exciton dissociation efficiency,  $\eta_{CC}$  is the charge collection efficiency of the OPV, and  $E_{ph}$  is the photon energy. Under sufficiently high reverse bias,  $\eta_{diss}$  and  $\eta_{CC}$  approach unity, as implied by the first equality in Eq. 3.2. The exciton diffusion efficiency is  $\eta_{diff} \approx 1$  in the 90 and 50%  $C_{70}$  blends, which is justified by the absence of DBP or  $C_{70}$  Frenkel exciton emission under direct laser excitation at  $\lambda = 442$  nm, as shown in Fig. 3.2. Thus, according to Eq. 3.2,  $\eta_{EQE}(0V)/\eta_{EQE}(-5V)$  is approximately equal to  $IQE$ . Since  $\eta_{CC}$  is independent of photon energy, the decrease of  $IQE$  at  $E_{ph} < 1.55 \pm 0.02$  eV for 90%  $C_{70}$  concentration shown in Figure 3.8(a) is attributed entirely to the decrease of  $\eta_{diss}$  for CT states. From this, we infer that the difference in  $IQE$  versus  $E_{ph}$  below and above 1.55 eV corresponds to the relative importance of dissociation from the localized CT1 and delocalized CT2 states, respectively. The delocalization of polaron pairs in the crystalline phase facilitates the escape from their mutual Coulomb attraction, which leads to a larger  $\eta_{diss}$  than the localized CT1 states in the amorphous phase.

The  $IQE$  spectrum in Figure 3.8(a) has three distinct regions: (i)  $E_{ph} > 1.70 \pm$

0.02 eV, where DBP or C<sub>70</sub> Frenkel excitons are excited and can subsequently transfer to CT states leading to dissociation; (ii)  $1.55 \pm 0.02 \text{ eV} < E_{ph} < 1.70 \pm 0.02 \text{ eV}$ , where CT2 states are directly excited; and (iii)  $E_{ph} < 1.55 \pm 0.02 \text{ eV}$ , where localized CT1 states are predominantly excited. The *IQE* in regions (i) and (ii) are  $0.91 \pm 0.02$ , suggesting that the relative contributions of CT1 and CT2 to the photocurrent remain unchanged across these two regions. As shown in the steady-state PL spectra at 90% C<sub>70</sub> concentration in Figure 3.2(a), nearly 100% of the Frenkel excitons generated in DBP and C<sub>70</sub> transfer to interfacial CT states. Assuming that  $a$  is the fraction of CT2 states and  $(1 - a)$  is the fraction of CT1 states generated at the HJ at  $E_{ph} > 1.55 \pm 0.02 \text{ eV}$  and that only CT1 is generated at  $E_{ph} = 1.30 \text{ eV}$ , then:

$$\begin{cases} \eta_{IQE} = a \cdot \eta_{diss(CT2)}\eta_{CC} + (1 - a)\eta_{diss(CT1)}\eta_{CC} = 0.91 \pm 0.02 & E_{ph} > 1.55eV \\ \eta_{IQE} \approx \eta_{diss(CT1)}\eta_{CC} = 0.20 \pm 0.01 & E_{ph} = 1.30eV \end{cases} \quad (3.3)$$

Since the values of  $a$  and  $\eta_{diss(CT2)}\eta_{CC}$  are in the range of 0 and 1, using Eq. 3.3 we infer that  $0.91 \pm 0.02 < \eta_{diss(CT2)}\eta_{CC} < 1$  and  $0.88 \pm 0.03 < a < 1$ . This implies that greater than 88% of excitons generated at  $E_{ph} > 1.55 \pm 0.02 \text{ eV}$  are CT2 states at 90% C<sub>70</sub> concentration. The dissociation efficiency of CT2 is greater than 91%, leading to efficient photogeneration in the OPV. In contrast, the OPV with 50% C<sub>70</sub> concentration shown in Figure 3.8(b) exhibits a low *IQE* due to a decreased population of CT2 states in the amorphous blends. These provide an explanation for the very high efficiencies observed in significantly diluted donor blends in this material system. This differs from material systems examined by Vandewal et al., who find that *IQE* is independent of the photon energy, and where the lowest energy CT state contributes to efficient photocurrent generation.<sup>[60]</sup>

## CHAPTER IV

# Energy Losses in Organic Photovoltaics

### 4.1 Introduction

Excitons in organic semiconductors are tightly bound electron-hole pairs with binding energies of  $E_B = 0.2$  to  $1.5$  eV.<sup>[103–106]</sup> A large driving force is required to overcome the binding energy to separate the electron and hole in the photocurrent generation process. This force is provided by the offset of the LUMO and HOMO energies, i.e.  $\Delta E_{LUMO}$  and  $\Delta E_{HOMO}$ , respectively, between donor and acceptor molecules at a type-II HJ. As a result, the dissociation process incurs an energy loss during CT at the interface:

$$\Delta E_{CT} = E_{ex} - E_{CT} \approx \Delta E_{HOMO(LUMO)} - E_B, \quad (4.1)$$

where  $E_{ex}$  is the exciton energy of the donor or acceptor that is generally equal to the HOMO-LUMO energy gap less  $E_B$ . Also,  $E_{CT}$  is the CT state energy. Additional losses arise from both radiative ( $\Delta E_r$ ) and nonradiative ( $\Delta E_{nr}$ ) recombination in charge separation and extraction:

$$\Delta E_{rec} = E_{CT} - qV_{OC} = \Delta E_r + \Delta E_{nr}, \quad (4.2)$$

where  $V_{OC}$  is the open circuit voltage and  $q$  is the electron charge. Therefore, the total energy loss at the donor-acceptor HJ is:<sup>[107]</sup>

$$E_{loss} = \Delta E_{CT} + \Delta E_{rec} = E_{ex} - qV_{OC}. \quad (4.3)$$

Heterojunctions employing fullerene derivatives usually suffer from a loss of  $E_{loss} \sim 0.7$  eV. Alternatives to fullerene acceptors have therefore been sought to reduce  $E_{loss}$  while extending the absorption spectrum into the infrared. The development of nonfullerene acceptors (NFAs) with acceptor-donor-acceptor (a-d-a) or perylene diimide (PDI)-based molecular motifs give freedom to tune the molecular energetics, absorption spectra and thin film morphologies through molecular design.<sup>[108–112]</sup> As a result, HJs using NFAs show  $\Delta E_{CT}$  as low as 0.1 to 0.2 eV, and a total  $E_{loss} \leq 0.5$  eV,<sup>[113–115]</sup> compared to fullerene-based HJs with  $\Delta E_{CT} > 0.3$  eV, and a  $E_{loss} > 0.7$ eV.<sup>[116–118]</sup> While energy loss mechanisms have been discussed for years,<sup>[107,119–121]</sup> to our knowledge there has been no *quantitative* analysis as to why NFAs have both  $\Delta E_{CT}$  and  $\Delta E_{rec}$  comparatively low. As a result, unambiguous guidelines for molecular designs have been lacking.

In this chapter, we use semiclassical Marcus charge transfer theory to quantify both the charge transfer,  $k_{CT}$ , and non-radiative recombination,  $k_{nr}$ , rates. These rates are used to analyze the energy losses,  $\Delta E_{CT}$  and  $\Delta E_{nr}$ , as functions of  $E_B$  and the intra- and inter-molecular electron-phonon coupling. We compare the energy losses during exciton dissociation of a family of acceptors in type-II bulk HJs, where  $k_{CT}$  vs.  $\Delta E_{CT}$  are studied using temperature dependent transient PL spectroscopy. Also,  $\Delta E_{nr}$  is determined from the EL quantum yield of the CT states. The large and rigid molecular backbone of thiophene-based NFAs, and the presence of non-bonding orbitals introduced by cyano or chloro group substitutions extend the electron density distribution along the molecules to reduce  $E_B$ , electron-phonon coupling, and hence

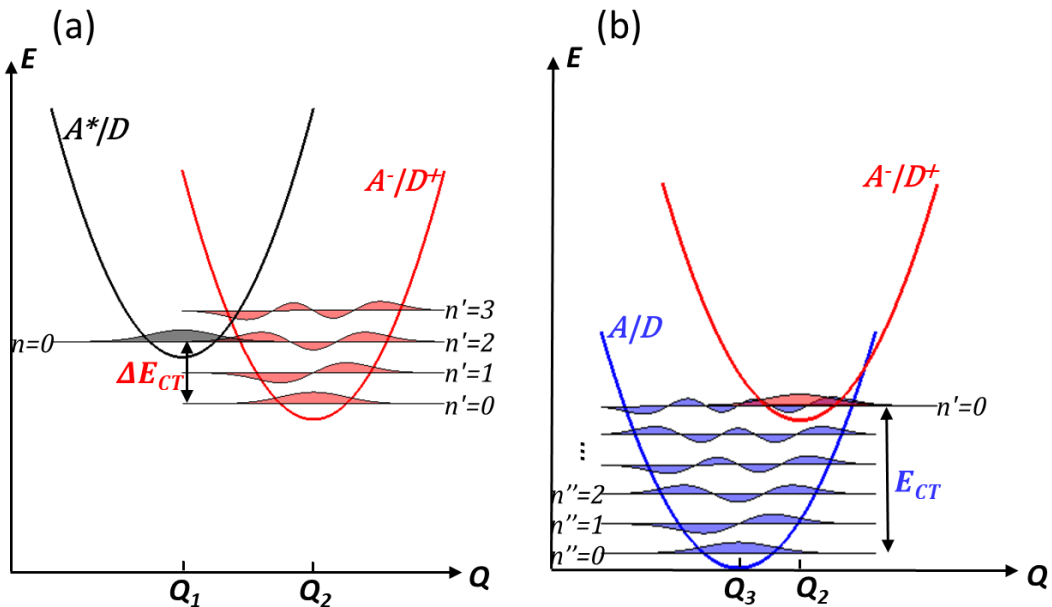


Figure 4.1: Energy diagrams of (a) charge transfer from the acceptor exciton ( $A^*$ ) to the charge transfer (CT) state ( $A^-/D^+$ ), and (b) non-radiative recombination from the CT state ( $A^-/D^+$ ) to the ground state ( $A/D$ ). The Gibbs free energies are  $\Delta E_{CT}$  in (a) and  $E_{CT}$  in (b). Symmetric parabolic potentials are assumed for the initial and final states. The vibrational levels ( $n$ ,  $n'$ , and  $n'' = \{0, 1, 2 \dots\}$ ) are equally spaced. Equilibrium configurations of  $A^*/D$ ,  $A^-/D^+$ , and  $A/D$  manifolds are indicated by  $Q_1$ ,  $Q_2$  and  $Q_3$ , respectively.

reduce energy losses. Calculations using DFT and quantum mechanical modeling lead to strategies for the design of molecular structures with low energy losses.

## 4.2 Theory and Modeling

We focus our attention on comparing charge transfer of excitons from a variety of acceptor to donor molecules. The transition from an acceptor exciton ( $A^*$ ) to a CT state ( $A^-/D^+$ ) is illustrated in Fig. 4.1(a). In semiclassical Marcus theory,<sup>[11,72]</sup> the rate for non-adiabatic transfer is given by:

$$k_{CT} = \frac{2\pi}{\hbar} V^2 F = \frac{2\pi}{\hbar} V^2 \frac{1}{\sqrt{4\pi\lambda_O k_B T}} \sum_{n'} (-S) \frac{S^{n'}}{n'!} \exp\left(-\frac{(-\Delta E_{CT} + \lambda_O + n'\hbar\langle\omega_I\rangle)^2}{4\lambda_O k_B T}\right). \quad (4.4)$$

Here,  $V = \langle \psi_{A^*/D} | H | \psi_{A^-/D^+} \rangle$  is the electronic coupling between the acceptor excited state ( $\psi_{A^*/D}$ ) and CT ( $\psi_{A^-/D^+}$ ) wavefunctions,  $H$  is the Hamiltonian,  $F$  denotes the nuclear Franck-Condon factor,  $\lambda_O$  is the intermolecular reorganization energy,  $k_B$  is the Boltzmann constant, and  $T$  is the temperature. Also,  $S$  is the mean intramolecular electron-phonon coupling constant known as the Huang-Rhys factor, given by  $S = \lambda_I/\hbar\langle\omega_I\rangle$  where  $\lambda_I$  is the intramolecular reorganization energy incorporating all the coupled modes. Conveniently, the intramolecular phonon modes can be subsumed into a single mode with mean energy  $\hbar\langle\omega_I\rangle$ , since the dominant mode in organic molecules is carbon-carbon (C-C) bond stretching with  $\hbar\langle\omega_I\rangle \approx 0.17$  eV. Neglecting the contribution of entropy to the free energy for charge transfer, the Gibbs free energy in Eq. 4.4 is:

$$\begin{aligned} -\Delta E_{CT} &= E_{CT} - E_{ex} \approx |E_{HOMO_D} - E_{LUMO_A}| - (|E_{HOMO_A} - E_{LUMO_A}| - E_B) \\ &= -(\Delta E_{HOMO} - E_B), \end{aligned} \quad (4.5)$$

where  $E_{HOMO_{D(A)}}$  and  $E_{LUMO_{D(A)}}$  are the HOMO and LUMO energies of the donor (acceptor) molecule, respectively.

The Franck-Condon factor in Eq. 4.4 contains contributions from high frequency intramolecular phonon modes ( $\hbar\omega_I \gg k_B T$ ) and low frequency intermolecular modes in the medium ( $\hbar\omega_O \ll k_B T$ ). The high frequency modes are quantum mechanically treated with quantized levels ( $n = \{0, 1, 2 \dots\}$ ) depicted in Fig. 4.1. The transition occurs from the lowest vibrational state ( $n=0$ ) of acceptor excitons ( $A^*$ ) to the vibrational state  $n'$  in the CT ( $A^-/D^+$ ) manifold. The Frank-Condon integral of the transition is then simplified to  $\exp(-S) \frac{S^{n'}}{n'!}$ . The contribution of low frequency

intermolecular modes is lumped into  $\lambda_O$  in the classical Arrhenius-type exponential in Eq. 4.4.

The reorganization energy,  $\lambda$ , during charge transfer is the sum of intramolecular ( $\lambda_I$ ) and intermolecular ( $\lambda_O$ ) contributions. Intramolecular reorganization arises from local electron-phonon coupling leading to a nuclear coordinate displacement  $\langle\Delta Q\rangle$  between two equilibrium positions  $Q_1$  and  $Q_2$  (or  $Q_2$  and  $Q_3$  in Fig. 4.1(b)). In the harmonic approximation,

$$\lambda_I = \frac{1}{2}(M\langle\omega_I\rangle^2)\langle\Delta Q\rangle^2, \quad (4.6)$$

$$S = \frac{1}{2}\left(\frac{M\langle\omega_I\rangle}{\hbar}\right)\langle\Delta Q\rangle^2, \quad (4.7)$$

where  $M$  is the reduced nuclear mass of the molecule.

Intermolecular reorganization is due to the electronic polarization, and consequently lattice relaxation of the surrounding medium. Assuming a spherically symmetric charge distribution on the donor and acceptor, and treating the medium as an isotropic dielectric continuum, we have:<sup>[122]</sup>

$$\lambda_O = \frac{e^2}{4\pi\epsilon_0}\left(\frac{1}{\epsilon_{opt}} - \frac{1}{\epsilon_s}\right)\left(\frac{1}{2r_D} + \frac{1}{2r_A} - \frac{1}{R_{DA}}\right), \quad (4.8)$$

where  $\epsilon_{opt}$  and  $\epsilon_s$  are the optical and static dielectric constants, respectively,  $r_{D(A)}$  is the effective radius of the donor (acceptor) molecule, and  $R_{DA}$  is the distance between acceptor and donor.

Non-radiative recombination energy losses ( $\Delta E_{nr}$ ) that occur through coupling from the CT ( $A^-/D^+$ ) to the ground state ( $A/D$ ) are illustrated in Fig. 4.1(b). The transfer rate is:

$$k_{nr} = \frac{2\pi}{\hbar}V'^2 \frac{1}{\sqrt{4\pi\lambda'_O k_B T}} \sum_{n''} (-S') \frac{S'^{n''}}{n''!} \exp\left(-\frac{(-E_{CT} + \lambda'_O + n''\hbar\langle\omega_I\rangle)^2}{4\lambda'_O k_B T}\right), \quad (4.9)$$

where,  $V' = \langle\psi_{A^-/D^+} | H | \psi_{A/D}\rangle$  is the electronic coupling between the CT and

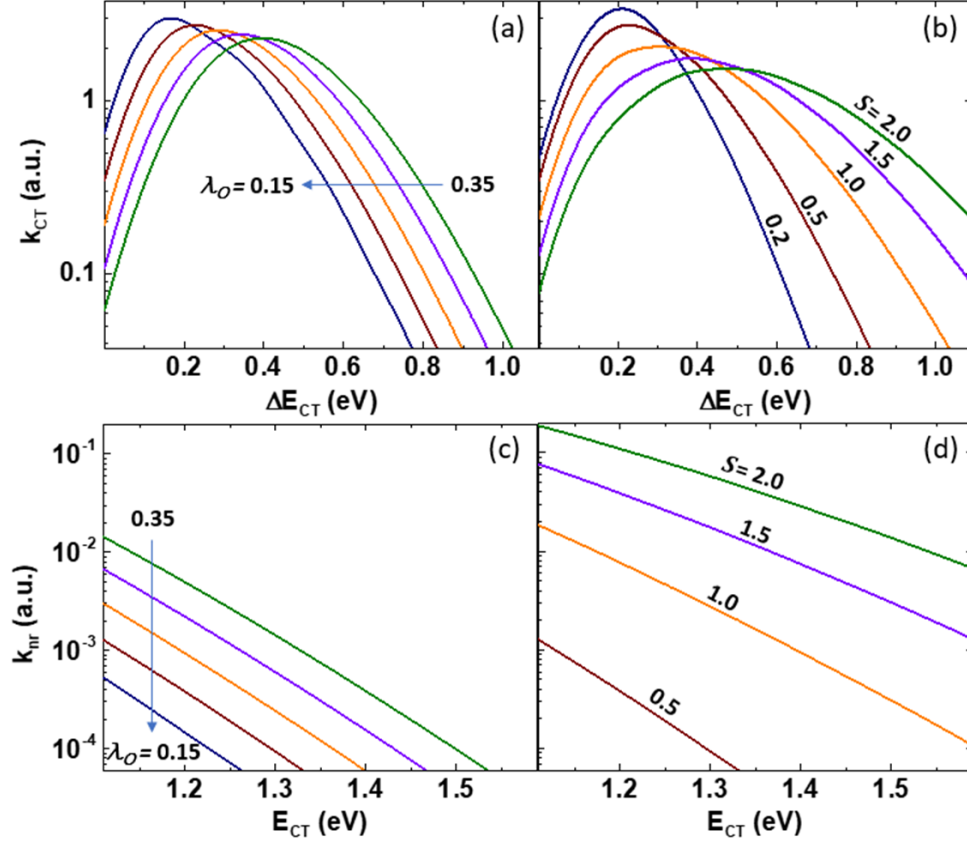


Figure 4.2: Charge transfer rate,  $k_{CT}$ , vs. the energy loss on CT state formation,  $\Delta E_{CT}$  as functions of (a) the intermolecular reorganization energy,  $\lambda_O$ , and (b) intramolecular coupling strength,  $S$ . (c) Non-radiative recombination rate,  $k_{nr}$ , vs.  $E_{CT}$  as functions of  $\lambda_O$  and (d)  $S$ .

ground states. The Gibbs free energy in Eq. 4.9 is equal to  $E_{CT}$ , leading to a nonradiative energy loss of:

$$\Delta E_{nr} = k_B T \ln \left( \frac{1}{\eta_{EL}} \right) = k_B T \ln \left( \frac{k_r + k_{nr}}{k_r} \right), \quad (4.10)$$

Here,  $\eta_{EL}$  is the IQE of the CT state EL.

To achieve low energy loss yet efficient charge transfer,  $E_B$  and  $\Delta E_{HOMO}$  must be minimized at the same time (c.f. Eqs. 4.4 and 4.5). Secondly, decreasing both intra- and intermolecular electron-phonon coupling leads to an increased  $k_{CT}$  at a minimum cost to  $\Delta E_{CT}$ , as well as a decrease in  $k_{nr}$  and consequently,  $\Delta E_{nr}$ . Calculations



of  $k_{CT}$  and  $k_{nr}$  using Eqs. 4.4 and 4.9 at  $T=300\text{ K}$  are shown in Fig. 4.2. For convenience, we set  $V^2$  and  $V'^2$  equal to unity. Figures 4.2(a) and (b) show that reducing  $\lambda_O$  and  $S$ , respectively, lead to an increased maximum in  $k_{CT}$  that occurs at a lower  $\Delta E_{CT}$ . Note that  $k_{nr}$  vs.  $E_{CT}$  in Figs. 4.2(c) and (d) have a Marcus inverted relationship in the range of  $E_{CT}$  we consider. This is a version of the "energy gap law" [120,123] where  $k_{nr}$  decreases with increasing  $E_{CT}$ . Decreasing  $\lambda_O$  and  $S$  further reduces  $k_{nr}$  at a given  $E_{CT}$ , and hence non-radiative recombination  $\Delta E_{nr}$ , according to Eq. 4.10. All four figures show that a decrease of  $S$  results in a more pronounced change of  $k_{CT}$  and  $k_{nr}$  than that for  $\lambda_O$ .

### 4.3 Experimental Section

Molecular level electron density distributions of NFAs and fullerenes, and their energy levels were modeled using DFT/TDDFT in the Gaussian 09w package.<sup>[97]</sup> The calculation of exciton binding energy and reorganization energy was based on the B3LYP functional and the 6-31G(d) basis set, since B3LYP is one the most widely used functional and has been used to give reasonable results for both excited and ionic states of some NFAs.<sup>[124–126]</sup> Molecular solvation effects are considered by combining the DFT calculations with the Polarizable Continuum Model.<sup>[127]</sup>

The  $k_{CT}$  as a function of  $\Delta E_{CT}$  was studied by blending the acceptors with a variety of donors at a concentration of  $2 \pm 1\text{ wt}\%$ , and with a wide energy gap poly(methylmethacrylate) (PMMA) or Bphen matrix as a reference. The mixture was either made by thermal evaporation at a chamber base pressure of  $2 \times 10^{-7}$  torr, or dissolved in chlorobenzene at a concentration of  $20\text{ mg mL}^{-1}$ , and then spin-coated onto a Si substrate to form 100 nm thick films. Donors were chosen to have non-overlapping absorption spectra with the acceptors such that excitons are generated only on the acceptor molecules using appropriately chosen excitation wavelengths. In the dilute blends, the acceptor domains are small compared to the exciton diffusion

length, thereby eliminating the dynamics of exciton diffusion. Then,  $k_{CT}$  is calculated from the difference between the acceptor exciton lifetime in the type-I PMMA(or Bphen)/acceptor HJ, and at the type-II donor/acceptor HJ.

Exciton dynamics were measured by time-resolved PL using a time-correlated single photon counter (PicoHarp 300, PicoQuant GmbH) coupled to a Si single photon avalanche detector (PDM Series, PicoQuant GmbH). The acceptor molecules were excited at  $\lambda = 725$  nm for NFAs, and 560 nm for fullerene derivatives using 150 fs pulses at a 1 kHz repetition rate from a Ti:sapphire laser (CPA-2110, Clark-MXR Inc.)-pumped optical parametric amplifier (TOPAS-C, Coherent). Charge transfer dynamics vs. temperature in the range between 295 K and 25 K were obtained in a closed-cycle cryostat (SHI-4-5, Janis Research Company LLC).

Organic photovoltaic cell structures were: indium tin oxide (ITO)/ ZnO/ BHJ/ MoO<sub>3</sub>/ Al. The 20 nm thick ZnO layer was spin-coated onto a precleaned, UV-ozone-treated ITO anode, followed by 30 min thermal annealing at 150 °C in air. The 100 nm thick BHJ layer was spin-coated on the ZnO, followed by thermal evaporation of a 10 nm thick MoO<sub>3</sub> buffer and a 100 nm thick Al cathode at a chamber base pressure of  $2 \times 10^{-7}$  torr. The external quantum efficiency was measured using the photocurrent of devices coupled to a lock-in amplifier (Stanford Research Systems SR830) while being excited by monochromated light from a Xe arc-discharge lamp chopped at 200 Hz. Photoluminescence and EL spectra were measured using a fiber-coupled monochromator (Acton series SP2300i, Princeton Instruments) equipped with a Si charge-coupled device array (PIXIS:400, Princeton Instruments).

## 4.4 Results

The parameters,  $E_B$ ,  $S$  and  $\lambda_O$  in Eqs. 4.4, 4.5 and 4.9 that determine energy losses are closely correlated with the molecular structure. We, therefore, systematically analyzed the exciton binding energies, molecular polarizabilities and intramolec-

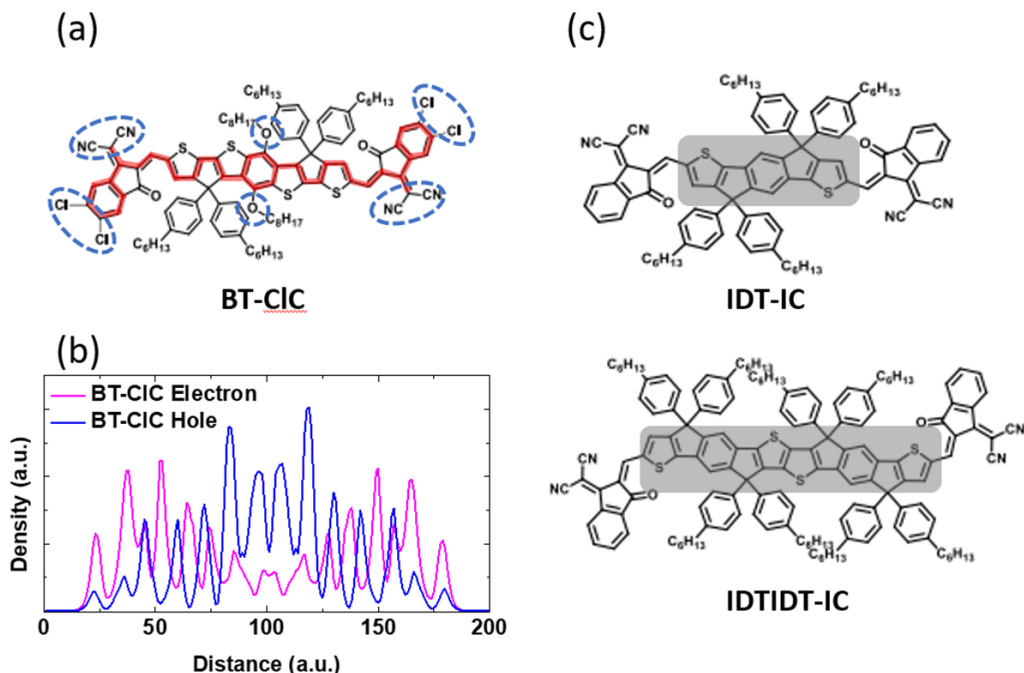


Figure 4.3: (a) The molecular structure of BT-C1C. The red bold line traces the electron conjugation path comprising alternating C-C single and double bonds. Blue dashed circles indicate the electron-rich (i.e. oxy-) and deficient (i.e. chloro- and cyano-) moieties that affects the electron distributions in the molecules. (b) The electron and hole density distributions along the molecular length of BT-C1C calculated using density functional theory (DFT). (c) The molecular structural formulae of IDT-IC and IDTIDT-IC, that have different length of the electron-donating cores as indicated in the shaded regions.

ular reorganization of fullerenes and NFAs by DFT. The exciton binding energy is  $E_B = (E_- + E_+) - (E_{gnd} + E_{ex})$ , where  $E_-$  and  $E_+$  are the optimized energies of radical anions and cations of the molecule, respectively. Also,  $E_{gnd}$  and  $E_{ex}$  are the ground and first singlet excited state energies, respectively.

Figure 4.3 shows the molecular structures of archetypical a-d-a type NFAs. The electron-donating conjugate backbone is capped with two electron-withdrawing side groups. The electron and hole distributions of the excited state along the long molecular axis of BT-C1C is shown in Fig. 4.3(b). All the chemical names and structures of the molecules are provided in the Appendix A. The conjugated electron system is

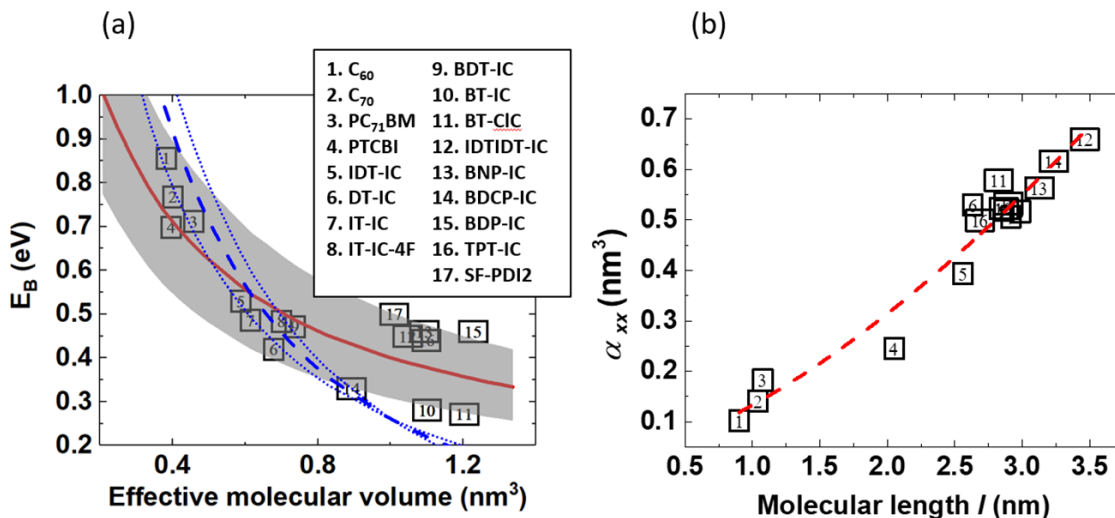


Figure 4.4: (a) Exciton binding energy,  $E_B$ , found via DFT vs. effective molecular volume for several acceptor molecules indicated in legend, and whose molecular formulae are in Appendix A. The red solid line is a fit assuming electron confinement within the effective molecular volume for each molecule. The calculation assumes a dielectric parameter,  $f=5.4$ . The shaded area is the 95% confidence band. The blue dashed line assumes  $f$  depends on molecular polarizability from (b). The confidence limits of the calculations are shown by dotted lines. (b) The calculated molecular polarizability along the molecular longitudinal axis,  $\alpha_{xx}$ , vs. the effective molecular length  $l$ . The dashed line is the fit using an empirical power-law described in text.

shown by the bold red line bridging the electron-donating thiophene backbone to the electron deficient cyano and Cl groups. This charge distribution results in symmetric intramolecular charge transfer (ICT) from the middle to the two ends of the optically excited molecule. Also, the relative segregation of electron and hole densities results in a reduced  $E_B$  (see below). Two other molecules with different numbers of thiophene rings, and hence a shorter conjugation length with reduced ICT are shown for comparison in Fig. 4.3(c).

Figure 4.4(a) shows calculated  $E_B$  of a variety of acceptors vs. the *effective molecular volume*. The effective molecular volume  $v = l \cdot w \cdot h$  is determined from the molecular length  $l$ , width  $w$ , and height  $h$  that are defined by a box whose boundaries are

Table 4.1: The intramolecular reorganization energy due to electron transfer of archetypical fullerenes and NFAs.

	PC <sub>71</sub> BM	IDT-IC	IDTIDT-IC	BT-ClC
$\lambda_I^-$ (eV)	0.180	0.179	0.101	0.157

defined at an electron density of  $0.02 \text{ au}^{-3}$ . Figure 4.4(a) shows that  $E_B$  decreases with increasing  $v$ . Also, the slope of  $E_B$  vs.  $v$  decreases until  $v > 1.5 \text{ nm}^3$ . Figure 4.4(b) shows the calculated static polarizabilities,  $\alpha_{xx}$ , along the molecular length,  $l$  of this same population of acceptors. Since the electron distribution is spread along the molecular backbone,  $\alpha_{xx}$  increases with  $l$ . This corresponds to the  $x$  coordinate, with  $y$  and  $z$  along  $w$  and  $h$ , respectively. The full polarizability tensors of the acceptors are provided in the Appendix B.

The intramolecular reorganization energy of electron transfer is  $\lambda_I^- = (E_0^* - E_0) + (E_-^* - E_-)$ , where  $E_0$  and  $E_-$  are the energies of the neutral and radical anion molecules in their optimized geometries, respectively, and  $E_0^*$  and  $E_-^*$  are energies of the neutral and radical anion molecules in their unrelaxed geometries, respectively. Table 4.1 lists the calculated  $\lambda_I^-$  of [6,6]-phenyl-C<sub>71</sub>-butyric acid methyl ester (PC<sub>71</sub>BM) and the three a-d-a NFAs in Fig. 4.3(a) and (c). Non-fullerene acceptors have smaller intramolecular reorganization energies on electron transfer than PC<sub>71</sub>BM. Introducing electron-donating oxy-, and electron-withdrawing cyano-, and chloro- moieties (Fig. 4.3(a)), or extending the conjugation length of the donor subgroup (Fig. 4.3(c)) further reduces  $\lambda_I^-$ .

The  $k_{CT}$  from BT-ClC (or BT-IC), IT-IC and fullerene derivatives are measured as functions of  $\Delta E_{CT}$ , with results shown in Fig. 4.5. The NFA-based HJs show non-monotonic changes of  $k_{CT}$  as  $\Delta E_{CT}$  increases, indicative of the Marcus normal (non-shaded) and inverted (shaded) regimes that are separated by the  $\Delta E_{CT}$  corresponding to the maximum value of  $k_{CT}$ . The  $k_{CT}$  of fullerene derivatives in Fig. 4.5(c), however,

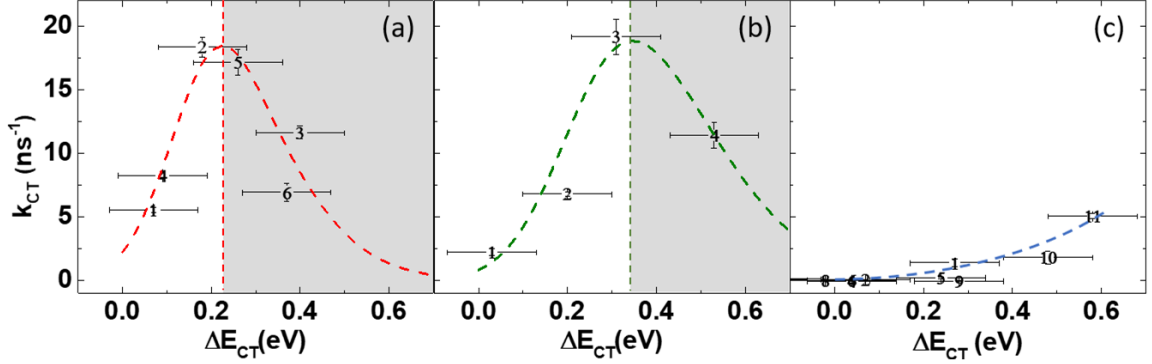


Figure 4.5: Measured  $k_{CT}$  vs.  $\Delta E_{CT}$  for HJs comprising (a) 1. BT-IC/PBDBT, 2. BT-IC/J61, 3. BT-IC/P3HT, 4. BT-CIC/PCDTBT, 5. BT-CIC/PBDBT, 6. BT-CIC/J61, (b) 1. IT-IC/PCDTBT, 2. IT-IC/PBDBT, 3. IT-IC/J61, 4. IT-IC/P3HT, and (c) 1. PC<sub>71</sub>BM/F8T2, 2. PC<sub>71</sub>BM/F8, 3. PC<sub>71</sub>BM/F8BT, 4. ICBA/F8T2, 5. PC<sub>61</sub>BM/F8T2, 6. PC<sub>61</sub>BM/F8, 7. PC<sub>61</sub>BM/F8BT, 8. C<sub>70</sub>/CBP, 9. C<sub>70</sub>/TCTA, 10. C<sub>70</sub>/NPD, and 11. C<sub>70</sub>/TPTPA. The dashed lines in (a) and (b) are the fits using semi-classical Marcus theory (Eq. 4.4 in text). The blue dashed line in (c) is a guide to the eye. All molecular structural formulae are found in Appendix A.

do not reach a maximum, but rather increase monotonically until  $\Delta E_{CT} = 0.6$  eV which is at energies short of the inverted region.

We also measured  $k_{CT}$  as a function of temperature for two HJs, BT-IC/PBDBT and IT-IC/PBDBT, with results shown in Fig. 4.6 (a) and (b), respectively. Both systems show two distinct regimes with a transition at  $T_X = \sim 150$  K. At  $T > T_X$ ,  $k_{CT}$  decreases rapidly with temperature, characteristic of thermally activated behavior for charge transfer. At  $T < T_X$ ,  $k_{CT}$  is relatively temperature independent due to the dominance of tunneling in the charge transfer process.

We also compared  $\Delta E_{nr}$  in HJs employing NFAs and fullerenes by measuring the quantum efficiency of the CT state EL ( $\eta_{EL}$ ) obtained by driving PC<sub>71</sub>BM/PBDBT and IT-IC/PBDBT HJ devices in forward bias. In Fig. 4.7, we find that  $\eta_{EL}$  of IT-IC/PBDBT is approximately one order of magnitude higher than that of PC<sub>71</sub>BM/PBDBT.

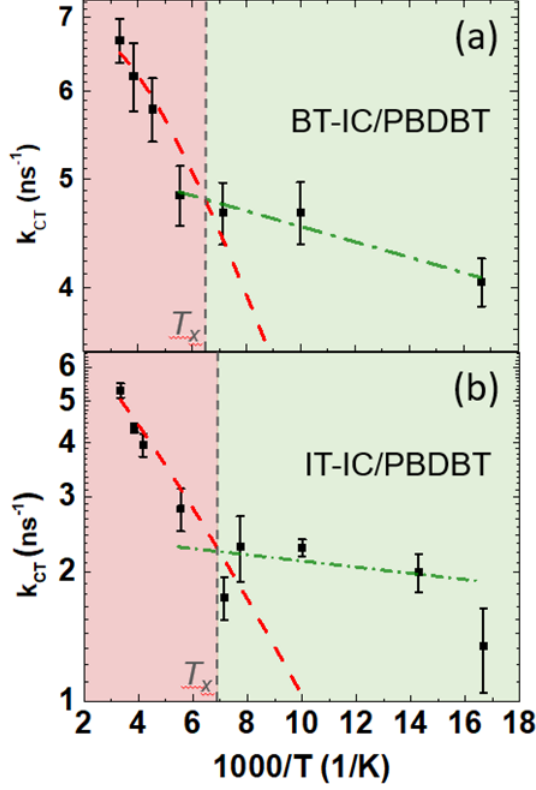


Figure 4.6: Measured  $k_{CT}$  vs. temperature,  $T$ , at (a) BT-IC/PBDBT and (b) IT-IC/PBDBT HJs. The dashed lines are the fits assuming thermal activation.

Nonradiative coupling between the CT and ground states possesses the same Franck-Condon factor as in radiative coupling.<sup>[120]</sup> We therefore measured the Franck-Condon shift between absorption and emission spectra of CT state to probe the electron-phonon coupling strength during the nonradiative recombination. Electroluminescence spectra of  $PC_{71}BM/PBDBT$  and IT-IC/PBDBT OPV in Fig. 4.8 show CT emission peaks at  $1.24 \pm 0.01$  eV and  $1.37 \pm 0.01$  eV, respectively. We extract the CT state absorption spectra using Gaussian fits to the  $EQE$  at the low energy shoulders using the same full width at half maximum (FWHM) as the corresponding emission spectrum. The Franck-Condon shift of the  $PC_{71}BM/PBDBT$  HJ is  $E_{FC} = 0.49 \pm 0.02$  eV, while for IT-IC/PBDBT,  $E_{FC} = 0.22 \pm 0.02$  eV.

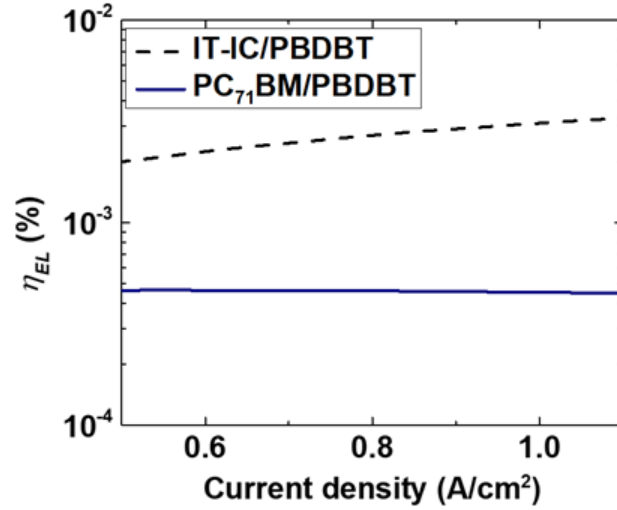


Figure 4.7: External quantum efficiency ( $EQE$ ) of CT state electroluminescence ( $\eta_{EL}$ ) from OPVs using IT-IC/PBDBT and PC<sub>71</sub>BM/PBDBT HJs.

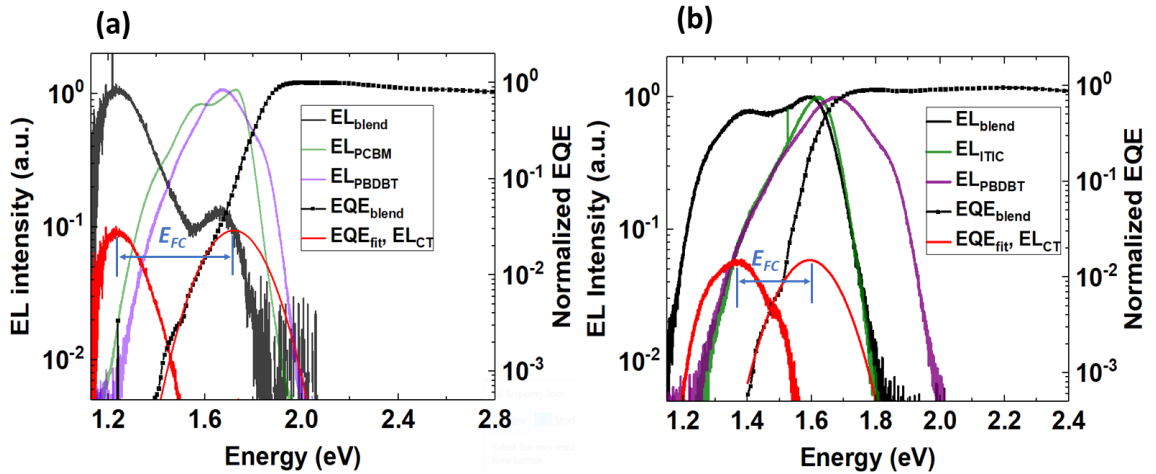


Figure 4.8: Electroluminescence (EL) and external quantum efficiency ( $EQE$ ) spectra of OPVs based on (a) neat IT-IC, PBDBT, and their blended heterojunction. (b) Neat PC<sub>71</sub>BM, PBDBT, and their blended heterojunction. The CT state emission at low energy is extracted from the EL spectra by subtracting the spectra from the neat layers. The CT state absorption spectra is extracted by a Gaussian fit of the  $EQE$  spectra along the low energy shoulders. The arrows between the short lines indicate the Franck-Condon shift,  $E_{FC}$ , of CT spectra.



## 4.5 Discussion

For a given offset of the donor and acceptor HOMO energies, the Gibbs free energy of hole transfer from acceptor to donor,  $\Delta E_{CT}$ , is maximized by minimizing the acceptor exciton binding energy, which in turn increases  $k_{CT}$  in the Marcus non-inverted regime. The combined influences of molecular size, conjugation length, and strength of the electron donating and withdrawing groups determines the magnitude of ICT in the acceptors,<sup>[128,129]</sup> and this ultimately determines  $E_B$ . The molecular size and the availability of  $sp^2$  hybridized atoms in the molecules determine the extent of conjugation, and hence the mean separation of the electron and hole orbital distributions. The rigid coplanar structure of a-d-a NFAs ensures that the electron wavefunction is delocalized over the entire molecular backbone, unlike polymers that can twist at C-C single bonds that ultimately terminates the extent of the excited state.<sup>[130]</sup> This is apparent from DFT calculations of the electron and hole densities of BT-CIC in Fig. 4.3(b). The oscillations in the densities are due to variations in electron and hole wavefunctions at each of the thiophene rings that terminate at the end caps. The low electron concentration at the molecular center of mass relative to the capping groups results from their electron donating and withdrawing character, respectively, and leads to a reduction in the electron-hole (i.e. exciton) binding energy.

To estimate the effects of molecular size on the exciton binding energy, we use a simplified electron wavefunction for a particle in a three dimensional box, i.e.  $\psi_{n_x, n_y, n_z} = \sqrt{\frac{8}{v}} \sin\left(\frac{n_x \pi x}{l}\right) \sin\left(\frac{n_y \pi y}{w}\right) \sin\left(\frac{n_z \pi z}{h}\right)$ , where  $n_x$ ,  $n_y$ ,  $n_z$  are quantum numbers. This fits the results in Fig. 4.4(a), whereby the  $E_B$  vs. effective molecular volume monotonically decreases, independent of the details of the molecules studied (i.e. fullerenes or NFAs). For this analysis, we use an average molecular height of  $h = 0.3$  nm and width of  $w = 0.8$  nm, and vary the length  $l$  according to the dimensions of the molecule. Then the wavefunctions  $\psi_{n_x, n_y, n_z}$  and exciton binding energies are

solved using Schrödinger’s equation to give the binding energy:

$$E_B = q^2 \int \frac{|\psi_{0,0,0}(\mathbf{r}_h)|^2 |\psi_{1,0,0}(\mathbf{r}_e)|^2}{f \cdot 4\pi\epsilon_0 |\mathbf{r}_h - \mathbf{r}_e|} d\mathbf{r}_h^3 d\mathbf{r}_e^3, \quad (4.11)$$

where the hole and electron wavefunctions are  $\psi_{0,0,0}$  and  $\psi_{1,0,0}$ , respectively,  $\mathbf{r}_h$  and  $\mathbf{r}_e$  are the coordinate vectors of the hole and electron, respectively, and  $q$  is the electron charge. Here,  $f$  is a parameter that accounts for the relative dielectric constant of the molecule and the relaxation energy of ionic species. The solid line in Fig. 4.4(a) corresponds to only a single value of  $f = 5.4$  that approximately fits the entire population of acceptors. This is indeed remarkable, given that the molecular structures vary significantly from molecule to molecule, and from highly symmetric fullerenes to planar NFAs. The shaded region depicts the 95% confidence band between  $f = 6.8$  and 4. The deviations of the data from the solid line are associated with details of the molecular structures that impact the molecular polarizabilities and relative dielectric constants in the solid.

As shown in Fig. 4.4(b), the polarizability  $\alpha_{xx}$  vs. molecular length  $l$  follows an empirical power-law dependence:<sup>[131,132]</sup>

$$\alpha_{xx} = \alpha_0 + \alpha_1 l^n. \quad (4.12)$$

Here,  $\alpha_0$  is the polarizability of terminal bonds such as C-H, and  $\alpha_1$  is related to the polarizability of conjugated or non-conjugated chains of length  $l$ . A fit to the data gives  $\alpha_0 = 0.035 \pm 0.075 \text{ nm}^3$ ,  $\alpha_1 = 0.098 \pm 0.060 \text{ nm}^{3-n}$ , and  $n = 1.51 \pm 0.44$ . A superlinear increase of polarizability ( $n > 1$ ) is due to the contributions of conjugation and ICT<sup>[128]</sup>. The relationship between the dielectric constant of the medium and the polarizabilities of each constituent,  $\alpha_i$ , is given by the Clausius-Mosotti relationship:

$$\frac{\epsilon - 1}{\epsilon + 2} = \frac{4\pi}{3} \sum_i (N_i \alpha_i), \quad (4.13)$$

where the molecular packing density is  $N_i$ . The effect of the dielectric constant change on  $E_B$  can be estimated using Eqs. 4.12 and 4.13 to replace constant  $f$  of Eq. 4.11, and assuming an isotropically polarizable medium comprising randomly oriented molecules with  $N = 1.3 \text{ nm}^{-3}$ . This yields the blue dashed line in Fig. 4.4(a). Two blue dotted lines indicate the confidence limits of the calculation from the fit to the data in Fig. 4.4(b). The fit closely follows the data for molecules 1 to 11 compared to the that using a constant  $f$ , despite a slight overestimation due to simplifications used to approximate molecular structure and the molecular relaxation of ionic species that are considered DFT calculations. The less accurate fits to molecules 12, 13, 15 - 17 is attributed to molecular bends that disturb the electron conjugation, thereby increasing  $E_B$ .

Achieving a small  $\Delta E_{CT}$  and  $\Delta E_{nr}$  requires simultaneously reducing both the intra- and intermolecular electron-phonon coupling. Increased dielectric constant of NFAs as shown above reduce the intermolecular coupling,  $\lambda_O$  (c.f. Eq. 4.8). The intramolecular coupling,  $S$ , also changes with the size and rigidity of the molecules. Studies of oligoacenes, polythiophenes, fused thiophenes, etc.<sup>[133]</sup> have shown that  $S \propto \frac{1}{N_{C-C}} \propto \frac{1}{n}$ , where,  $N_{C-C}$  is the number of carbon-carbon bonds, and  $n$  is the number of aromatic rings. Bond length adjustment is smaller when accommodating a more delocalized charge distribution. In NFAs, extending the conjugation length along the donor subgroup is one such effective method in reducing  $S$ , and therefore  $\lambda_I \approx S\hbar\langle\omega_I\rangle$ , as shown in Table 4.1. Another feature that leads to a reduced  $S$  (see Fig. 4.3(a)) is the nonbonding character of the molecules. Calculations suggest that the primary intramolecular mode appears along the conjugated carbon chains forming the backbone, indicated by the bold line tracing the conjugation path. The presence of nonbonding orbitals in the cyano, chloro or oxy groups introduce lone pair electrons that do not participate in bonding, and that avoid electron-phonon coupling. At the same time, the cyano and chloro groups attract electrons and reduce the charge

density along the backbones, effectively reducing electron-phonon coupling.

A small,  $S$ , and intermolecular coupling  $\lambda_O$  in NFAs, leads to a reduced Gibbs free energy change  $-\Delta E_{CT}$  for achieving a maximum  $k_{CT}$  than for the more compact fullerenes. In particular, HJs using BT-IC achieve a maximum  $k_{CT}$  at only  $\Delta E_{CT} = 0.22$  eV, which is slightly lower than IT-IC, of  $\Delta E_{CT} = 0.35$  eV. Equation 4.4 is applied to fit both Fig. 4.5 and the temperature dependent results above  $T_X$  in Fig. 4.6 to obtain  $\lambda_O = 0.21 \pm 0.03$  eV and  $S = 0.30 \pm 0.10$  for BT-IC (BT-IC)/donor HJs, and  $\lambda_O = 0.35 \pm 0.11$  eV and  $S = 0.54 \pm 0.12$  for IT-IC/donor HJs. In contrast, fullerene/donor HJs show an unconstrained fit where  $\lambda_I + \lambda_O \geq 0.6$  eV.

Charge transfer states are characterized by the strength of electron-phonon coupling and reorganization energy,  $\lambda_{CT}$ , during recombination, that can be determined via their Franck-Condon shifts (see Fig. 4.8). The Franck-Condon shift is twice the total reorganization energy,<sup>[134]</sup> i.e.  $E_{FC} \approx 2\lambda_{CT}$ , yielding  $\lambda_{CT} = 0.11$  eV for IT-IC/PBDBT compared to  $\lambda_{CT} = 0.24$  eV for PC<sub>71</sub>BM/PBDBT. This results in a higher  $k_{nr}$  for the latter system, according to Fig. 4.2. Thus,  $\eta_{EL} = \frac{k_r}{k_r + k_{nr}}$  is higher in the IT-IC/PBDBT HJ. Calculations of the non-radiative recombination loss using Eq. 4.10 and  $\eta_{EL}$  of IT-IC/PBDBT and PC<sub>71</sub>BM/PBDBT HJs result in a  $0.05 \pm 0.01$  eV smaller  $\Delta E_{nr}$  in the IT-IC system, leading to the generally higher power conversion efficiencies observed for NFA vs. fullerene based OPVs.

## 4.6 Designing Strategies for Low Energy Loss

The foregoing analysis suggests molecular design strategies that can further reduce energy loss. Currently, all a-d-a-type NFA have symmetric electron-withdrawing end groups that possess a nearly zero dipole moment. However, asymmetric electron withdrawing end groups in a-d-a molecules can provide freedom to tune the dipole moment and further reduce  $E_B$ ,  $S$ , and  $\lambda_O$  by changing the effective intramolecular electron-hole separation and molecular packing in bulk HJs. Additionally, the rela-

tionship between molecular dimension, rigidity and energy loss points to the benefits of increasing the molecular volume. However, there is a limit to the extent to which the length of the donor backbone can be increased without bending, and hence terminating the effective conjugation length. Extending the conjugation into two and three dimensions can further reduce  $E_B$ ,  $S$ , and  $\lambda_O$ , as compared to one-dimensional conjugation used up to now. This additional degree of freedom may also enhance intermolecular  $\pi - \pi$  interactions along all directions, leading to increased charge carrier mobilities. Indeed, early demonstrations of increasing the molecular volume in two dimensions based on dithienopicenocarbazole-based a-d-a-type<sup>[113]</sup> or spiro-fused perylene diimide NFAs<sup>[135]</sup> provide an illustration of the benefit of this strategy.

In conclusion, this chapter presents a theory that connects molecular structure of a wide range of fullerenes and nonfullerene acceptors to energy losses in the charge photogeneration process at organic HJs. Based on a combination of DFT, semi-classical Marcus theory and quantum mechanics, derived universal relationships connecting the polarizabilities and exciton binding energies to molecular geometry. The large conjugated volumes along with the juxtaposition of electron donating and withdrawing groups characteristic of thiophene-based NFAs leads to significant decreases of their exciton binding energy, intra- and intermolecular electron-phonon couplings, compared to more compact and symmetric fullerenes. As a result, HJs employing NFAs, such as BT-IC(BT-ClC) and IT-IC, reach a maximum  $k_{CT}$  at a small CT state energy loss of only  $\Delta E_{CT}=0.22$  and  $0.35$  eV, respectively, compared to that for fullerenes with  $\Delta E_{CT} \geq 0.6$  eV. Furthermore, nonradiative recombination losses are concomitantly reduced in NFAs. Semi-classical Marcus theory is applied to quantify the impact of exciton binding energy and electron-phonon coupling on both  $\Delta E_{CT}$  and  $\Delta E_{nr}$ . A significant outcome of our analysis is to provide guidelines for the design of molecules with reduced energy losses by increasing the effective molecular volume. One particular approach is to extend the one-dimensional molecular motifs currently

employed in thiophene-based NFAs into two or three dimensions. Ultimately, the use of these larger molecules should lead to higher OPV efficiencies when employed in HJs with appropriate donor, provided that their steric structure allows for the achievement of bulk HJ morphologies that encourage exciton dissociation and charge extraction.

## CHAPTER V

# Exciton Dynamics in an Organic Type-I Guest-Host Heterojunction

### 5.1 Introduction

Excitons can migrate within an organic material via a succession of energy transfer steps mediated by either Dexter exchange<sup>[15]</sup> or electrostatic Förster interactions<sup>[16]</sup>. While spin antisymmetric singlet excitons favor transport via FRET, spin-forbidden symmetric triplet excitons diffuse primarily via hopping between molecules. Inelastic exciton-exciton interaction (i.e. annihilation) occurs when two excitons “meet” each other. One exciton transfers the energy to the other and promotes it to an upper electronic state, which is usually followed by a loss of excess energy through vibrational relaxation. Annihilation reactions usually involve either two excitons or one exciton one polaron, including singlet-singlet annihilation (SSA), singlet-triplet annihilation (STA), triplet-triplet annihilation (TTA), singlet-polaron annihilation (SPA), and triplet-polaron annihilation (TPA).

Such phenomena are ignored in previous Chapters since the steady-state exciton density at donor-acceptor HJ is only on the order of  $10^{13} \text{ cm}^{-3}$  in the context of photovoltaic operation at one sun ( $100 \text{ mW/cm}^2$ ) illumination (assuming 100% absorption within a 100nm thick active layer, average incident photon energy of 2 eV, and aver-

age exciton lifetime of 1 ns). An example of excitation intensity dependent STA will be shown in Section 5.4. The annihilation becomes prevalent as the exciton density increases to  $> 10^{16} \text{ cm}^{-3}$ . That is, the average distance between excitons significantly decreases. Such an exciton density is usually required in the applications such as organic lasers and solid state lighting using OLEDs. An adequate management of singlet and triplet energy transfer is essential for mitigating triplet-induced losses in organic lasers<sup>[136]</sup>, and determines the efficiency<sup>[137–139]</sup> and reliability<sup>[140]</sup> of OLEDs.

In this Chapter, we present the exciton dynamics in an archetypical small molecule fluorescent guest-host heterojunction (type-I), comprising 4-(dicyanomethylene)-2-methyl-6-julolidyl-9-enyl-4H-pyran (DCM2) (guest) and tris(8-hydroxyquinolato) aluminum ( $\text{Alq}_3$ ) (host). Such a system has been used in devices such as fluorescent OLED and organic laser.<sup>[136,138,141]</sup> The red emitting DCM2 is usually doped in the  $\text{Alq}_3$  host at 1-5% concentration, enabling a high luminescence efficiency of close to 100%.<sup>[142]</sup> Here, we measure the temperature and excitation intensity dependence of the exciton dynamics to provide us insight into the mechanisms that govern both exciton transfer and annihilation processes.

## 5.2 Theory

As shown in Fig. 5.1, by the appropriate choice of illumination wavelength, singlets are directly generated on the host followed by their Förster transfer to the guest. Triplets can also be generated on the host through intersystem crossing of singlets. Host triplets then transfer to the guest via hopping (i.e., via a Dexter process). The singlet ( $S$ ), host triplet ( $T_h$ ), and guest triplet ( $T_g$ ) densities as functions of time  $t$  are described using:<sup>[136]</sup>

$$\frac{dS}{dt} = \frac{\eta I}{e_p d} - k_S S - k_{ISC} S - k_{ST} S T_g, \quad (5.1)$$



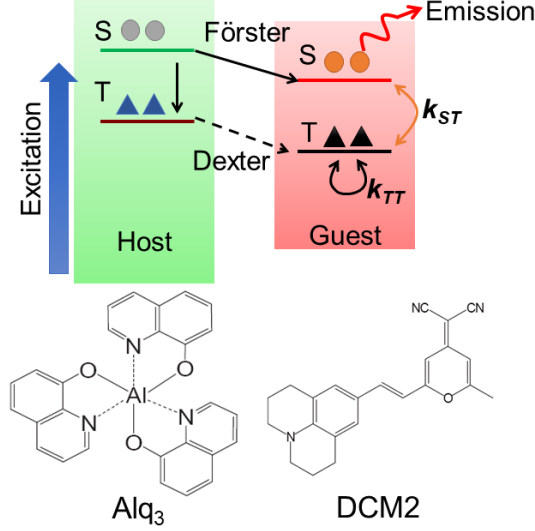


Figure 5.1: An archetypical fluorescent guest-host heterojunction, comprising a red emitting dopant, DCM2, and a host material, Alq<sub>3</sub>. After excitation of the host, Förster (Dexter) transfer occurs from the emissive singlet (non-emissive triplet) state of Alq<sub>3</sub> to that in DCM2. Singlet-triplet annihilation ( $k_{ST}$ ) and triplet-triplet annihilation ( $k_{TT}$ ) at the guest molecule are shown.

$$\frac{dT_h}{dt} = k_{ISC}S - k_{hg}exp\left(-\frac{2}{L}\sqrt[3]{\frac{1}{N_0 - T_g}}\right)T_h - k_{T(h)}T_h - \frac{1}{2}k_{TT(h)}T_h^2, \quad (5.2)$$

$$\frac{dT_g}{dt} = k_{hg}exp\left(-\frac{2}{L}\sqrt[3]{\frac{1}{N_0 - T_g}}\right)T_h - k_{T(g)}T_g - \frac{1}{2}k_{TT(g)}T_g^2. \quad (5.3)$$

Here  $I$  is the optical pump power density,  $\eta$  is the fraction of the pump power absorbed by the film,  $e_p$  is the photon energy, and  $d$  is the film thickness. Singlet decay processes are described by several rates, including natural decay ( $k_S$ ), intersystem crossing ( $k_{ISC}$ ), and annihilation between a guest singlet and triplet ( $k_{ST}$ ). We neglect guest singlet and host triplet interactions since the large host triplet TTA rate results in a relatively low host triplet density. For example, a TTA rate of  $k_{TT} = 10^{-12} \text{ cm}^3 \text{ s}^{-1}$  has been reported for Alq<sub>3</sub> at room temperature,<sup>[143]</sup> which is three orders of magnitude larger than the rate of the TTA on the relatively low density of DCM2 dopant molecules. This assumption will be discussed further in Sec. 5.4. Also,  $N_0$

is the guest triplet saturation density,<sup>[136]</sup>  $k_{hg}$  is the prefactor for host-guest Dexter transfer, and  $L$  is the effective localization radius of the exciton on the molecule ( $\sim 1$  nm).<sup>[136]</sup> The triplet decay rate includes the triplet natural decay ( $k_T$ ) and TTA ( $k_{TT}$ ). Following the pump pulse, only guest triplet dynamics are considered due to the fast decay of singlets and host triplets,<sup>[143]</sup> in which case Eq. 5.3 becomes

$$\frac{dT_g}{dt} = -k_{T(g)}T_g - \frac{1}{2}k_{TT(g)}T_g^2. \quad (5.4)$$

Based on this theory, we analyze: (i) the singlet evolution in the presence of host and guest triplet annihilation model described in Eqs. 5.1–5.3 by measuring the PL turn-on transient using a  $>20 \mu\text{s}$  pump pulse; (ii) the singlet decay by measuring the PL response to a short (1 ns) pump pulse; and (iii) the triplet density decay described in Eq. 5.4 by measuring its transient absorption following the pump pulse.

### 5.3 Experimental Section

Organic films were deposited by vacuum thermal evaporation at a base pressure of  $8 \times 10^{-7}$  torr. Films of DCM2 co-deposited with Alq<sub>3</sub> at a 3% vol. concentration were grown on a Si substrate to a thickness of 50 nm for use in the PL turn-on transient and singlet decay measurements. 200 nm thick 3%, 8%, and 15% vol. DCM2 doped in Alq<sub>3</sub> and undoped Alq<sub>3</sub> films were grown on 2- $\mu\text{m}$ -thick SiO<sub>2</sub>-on-Si substrates forming an air-organic-SiO<sub>2</sub> slab waveguide for pump-probe guest triplet density measurements.<sup>[143]</sup> Temperature was controlled in the range between 295 and 80 K using a closed-cycle cryostat (Janis SHI 4-5).

For PL turn-on transient measurements, the sample was pumped using a laser diode at a wavelength of  $\lambda = 405$  nm (Nichia NDV7116), whose beam power density was 15 to 150 W/cm<sup>2</sup> focused on a 490  $\mu\text{m} \times 900 \mu\text{m}$  spot on the film. The laser was driven using 30 $\mu\text{s}$  pulses at a 1 Hz repetition rate (HP 8114A pulse generator). The

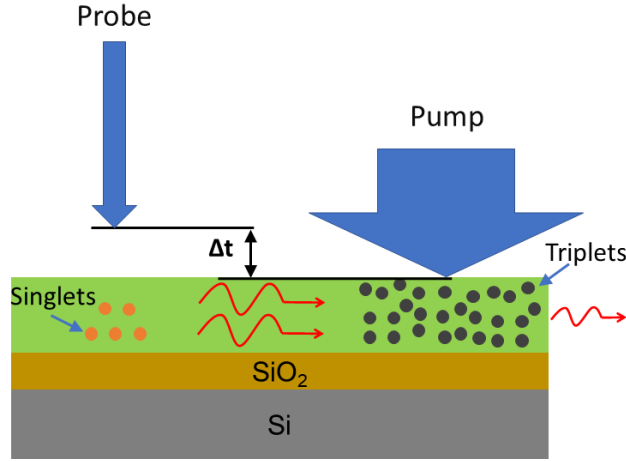


Figure 5.2: Schematic of the pump-probe triplet absorption measurement, determining the triplet exciton dynamics in DCM2:Alq<sub>3</sub> film. The probe beam was spatially separated from the pump beam and delayed by  $\Delta t$  in time. Photons generated by the probe were waveguided through the triplet populated region, got attenuated by the triplet absorption and emitted from the cleaved edge where intensity was measured using a streak camera.

PL transients were measured using a photodiode (FPD 510-FV) and an oscilloscope. Singlet lifetimes were measured using a N<sub>2</sub> laser pump ( $\lambda = 337$  nm, pulse width = 1.5 ns) and a streak camera (Hamamatsu C4334) with a time resolution of 40 ps.

Triplet exciton density decay following the pump pulse was determined by pump-probe triplet absorption, schematic of which is shown in Fig. 5.2.<sup>[143]</sup> The  $\lambda = 405$  nm laser diode was used as the pump with a power of 680 mW and spot size of  $2900 \mu\text{m} \times 1500 \mu\text{m}$  positioned adjacent to a cleaved edge of the substrate. The pulse conditions were the same as in PL turn-on transient measurements. The probe (N<sub>2</sub> laser) beam was focused to a  $1500 \mu\text{m} \times 390 \mu\text{m}$  spot separated by  $1600 \mu\text{m}$  from the pump spot, and delayed by  $1 \mu\text{s}$  to  $800$  ms following the pump. Photons generated by the probe were waveguided through the triplet populated region created by the pump, and emitted from the cleaved edge where both spectrally and temporally resolved emission were measured using a streak camera. Measurement of the attenuated edge emission intensity vs. the length of the pump region yields the triplet absorption coefficient  $\alpha$

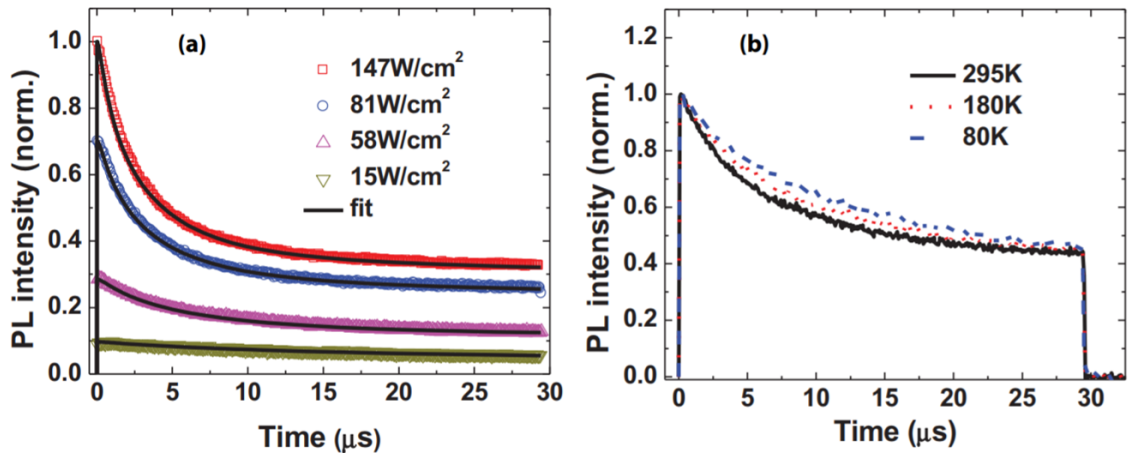


Figure 5.3: (a) Photoluminescence (PL) turn-on transient for a 3% vol. DCM2 doped in  $\text{Alq}_3$  film at  $T = 295$  K under four different power densities. The data are normalized to the peak PL at  $147 \text{ W/cm}^2$ . Solid lines are fits to the annihilation model in Eqs. 5.1-5.3. (b) Temperature dependence of the time resolved PL at  $58 \text{ W/cm}^2$ . The PL transient decay duration slightly increases as the temperature decreases.

at each wavelength. The average triplet absorption is calculated between wavelengths from 520 to 640 nm for  $\text{Alq}_3$  and 640–750 nm for  $\text{DCM2:Alq}_3$ .

## 5.4 Results

Photoluminescence turn-on transients for a 3% vol.  $\text{DCM2:Alq}_3$  film at four different power densities at room temperature (295 K) are shown in Fig. 5.3(a). Figure 5.3(b) shows the PL vs. temperature for a power density of  $58 \text{ mW/cm}^2$ . From these data, the PL turn-on transients show only a minor temperature dependence. The PL data at four different power densities are fit simultaneously using Eqs. 5.1-5.3 with  $N_0$ ,  $k_{ST}$ , and  $k_{ISC}$  as parameters, which are indicated by the solid lines. Guest triplet natural decay, annihilation on the guest, and triplet natural decay on the host (described by rates  $k_{T(g)}$ ,  $k_{TT(g)}$ , and  $k_{T(h)}$ , respectively) are neglected in modeling the turn-on transient of the PL signal due to their relatively minor influence during the

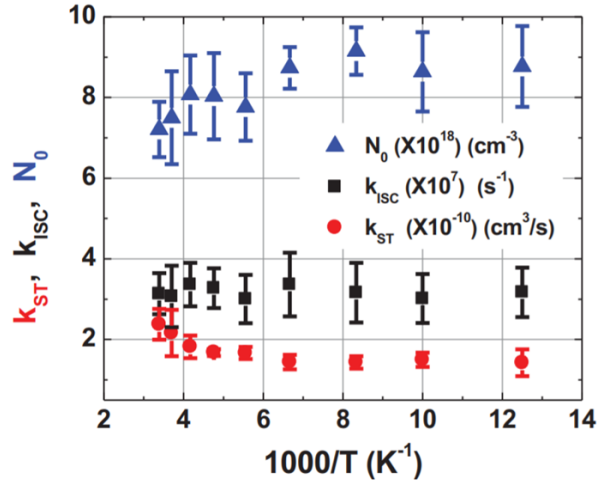


Figure 5.4: Temperature dependence of the rates of singlet-triplet annihilation  $k_{ST}$ , intersystem crossing  $k_{ISC}$ , and the guest triplet saturation density  $N_0$  for 3% vol. DCM2 doped in  $Alq_3$ .

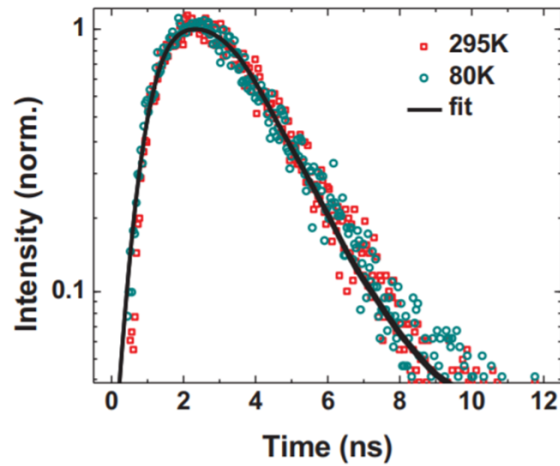


Figure 5.5: Time resolved PL response of a 3% vol. DCM2 in  $Alq_3$  film to the 1.5 ns pump pulse at 300 and 80 K. The fits (solid lines) to the singlet exponential decay model convolved with the temporal profile of the pump laser are shown.

Table 5.1: Singlet lifetime of a 3% vol. DCM2 doped in Alq<sub>3</sub> film vs. temperature.

Temperature (K)	295	270	240	210	180	150	120	80
Lifetime	1.14	1.21	1.33	1.38	1.30	1.26	1.37	1.28
(ns)	±0.02	±0.01	±0.02	±0.03	±0.02	±0.02	±0.03	±0.02

build-up of the triplet population. Note that  $k_S$  at each temperature is obtained from the singlet lifetime measurement, and  $k_{TT(h)}$  is measured using pump-probe triplet absorption where the sample is an undoped, 200-nm-thick Alq<sub>3</sub> film on the SiO<sub>2</sub>-on-Si substrate. Finally,  $k_{hg} = 4 \times 10^{10} \text{ s}^{-1}$  is obtained from Ref.<sup>[136]</sup>. Figure 5.4 shows the result of fits that yield  $N_0$ ,  $k_{ST}$ , and  $k_{ISC}$  from the PL transients in Fig. 5.3. The STA rate  $k_{ST}$  decreases by <50% when the temperature is decreased from room temperature to 80 K. In contrast, the intersystem crossing rate  $k_{ISC}$  remains relatively constant over this same temperature range while the guest triplet saturation density  $N_0$  increases slightly.

Figure 5.5 shows the transient PL response following a 1.5 ns pump pulse for the sample in Fig. 5.3. We assume only the singlet density is important given the low intersystem crossing rate of  $10^7 \text{ s}^{-1}$ . The singlet lifetime is calculated by deconvolving the temporal profiles of the laser pulse and PL for a pump intensity of  $4 \mu\text{J}/\text{cm}^2$ , where singlet-singlet annihilation is neglected. Table 5.1 provides the singlet lifetimes inferred from the fits.

The edge emission at room temperature obtained in the guest triplet absorption measurement is shown in Fig. 5.6(a). Figure 5.6(b) shows a minor change of guest triplet absorption across the spectral region of the probe. For simplicity of analysis, the average triplet absorption coefficient is converted to the triplet density when divided by the DCM2 guest triplet absorption cross section of  $4 \times 10^{-17} \text{ cm}^2$ .<sup>[136]</sup> The normalized guest triplet density in DCM2:Alq<sub>3</sub> vs. temperature and time following

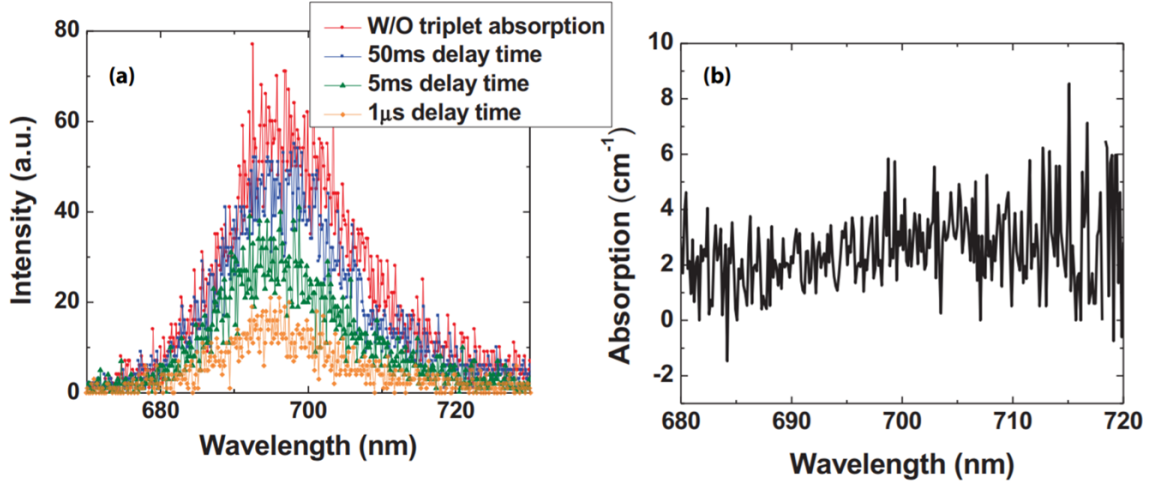


Figure 5.6: (a) The edge emission obtained in the guest triplet absorption measurement of a 3% vol. DCM2 in Alq<sub>3</sub> film at room temperature. (b) Guest triplet absorption coefficient vs. wavelength after a 1  $\mu$ s delay.

the pump pulse is shown in Fig. 5.7. Equation 5.4 is used to fit the data (solid lines). The triplet density at 80 K takes ten times longer to decrease to 10% of its original value compared to room temperature. Comparison of Figs. 5.5 and 5.7 indicates that the triplet decay is temperature dependent from 80 to 295 K, whereas singlet decay is not.

We can obtain the host triplet density when applying the same method to an undoped Alq<sub>3</sub> film, as shown in the inset of Fig. 5.7. The results of the fits to the data are provided in Table 5.2. Our observations indicate that the TTA rate of host triplets is several orders of magnitude larger than that of guest triplets. Following the pump pulse, fast decay of host triplets results in their limited contribution to the long-lived guest triplet decay.

Table 5.3 and Fig. 5.8(a) show the triplet lifetime and  $k_{TT}$  obtained from the fits in Fig. 5.7, respectively. The temperature dependence of the  $k_{TT}$  and triplet natural lifetime in films with 3%, 8%, and 15% vol. doping concentration follows similar trends, as indicated in Figs. 5.8(b) and 5.8(c) and Table 5.3. For 3% vol. DCM2 in Alq<sub>3</sub>,  $k_{TT} = (1.6 \pm 0.1) \times 10^{-15} \text{ cm}^3 \text{ s}^{-1}$  at room temperature, which is close to  $k_{TT}$

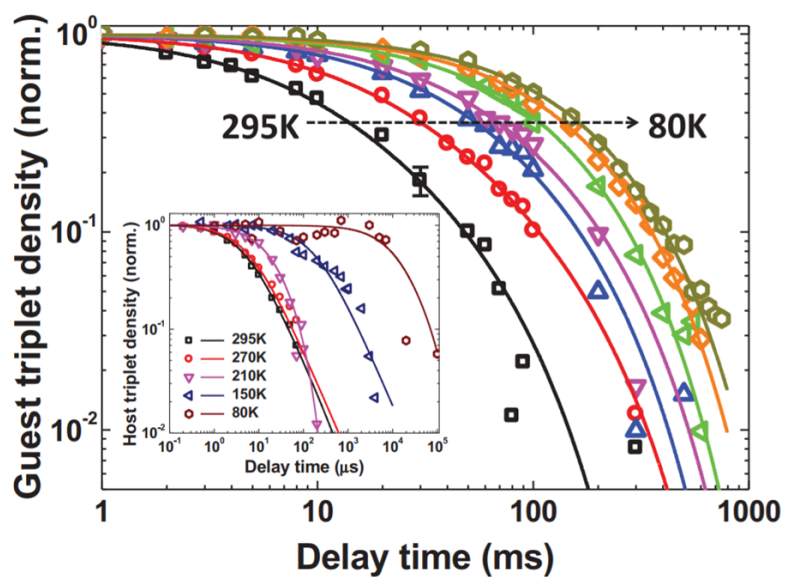


Figure 5.7: Transient response of the guest triplet density vs. temperature of a 3% vol. DCM2 doped in  $\text{Alq}_3$  film following the turn-off of the pump pulse. Films of 8% and 15% vol. DCM2 in  $\text{Alq}_3$  have a similar transient response, and are omitted for clarity. The solid lines are the fits to the guest triplet decay model [Eq. 5.4]. Each data set is normalized to its initial value. A representative error bar of this pump probe measurement is shown. Inset: Transient response of the triplet density vs. temperature in an undoped  $\text{Alq}_3$  film following a  $30 \mu\text{s}$  pump pulse.



Table 5.2: Triplet-triplet annihilation rate vs. temperature for Alq<sub>3</sub>.

Temperature (K)	295	270	240	210	180	150	120	100	80
$k_{TT}$	1.90	1.10	0.81	0.27	0.22	0.079	0.029	0.0081	0.0018
( $\times 10^{-12} \text{cm}^3/\text{s}$ )	$\pm 0.27$	$\pm 0.25$	$\pm 0.39$	$\pm 0.22$	$\pm 0.26$	$\pm 0.034$	$\pm 0.027$	$\pm 0.0069$	$\pm 0.0043$

$= 1 \times 10^{-15} \text{ cm}^3 \text{ s}^{-1}$  previously reported for the DCM2:Alq<sub>3</sub> system.<sup>[136,143]</sup> Reducing the temperature to 80 K results in a 20 times reduction to  $k_{TT} = 5.1 \times 10^{-17} \text{ cm}^3 \text{ s}^{-1}$ . This is in striking contrast to the temperature dependence of  $k_{ST}$  in Fig. 5.4. When  $\log(k_{TT})$  vs.  $1000/T$  is plotted in Fig. 5.8, two distinct slopes with a transition temperature  $T_{trans} \approx 180 \text{ K}$  are observed.

## 5.5 Discussion

In fluorescent systems, the natural decay rate ( $k_T$ ) of nonemissive triplets has a limited contribution to the triplet density. The temperature dependence of the triplet density is therefore determined by the temperature dependence of the TTA. Now<sup>[144]</sup>

$$k_{TT} = 8\pi R_Q D_T, \quad (5.5)$$

where  $D_T$  is the triplet diffusivity and  $R_Q$  is the triplet interaction radius. Since  $R_Q$  is temperature independent,  $D_T$  provides the temperature dependence of  $k_{TT}$ .

The temperature dependent triplet diffusivity corresponding to  $k_{TT}$  in Fig. 5.8 reveals two separate temperature activated regimes indicative of two different triplet energy transfer mechanisms. At temperatures above the transition between rates (i.e.,  $T > T_{trans} \approx 180 \text{ K}$ ), triplet diffusion is described by Marcus transfer.<sup>[145]</sup> During Dexter transfer, the simultaneous exchange of two electrons occurs between

Table 5.3: Guest triplet natural lifetime vs. temperature of 3%, 8%, and 15% vol. DCM2 doped in Alq<sub>3</sub> films.

Temperature (K)	295	270	240	210	180	150	120	100	80
	3% vol.								
	50.0	120.2	122.7	150.7	154.1	170.5	194.0	177.3	215.1
Lifetime (ms)	±11.5	±22.3	±20.7	±30.8	±16.4	±17.5	±12.6	±12.3	±14.8
	8% vol.								
	73.1	107.0	137.5	141.3	136.5	150.1	175.3	167.2	178.0
	±11.3	±24.5	±18.7	±10.1	±7.8	±8.9	±8.1	±11.1	±14.3
	15% vol.								
	44.9	101.4	126.5	139.5	168.5	182.7	172.8	231.9	230.5
	±7.5	±16.8	±19.1	±8.2	±6.9	±13.0	±11.0	±19.5	±21.3
Average	56.0	109.5	128.9	143.8	153.0	167.8	180.7	192.1	207.9

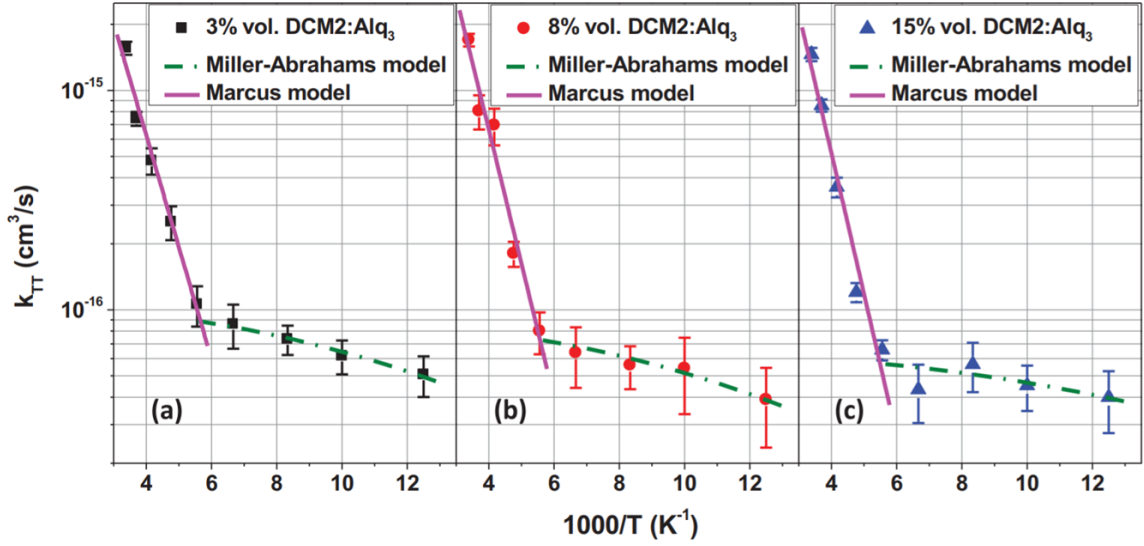


Figure 5.8: Arrhenius plots of the triplet-triplet annihilation rate ( $k_{TT}$ ) obtained for (a) 3%, (b) 8%, and (c) 15% vol. DCM2 in Alq<sub>3</sub> films between  $T = 295$  and 80 K. The solid lines are the fits to models based on Marcus triplet transfer at high temperatures, and Miller-Abrahams transfer at low temperatures. The error bars correspond to the standard errors calculated from the fits.

the HOMO and LUMO levels of adjacent donor and acceptor molecules which undergo a configuration change during transfer. During Marcus transfer, multiple phonons are required to overcome the energy barriers separating the sites (denoted by an activation energy  $E_a$ ) and the differences in the site energies.<sup>[145,146]</sup> The site energy difference itself is attributed to morphological disorder in the amorphous thin film, where the site-specific orientation of dipoles between molecules leads to an inhomogeneously broadened density of states (DOS). The half-width of the Gaussian DOS distribution ( $\sigma$ ) corresponds to the degree of orientational order; narrow distributions reflect a more ordered environment.

At temperatures below the transition (i.e.,  $T < T_{trans}$ ), multiphonon Marcus transfer is less probable. In this case, phonon-assisted tunneling between energetically disordered sites described by Miller-Abrahams transfer theory is more appropriate.<sup>[71,145]</sup> Moreover, dispersive triplet diffusion is prevalent at low temperatures.<sup>[147-149]</sup> Follow-

ing excitation, triplets relax towards the low-energy tail of the DOS, resulting in a hopping towards acceptor sites at lower energies.<sup>[147,150]</sup> Decreasing the temperature slows hopping, thereby reducing  $D_T$ .

The respective diffusivity  $D_T$  (proportional to the triplet energy transfer rate  $W$ ) vs. temperature ( $T$ ) above and below  $T_{trans}$  is thus described by<sup>[145,146]</sup>

$$D_T \propto W = \frac{J_0^2}{\hbar} \sqrt{\frac{\pi}{4E_a k_B T}} \exp\left(-2\frac{a}{L}\right) \exp\left[-\frac{E_a}{k_B T} - \frac{1}{8} \left(\frac{\sigma}{k_B T}\right)^2\right], \quad T > T_{trans}, \quad (5.6)$$

$$D_T \propto W = \gamma_0 \exp\left(-2\frac{a}{L}\right) \exp\left[-\frac{1}{2} \left(\frac{\sigma}{k_B T}\right)^2\right], \quad T < T_{trans}, \quad (5.7)$$

where  $k_B$  is Boltzmann's constant,  $\hbar$  is Planck's constant divided by  $2\pi$ ,  $a$  is the average distance between donor and acceptor sites,  $L$  is the effective localization radius of triplets,  $J_0$  is the electronic coupling integral prefactor, and  $\gamma_0$  is the characteristic frequency of the phonon.

In Fig. 5.8 we fit the data above (Marcus) and below (Miller-Abrahams)  $T_{trans}$  to Eqs. 5.6 and 5.7, respectively, at three different DCM2 doping concentrations. The  $\sigma$  from three fits are identical within the experimental confidence limits, with an average of  $\sigma = 7.8 \pm 0.9$  meV. Energetic disorder ( $\sigma$ ) of some organic systems can be large, for example, for poly[methyl(phenyl)silylene] (PMPSi),  $\sigma = 89$  meV; for poly[biphenyl(methyl)silylene] (PBPMPSi),  $\sigma = 94$  meV,<sup>[151]</sup> and for poly(2,7-(9,9-bis(2-ethylhexyl)fluorene)) (PF2/6),  $\sigma = 40$  meV.<sup>[152]</sup> In contrast, DCM2:Alq<sub>3</sub> films possess considerably less disorder as reflected in their narrow DOS. Fits of Eq. 5.7 to the data yields a ratio of  $\exp(-\frac{2a_{3\%}}{L}) : \exp(-\frac{2a_{8\%}}{L}) : \exp(-\frac{2a_{15\%}}{L}) \approx 1.7:1.4:1$ , which indicates that 15% vol. doping concentration has the largest average distance between neighboring triplets. This is likely due to concentration quenching, where a large DCM2 concentration leads to a low quantum yield and large separation of guest triplets.<sup>[153]</sup>

Activation energies of  $E_a = 105 \pm 8$ ,  $124 \pm 12$ , and  $131 \pm 13$  meV are obtained

from the fits for 3%, 8%, and 15% vol. DCM2 doped in Alq<sub>3</sub>, respectively. The electron coupling integral  $J = J_0 \exp(-\frac{a}{L})$  between the neighboring sites has a measured ratio of  $J_{3\%} : J_{8\%} : J_{15\%} \approx 1:1.7:1.8$ . This suggests that higher guest concentrations lead to an increased overlap of the donor and acceptor electronic wave functions, as expected.

The temperature dependence above and below  $T_{trans}$  is dominated by  $E_a$  and  $\sigma$ , respectively. A low ratio of  $\frac{\sigma}{E_a}$  leads to a more obvious distinction in slopes between the two regimes. Small disorder, and thus a large distinction between  $\sigma$  and  $E_a$  increases the transition temperature.<sup>[145]</sup> In our case, a low disorder results in a transition at  $T \approx 180$  K which is higher than reported for other systems. For example, the Pt-polymer (poly[trans(bis(tributylphosphine))Pt(1,4)phenylenediethynylene] transition occurs at 80 K,<sup>[146]</sup> and for MDMO-PPV, the temperature is 150 K.<sup>[150]</sup>

Thermal activation of exciton transport is observed only if the hopping occurs between nearest neighbors coupled by the exchange interaction. Therefore, it is a dominant factor governing triplet rather than singlet transport. Förster transfer of singlets occurs by long range electrostatic interactions leading to its temperature independence.<sup>[149]</sup> In our measurements, the PL response of the films (Figs. 5.3 and 5.5) is dominated by singlet dynamics, and hence is only weakly dependent on temperature. Now, the singlet-triplet annihilation rate is<sup>[145,154]</sup>

$$k_{ST} = 0.676 \times 4\pi \left( \frac{R_{ST}^6}{\tau_s \phi_F} \right)^{1/4} D_{ST}^{3/4}, \quad (5.8)$$

where  $D_{ST}$  is the combined diffusivity of the singlet and triplet states,  $R_{ST}$  is their interaction radius,  $\tau_s$  is the singlet lifetime, and  $\phi_F$  is the FRET efficiency. The singlet diffusivity ( $D_S$ ) is usually much larger than that of triplets ( $D_T$ ): For example,  $D_S$  is between 0.1 and 1 cm<sup>2</sup>/s,<sup>[155]</sup> while  $D_T = 2 \times 10^{-4}$  cm<sup>2</sup>/s in anthracene.<sup>[156]</sup> Thus, we expect  $D_S$  to dominate  $D_{ST}$  in the DCM2:Alq<sub>3</sub> system, leading to the weak

temperature dependence observed for  $k_{ST}$ .

To conclude We have observed significantly different temperature dependences of the singlet and triplet density dynamics in the archetype small molecule fluorescent organic system comprised of Alq<sub>3</sub> doped with DCM2. From 295 to 80 K the large temperature dependence of the nonemissive guest triplet diffusivity results in a decrease in the triplet-triplet annihilation rate of 20 times. The two temperature regimes observed for  $k_{TT}$  reveal that the diffusivity of triplets is determined by the dominance of thermally activated multiphonon Marcus transfer at high temperatures, and Miller-Abrahams single phonon assisted hopping at low temperatures. Förster transfer leads to a weakly temperature dependent singlet diffusivity, resulting in a similarly weak temperature dependent singlet-triplet annihilation process. This suggests that singlet and triplet diffusion can be separately controlled due to their different energy transfer mechanisms. For example, the triplet is localized at low temperature without affecting the singlet dynamics, eventually allowing for improved management of exciton energy transport in luminescent materials systems.

## PART II

# Energy Transfer in van der Waals Bonded Organic-Inorganic Heterojunctions

## CHAPTER VI

# Introduction to Organic-Inorganic Heterojunctions

### 6.1 Why Use an Organic-Inorganic Heterojunction

As we discussed in Chapter I, distinctive physical properties of organic and inorganic semiconductors are the result of their different bonding characteristics. Intimate covalent or ionic bonding between atoms in inorganic semiconductors give rise to their continuous conduction and valence band structures, and hence high charge mobility of  $\sim 1000 \text{ cm}^2/(\text{V}\cdot\text{s})$ . This is compared to a low mobility ( $< 1 \text{ cm}^2/(\text{V}\cdot\text{s})$ ) polaron hopping in organic semiconductors due to the weak electrostatic coupling between molecules (See Table 6.1). Chemical bonding in an inorganic semiconductor also leads to large dielectric screening and therefore weak binding between photogenerated electron-hole pairs, i.e. large-radius Wannier-Mott excitons, as compared to the tightly-bound Frenkel excitons in organic molecules. The optical spectra of organic semiconductors are hence narrower but more intense than that in inorganics.

Organic-inorganic hybrid HJs that synergistically combine the distinct optoelectronic properties of two contacting materials systems, e.g. coupling the high absorption efficiency of organics with the high charge transport mobility of inorganics, is an attractive platform for realizing enhanced optoelectronic device performance as well as for observing emergent properties. Coupling organic and inorganic semiconductors through resonant energy transfer, such as FRET, has been widely demon-



Table 6.1: Comparison of the physical properties of organic and inorganic semiconductors.

<b>Property</b>	<b>Inorganics</b>	<b>Organics</b>
<b>Bond Type</b>	Covalent/Ionic	van der Waals
<b>Charge Transport</b>	Band Transport	Polaron Hopping
<b>Charge Mobility</b>	$\sim 1000 \text{ cm}^2/(\text{V}\cdot\text{s})$	$< 1 \text{ cm}^2/(\text{V}\cdot\text{s})$
<b>Peak Absorption Coefficient</b>	$10^3\text{-}10^4 \text{ cm}^{-1}$	$10^5\text{-}10^6 \text{ cm}^{-1}$
<b>Exciton Species</b>	Wannier-Mott	Frenkel
<b>Exciton Binding Energy</b>	$\sim 5\text{-}10 \text{ meV}$	$> 200 \text{ meV}$
<b>Exciton Radius</b>	$\sim 100 \text{ \AA}$	$\sim 10 \text{ \AA}$

strated. Control over the dimensionality of the loosely-bound Wannier excitons through temperature and structure of inorganic layers at the junction can effectively tune the FRET efficiency.<sup>[157–161]</sup> In addition, photon mediated hybridization between Frenkel and Wannier-Mott excitons and strong exciton-photon coupling in an organic-inorganic (OI) hybrid optical microcavity has been observed.<sup>[162–164]</sup>

Hybrid type-II OI HJs have attracted considerable interest over the years. The charge generation between a metal oxide, such as  $\text{TiO}_2$ , and an organic dye interface has been utilized for the operation of the dye-sensitized solar cell (DSSC), where *PCE* of 10-12% has been achieved.<sup>[165,166]</sup> The studies of optical and electronic properties of OI HJs and their potential applications to photodetectors,<sup>[167–169]</sup> solar cells,<sup>[170]</sup> and light-emitting diodes<sup>[171]</sup> have shown promise. Furthermore, organic layers are often used for surface passivation of inorganic devices,<sup>[172–175]</sup> and as the charge transport layers in colloidal quantum dot (QD)<sup>[176]</sup> and perovskite<sup>[177]</sup> devices. Other structures, such as multilayer OI superlattices, provide unprecedented abilities to tune the dielectric screening, electron mobility, and thermal conductivity of the material systems, providing access to thermoelectric and optoelectric applications.<sup>[178]</sup>

## 6.2 Fundamentals of Organic-Inorganic Heterojunctions

In addition to efforts by thriving research communities contributing to demonstration and improvement in the application of OI material systems, comprehensive models describing charge transport and excited state dynamics in OI systems have also been developed to aid in the understanding, and ultimately, the optimization of the devices in which they are used.<sup>[179,180]</sup> Figure 6.1 depicts a hybrid type-II HJ of an n-type inorganic semiconductor in contact with a p-type organic semiconductor, where the Fermi level of inorganics is in alignment with the organics ( $V_a = 0$ ). We begin by assuming defect states at the OI HJ are inactive. Indeed, the presence of organic semiconductors at the surface, in some cases,<sup>[172–175]</sup> passivate the surface states of inorganic semiconductors. The general photogeneration processes in the type-II OI HJ are as follows: Photon absorption leads to free carrier generation in the inorganic semiconductor ( $G_I$ ) where the majority carriers, i.e. electrons in this case, are extracted through the cathode and contribute to the photocurrent ( $J_I$ ). Minority carriers, i.e. holes, either travel across the HJ and reach the anode, or recombine through a hybrid charge transfer exciton (HCTE) state at the junction. Tightly-bound electron-hole pairs generated at the organic layer ( $G_O$ ) travel to the OI interface at a flux of  $J_x$  and dissociate through an intermediate HCTE state at a rate,  $k_d$ . Losses occur through recombination of electrons ( $n_{HJ}$ ) and holes ( $p_{HJ}$ ) near the interface at a rate of  $k_{rec}$ , and recombination of HCTE at a rate of  $k_r$ . The total charge generation rate out of the OI HJ is  $\frac{J+J_I}{q\langle a \rangle}$ .

The dynamics of photogeneration processes that occur at the interfacial region of width  $\langle a \rangle$ , i.e. the characteristic HCTE diameter, can be described using the

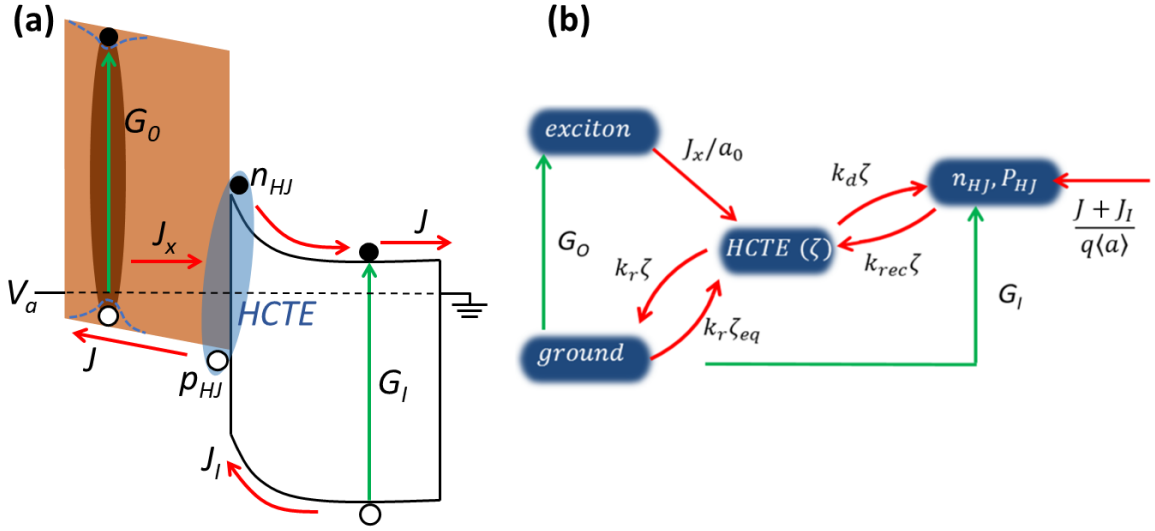


Figure 6.1: (a) Schematic of photogeneration processes at the hybrid type-II HJ. Photoexcitation generates free carriers in the inorganic semiconductor, yet Frenkel excitons in the organic semiconductor. The excitons diffuse to the interface at a flux  $J_x$ , where charge transfer at the HJ region of width  $\langle a \rangle$  gives rise to the formation of HCTE (with a population of  $\zeta$ ). The charge generation efficiency is determined by the ratio of HCTE dissociation ( $k_d$ ) and recombination ( $k_r$ ) rate. Free charge carriers ( $n_{HJ}$  and  $p_{HJ}$ ) near the interface can also recombine at a rate of  $k_{rec}$  to form HCTE. (b) State diagram that shows the rate of all processes. Figure adapted from ref. [181]

steady-state rate equations analogous to Eq. 1.24 for an organic donor-acceptor HJ:

$$\begin{cases} \frac{J_x}{\langle a \rangle} - k_r(\zeta - \zeta_{eq}) - k_d\zeta + k_{rec}n_{HJ}p_{HJ} = 0 \\ k_d\zeta - k_{rec}n_{HJ}p_{HJ} + \frac{J+J_I}{q\langle a \rangle} = 0 \end{cases} \quad (6.1)$$

Here  $\zeta$  is the steady state population of HCTE, and  $\zeta_{eq}$  is the thermal equilibrium population of the CT state in the absence of bias and illumination, where  $\zeta_{eq} = k_{rec}n_{eq}p_{eq}/k_{d,eq}$ . Solving Eq. 6.1 yields:

$$J = q\langle a \rangle k_{rec}(1 - \eta_d) \left( n_{HJ}p_{HJ} - \frac{k_d}{k_{d,eq}} n_{eq}p_{eq} \right) - (qJ_x\eta_d + J_I), \quad (6.2)$$

where  $\eta_d = \frac{k_d}{(k_d+k_r)}$  is the dissociation efficiency of the HCTE. Assuming quasi-equilibrium, and  $J$  is sufficiently small so that the quasi-Fermi levels of both the electron and hole are constant throughout the respective layers, the electron and hole densities at the OI HJ are given by:<sup>[179]</sup>

$$\begin{cases} n_{HJ} = N_C \exp\left(\frac{q(V_I - \phi_I)}{k_B T}\right) \\ p_{HJ} = N_{HOMO} \exp\left(\frac{q(V_O - \phi_O)}{k_B T}\right) \end{cases}, \quad (6.3)$$

where  $N_C$  and  $N_{HOMO}$  are the density of states of the conduction band of an inorganic and the HOMO of an organic semiconductor,  $V_I$  and  $V_O$  are the voltage drops across the inorganic and organic layers,  $\phi_I$  and  $\phi_O$  are the injection barriers of cathode-to-inorganics and anode-to-organics, respectively. Combining Eq. 6.2 and 6.3 leads to:

$$J = q\langle a \rangle k_{rec} (1 - \eta_d) N_{HOMO} N_C \exp\left(-\frac{\Delta E_{OI}}{k_B T}\right) \left[ \exp\left(\frac{qV_a}{k_B T}\right) - \frac{k_d}{k_{d,eq}} \right] - q\eta_d J_x, \quad (6.4)$$

where  $\Delta E_{OI} = q(V_{bi} + \psi_O + \psi_I)$ , and  $V_{bi}$  is the built-in potential of the device corresponding to the difference in contact work functions,  $V_a = V_O + V_I + V_{bi}$ . Equation 6.4 can be further expanded to account for the case where a significant density of surface defects and trapped charges at the OI HJ is present. More details of the  $J - V$  characteristics of hybrid HJ under equilibrium and non-equilibrium conditions can be found in refs.<sup>[179–181]</sup>

The HCTE, analogous to the CT excitons described in Chapters I and III, is generally considered as a precursor to HCTE dissociation. Studies of hybrid HJ between inorganic semiconductors such as CdS,<sup>[182]</sup> ZnO,<sup>[183,184]</sup> ZnMgO,<sup>[185]</sup> GaAs,<sup>[186]</sup> WS<sub>2</sub><sup>[187]</sup> and organic semiconductors have shown direct evidence for the existence of an HCTE. Figure 6.2(a) shows the EL spectra of the HCTE as a function of temperature (T) of a ZnO/4,4-bis(N-carbazolyl)-1,1-biphenyl (CBP) HJ device un-

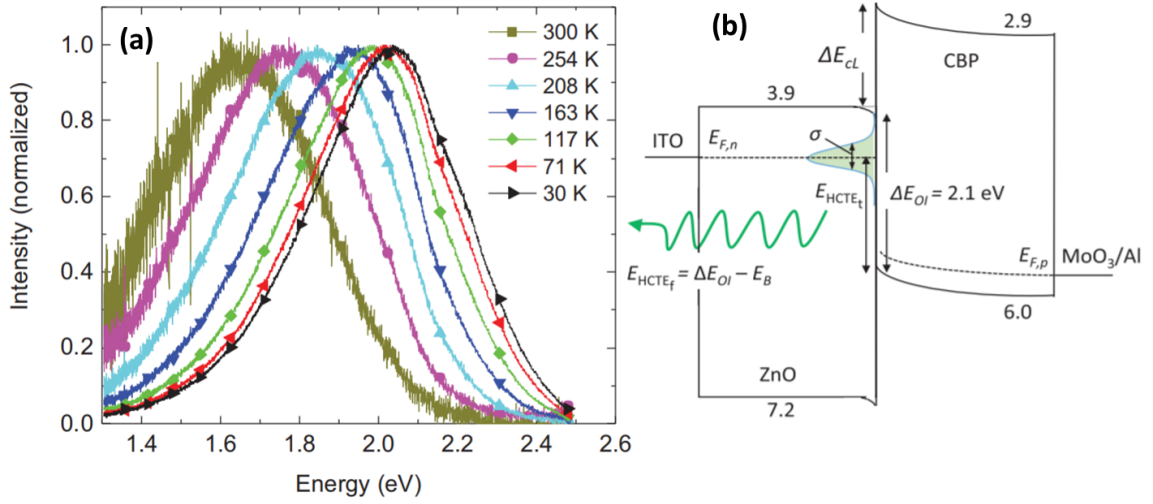


Figure 6.2: (a) Electroluminescence spectra of HCTE at the ZnO/CBP HJ vs. temperature. (b) Energy level diagram of ZnO/CBP OI HJ under forward bias. Due to the asymmetry in charge mobilities of the two materials, under forward bias, ZnO remains in equilibrium while the applied voltage is primarily dropped across CBP. The energy of the free singlet HCTE ( $E_{HCTE_f}$ ) is the difference between the ZnO conduction band maximum energy and CBP HOMO energy ( $E_{OI} = 2.1 \pm 0.1$  eV) minus the binding energy ( $E_B = 9$  meV). The trapped singlet HCTE ( $E_{HCTE_t}$ ) has an emission energy of  $E_{OI}$  minus the electron Fermi level in ZnO with respect to the ZnO conduction band minimum ( $E_{F,n} = 0.2 - 0.8$  eV), with a full width at half maximum  $\sigma = 300 \pm 10$  meV as determined from its spectral half width.

der forward bias.<sup>[183]</sup> The hybrid device structure is ITO (75 nm)/ZnO (15 nm)/CBP (15 nm)/MoO<sub>3</sub> (15 nm)/Al (100 nm). Here, ZnO film was grown on the pre-cleaned ITO substrate by sputtering a ZnO target at 0.25 Å/s with RF power (175 W) and 1 cm<sup>3</sup>/min O<sub>2</sub> flow while maintaining the chamber pressure at 2.5 mTorr. The CBP, MoO<sub>3</sub>, and Al layers were deposited by vacuum thermal evaporation at 1 Å/s in a chamber with a base pressure of  $1 \pm 10^{-7}$  Torr.

The proposed energy level diagram of the device under high forward bias and the energetic levels of relevant states are shown in Fig. 6.2(b). We employed CBP due to its wide energy gap which maximizes the difference between the ZnO conduction band maximum energy and the CBP HOMO energy,  $E_{OI} = 2.1 \pm 0.1$  eV, at the

HJ. Then,  $E_{OI} - E_B$  (where  $E_B$  is the HCTE binding energy,  $E_B = 9$  meV<sup>[183]</sup>) corresponds to the expected free HCTE emission energy, denoted as  $E_{HCTE_f}$ . The electrons localized at defect states of the ZnO surface can also bound to holes in CBP forming a trapped HCTE with binding energies of 60–430 meV<sup>[183]</sup>. The trapped HCTE has an emission energy ( $E_{HCTE_t}$ ) of  $E_{OI}$  minus the electron Fermi level in ZnO with respect to the ZnO conduction band minimum ( $E_{F,n} = 0.2 - 0.8$  eV).<sup>[188]</sup> Due to the binding energy and oscillator strength of free HCTE, only EL spectra of trapped HCTE can be observed in Fig. 6.2. The spectra exhibit a rigidochromic blue shift as the temperature is reduced from  $1.65 \pm 0.01$  eV at 300 K to  $2.05 \pm 0.01$  eV at 30 K, with a temperature-independent full width at half maximum of  $\sigma = 300 \pm 10$  meV. This shift is attributed to the Fermi level shift as a function of temperature at the same current density of the device.

## 6.3 Hybrid Heterojunction Employing Two-Dimensional Transition Metal Dichalcogenides

### 6.3.1 Two-Dimensional Transition Metal Dichalcogenides

Since the first exfoliation of graphene in 2004,<sup>[189]</sup> two-dimensional (2D) materials have provided unprecedented access to fascinating optical and electronic properties at the atomic scale. In recent years, rapid developments of synthesis and processing techniques give rise to a flourishing 2D material family beyond graphene, including 2D insulators (hexagonal boron nitride (h-BN), transition metal oxide, etc.), 2D semiconductors ( $WS_2$ ,  $MoSe_2$ , black phosphorus (BP), etc.), 2D semimetals ( $TiS_2$ ,  $TiSe_2$ , etc.), and 2D superconductors ( $NbSe_2$ ). Weak interlayer van der Waals bonding of 2D materials and high-quality interfaces free of surface dangling bonds make it possible to assemble individual layers into functional multilayer heterostructures and achieve intriguing device applications. Figure 6.3(a) shows an example of 2D heterostructures

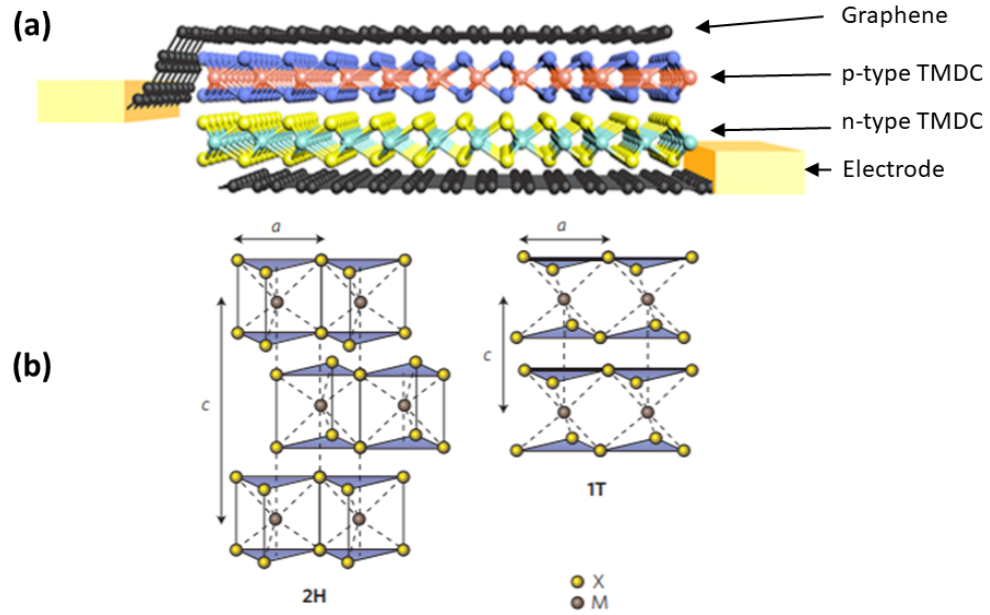


Figure 6.3: (a) A device structure of 2D TMDC p-n HJ sandwiched between graphenes that are connected to the electrodes on the sides. (b) The crystalline structure and stacking symmetry of 2H and 1T phase in TMDC, where M is the transition metal atom, X is the chalcogen atom,  $a$  is the lattice constant, and  $c$  is the stacking index. Figure adapted from refs. [190,193,194]

comprised of p-type and n-type transition metal dichalcogenide (TMDC) semiconductors sandwiched between two graphene layers that are connected to the electrodes. This structure can be used as both photodetector and light emitting diode where graphene transports charges from and to the 2D HJ in the middle, respectively. [190–192]

Among 2D materials, TMDCs with finite bandgaps ranging from ultraviolet (UV) to near infrared (NIR) are of particular interest for semiconductor physics and optoelectronic device applications. The general chemical formula of TMDC is  $\text{MX}_2$ , where M is the transition metal atom (e.g., W, Mo) and X is the chalcogen atom (e.g., S, Se, Te). The M atoms are sandwiched by two X atom layers in either trigonal or octahedral prismatic coordination, as shown in Fig. 6.3(b) left and right, respectively. The stacks of TMDC having a hexagonal interlayer symmetry with two layers per repeat unit (trigonal intralayer coordination) are denoted as 2H. Those in tetrag-

onal symmetry with one layer per repeat unit (octahedral intralayer coordination) are termed 1T. The lattice constants  $a$  are in the range of 3.1 to 3.7 Å for different materials.<sup>[195]</sup> The interlayer spacing is  $\sim 6.5$  Å, and the stacking index  $c$  indicates the number of layers. A transition of crystalline phases between 2H and 1T results in significant band structure and, therefore, electronic property changes of TMDC between semiconducting and metallic. For most TMDC material, the 1T crystalline phase is not thermally stable even at room temperature.<sup>[196]</sup> A phase transition from semiconducting 2H phase to metallic 1T phase can be achieved by chemical treatment (e.g. lithiation using butyllithium),<sup>[197]</sup> plasmonic hot electron transfer,<sup>[198]</sup> electron beam irradiation,<sup>[199]</sup> or strain.<sup>[200]</sup> Subsequent annealing can transfer 1T back to 2H.

The band structures of TMDCs also exhibit a significant dependence on the number of layers due to quantum confinement,<sup>[201]</sup> whereby the bandgap increases and a transition from indirect to direct bandgap occurs as the layer number decreases. Reduced Coulomb screening in low dimensional TMDCs results in the formation of room-temperature stable exciton states. The exciton binding energy in monolayer MoS<sub>2</sub>, for example, is shown to be in the range of 0.48 to 0.89 eV.<sup>[202,203]</sup> The effective exciton radius is around 1 to 2 nm,<sup>[203,204]</sup> which is relatively small yet still at least three times larger than the in-plane lattice constant (0.31 nm). Therefore, the excitons in 2D TMDC are still considered as Wannier-Mott type. Wannier-Mott calculations, although at the limit of applicable range, agree with experiment.<sup>[203]</sup>

Figure 6.4(a) shows the simplified band diagram of monolayer TMDC near the valley of wavevector  $k=0$ . The exciton level is depicted by the dashed line. The energy difference between the conduction band (CB) edge and the exciton level is the exciton binding energy. The A and B exciton arise from the valence-band splitting which is due to spin-orbit coupling in the monolayer TMDC. Figure 6.4 (b) shows optical spectra of monolayer MoSe<sub>2</sub> as an example. The A and B exciton absorption peaks are labeled in the spectrum. The large absorption feature, C, corresponds to



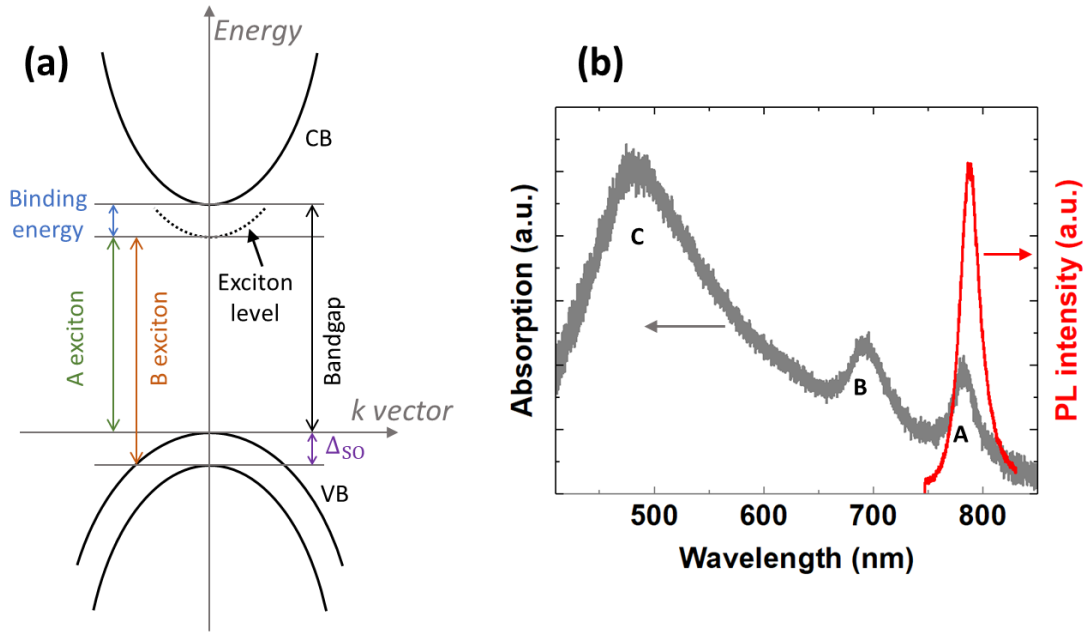


Figure 6.4: (a) The simplified band diagram of a monolayer of TMDC. The conduction and valence band are denoted as CB and VB, and  $\Delta_{so}$  indicates the spin orbit energy splitting. (b) Normalized absorption and photoluminescence spectra of a monolayer of MoSe<sub>2</sub>, where the A, B, C exciton features in absorption spectrum are labeled.

the phenomenon known as *band nesting*. In the nesting region, the CB and valence band (VB) are parallel to each other in the energy-wavevector ( $E - k$ ) diagram. The materials absorb photons of same energy and produce electrons and holes that propagate with exactly the same, but opposite, velocities. Significant band nesting phenomenon contribute to the strong light-matter interactions in 2D TMDCs.<sup>[205]</sup> The narrow PL spectrum of MoSe<sub>2</sub> shown in Fig. 6.4(b) ( $\sim 30$ nm full width at half maximum) is a result of the A exciton transition. In some systems, such as monolayer MoS<sub>2</sub>, the A and B exciton emission both appear.

The 2D TMDC exhibits complementary electronic properties to those of graphene. Graphene displays exceptionally high charge mobilities of  $> 10^5 \text{ cm}^2\text{V}^{-1}\text{s}^{-1}$  at room temperature when encapsulated in BN layers.<sup>[206]</sup> Field-effect transistors (FETs) made from pristine graphene, however, have low on/off switching ratios due to a lack of

a bandgap. The devices employing TMDCs present charge mobilities of  $10^2$ - $10^3$   $\text{cm}^2\text{V}^{-1}\text{s}^{-1}$  and on/off switching ratios exceeding  $10^8$ .<sup>[207–209]</sup> More in-depth reviews of the optical and electronic properties of TMDCs and other extraordinary phenomena such as trions and valley polarization can be found in Refs<sup>[194,210–212]</sup>.

### 6.3.2 Synthesis and Transfer Techniques

Reliable production of high quality 2D material is essential for achieving repeatable electronic and optical properties, and successful applications to devices. Processing techniques can be categorized into top-down and bottom-up approaches.

#### *Top-down exfoliation*

Top-down processing of 2D materials, as shown in Fig. 6.5(a,b), includes mechanical and liquid phase exfoliation from layered bulk crystals. Ever since the first demonstration of mechanical exfoliation of graphene using adhesive tape,<sup>[189]</sup> exfoliation of other 2D materials has adopted the same method and produces high-quality monolayers with few defects. Such a handy method is widely used for proof-of-concept device demonstrations and spectroscopic measurements, although controls of the exfoliation yield and sample size are difficult. Liquid phase exfoliation of 2D TMDC is a promising method for high yield production of scalable monolayer nanosheets. Interlayer van der Waals bonding is broken via sonication of layered crystals that are submerged in the solvents (such as N-methyl-pyrrolidone and dimethylformamide) or *intercalators* (such as butyllithium and metal naphthalenide).<sup>[213–218]</sup> Both mechanical and liquid phase exfoliation leave residues, i.e. adhesive materials and solvent molecules, respectively, which may affect the properties of 2D materials.

#### *Bottom-up synthesis*

Chemical vapor deposition (CVD) is one of the most widely used and reliable

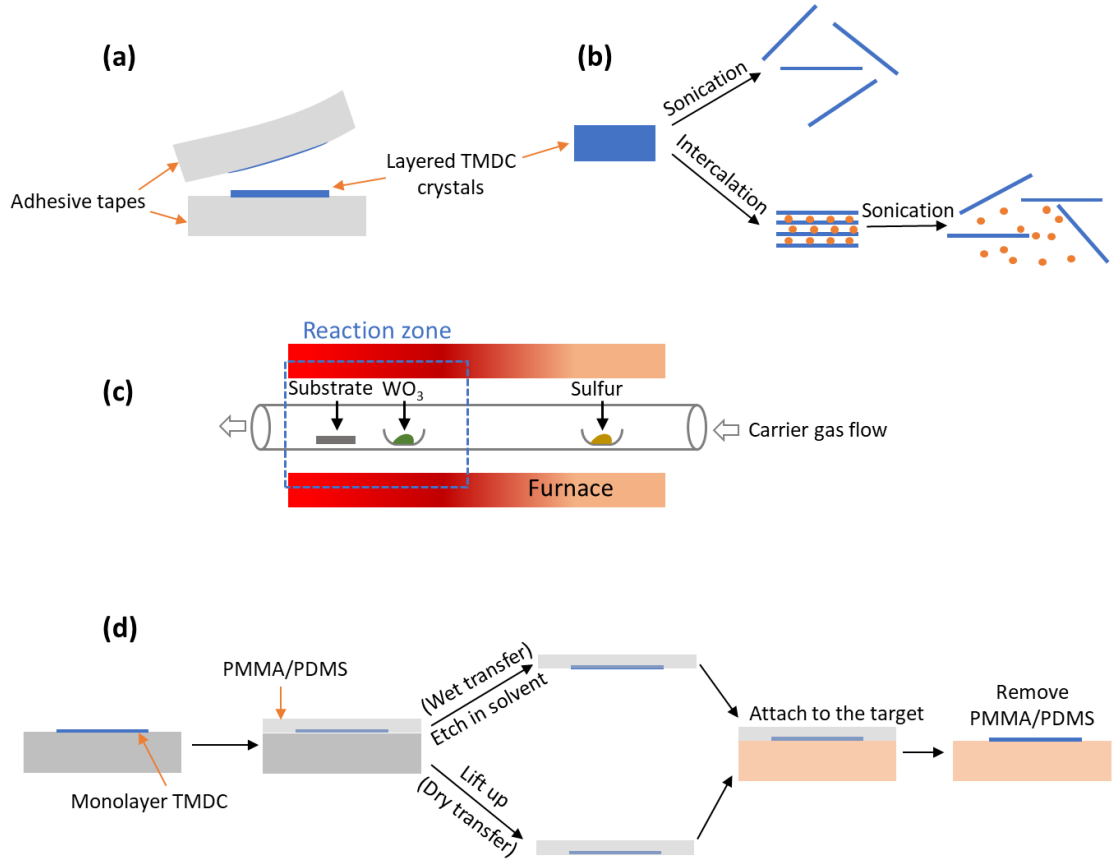


Figure 6.5: Two-dimensional materials processing techniques: (a) mechanical exfoliation; (b) liquid phase exfoliation; (c) chemical vapor deposition (CVD) for 2D  $\text{WS}_2$  growth; and (d) wet and dry transfer approaches. Figure adapted from ref. <sup>[193]</sup>

bottom-up approaches for synthesizing large-area and uniform 2D materials. Growth of graphene, <sup>[219]</sup> 2D  $\text{MoS}_2$ , <sup>[220,221]</sup>  $\text{WS}_2$ , <sup>[222]</sup>  $\text{MoSe}_2$ , <sup>[223]</sup> and  $\text{WSe}_2$ , <sup>[224]</sup> etc. using CVD have been reported. A schematic CVD setup of 2D TMDC growth is shown in Fig. 6.5(c). Solid precursors (i.e. transition metal oxide and chalcogenide powders) as shown in Fig. 6.5(c) are vaporized in the furnace and carried by an inert gas (Ar or  $\text{N}_2$ ) to the substrate where two precursors react and form atomic layers. Due to different evaporation temperatures, the chalcogenide powder is usually placed in the low temperature zone while the transition metal oxide powder is placed in the high temperature reaction zone near the substrate. Temperature at the substrate is

slightly lower than at the metal oxide zone to assist reactions. It has been shown that seeding the substrate prior to growth via surface functionalization<sup>[225]</sup> or covering the substrate with organic molecules<sup>[226]</sup> can improve the film quality. A selective-site growth can also be achieved by pre-patterning the substrate surface.<sup>[225]</sup>

### *Transfer techniques*

The assembly of multilayer heterostructures requires efficient and non-destructive transfer techniques. As illustrated in Fig. 6.5(d), a polydimethylsiloxane (PDMS) stamp or spin-coated PMMA film is brought in contact with the 2D materials on the substrate. The 2D samples are detached from the substrate via mechanical peeling (known as dry transfer) or wet-etching (known as wet transfer) using NaOH, KOH, or HF for SiO<sub>2</sub> substrates and a liquid etchant (e.g. FeCl<sub>3</sub>, CuCl<sub>2</sub>) for Cu substrates. The 2D materials are then transferred to the target substrate and released from the PMMA or PDMS film with the help of organic solvent or heating.

### **6.3.3 Two-Dimensional Organic/Transition Metal Dichalcogenide Heterojunctions**

Two dimensional TMDCs with their intriguing optical and electronic properties<sup>[227-230]</sup> have provided a unique platform for developing an entirely new class of hybrid HJs. Van der Waals bonded HJs comprising organic semiconductors and TMDC monolayers benefit from access to a wide variety of materials and structural designs compared to 3D inorganic semiconductors that require lattice matching to the substrate. The assembly of multilayer organic/TMDC heterostructures in various geometries has the potential to lead to unique physical properties and functionalities that are unachievable using other, more conventional material systems.<sup>[230]</sup>

Generally, the interactions between organic molecules and 2D TMDCs are divided into two types: van der Waals and covalent bonding. High quality, pristine TMDC

layers have atomically smooth interfaces absent of dangling bonds. Bonding between the TMDC and organic molecules in this case is predominantly driven by weak electrostatic interactions. The weak organic-TMDC interactions enable self-assembly of organic molecules depending on the intermolecular interactions. The growth of 3,4,9,10-perylene tetracarboxylic dianhydride (PTCDA) on WSe<sub>2</sub>, for example, results in well-ordered monolayer PTCDA islands with the characteristic herringbone molecular packing structure,<sup>[231]</sup> similar to the structure formed on Au (111) and graphite surfaces.<sup>[232,233]</sup> In cases where defects at the interface (e.g. chalcogenide vacancies) or chemically active 1T metallic phases of TMDC exist,<sup>[197,234–236]</sup> organic compounds can be covalently bonded to the TMDC surface, which leads to a significant change of their electronic and photoelectric properties.<sup>[237,238]</sup> In this thesis, we only focus on the van der Waals bonded organic/TMDC HJ.

Depending on the energy level alignment between the HOMO (LUMO) of organic molecules and the VB maximum (CB minimum) of TMDC, hybrid 2D HJs are also categorized into type-I, -II, and -III, similar to those shown in Fig. 1.13. The energy level alignment of two contacting materials is affected by charge transfer and electronic screening at the interface. The amount of charge transfer per molecule at the organic/TMDC interface is determined by the strength of electron donating and accepting groups of the molecules, molecular orientation, and crystalline phase of TMDC. The existence of strong electron donating and accepting groups, horizontal alignment of the organic molecules, and 1T metallic phase of TMDC facilitate charge transfer across the HJ and shift the energy levels.<sup>[239–241]</sup> For instance,  $\sim 0.13$  electron transfer per molecule occurs from flat-lying tetrathiafulvalene (TTF) to the monolayer 2H phase MoS<sub>2</sub> in contact,<sup>[242]</sup> while only  $\sim 0.015$  electrons per molecule from flat-lying pentacene to 2H phase MoS<sub>2</sub>. This value is significantly increased to  $\sim 0.437$  at flat-lying pentacene/ 1T phase MoS<sub>2</sub> HJ.<sup>[241]</sup>

The 2D TMDCs in contact with organic molecules benefit from surface passiva-

tion, which gives rise to an improved carrier mobility and PL quantum yield. Monolayer MoS<sub>2</sub> coated by (3-mercaptopropyl) trimethoxysilane (MPS) molecules has the density of sulfur vacancies reduced from  $\sim 6.5 \times 10^{13} \text{ cm}^{-2}$  to  $\sim 1.6 \times 10^{13} \text{ cm}^{-2}$ , and achieves  $\mu = 81 \text{ cm}^2\text{V}^{-1}\text{s}^{-1}$ . MoS<sub>2</sub> coated with p-type organics, e.g. 2,3,5,6-tetrafluoro-7,7,8,8-tetracyanoquinodimethane (F4TCNQ) or TCNQ, passivates sulfur vacancies, leading to a decrease of trion (i.e. a composite of an exciton and an electron or hole) emission and a pronounced increase in exciton emission.<sup>[243]</sup> The MoS<sub>2</sub> treated with an organic superacid bis(trifluoromethane) (TFSI) achieves > 95 % PL quantum yield.

Hybrid electronic devices employing type-II 2D organic/TMDC HJs have been demonstrated, including photodetectors,<sup>[244-246]</sup> photovoltaics,<sup>[247]</sup> field-effect transistors (FETs),<sup>[248-251]</sup> etc. The absorption coefficient of the hybrid HJ is greatly enhanced compared to the 2D TMDC alone. Type-II alignment at the interface facilitates ultrafast charge transfer between the photoexcited TMDC and organic layer. The long charge recombination time for the HCTE,  $\sim 2 - 60$  times longer than CT excitons in type-II heterojunctions based on 2D TMDCs alone, enables a larger photodiode quantum efficiency.<sup>[237,252,253]</sup> As an emerging and rapidly progressing field, the studies of 2D organic/TMDC hybrid HJ and devices are still in the early stage yet offer potential for further applications.

## CHAPTER VII

# Dipole Aligned Energy Transfer Between Excitons in a Two-dimensional Transition Metal Dichalcogenide and an Organic Semiconductor

### 7.1 Introduction

Despite advantageous characteristics, some critical issues need to be addressed before TMDCs can be used in practical optoelectronic devices. One is their low absorption per layer despite a large oscillator strength. This shortcoming can be mitigated by using an efficient light absorber such as an organic layer that efficiently transfers energy to the high mobility TMDC. Such hybrid systems can enjoy broadband absorption along with efficient energy harvesting.<sup>[254]</sup> Nonradiative FRET<sup>[16]</sup> occurs via dipole coupling between donor and acceptor molecules. The parameters that determine the efficiency of nonradiative energy transfer include the spectral overlap between emission of the donor and absorption of the acceptor, the physical distance between the donor and acceptor, dimensionality of the materials, and relative orientation of the donor and acceptor dipole moments.<sup>[255]</sup> There have been reports of energy transfer to 2D TMDC using colloidal QD as donors<sup>[256-259]</sup> where a decrease in the lifetime of the donor QD provided evidence of energy transfer. However, the dipole orientation of the donors and acceptors could not be controlled in such sys-

tems. Here we demonstrate energy transfer between in-plane dipoles of PTCDA and 2D MoSe<sub>2</sub>.<sup>[260]</sup> To exploit the unique advantages of both materials, i.e. large absorption coefficient in organic molecules and high mobility in 2D TMDC, the energy transfer should occur from the organic PTCDA to the 2D MoSe<sub>2</sub>.

By stacking a monolayer MoSe<sub>2</sub> on top of 2 nm thick film of PTCDA, we observe the direct quenching of PL in PTCDA as well as the increase in PL of MoSe<sub>2</sub>. The PL lifetime of PTCDA is found to decrease in the presence of the MoSe<sub>2</sub>, while that for MoSe<sub>2</sub> increases. This change is explained using a rate equation model. Finally, photoluminescence excitation (PLE) spectra showed an increase in steady state PL of MoSe<sub>2</sub> when excited at the absorption maximum of PTCDA.

## 7.2 Experimental Section

The structures of MoSe<sub>2</sub> and PTCDA, along with a schematic of the HJ are shown in Fig. 7.1(a). A thin layer PTCDA (2 nm) was grown on a glass slide (150  $\mu\text{m}$  thick) by vacuum thermal evaporation in a system with base pressure of  $2 \pm 10^{-7}$  Torr. Monolayer MoSe<sub>2</sub> was grown on an SiO<sub>2</sub>/Si substrate by CVD and then dry-transferred on top of the PTCDA film.<sup>[261]</sup>

Samples were excited by a 500 fs pulsed laser (Toptica, FemtoFiber pro TVIS with repetition rate 80 MHz) at a wavelength of 510 nm. The beam was focused to a  $\sim 2$   $\mu\text{m}$  diameter spot via a 50 $\times$  objective. The PL spectrum was collected by the same objective and coupled to a monochromator (Princeton Instruments Acton SpectraPro SP-2500) with a 1024  $\times$  1024 CCD camera (Princeton Instruments 1024 PIXIS). Time-resolved PL was measured by a time correlated single photon counting detector. The excited state dipole orientation of PTCDA and MoSe<sub>2</sub> were measured using Fourier plane imaging by confocal microscopy shown in Fig. 7.1(b). An oil immersion objective (Olympus MPLAPON100XO) with numerical aperture 1.4 was used to ensure a large collection angle. Different dipole orientations (with respect



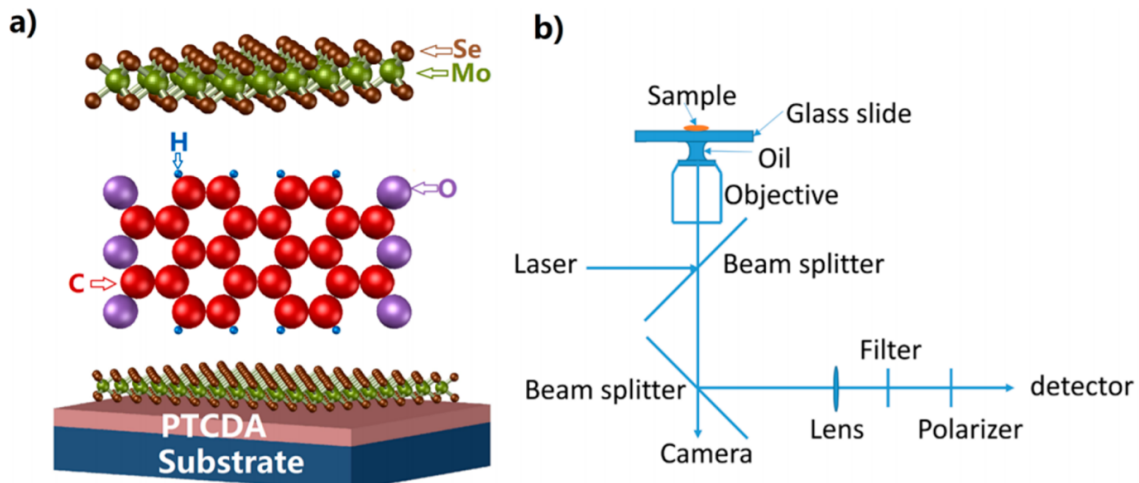


Figure 7.1: (a) Top:  $\text{MoSe}_2$  monolayer; Middle: Structural molecular formula of PTCDA; Bottom: schematic of the hybrid sample. (b) Schematic of the Fourier space imaging setup.

to the glass substrate surface) resulted in distinguishable orthogonal image patterns in the Fourier plane of the objective.<sup>[255,262]</sup> The monochromator was maintained in the reflection geometry so that the two orthogonal momentum directions parallel to the sample surface could be simultaneously detected by the CCD camera. Different band-pass filters ( $670 \pm 5$  nm for PTCDA and  $790 \pm 5$  nm for  $\text{MoSe}_2$ ) were placed in front of the entrance slit of the monochromator to reduce chromatic aberration of the Fourier plane image. The absorption of  $\text{MoSe}_2$  and PTCDA were obtained using differential reflectivity carried out under white light illumination.

### 7.3 Dipole Aligned Förster Transfer at PTCDA/ $\text{MoSe}_2$ Heterojunction

The Fourier plane images of the emission intensity for both  $\text{MoSe}_2$  and PTCDA in Fig. 7.2 show that the excited state dipoles are horizontally aligned. These patterns are similar to that from a calculation of an in-plane dipole shown in Fig. 7.2(3). As a comparison, the calculated pattern of an out-of-plane dipole is shown in Fig. 7.2(4).

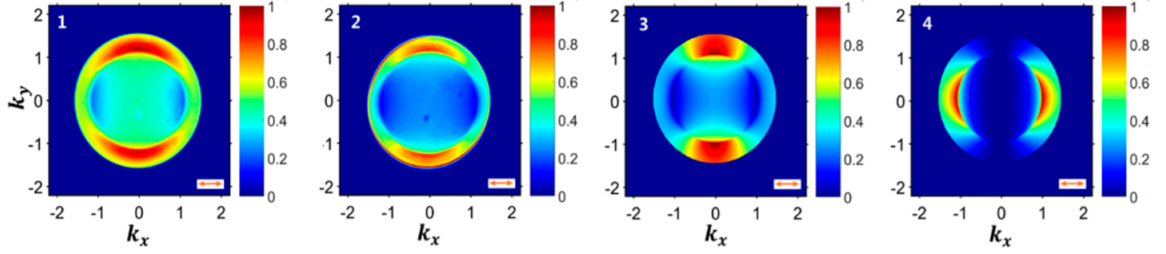


Figure 7.2: Fourier space images of (1) MoSe<sub>2</sub>, (2) PTCDA, (3) the calculated emission pattern of an in-plane dipole and (4) an out-of-plane dipole. All the wave vectors are scaled with respect to emission wave vector of individual material in vacuum,  $k_0$ . The arrow indicates the direction of the polarizer.

In Fig. 7.3(a), the absorption peaks of A, B, and C excitons in MoSe<sub>2</sub> and excitons in PTCDA are shown. The PL spectrum of PTCDA shown as the black curve in Fig. 7.3(a) indicates overlap with the B exciton absorption in MoSe<sub>2</sub>, which enables FRET from PTCDA to MoSe<sub>2</sub>.

A theoretical FRET radius can be estimated by Eq. 1.21:

$$R_F^6 = \frac{9\kappa^2\eta_D}{128\pi^5n^4} \int f_D(\lambda)\sigma_D(\lambda)\lambda^4d\lambda. \quad (7.1)$$

Here, the orientation factor  $\kappa \approx \frac{1}{4\pi^2} \int_0^{2\pi} \int_0^{2\pi} |\cos(\alpha - \beta)| d\alpha d\beta = \frac{2}{\pi}$ , assuming the interaction of two in-inplane dipoles at angle  $\alpha$  and  $\beta$ , respectively. The quantum yield of PTCDA  $\eta_D \approx 0.009$ .<sup>[263]</sup> An effective refractive index  $n \approx 3$ .<sup>[264,265]</sup> The spectral overlap calculated from Fig. 7.3(a) gives rise to  $R_F^6 \approx 4.91nm^6$ . (See detailed calculation in ref.<sup>[260]</sup>) Therefore, the FRET efficiency is approximately  $\eta_{FRET} = \frac{1}{1+(r/R_F)^6} = \frac{1}{1+1.33^6/4.91} = 0.47$ . Here  $r \approx \frac{L_{PTCDA}+L_{MoSe2}}{2} = 1.33$  nm, in which  $L_{PTCDA}$  and  $L_{MoSe2}$  are the layer thickness of PTCDA and MoSe<sub>2</sub>, respectively.

The PL spectra of PTCDA and MoSe<sub>2</sub> are compared to that of the hybrid sample. The PL spectrum from the same MoSe<sub>2</sub> island was measured before and after transferring to the PTCDA. All the measurements were done under a laser power of 1.28  $\mu\text{W}/\text{mm}^2$ . Figure 7.3(b) shows the PL spectrum of PTCDA, MoSe<sub>2</sub>, and

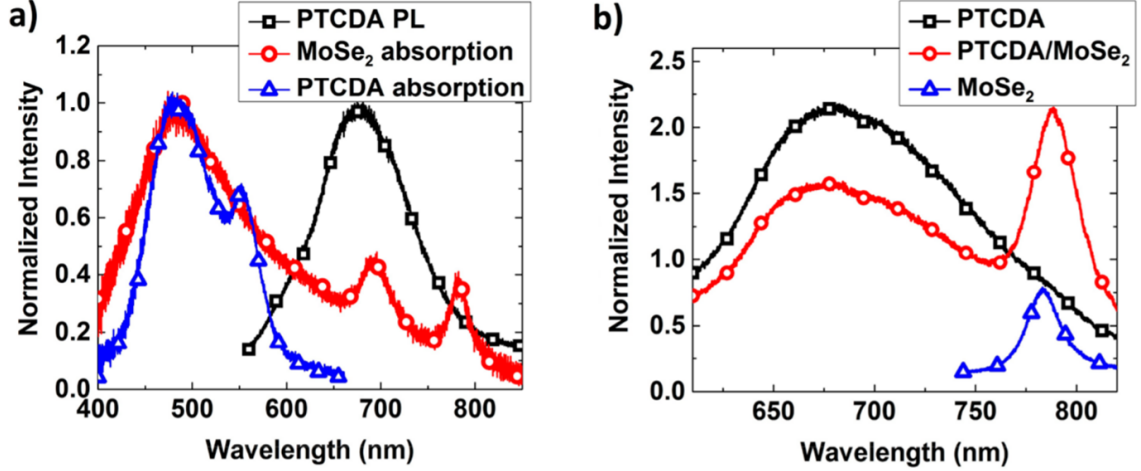


Figure 7.3: (a) Differential reflectivity of PTCDA (blue triangles) and MoSe<sub>2</sub> (red circles), and PL of PTCDA (black squares). The intensities are normalized. (b) Photoluminescence of PTCDA (black squares), MoSe<sub>2</sub> (blue triangles), and the hybrid sample (red circles).

the hybrid sample. The PL intensity of PTCDA is quenched while that of MoSe<sub>2</sub> increases in the hybrid sample. The FRET efficiency,  $\eta = 1 - I_{DA}/I_D = 30\%$ . Here  $I_{DA}$  and  $I_D$  are the spectrally integrated donor emission intensities with and without the acceptor layer on the PTCDA surface, respectively. This value is smaller than the theoretically predicted value of 47%. This is attributed to disorder at the interface, possible formation of charge transfer states and finite spectral overlap between the donor and the acceptor.

The exciton dynamics of PTCDA, MoSe<sub>2</sub>, and the hybrid sample are shown in Figure 7.4. Band pass filters were used ( $670 \pm 5$  nm for PTCDA and  $790 \pm 5$  nm for MoSe<sub>2</sub>) to obtain the lifetimes of the corresponding materials. For PTCDA, a biexponential fit yields  $\tau_1 = 80$  ps and  $\tau_2 = 521$  ps, while for the hybrid sample,  $\tau_1 = 56$  ps and  $\tau_2 = 383$  ps. This 30% decrease of PTCDA exciton lifetime in the hybrid sample is consistent with the FRET efficiency calculated from the PL intensity quenching data. Since the FRET efficiency decreases with the sixth power of the distance between donor and acceptor, an experiment was carried out by growing a

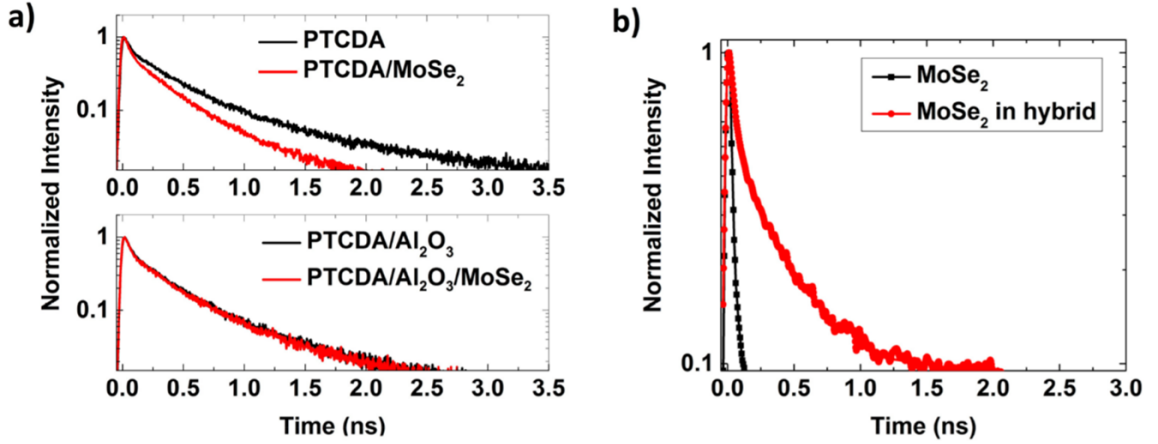


Figure 7.4: (a) Top: time-resolved PL of PTCDA with (red) and without (black) MoSe<sub>2</sub> on its surface; Bottom: time-resolved PL of PTCDA with (red) and without (black) MoSe<sub>2</sub> in the presence of a 10 nm thick Al<sub>2</sub>O<sub>3</sub> spacer. (b) Time-resolved PL of MoSe<sub>2</sub> on a bare substrate (black squares) and PTCDA (red circles).

10 nm Al<sub>2</sub>O<sub>3</sub> spacer via atomic layer deposition (ALD) at 80 °C on top of PTCDA prior to the MoSe<sub>2</sub> transfer. The PTCDA lifetime was measured with and without the MoSe<sub>2</sub> in the presence of the spacer. No discernible change in lifetime is observed in the presence of the acceptor, indicating that FRET is suppressed by the presence of the 10 nm thick spacer.

The MoSe<sub>2</sub> exciton lifetime was found to increase in the hybrid structure compared to that for MoSe<sub>2</sub> only. In the hybrid sample, PTCDA undergoes FRET to MoSe<sub>2</sub>. The MoSe<sub>2</sub> exciton itself has a much shorter lifetime (Figure 7.4(b), black curve) compared to that for PTCDA, but the excited state of MoSe<sub>2</sub> continues to be populated by FRET, which results in an increase in the effective PL lifetime of MoSe<sub>2</sub> (Figure 7.4(b), red curve). This effect can be quantitatively explained using the following rate equations:

$$\begin{cases} \frac{dN_p}{dt} = -\frac{N_p}{\tau_p} - \frac{N_p}{\tau_{FRET}} \\ \frac{dN_m}{dt} = -\frac{N_m}{\tau_m} + \frac{N_p}{\tau_{FRET}} \end{cases} \quad (7.2)$$

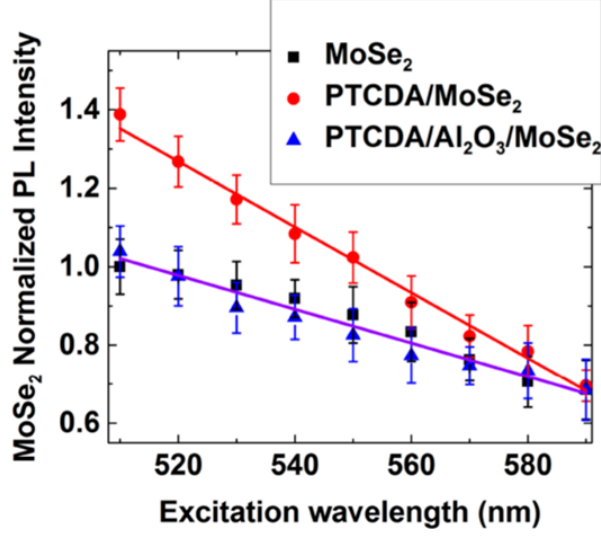


Figure 7.5: Photoluminescence excitation spectral intensity of MoSe<sub>2</sub> at a wavelength of 787 nm under different excitation wavelengths. The data are scaled so that the intensities at excitation wavelength of 590 nm are the same for all the samples. The hybrid PTCDA/MoSe<sub>2</sub> samples with (blue triangles) and without (red circles) a 10 nm thick Al<sub>2</sub>O<sub>3</sub> spacer between the semiconductors is compared to the MoSe<sub>2</sub> sample (black square). The red and violet are the guide lines.

Here,  $N_p$  and  $N_m$  are the exciton populations of PTCDA and MoSe<sub>2</sub>, respectively.  $\tau_p$  and  $\tau_m$  are the lifetimes of PTCDA and MoSe<sub>2</sub> excitons, respectively, and  $\tau_{FRET}$  is the energy transfer time constant. Solution of Eq. 7.2 yields the exciton population in PTCDA of  $N_p = N_p^0 \exp(-t/\tilde{\tau}_p)$ . Here  $\tilde{\tau}_p = \frac{\tau_p \tau_{FRET}}{\tau_p + \tau_{FRET}}$  is the modified PTCDA exciton lifetime in hybrid sample. Therefore,

$$N_m = \frac{N_p^0 \tilde{\tau}_p \tau_m}{\tau_{FRET}(\tilde{\tau}_p - \tau_m)} e^{-t/\tilde{\tau}_p} + \left( N_m^0 - \frac{N_p^0 \tilde{\tau}_p \tau_m}{\tau_{FRET}(\tilde{\tau}_p - \tau_m)} \right) e^{-t/\tau_m}, \quad (7.3)$$

suggesting that the effective PL lifetime of MoSe<sub>2</sub> is directly related to the modified PTCDA lifetime,  $\tilde{\tau}_p$ , in the hybrid sample, which is much longer than the pristine MoSe<sub>2</sub> lifetime  $\tau_m$ .

To further substantiate the existence of energy transfer, we carried out PLE experiments where the excitation laser wavelength is tuned across the absorption spectrum

of PTCDA at constant power ( $1.28 \mu\text{W}/\text{mm}^2$ ) while monitoring the emission intensity of  $\text{MoSe}_2$  at a wavelength of 787 nm corresponding to its emission maximum. A  $\text{MoSe}_2$  monolayer transferred to a bare substrate was used as a control. The same  $\text{MoSe}_2$  sample was then transferred onto PTCDA for PLE measurements. Similar measurements were also carried out on the hybrid sample with the 10 nm  $\text{Al}_2\text{O}_3$  spacer. Results of the PLE experiments are shown in Figure 7.5 where the emission intensity of  $\text{MoSe}_2$  is maximum at the absorption peak of PTCDA in the hybrid structure. In contrast, the hybrid structure with the spacer shows almost no dependence on the excitation wavelength besides the trend shown by the control ( $\text{MoSe}_2$  only) due to suppression of FRET. The wavelength dependence of the acceptor emission on the excitation wavelength in the hybrid structure once again provides evidence for energy transfer occurring from PTCDA to  $\text{MoSe}_2$ .

In summary, we have observed 30% energy transfer efficiency in the dipole-aligned OI hybrid HJ. The PL intensity quenching of PTCDA accompanied by the decrease in its PL lifetime and the increase of  $\text{MoSe}_2$  acceptor emission provide a direct observation of energy transfer which is controlled by the distance and orientation between the donor and acceptor dipoles. Additionally, the energy transfer process was found to modify the exciton lifetime in the acceptor due to the large difference in the inherent lifetimes of the donor (PTCDA) and acceptor ( $\text{MoSe}_2$ ) materials. We also demonstrated the dependence of the energy transfer efficiency on excitation wavelength, with a maximum efficiency occurring when the hybrid structure is excited at the absorption maximum of the donor. Such hybrid systems with efficient energy transfer between organic molecules and inorganic 2D TMDC provide a platform to develop enhanced light harvesting systems, as well as thin film optoelectronic devices.

## CHAPTER VIII

# Photoresponse of an Organic Semiconductor/Two-Dimensional Transition Metal Dichalcogenide Heterojunction

### 8.1 Introduction

While most previous research has focused on junction fabrication, device performance, and optical and electric characterizations, the fundamental physics behind the excitonic and optoelectronic properties of the 2D type-II HJ have yet to be fully studied. In this work, we report on the photoresponse of a HJ comprising a PTCDA thin film deposited onto a monolayer of the TMDC, WS<sub>2</sub>. The well-known properties of PTCDA and easily achieved planar morphology at monolayer thicknesses extending over macroscopic distances, resulting in a high mobility<sup>[266]</sup> make it an ideal system to couple with monolayer TMDC. The energy landscape of the 2D hybrid charge transfer states at the heterointerface is studied using an *ab initio* quantum mechanical model. Using insights developed, we fabricate a HJ photodetector with an external quantum efficiency  $EQE = 1.8 \pm 0.2\%$  at a wavelength of  $430 \pm 10$  nm, corresponding to an  $IQE$  as high as  $\eta_{IQE} = 11 \pm 1\%$  in these ultrathin devices. We clearly resolve features in the  $EQE$  spectrum due to the dissociation at the heterointerface of both Frenkel/CT excitons of PTCDA and Wannier-Mott excitons of WS<sub>2</sub>.

We study the steady state PL of PTCDA and PTCDA/WS<sub>2</sub> thin films and find a pronounced asymmetry of dissociation efficiency between WS<sub>2</sub> and PTCDA excitons, which leads to a wavelength dependent *IQE* of the photodiode.

## 8.2 Theoretical Calculations of 2D Hybrid Charge Transfer State

The energy level diagram of the PTCDA/WS<sub>2</sub> HJ,<sup>[267,268]</sup> is shown in Fig. 8.1(a). The type-II (staggered) HJ can efficiently dissociate excitons due to the approximately 1 eV energy offset between the highest occupied energy levels (HOEL) and the lowest unoccupied energy levels (LUEL) at the interface. A HCTE formed during the dissociation process enables exciton-to-charge conversion and charge recombination at the HJ. Previously, the existence of longlived charge transfer states has been shown at a pentacene/MoS<sub>2</sub><sup>[237]</sup> and tetracene/WS<sub>2</sub><sup>[187]</sup> HJ.

To model the HCTE,<sup>[183,269]</sup> we assume that the 2D WS<sub>2</sub> has only in-plane polarizability and that holes are delocalized in the plane. Due to the asymmetry of the dielectric constants and effective masses of charges in the two contacting materials, the HCTE wave function is expected to be delocalized on the inorganic side having primarily Wannier-Mott character, whereas it is more confined on the organic side with Frenkel character.<sup>[179]</sup> In our model, the hole is bound to an electron fixed at an adjacent PTCDA molecule. This assumption is justified by the lower dielectric constant and larger effective mass of electrons in PTCDA as compared to holes in WS<sub>2</sub>. The potential energy of the hole is  $V(r) = V_{xy}(x, y) + V_z(z)$ , where  $V_{xy}(x, y)$  is the Coulomb potential between the electron and the hole which primarily depends on the 2D distribution of the hole in x-y (WS<sub>2</sub>) plane, and  $V_z(z)$  includes other potential terms such as image charge potential and LUEL offset, which are constant in the x-y plane. We also assume that the hole wave function is separable:



$\psi(r) = \psi_{xy}(x, y)\psi_z(z)$ , where  $r = \sqrt{x^2 + y^2 + z^2}$ . Schrödinger's equation is then:

$$\left[ -\frac{\hbar^2}{2m^*} \nabla_{xy}^2 + V_{xy}(x, y) \right] \psi_{xy}(x, y) = E' \psi_{xy}(x, y) \quad (8.1)$$

where  $\hbar$  is the reduced Planck's constant,  $m^*$  is the reduced effective mass of the HCTE, and  $E' = E + \frac{\hbar}{2m^*} \frac{\psi_z''(z)}{\psi_z(z)} - V_z(z) = E - E_{free}$ , which is approximately the HCTE relative to the free hole energy in WS<sub>2</sub>. Also,  $\psi_z''(z)$  is the second spatial derivative of the wave function with respect to  $z$ . The Coulomb potential is  $V_{xy}(x, y) = -\sum_{i=1}^n \frac{e^2/n}{4\pi\epsilon_0\epsilon_r|r_h-r_i|}$  where  $e$  is the elementary charge,  $\epsilon_0$  is the vacuum permittivity,  $\epsilon_r$  is the dielectric constant of WS<sub>2</sub>, and  $r_h = \sqrt{x^2 + y^2}$  is the position of the hole in the WS<sub>2</sub> plane. The charge distribution of the anionic PTCDA is found via DFT calculations employing the Gaussian 09w package<sup>[97]</sup> with the B3LYP functional and 6-31G basis set. The electric field from the hole is not included in the DFT calculation of the PTCDA polaron state. The impact of this approximation is expected to be small since the extent of the electron charge distribution on PTCDA is much smaller than that for the hole on WS<sub>2</sub>. Therefore, the binding energy is determined primarily by the hole rather than electron. The electron distribution on PTCDA is simplified by using a summation over  $n$  discrete, fractional point charges at positions,  $r_i$ . Due to the mirror symmetry of PTCDA, it is adequate to use  $n = 2$  located at the symmetry points separated by 0.56 nm on the two halves of the PTCDA molecule.

We obtain the energy eigenvalues of the Hamiltonian by solving Eq. 8.1, which yields the energy landscape shown in Fig. 8.1(c). The lowest (1s) CT state has a binding energy of 38.2 meV, making it stable at room temperature. Overcoming the binding energy, as well as recombination via the HCTE state, should therefore affect photogeneration in this hybrid system. Also shown are the hole wave functions of the lowest four states corresponding to the 1s, 1p, 2s, and 1d orbitals, with average electron-hole separations of  $r_0 = 2.2, 7.5, 11.0, 18.3$  nm, respectively. The relative

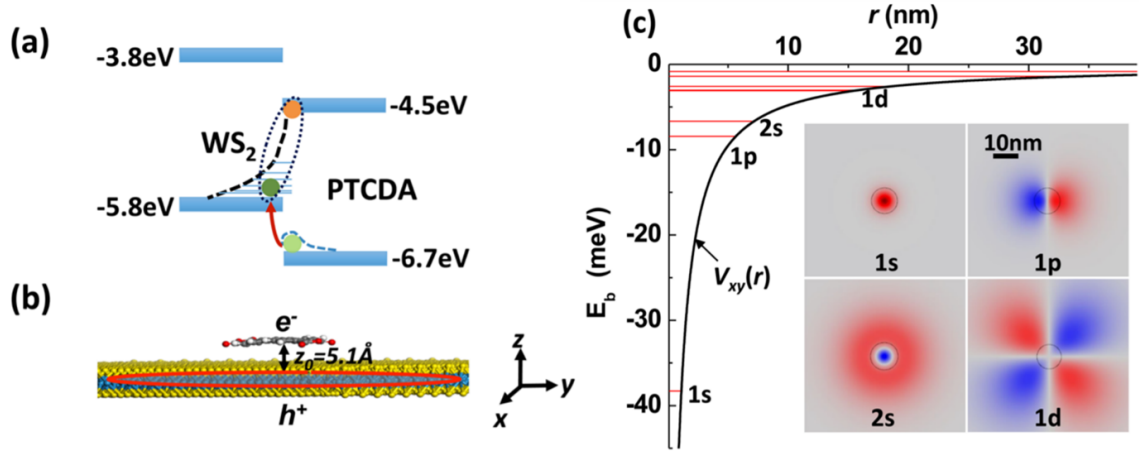


Figure 8.1: (a) Energy level diagram<sup>[267,268]</sup> of  $\text{WS}_2$  and PTCDA showing a type-II HJ. (b) Illustration of a molecule of PTCDA on  $\text{WS}_2$  with distance calculated using molecular dynamics simulations. (c) Energy eigenvalues of HCTE ( $E_b$ ) vs Coulombic potential  $V_{xy}(r)$  for an electron on PTCDA. Inset: hole wave function of lowest four eigenstates within the 2D  $\text{WS}_2$  (x-y) plane. The black circle in the middle of each graph is a 10 nm diameter reference.

sizes of these several states are illustrated in the figure. Note that, in the 2D system, the angular momentum quantum number is not necessarily smaller than the principal quantum number.

### 8.3 Experimental Section

Organic and metal films were grown via vacuum thermal evaporation in a system with base pressure  $\sim 2 \times 10^{-7}$  Torr on an ITO ( $15 \Omega/\text{sq.}$ ) coated glass substrate. The ITO surface is precleaned in Tergitol solution, acetone, and isopropanol, followed by 10 min ultraviolet-ozone treatment. The structure of the hybrid photodiode is ITO/TMDC/10 nm PTCDA/8 nm Bphen/100 nm Al. The Bphen acts as an exciton blocking layer and provides protection of the active layers during the Al deposition. The Al electrode is patterned by deposition through a shadow mask comprised of a transmission electron microscope grid with  $38 \times 38 \mu\text{m}^2$  square apertures. A reference

photoconductive device lacking a HJ was fabricated with the structure: ITO/60 nm PTCDA/100 nm Al.

Monolayer TMDCs were grown on SiO<sub>2</sub> substrates by CVD. A PDMS stamp was brought into contact with the TMDC, subsequently submerged in 1 mol/L KOH solution for 1 h, followed by rinsing in deionized water. The TMDC attached to the PDMS layer was lifted off from the growth substrate, then brought into contact with, and released onto the ITO surface.

PL samples were prepared on quartz substrates with monolayer WS<sub>2</sub> transferred onto a predeposited, 10 nm thick PTCDA film, and also directly onto an uncoated substrate. The HJ sample was excited via the WS<sub>2</sub> side at a wavelength of  $\lambda = 532$  nm using a tunable pulsed fiber laser (FemtoFiber Pro TVIS). Due to the absorption of the WS<sub>2</sub>, the fluence absorbed by PTCDA was approximately 2% less than that for direct excitation of PTCDA. The incident light was focused to a 5  $\mu$ m diameter spot at the sample plane using a 50 $\times$  objective lens, and the PL signal was collected by the same objective and guided into the spectrometer. A time-correlated single photon counter (PicoHarp 300) coupled to a Si single photon avalanche photodetector (PDM Series) was used for the time-resolved PL measurements. All spectra shown are averages taken from several WS<sub>2</sub> islands. The photodiode *EQE* was measured by exciting the device normal to the substrate with monochromated light from a Xe arc-discharge lamp chopped at 200 Hz. The incident beam was focused to a  $\sim 20$   $\mu$ m diameter spot via a 20 $\times$  objective. The photocurrent was measured using a lock-in amplifier (Stanford Research Systems SR830).

Quantum chemical calculations were carried out via DFT employing the Gaussian 09w package<sup>[97]</sup> with the B3LYP functional and the 6-31G basis set. The time-independent Schrödinger's equation (see Eq. 8.1) was solved via COMSOL Multiphysics.

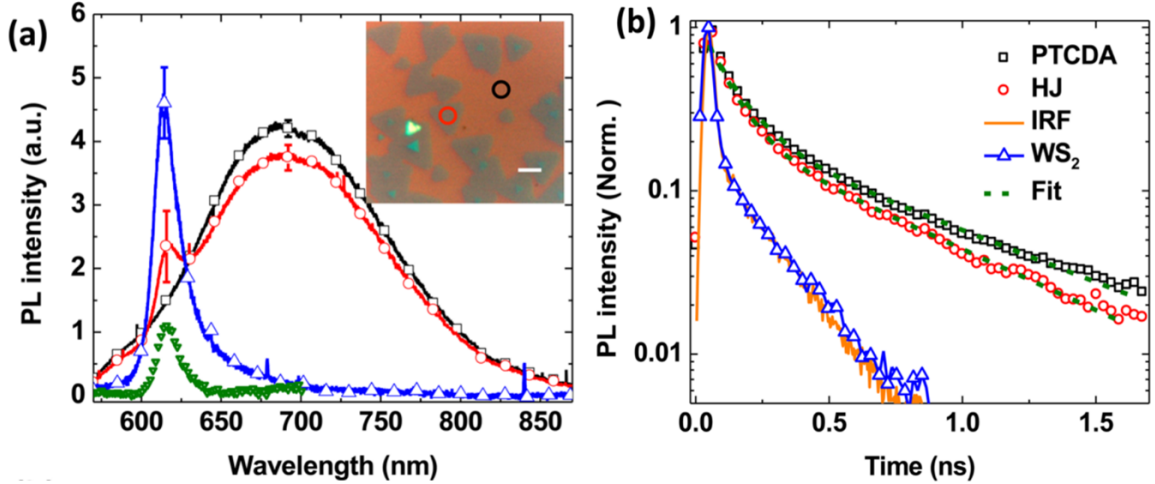


Figure 8.2: (a) Photoluminescence spectra of 10 nm PTCDA (black squares), WS<sub>2</sub> (blue triangles), and PTCDA/WS<sub>2</sub> HJ (red circles). The WS<sub>2</sub> PL extracted from the mixed emission spectrum of the HJ is shown by the green down-triangles. The spectral shapes are identical for different excitation wavelengths. Inset: Optical microscopic image of WS<sub>2</sub> islands transferred onto the PTCDA film. Photoluminescence detection spots are circled. The scale bar in the image is 10  $\mu\text{m}$ . (b) Time-resolved PL of PTCDA (squares), PTCDA/WS<sub>2</sub> HJ (circles), and WS<sub>2</sub> (triangles). The orange line is the IRF. The green dashed lines are biexponential fits to the data.

#### 8.4 Photoresponse of PTCDA/WS<sub>2</sub> Heterojunction

Figure 8.2(a) shows the PL spectra of PTCDA and the excitonic emission from a monolayer of WS<sub>2</sub> with a narrow peak at  $\lambda = 615$  nm. These spectra are obtained from a region consisting only of PTCDA and as well as from a PTCDA/WS<sub>2</sub> HJ, as indicated by circles in the optical microscope image shown in Fig. 8.2(a), inset. The PL intensity of PTCDA and WS<sub>2</sub> decreases in the PTCDA/WS<sub>2</sub> HJ by  $12 \pm 5\%$  and  $80 \pm 10\%$ , respectively, suggesting that excitons generated in both PTCDA and WS<sub>2</sub> are dissociated at the heterointerface, with the dissociation probability of WS<sub>2</sub> excitons approximately seven times higher than for PTCDA. We did not observe spectral features that directly relate to HCTE transitions, possibly due to the low PL quantum yield and ultrashort lifetime of this intermediate state.<sup>[270]</sup> A direct

observation of the HCTE signal may require more sensitive methods than employed here.

We investigate time-resolved PL to study the exciton dynamics in PTCDA, as well as its dependence on the presence of the PTCDA/WS<sub>2</sub> HJ, with results shown in Fig. 8.2(b). Note that the time-resolved PL of WS<sub>2</sub> has a faster decay than the IRF. Therefore, only the dynamics of PTCDA excitons can be inferred from PL transient of HJ. Biexponential fits to the data yield the time constants  $\tau_1 = 100 \pm 10$  ps,  $\tau_2 = 660 \pm 20$  ps for PTCDA, and  $\tau'_1 = 90 \pm 10$  ps,  $\tau'_2 = 580 \pm 20$  ps for the HJ. The PL transients show multiexponential decays regardless of excitation fluence. This is primarily due to the existence of energetically overlapping exciton species in PTCDA that have different lifetimes. Closely packed PTCDA molecules along the substrate normal with an intermolecular separation distance of 3.21 Å<sup>[271]</sup> result in strong interlayer interactions, and therefore a mix of intra- and intermolecular excitons, e.g. Frenkel states and dimer CT states.<sup>[7,255,272,273]</sup> The lifetimes of PTCDA excitons in the HJ decrease by  $12 \pm 2\%$  on average, which is consistent with the steady state PL quenching ratio in Figure 8.2(a).

We fabricated a photodiode employing the PTCDA/WS<sub>2</sub> HJ as described in the experimental section. The top electrode is patterned by a shadow mask with  $38 \times 38 \mu\text{m}^2$  square holes aligned to the WS<sub>2</sub> islands. The electrodes are sufficiently large to cover the entire island. Figure 8.3(a) shows the absorbed power for light incident normal to the substrate via the ITO anode as a function of position across the device cross section, calculated using the transfer matrix model described previously.<sup>[80]</sup> The inset of Figure 8.3(b) shows the device structure. Greater than 60% of the exciton population is generated in the WS<sub>2</sub> layer when the junction is excited at  $\lambda < 450$  and  $\lambda > 600$  nm, whereas >85% of excitons are generated in the PTCDA for illumination at  $450 < \lambda < 600$  nm. Integration of the absorbed power over the total HJ thickness yields the absorption coefficient of the active layers as a function of wavelength, shown

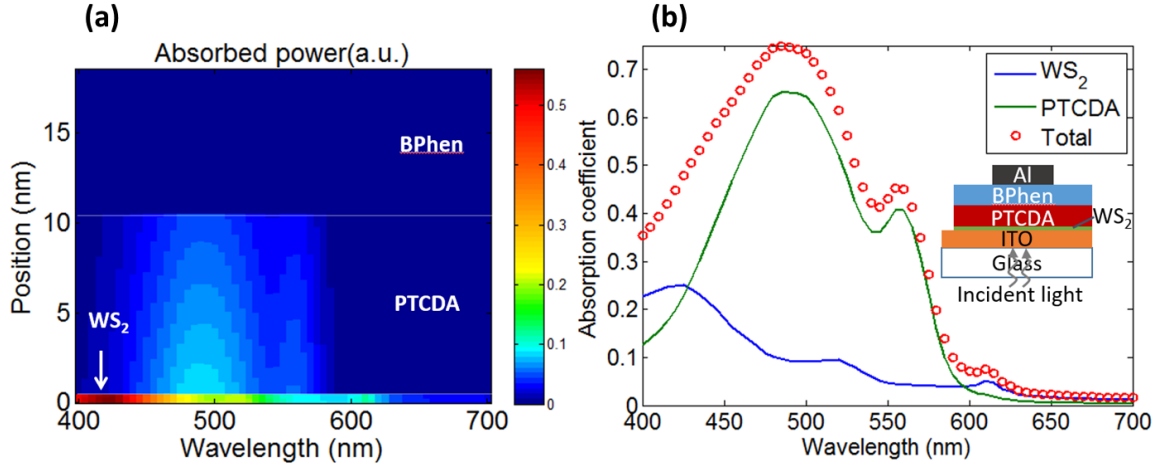


Figure 8.3: (a) Absorbed power distribution in the hybrid cell. The real and imaginary parts of the refractive index of each layer were measured by variable angle spectroscopic ellipsometry. (b) Absorption coefficients of  $\text{WS}_2$  (donor) and PTCDA (acceptor) layers in the cell, as well as their sum.

in Figure 8.3(b).

The  $EQE$  was obtained by focusing the excitation beam to a  $\sim 20 \mu\text{m}$  diameter spot on the device. The peak  $EQE = 1.8 \pm 0.2\%$  at  $\lambda = 430 \text{ nm}$ , as shown in Figure 8.4(a). The photoresponse peaks at  $\lambda = 430, 520, \text{ and } 625 \text{ nm}$  correspond to the absorption maxima of  $\text{WS}_2$ , while others match those of PTCDA. Figure 8.4(b) shows the  $IQE$  of the hybrid photodiodes calculated using  $\eta_{IQE} = \eta_{EQE}/\eta_A$ , where  $\eta_A$  is the absorption coefficient in Figure 8.3(b). The  $IQE$  is wavelength dependent; i.e., it is approximately 2% between  $\lambda = 450$  and  $600 \text{ nm}$  and increases to  $11 \pm 1.0\%$  at  $\lambda < 450 \text{ nm}$  and  $\lambda > 600 \text{ nm}$ .

Figure 8.5(a) shows the photocurrent vs applied electric field ( $F$ ) of a PTCDA photoconductor (see Experimental section) illuminated using a light-emitting diode with a peak emission at  $\lambda = 505 \text{ nm}$  and a  $30 \text{ nm}$  full width at half-maximum. The photocurrent is linearly dependent on  $F$  and is symmetric about  $F = 0$  as expected for a photoconductor with both anode and cathode ohmic contacts. A linear fit to the data yields the photoconductance,  $G_{pc}$ , of PTCDA that increases linearly with

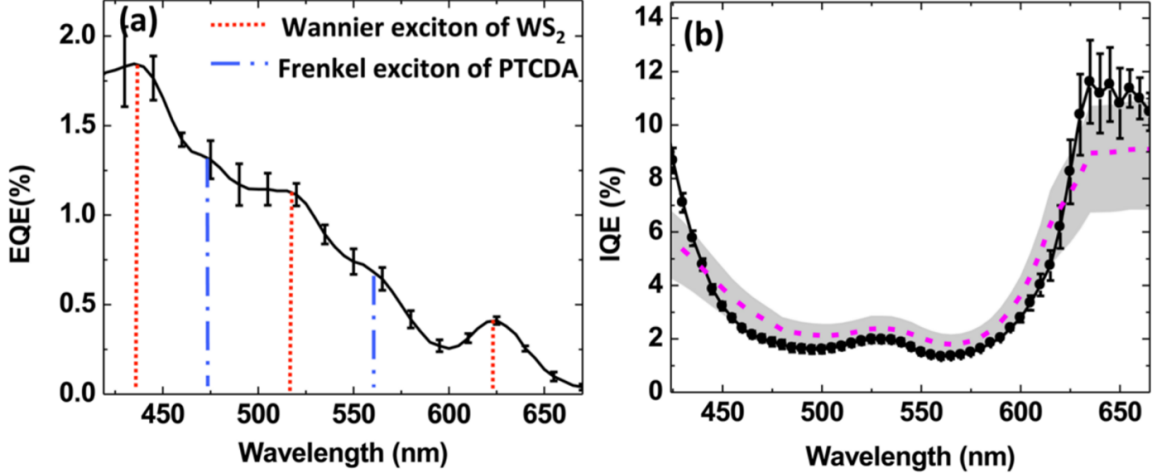


Figure 8.4: (a) External quantum efficiency ( $EQE$ ) of the PTCDA/WS<sub>2</sub> hybrid cell, indicating the positions of the various spectral features in the standalone layers. (b) Internal quantum efficiency ( $IQE$ ) of the hybrid cell. The dashed line in panel b is the fit to the data, and the 95% confidence interval is illustrated by the shaded region.

the illumination intensity, as shown in Figure 5a, inset. Figure 8.5(b) shows the  $EQE$  spectrum vs  $F$ . The quantum yield is zero at  $F = 0$  and increases with  $F$ , regardless of contact polarity.

## 8.5 Discussion

We define the PL quenching rate, i.e., the decrease of the total exciton population at layer  $j$  of the HJ to be  $\eta_{PL}^j = \frac{PL_0^j - PL_{HJ}^j}{PL_0^j} = \eta_{diff}^j \eta_Q^j$ , where  $PL_0^j$  is the PL intensity of a stand-alone layer  $j$ ,  $PL_{HJ}^j$  is the PL from layer  $j$  when employed in a PTCDA/WS<sub>2</sub> HJ,  $\eta_{diff}^j$  is the exciton diffusion efficiency to the heterointerface, and  $\eta_Q^j$  is the fraction of excitons that reach the interface and are quenched. That is,  $\eta_Q^j$  includes the efficiency of recombination at surface states (e.g., trap states) and HCTE dissociation and recombination at the heterointerface. Thus,  $\eta_Q^j = 100\%$  for an ideal quenching interface and  $\eta_Q^j = 0\%$  for an ideal blocking interface (i.e., a type-I heterojunction). As shown in Fig. 8.2(a), the quenching rate of WS<sub>2</sub> excitons is  $\eta_{PL}^{WS_2} = 80 \pm 10\%$ ,

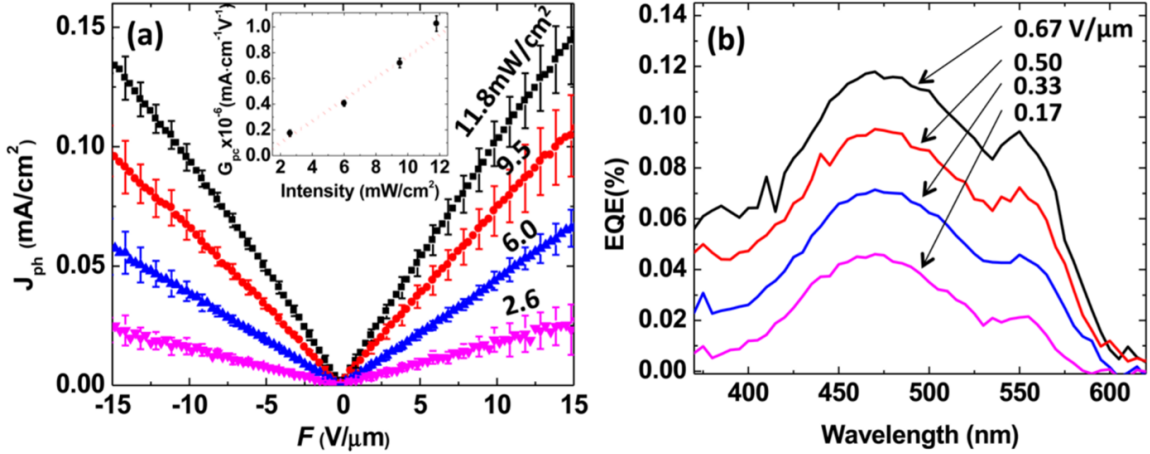


Figure 8.5: (a) Photocurrent density-electric field characteristics of a PTCDA photoconductor illuminated at  $\lambda = 505$  nm using different intensities. Inset: calculated photoconductance of the PTCDA photoconductor as a function of light intensity. (b)  $EQE$  spectrum of PTCDA at different applied electric fields.

which is approximately seven times greater than that of excitons generated in PTCDA where  $\eta_{PL}^{PTCDA} = 12 \pm 5\%$ . The exciton diffusion efficiency  $\eta_{diff}^j$  can be independently calculated as follows:<sup>[274,275]</sup> Assuming that layer  $j$  of thickness  $d$  has one quenching and one blocking interface corresponding to boundary conditions of  $n(x = 0) = 0$  and  $\left. \frac{dn}{dx} \right|_{x=d} = 0$ , respectively, we can solve the one-dimensional steady state diffusion equation:

$$L_d^2 \frac{d^2 n(x)}{dx^2} - n(x) + \tau G = 0 \quad (8.2)$$

Here,  $n(x)$  is the exciton density distribution,  $\tau$  is the exciton lifetime, and  $G = \frac{2\pi\epsilon_0 k_j n_j}{h} |E_j(\lambda, x)|^2$  is the time-averaged exciton generation rate<sup>[80]</sup> in layer  $j$ . Also,  $E$  is the optical electric field,  $h$  is Planck's constant,  $\epsilon_0$  is the permittivity of free space, and  $n_j$  and  $k_j$  are the real and imaginary parts of the refractive index of layer  $j$ . A PTCDA layer with  $d = 10$  nm and diffusion length,  $L_d = 10.4 \pm 1$  nm,<sup>[274]</sup> yields  $\eta_{diff}^{PTCDA} = 79 \pm 3\%$ . For the  $WS_2$  layer,  $\eta_{diff}^{WS_2} \approx 100\%$ . That is, since it is only a monolayer, all excitons generated within  $WS_2$  are in immediate contact with



the heterointerface, and hence there is no diffusion-related loss. Thus, we infer that  $\eta_Q^{PTCDA} = 15 \pm 6\%$  and  $\eta_Q^{WS_2} = 80 \pm 10\%$ , respectively. For the nonideal quenching interface, a higher quenching efficiency of  $WS_2$  excitons is due to the confinement of all the excitons within the 2D  $WS_2$  plane, as compared to that for PTCDA excitons which may escape from the interface without quenching. In addition, the interface quenching efficiency,  $\eta_Q^j$ , is affected by the charge transfer rate at the type-II HJ, which has been described by nonadiabatic Marcus theory.<sup>[116]</sup> As inferred from the emission energy in Figure 8.2(a), an exciton in  $WS_2$  has a higher energy than in PTCDA and thus a larger Gibbs free energy change and smaller reorganization energy when transferring to the same HCTE state. Assuming electronic coupling matrix elements to be approximately equal for the electron transfers in this donor-acceptor pair, the charge transfer rate is also increased, leading to a higher quenching efficiency for  $WS_2$ .

As shown in Figure 8.5, PTCDA photoconductivity contributes to the photocurrent of the device when applying bias. The direct carrier generation from excitons in the organics may come from, for example, thermally induced exciton dissociation,<sup>[58]</sup> exciton-assisted polaron detrapping,<sup>[276]</sup> and so forth. However, this contribution vanishes at  $F = 0$ . Therefore, we conclude that the *EQE* spectrum of the PTCDA/ $WS_2$  HJ device shown in Figure 8.4(a) provides unambiguous evidence that excitons contribute to the photocurrent through HCTE dissociation. The photoresponse at 485 and 560 nm corresponds to the dissociation of PTCDA excitons at heterointerface, while the other spectral features are due to dissociation of Wannier states generated in the TMDC.

The *IQE* of the HJ photodiode is

$$\eta_{IQE}(\lambda) = [a(\lambda)\eta_{diff}^{PTCDA}\eta_Q^{PTCDA} + (1 - a(\lambda))\eta_{diff}^{WS_2}\eta_Q^{WS_2}]\eta_{diss}\eta_{CC} \quad (8.3)$$

where  $a(\lambda)$  is the percentage of excitons generated in the PTCDA which is calculated

from the optical profile in Fig. 8.3(a). Also,  $\eta_{diff}$  is the exciton dissociation efficiency at the HJ interface, and  $\eta_{CC}$  is the charge collection efficiency at the contacts. The wavelength dependence of  $IQE$  in Fig. 8.4(b) follows the absorbed power distribution as a function of wavelength in Figure 8.3(a). For wavelengths  $\lambda > 600$  nm and  $\lambda < 450$  nm, a majority of excitons are generated within the  $WS_2$  monolayer, minimizing their recombination loss and therefore resulting in a higher  $IQE$ . This is in contrast to illumination at  $450 < \lambda < 600$  nm, where excitons are primarily generated within the PTCDA bulk.

Using the calculated quenching efficiency of  $\eta_Q^{PTCDA} = 15 \pm 6\%$  and  $\eta_Q^{WS_2} = 80 \pm 10\%$ , we fit the  $IQE$  data as shown in Fig. 8.4(b), dashed line, to obtain  $\eta_{diss}\eta_{CC} = 10.6 \pm 2.2\%$ . The dissociation efficiency  $\eta_{diss}\eta_{CC}$  is lower than the value observed in organic/organic HJs<sup>[66]</sup> or organic/bulk inorganic HJs.<sup>[180]</sup> This somewhat diminished value may be due to TMDC surface defects from sulfur vacancies, contaminants, or grain boundaries,<sup>[277,278]</sup> which all may lead to HCTE recombination<sup>[279]</sup> and poor charge extraction.

## CHAPTER IX

### Outlook

#### 9.1 Prospects for Organic Photovoltaics

In part I, we explored the charge transfer properties and energy loss mechanisms vs. the morphological and molecular structures of organic donor-acceptor HJs. The studies extended from fullerene to NFA-based HJs to assist in our understanding of the photophysical origins of the recent increases of OPV efficiency. Indeed, the state-of-the-art power conversion efficiency exceeding 15% presents a very bright future for OPVs. However, to also realize long term stability and scalable low-cost fabrication of the devices, many compromises in the choice of materials, HJ morphologies, processing, and encapsulation techniques have to be made. To date, no OPV has reached a market-viable balance in every aspect of device performance. Furthermore, even after OPVs reach market-entry-level properties, challenges remain in gaining enough market share to compete with mature silicon and other thin film PV techniques.

One of the lessons we have learned from OLED commercialization is that the initial curiosities of customers may come from a “premium”-like product feature that creates new customer expectations such as a decorative appearance, and new functionality, even though such a product may have a higher price and lower reliability than conventional products. Future development of OPVs should therefore focus on the unique characteristics of organic materials, such as the intense and narrow-band

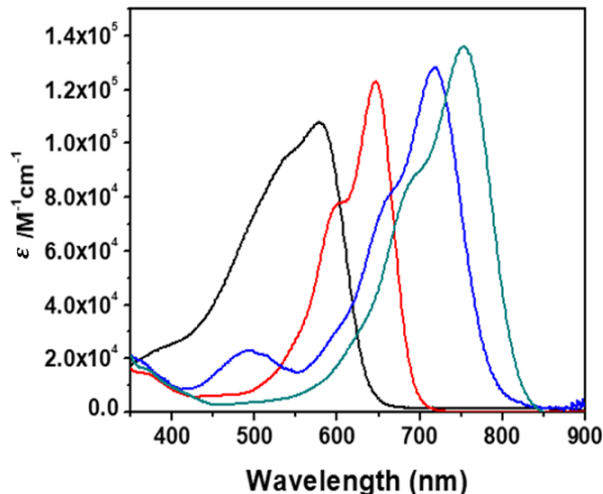


Figure 9.1: The narrow absorption bands of a-d-a-type NFAs at different wavelength. Figure courtesy of Yongxi Li

absorption, lightweight form and flexibility, and improve the performance of semi-transparent OPVs for building-integrated, car-integrated, and clothing-integrated power generation applications. Current acceptor-donor-acceptor(a-d-a)-type NFAs, as shown in Fig. 9.1, are candidates for these purposes. The big energy gap between the first ( $S_1$ ) and second ( $S_2$ ) excited state manifolds gives rise to transparency in the visible. The energy of narrow absorption bands can be varied from visible to near infrared by either changing the conjugation length or the electron donating and withdrawing groups of the molecules.

Organic HJs employing NFAs, therefore, exhibit potential for future OPV applications. To further understand this new class of organic HJs from a photophysical perspective, we highlight a few open questions worthy of further study:

*Open-circuit voltage of ternary bulk HJs vs. blend ratio*

Due to the tunability of the NFA absorption wavelength, ternary bulk HJ comprised of either one donor and two acceptors, or two donors and one acceptor has been applied in OPVs. The extra donor or acceptor component increases the solar

spectral coverage compared to binary mixtures. As a result, power conversion efficiencies of  $\sim 13\%$  from ternary OPVs have been reported.<sup>[82,280]</sup> Ternary OPVs have been shown to have a *nonlinear* change of open-circuit voltage ( $V_{OC}$ ) as a function of the blend ratio between three constituents.<sup>[281–284]</sup> That is, the short-circuit current ( $J_{SC}$ ) increases with the ratio of the third component while the  $V_{OC}$  remains relatively unchanged. The mechanisms behind has not been conclusively established. One intriguing model claims that the formation of a “molecular alloy” by mixing the two acceptors in the active region gives rise to a nonlinear shift of the CT state energy.<sup>[285]</sup> In contrast to alloys comprising atomic constituents in inorganic semiconductors, the chemical bonds between neighbors in organic materials are replaced by far weaker van der Waals bonds. Indeed, the formation of a molecular alloy has been proposed in several instances, e.g. charge transfer complexes TTF-7,7,8,8-tetracyanoquinodimethane (TCNQ).<sup>[286–288]</sup> Solid evidence has been shown that the electronic structure of the charge transfer complex is distinguished from that of a simple blend. However, no such results have been seen in ternary HJs. The mechanisms to explain the change of  $V_{OC}$  in ternary OPVs have to be more fully studied.

*The role of singlet and triplet energy splitting in NFAs*

The small electron and hole wavefunction overlap of CT excitons at the HJ significantly reduces the exchange energy splitting  $2J$  (c.f. Eq. 1.12) between the singlet and triplet CT states, making them nearly degenerate. Fast intersystem crossing between them facilitates a spin-conservative back transfer from the CT state to  $T_1$  of acceptor or donor molecules, where non-radiative recombination loss from  $T_1$  follows, as shown in Fig. 9.2(a). This transfer is more significant in NFA-based HJs, where  $\Delta E_{CT} = E_{S_1} - E_{CT}$  is small, and hence the energy difference between the CT and  $T_1$  states is potentially large. Therefore, design of a thermally activated delayed fluorescence (TADF)-like NFA that minimizes the singlet-to-triplet energy difference

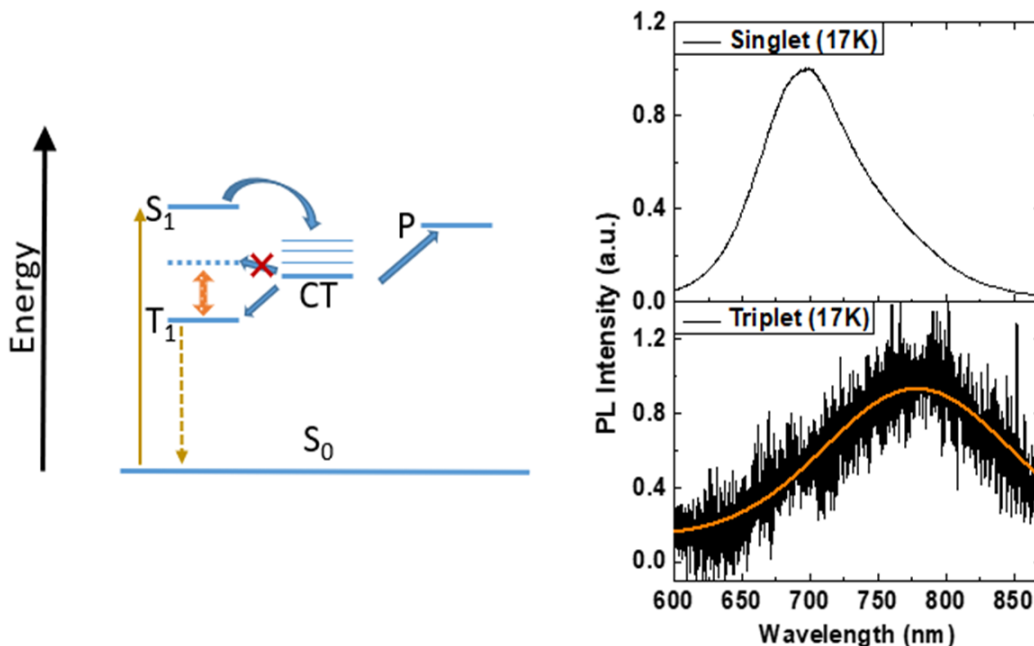


Figure 9.2: (a) Schematic of the transfer process from the singlet ( $S_1$ ) state of acceptor molecules to the charge separated state (P) via the charge transfer state (CT). The energy level of the triplet state ( $T_1$ ) determines the back transfer rate from CT to  $T_1$ , i.e. one of the non-radiative recombination loss pathways at the HJ (b) Low temperature (17K) PL of the singlet and triplet states of IT-IC diluted in PMMA matrix at a concentration of 0.07%. The triplet spectrum is fit by a Gaussian function to extract the peak position

is necessary for decreasing the transfer probability from CT to  $T_1$ .

A PL measurement of singlet and triplet excitons of an a-d-a-type NFA, IT-IC, is shown in Fig. 9.2(b). The spectra of the sample were taken at 17 K with an optical chopper coupled to the spectrometer. The timing of the chopper opening was coupled to a the pulsed diode laser at  $\lambda = 405\text{nm}$  using a delay generator. The singlet emission was measured at zero delay, while the triplet emission was measured at  $20 \pm 10$  ms after the excitation. The singlet and triplet energy difference of IT-IC is only  $0.20 \pm 0.02$  eV, which is much smaller than for common organic molecules. Further studies of the transfer rate between the singlet and triplet states, and the value of  $2J$  as a function of molecular structure are yet to be done.

### *Stability of HJs using NFAs*

While HJs employing NFAs have presented high power conversion efficiencies, their stability are as yet not thoroughly investigated. Since a high operational lifetime has been reported in all-carbon-based DBP/C<sub>70</sub> HJs,<sup>[289]</sup> questions remain as to whether the photochemical stability of NFAs, comprising relatively weak bonded heteroatoms and highly electron deficient moieties, is acceptable for long-term device stability. Additionally, the thermal stability of solution-processed blended HJs comprising NFAs has to be studied as another important figure of merit. Morphological changes as a function of temperature and aging time should be systematically measured using TEM and X-ray diffraction techniques, and interface sensitive spectroscopic tools.

## **9.2 Future Work on 2D Organic/Transition Metal Dichalcogenide Heterojunctions**

The field of organic/TMDC hybrid HJs is still in its infancy with much left to learn. Still, there are enormous gaps between proof-of-concept demonstrations, repeatable characterizations, and widespread applications. For future work, we propose that the following issues to be addressed:

1. Wafer-scale high-quality growth of monolayer TMDCs. Most experiments are still based on mechanically exfoliated 2D materials. This is due to their repeatable qualities and relatively low defect densities compared to CVD-grown samples. The existing large area CVD techniques for 2D TMDC growth suffer from batch-to-batch and vendor-to-vendor quality variations. Figure 9.3 shows examples of PL spectra of mechanically exfoliated and CVD-grown 2D WS<sub>2</sub> samples. A significant density of surface defects (e.g. sulfur vacancies) in the CVD sample gives rise to a large population of trions that emit at  $\lambda = \sim 660\text{nm}$ . Also note that the PL FWHM from CVD samples is larger than that from the mechanically exfoliated sample, suggesting

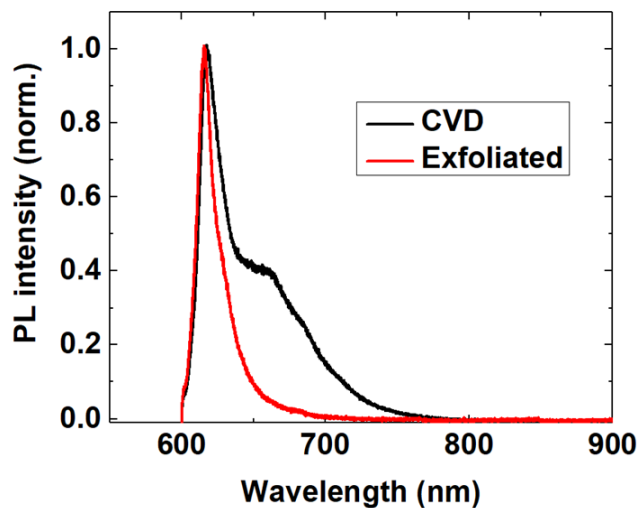


Figure 9.3: Photoluminescence of mechanically exfoliated and unsuccessful CVD-grown 2D WS<sub>2</sub> films

a larger inhomogeneous broadening due to the structural disorder. Improving the deposition techniques and/or developing reliable surface passivation methods are, therefore, essential for avoiding undesirable spectral features, misinterpretation of electronic properties, and for achieving repeatable device performance.

2. Reliable and nondestructive transfer techniques. A successful assembly of multilayer TMDC heterostructures also relies on the quality of monolayer transfer after film growth. Figure 9.4(a) shows extreme cases of unsuccessful large-area monolayer MoS<sub>2</sub> transfer. The PL intensity of the 2D MoS<sub>2</sub> is drastically decreased after wet-transferring via KOH(1M/L) etching at 60°C for 1.5 hours. The etching process in the highly active KOH solvent is one of the factors damaging the MoS<sub>2</sub> film. Finding a nondestructive etchant to replace KOH in wet-transfer, or application of dry-transfer is necessary for improving film quality. Figure 9.4(b) demonstrates another common problem. Due to the non-uniformity of PMMA/PDMS stamps used in transfer and the uneven pressure applied when attaching the 2D sample to the target substrate, the film is ripped. Current setups employing piezoelectric translation stages for precise positioning and pressure control lead to improved transfer quality than shown,



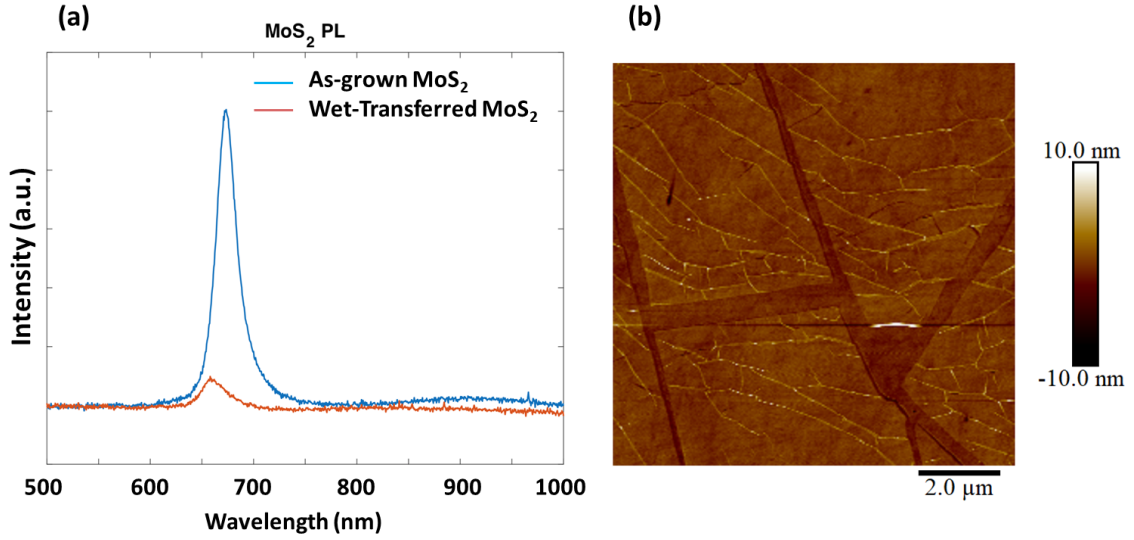


Figure 9.4: Unsuccessful examples of 2D TMDC transfer: (a) A drastic decrease of PL intensity of MoS<sub>2</sub> before and after the wet-transfer, indicating the damage of the film. (b) The MoS<sub>2</sub> film is broken into pieces, due to the uneven pressure applied during the transfer.

yet the quality is still far from ideal.

3. The dynamics of the HCTE and exciton dissociation processes. Recent observation of 2D HCTE emission at WS<sub>2</sub>/tetracene HJ<sup>[187]</sup> offers a direct spectroscopic probe to track the dynamics of the HCTE. Questions such as the impact of interface traps on the dissociation yield of HCTE, the diffusivity of the HCTE along the HJ interface, resonant energy transfer between bulk excitons and the HCTE, etc. can, therefore, be systematically studied, deepening our understanding of the photocurrent generation process at 2D organic/TMDC HJ. The tunable thickness of organic layers in hybrid quantum well systems provides the potential of systematically tuning the optoelectronic properties of the HCTE, including the binding energy and recombination quantum yield. This further assists the exploration of hybrid exciton dynamics.

4. Device applications. Device performance such as photocurrent generation and electroluminescence quantum yield of hybrid organic/TMDC devices, as seen in

Chapter VII, are still unacceptably low for applications. Future improvements via refining the 2D TMDC growth and transfer techniques, and using different material combinations and organic layer thicknesses, etc, are necessary. In addition, 2D hybrid HJs need to find their own unconventional applications that are inaccessible to bulk semiconductors. The following are two possible directions:

### *Hybrid superlattices*

The OI superlattice comprising van der Waals-bonded 2D TMDCs and organic semiconductors offers opportunities beyond the reach of existing materials. The significant contrast between the dielectric constants of organic and inorganic materials offers a wide range of tunability for capacitance, refractive index, charge screening, charge mobility, and thermal conductivity of the system. Typical bottom-up approaches of fabricating superlattices require tedious layer-by-layer deposition or stacking that have a limited fabrication yield and an increasing difficulty for high-order superlattices.<sup>[290,291]</sup> However, 2D TMDC/organic superlattices can also be fabricated by the top-down electrochemical molecular intercalation,<sup>[178,292]</sup> where organic cations or polar molecules in the solvent can be inserted uniformly between the TMDC layers with the assistance of electrochemical potentials provided by the electrodes.

Early demonstrations of TiS<sub>2</sub>/organic<sup>[178]</sup> and black phosphor/organic<sup>[292]</sup> superlattices have exhibited enhanced electron mobility and reduced thermal conductivity as the dielectric constant contrast between two contacting materials increases, leading to a high thermoelectric figure of merit:

$$ZT = \frac{\sigma S^2 T}{\kappa}, \quad (9.1)$$

where  $\sigma$  is the electric conductivity,  $T$  is the temperature,  $\kappa$  is the thermal conductivity, and  $S$  is the Seebeck coefficient accounting for the magnitude of an induced thermoelectric voltage in response to a temperature difference across the material.

The organic/TMDC superlattice therefore provides a new class of thermoelectric material systems that enables flexible cooling and power generation electronics.

*Photon-Mediated Hybridization of Excitons in Organics and TMDC*

Previous research has demonstrated the strong coupling between degenerated Wannier-Mott and Frenkel excitons and the photon mode in a microcavity comprising spatially separated ZnO and 3,4,7,8-naphthalene tetracarboxylic dianhydride (NTCDA) layers.<sup>[164]</sup> Such an intriguing scheme of hybridizing the electronic states of organic and inorganic semiconductors enables efficient energy transfer between two distinct materials. Selective electrical excitation of the inorganic material in the hybridized system bypasses the limitations of low-mobility and triplet formation in organics, and may eventually lead to electrically pumped organic lasing. Indeed, a promising demonstration of a highly efficient hybrid polariton light emitting device has been reported in GaAs and a J-aggregate cyanine dye.<sup>[293]</sup> Such a scheme can be used in an organic/TMDC superlattice, the strong oscillator strength of which facilitates a light-matter interactions and resonant energy transfer.

Due to the significant contribution of hybridized Frenkel-Wannier-Mott excitons, polariton states present pronounced nonlinear optical properties, such as large third-order susceptibilities. Such properties can be systematically tuned by changing the composition of the hybridized state via shifting the energy of the Wannier-Mott exciton. The hybrid system, such as J-aggregate organic dye 5,5',6,6'- tetrachloro-1,1'-diethyl-3,3'- di(4-sulfobutyl)- benzimidazolocarbo-cyanine (TDBC)/WS<sub>2</sub>,<sup>[294]</sup> exhibits tunability where the absorption peak of the TMDC can be shifted by  $\sim 100$ meV when a lateral bias of 200 to -200 V is applied.

To summarize, the superior optical properties of organic semiconductors combined with the desirable electrical properties of TMDCs in hybrid 2D organic/TMDC heterostructures have immense potential for future applications that are difficult to

achieve using conventional semiconductors. Scientific understandings and technological improvements are, however, still required for this material system to address practical applications.

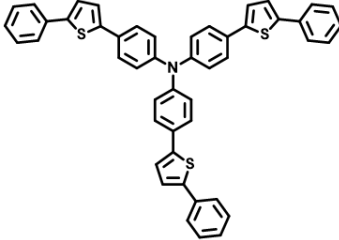
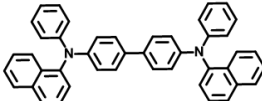
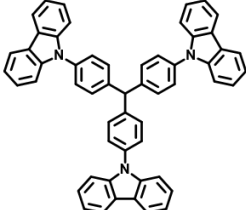
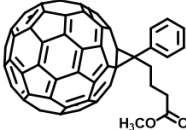
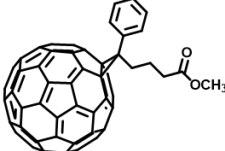

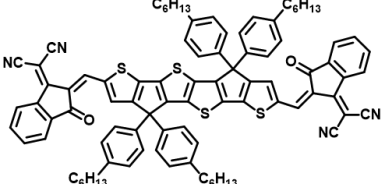
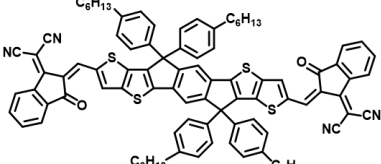
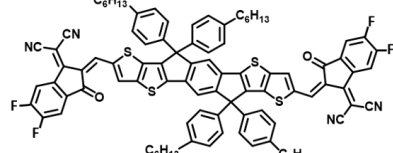
## APPENDICES

## APPENDIX A

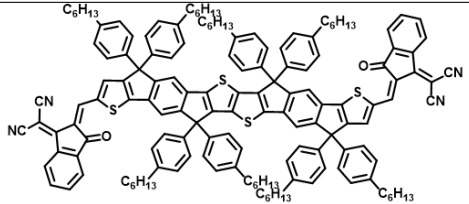
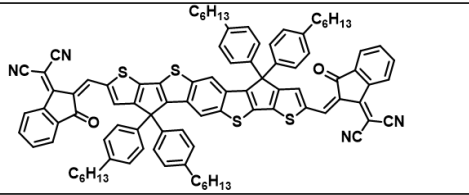
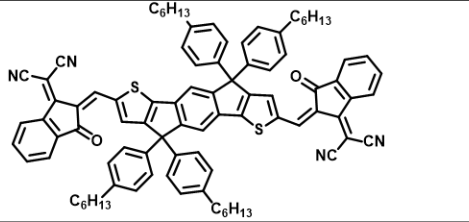
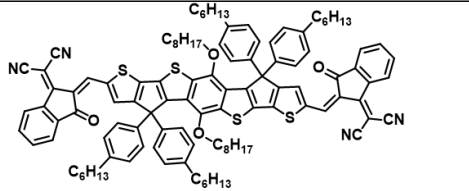
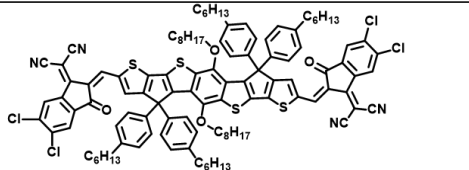
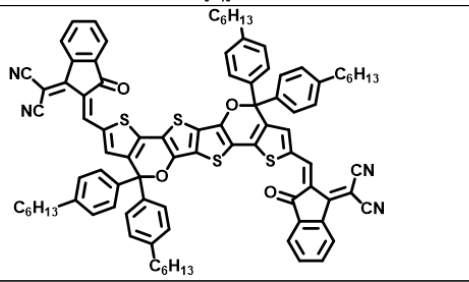
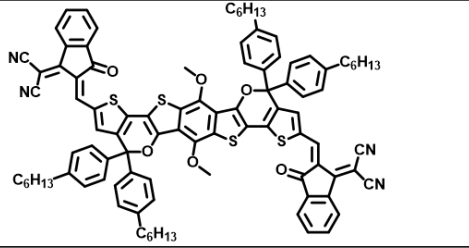
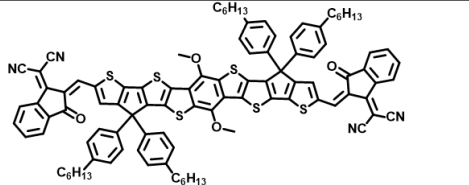
Chemical structures and short names of molecules  
used in Chapter IV.

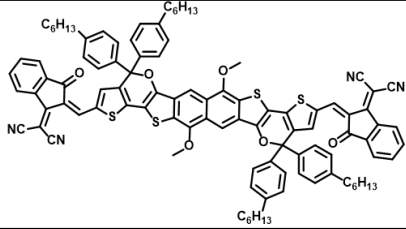
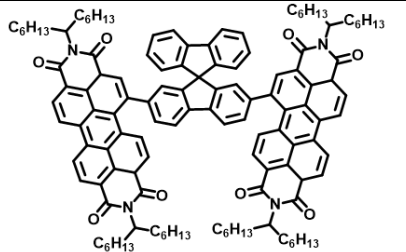
Table A.1: Chemical structures and short names of molecules used in Chapter IV.

Chemical Short Name	Chemical Structure
PBDBT	
J61	
P3HT	
PCDTBT	
F8	
F8BT	
F8T2	
CBP	

TPTPA	
NPD	
TCTA	
PC <sub>71</sub> BM	
PC <sub>61</sub> BM	
PTCBI	
DT-IC	
IT-IC	
IT-IC-4F	



<p style="text-align: center;"><b>IDTIDT-IC</b></p>	
<p style="text-align: center;"><b>BDT-IC</b></p>	
<p style="text-align: center;"><b>IDT-IC</b></p>	
<p style="text-align: center;"><b>BT-IC</b></p>	
<p style="text-align: center;"><b>BT-CIC</b></p>	
<p style="text-align: center;"><b>TPT-IC</b></p>	
<p style="text-align: center;"><b>BDP-IC</b></p>	
<p style="text-align: center;"><b>BDCP-IC</b></p>	

<p style="text-align: center;"><b>BNP-IC</b></p>	 <p>The structure of BNP-IC is a complex, multi-ring system. It features a central core with several fused and linked rings, including thiophene, furan, and benzene rings. The structure is highly substituted with various groups: multiple phenyl rings, some of which are further substituted with hexyl chains (C<sub>6</sub>H<sub>13</sub>), cyano groups (CN), and methoxy groups (OCH<sub>3</sub>). The overall structure is symmetrical and appears to be a macrocyclic or highly branched molecule.</p>
<p style="text-align: center;"><b>SF-PDI2</b></p>	 <p>The structure of SF-PDI2 is a large, complex molecule. It consists of a central core with multiple fused and linked rings, including benzene and pyridine rings. The structure is highly substituted with various groups: multiple phenyl rings, some of which are further substituted with hexyl chains (C<sub>6</sub>H<sub>13</sub>), cyano groups (CN), and methoxy groups (OCH<sub>3</sub>). The overall structure is symmetrical and appears to be a macrocyclic or highly branched molecule.</p>

## APPENDIX B

# Polarizability of Fullerene and Nonfullerene Acceptors

Table B.1: The static polarizability (Unit: nm<sup>3</sup>) tensor of fullerene and nonfullerene acceptors calculated by density functional theory. The polarizabilities along each direction are listed:

$\alpha^*$	$\alpha_{xx}$	$\alpha_{yx}$	$\alpha_{yy}$	$\alpha_{zx}$	$\alpha_{zy}$	$\alpha_{zz}$
C <sub>60</sub>	0.102	0.000	0.102	0.000	0.000	0.102
C <sub>70</sub>	0.141	0.000	0.127	0.000	0.000	0.127
PC <sub>71</sub> BM	0.182	-0.006	0.145	-0.004	-0.002	0.141
PTCBI	0.246	0.003	0.081	0.000	0.000	0.019
IDT-IC	0.394	0.012	0.165	-0.006	0.002	0.084
DT-IC	0.530	-0.031	0.167	0.000	0.000	0.087
IT-IC	0.505	0.001	0.172	0.000	0.000	0.089
IT-IC-4F	0.517	-0.014	0.174	0.000	0.000	0.090
BDT-IC	0.519	0.031	0.175	0.000	0.000	0.089
BT-IC	0.523	0.031	0.183	0.000	0.003	0.094
BT-CIC	0.579	-0.043	0.200	-0.002	0.002	0.096
IDTIDT-IC	0.660	-0.022	0.236	0.000	0.000	0.151
BNP-IC	0.563	0.036	0.190	-0.002	0.005	0.097
BDCP-IC	0.616	-0.034	0.197	0.005	0.001	0.098
BDP-IC	0.533	-0.053	0.185	0.003	0.001	0.095
TPT-IC	0.499	0.043	0.167	-0.004	0.003	0.095

$$^* \alpha = \begin{pmatrix} \alpha_{xx} & \alpha_{xy} & \alpha_{xz} \\ \alpha_{yx} & \alpha_{yy} & \alpha_{yz} \\ \alpha_{zx} & \alpha_{zy} & \alpha_{zz} \end{pmatrix}$$

## BIBLIOGRAPHY

- [1] London, F. The general theory of molecular forces. *Transactions of the Faraday Society* **33**, 8b–26 (1937).
- [2] Kittel, C. *et al.* *Introduction to solid state physics*, vol. 8 (Wiley New York, 1976).
- [3] Rols, S. *et al.* Unravelling low lying phonons and vibrations of carbon nanostructures: The contribution of inelastic and quasi-elastic neutron scattering. *The European Physical Journal Special Topics* **213**, 77–102 (2012).
- [4] Köhler, A. & Bäessler, H. *Electronic processes in organic semiconductors: An introduction* (John Wiley & Sons, 2015).
- [5] Sholl, D. & Steckel, J. A. *Density functional theory: a practical introduction* (John Wiley & Sons, 2011).
- [6] Mueller, M. P. *Fundamentals of quantum chemistry: molecular spectroscopy and modern electronic structure computations* (Springer Science & Business Media, 2007).
- [7] Bulović, V., Burrows, P., Forrest, S., Cronin, J. & Thompson, M. Study of localized and extended excitons in 3, 4, 9, 10-perylenetetracarboxylic dianhydride (ptcda) i. spectroscopic properties of thin films and solutions. *Chemical Physics* **210**, 1–12 (1996).
- [8] Kasha, M. Characterization of electronic transitions in complex molecules. *Discussions of the Faraday society* **9**, 14–19 (1950).
- [9] Fermi, E. *Nuclear physics: a course given by Enrico Fermi at the University of Chicago* (University of Chicago Press, 1950).
- [10] Bube, R. *Electronic properties of crystalline solids: an introduction to fundamentals* (Elsevier, 2012).
- [11] Bixon, M. & Jortner, J. Electron transfer—from isolated molecules to biomolecules. *Advances in Chemical Physics: Electron Transfer—from Isolated Molecules to Biomolecules. Part 1* **106**, 35–202 (1999).
- [12] Pope, M. & Swenberg, C. E. *Electronic processes in organic crystals and polymers*, vol. 2 (Oxford University Press New York, 1999).
- [13] Atkins, P. W. & Friedman, R. S. *Molecular quantum mechanics* (Oxford university press, 2011).
- [14] Baldo, M. A. *et al.* Highly efficient phosphorescent emission from organic electroluminescent devices. *Nature* **395**, 151 (1998).
- [15] Dexter, D. L. A theory of sensitized luminescence in solids. *The Journal of Chemical Physics* **21**, 836–850 (1953).

- [16] Förster, T. 10th spiers memorial lecture. transfer mechanisms of electronic excitation. *Discussions of the Faraday Society* **27**, 7–17 (1959).
- [17] Andrews, D. L. & Juzeliūnas, G. Intermolecular energy transfer: Retardation effects. *The Journal of chemical physics* **96**, 6606–6612 (1992).
- [18] Salzman, R. F. *et al.* The effects of copper phthalocyanine purity on organic solar cell performance. *Organic Electronics* **6**, 242–246 (2005).
- [19] Curtin, I. J., Blaylock, D. W. & Holmes, R. J. Role of impurities in determining the exciton diffusion length in organic semiconductors. *Applied Physics Letters* **108**, 163301 (2016).
- [20] Xihuang, Z. *et al.* Separation of  $c_{60}$  and  $c_{70}$  fullerenes in gram quantities by fractional crystallization. *Carbon* **32**, 935–937 (1994).
- [21] Cazes, J. *Encyclopedia of chromatography* (CRC Press, 2009).
- [22] Brakke, M. K. Density gradient centrifugation: a new separation technique. *Journal of the American Chemical Society* **73**, 1847–1848 (1951).
- [23] Forrest, S. R. Ultrathin organic films grown by organic molecular beam deposition and related techniques. *Chemical reviews* **97**, 1793–1896 (1997).
- [24] Smith, D. L. *Thin-film deposition: principles and practice*, vol. 108 (McGraw-hill New York etc, 1995).
- [25] Zhang, Y. Excited state interactions and management in organic light emitting diodes. (2014).
- [26] Lunt, R. R., Benziger, J. B. & Forrest, S. R. Growth of an ordered crystalline organic heterojunction. *Advanced Materials* **19**, 4229–4233 (2007).
- [27] Baldo, M. *et al.* Organic vapor phase deposition. *Advanced Materials* **10**, 1505–1514 (1998).
- [28] Lunt, R. R., Lassiter, B. E., Benziger, J. B. & Forrest, S. R. Organic vapor phase deposition for the growth of large area organic electronic devices. *Applied Physics Letters* **95**, 320 (2009).
- [29] Shtein, M., Gossenberger, H. F., Benziger, J. B. & Forrest, S. R. Material transport regimes and mechanisms for growth of molecular organic thin films using low-pressure organic vapor phase deposition. *Journal of Applied Physics* **89**, 1470–1476 (2001).
- [30] McGraw, G. J., Peters, D. L. & Forrest, S. R. Organic vapor jet printing at micrometer resolution using microfluidic nozzle arrays. *Applied Physics Letters* **98**, 2 (2011).

- [31] Arnold, M. S., McGraw, G. J., Forrest, S. R. & Lunt, R. R. Direct vapor jet printing of three color segment organic light emitting devices for white light illumination. *Applied Physics Letters* **92**, 29 (2008).
- [32] Hebner, T., Wu, C., Marcy, D., Lu, M. & Sturm, J. Ink-jet printing of doped polymers for organic light emitting devices. *Applied Physics Letters* **72**, 519–521 (1998).
- [33] Krebs, F. C. Fabrication and processing of polymer solar cells: a review of printing and coating techniques. *Solar energy materials and solar cells* **93**, 394–412 (2009).
- [34] So, F., Forrest, S., Shi, Y. & Steier, W. Quasi-epitaxial growth of organic multiple quantum well structures by organic molecular beam deposition. *Applied physics letters* **56**, 674–676 (1990).
- [35] Xiao, X., Zimmerman, J. D., Lassiter, B. E., Bergemann, K. J. & Forrest, S. R. A hybrid planar-mixed tetraphenyldibenzoperiflanthene/ $c_{70}$  photovoltaic cell. *Applied Physics Letters* **102**, 34 (2013).
- [36] Yang, F., Shtein, M. & Forrest, S. R. Controlled growth of a molecular bulk heterojunction photovoltaic cell. *Nature materials* **4**, 37 (2005).
- [37] Esaki, L. New phenomenon in narrow germanium p-n junctions. *Physical review* **109**, 603 (1958).
- [38] Giebink, N. C., Wiederrecht, G. P., Wasielewski, M. R. & Forrest, S. R. Ideal diode equation for organic heterojunctions. i. derivation and application. *Physical Review B* **82**, 155305 (2010).
- [39] Kirchartz, T., Mattheis, J. & Rau, U. Detailed balance theory of excitonic and bulk heterojunction solar cells. *Physical Review B* **78**, 235320 (2008).
- [40] Sze, S. M. & Ng, K. K. *Physics of semiconductor devices* (John wiley & sons, 2006).
- [41] Loi, M. A. *et al.* Charge transfer excitons in bulk heterojunctions of a polyfluorene copolymer and a fullerene derivative. *Advanced Functional Materials* **17**, 2111–2116 (2007).
- [42] Bernardo, B. *et al.* Delocalization and dielectric screening of charge transfer states in organic photovoltaic cells. *Nature communications* **5**, 3245 (2014).
- [43] Giebink, N. C., Lassiter, B. E., Wiederrecht, G. P., Wasielewski, M. R. & Forrest, S. R. Ideal diode equation for organic heterojunctions. ii. the role of polaron pair recombination. *Physical Review B* **82**, 155306 (2010).
- [44] Grancini, G. *et al.* Transient absorption imaging of p3ht: Pcbm photovoltaic blend: Evidence for interfacial charge transfer state. *The Journal of Physical Chemistry Letters* **2**, 1099–1105 (2011).



- [45] Arndt, A. P. *et al.* Time-resolved charge-transfer state emission in organic solar cells: Temperature and blend composition dependences of interfacial traps. *The Journal of Physical Chemistry C* **119**, 13516–13523 (2015).
- [46] Weiser, G. Absorption and electroabsorption on amorphous films of polyvinyl-carbazole and trinitrofluorenone. *physica status solidi (a)* **18**, 347–359 (1973).
- [47] Jailaubekov, A. E. *et al.* Hot charge-transfer excitons set the time limit for charge separation at donor/acceptor interfaces in organic photovoltaics. *Nature materials* **12**, 66 (2013).
- [48] Zhu, X.-Y., Yang, Q. & Muntwiler, M. Charge-transfer excitons at organic semiconductor surfaces and interfaces. *Accounts of chemical research* **42**, 1779–1787 (2009).
- [49] Wilcox, D. E. *et al.* Ultrafast charge-transfer dynamics at the boron subphthalocyanine chloride/ $c_{60}$  heterojunction: comparison between experiment and theory. *The journal of physical chemistry letters* **6**, 569–575 (2015).
- [50] Shen, X., Han, G., Fan, D., Xie, Y. & Yi, Y. Hot charge-transfer states determine exciton dissociation in the dtdctb/ $c_{60}$  complex for organic solar cells: A theoretical insight. *The Journal of Physical Chemistry C* **119**, 11320–11326 (2015).
- [51] Onsager, L. Initial recombination of ions. *Physical Review* **54**, 554 (1938).
- [52] Bäessler, H. & Köhler, A. “hot or cold”: how do charge transfer states at the donor–acceptor interface of an organic solar cell dissociate? *Physical Chemistry Chemical Physics* **17**, 28451–28462 (2015).
- [53] Braun, C. L. Electric field assisted dissociation of charge transfer states as a mechanism of photocarrier production. *The Journal of chemical physics* **80**, 4157–4161 (1984).
- [54] Goliber, T. & Perlstein, J. Analysis of photogeneration in a doped polymer system in terms of a kinetic model for electric-field-assisted dissociation of charge-transfer states. *The Journal of chemical physics* **80**, 4162–4167 (1984).
- [55] Peumans, P. & Forrest, S. R. Separation of geminate charge-pairs at donor–acceptor interfaces in disordered solids. *Chemical Physics Letters* **398**, 27–31 (2004).
- [56] Barth, S., Bäessler, H., Scherf, U. & Müllen, K. Photoconduction in thin films of a ladder-type poly-para-phenylene. *Chemical physics letters* **288**, 147–154 (1998).
- [57] Christ, N. *et al.* Intensity dependent but temperature independent charge carrier generation in organic photodiodes and solar cells. *Organic Electronics* **14**, 973–978 (2013).

- [58] Arkhipov, V., Emelianova, E. & Bäessler, H. Hot exciton dissociation in a conjugated polymer. *Physical review letters* **82**, 1321 (1999).
- [59] Basko, D. & Conwell, E. Hot exciton dissociation in conjugated polymers. *Physical Review B* **66**, 155210 (2002).
- [60] Vandewal, K. *et al.* Efficient charge generation by relaxed charge-transfer states at organic interfaces. *Nature materials* **13**, 63 (2014).
- [61] Arkhipov, V., Heremans, P. & Bäessler, H. Why is exciton dissociation so efficient at the interface between a conjugated polymer and an electron acceptor? *Applied Physics Letters* **82**, 4605–4607 (2003).
- [62] Schwarz, C. *et al.* Role of the effective mass and interfacial dipoles on exciton dissociation in organic donor-acceptor solar cells. *Physical Review B* **87**, 155205 (2013).
- [63] Wiemer, M., Nenashev, A., Jansson, F. & Baranovskii, S. On the efficiency of exciton dissociation at the interface between a conjugated polymer and an electron acceptor. *Applied Physics Letters* **99**, 127 (2011).
- [64] Gregg, B. A. Entropy of charge separation in organic photovoltaic cells: The benefit of higher dimensionality. *The Journal of Physical Chemistry Letters* **2**, 3013–3015 (2011).
- [65] Monahan, N. R., Williams, K. W., Kumar, B., Nuckolls, C. & Zhu, X.-Y. Direct observation of entropy-driven electron-hole pair separation at an organic semiconductor interface. *Physical review letters* **114**, 247003 (2015).
- [66] Liu, X., Ding, K., Panda, A. & Forrest, S. R. Charge transfer states in dilute donor–acceptor blend organic heterojunctions. *ACS nano* **10**, 7619–7626 (2016).
- [67] Kahle, F.-J. *et al.* Does electron delocalization influence charge separation at donor-acceptor interfaces in organic photovoltaic cells? *The Journal of Physical Chemistry C* (2018).
- [68] Lin, Y. L., Fusella, M. A. & Rand, B. P. The impact of local morphology on organic donor/acceptor charge transfer states. *Advanced Energy Materials* 1702816 (2018).
- [69] Ding, K., Liu, X. & Forrest, S. R. Charge transfer and collection in dilute organic donor–acceptor heterojunction blends. *Nano letters* **18**, 3180–3184 (2018).
- [70] Bäessler, H. Charge transport in disordered organic photoconductors a monte carlo simulation study. *physica status solidi (b)* **175**, 15–56 (1993).
- [71] Miller, A. & Abrahams, E. Impurity conduction at low concentrations. *Physical Review* **120**, 745 (1960).

- [72] Marcus, R. A. & Sutin, N. Electron transfers in chemistry and biology. *Biochimica et Biophysica Acta (BBA)-Reviews on Bioenergetics* **811**, 265–322 (1985).
- [73] Fishchuk, I., Kadashchuk, A., Bäessler, H. & Nespurek, S. Nondispersive polaron transport in disordered organic solids. *Physical Review B* **67**, 224303 (2003).
- [74] Parris, P. E., Kenkre, V. M. & Dunlap, D. H. Nature of charge carriers in disordered molecular solids: Are polarons compatible with observations? *Physical review letters* **87**, 126601 (2001).
- [75] Zhang, C. *et al.* An ultrathin, smooth, and low-loss al-doped ag film and its application as a transparent electrode in organic photovoltaics. *Advanced Materials* **26**, 5696–5701 (2014).
- [76] Tenent, R. C. *et al.* UltrasMOOTH, large-area, high-uniformity, conductive transparent single-walled-carbon-nanotube films for photovoltaics produced by ultrasonic spraying. *Advanced materials* **21**, 3210–3216 (2009).
- [77] Barnes, T. M. *et al.* Carbon nanotube network electrodes enabling efficient organic solar cells without a hole transport layer. *Applied Physics Letters* **96**, 118 (2010).
- [78] Zhang, L. L., Zhou, R. & Zhao, X. Graphene-based materials as supercapacitor electrodes. *Journal of Materials Chemistry* **20**, 5983–5992 (2010).
- [79] Wu, J. *et al.* Organic solar cells with solution-processed graphene transparent electrodes. *Applied Physics Letters* **92**, 237 (2008).
- [80] Peumans, P., Yakimov, A. & Forrest, S. R. Small molecular weight organic thin-film photodetectors and solar cells. *Journal of Applied Physics* **93**, 3693–3723 (2003).
- [81] Tang, C. W. Two-layer organic photovoltaic cell. *Applied Physics Letters* **48**, 183–185 (1986).
- [82] Meng, L. *et al.* Organic and solution-processed tandem solar cells with 17.3% efficiency. *Science* **361**, 1094–1098 (2018).
- [83] Mateker, W. R., Sachs-Quintana, I., Burkhard, G. F., Cheacharoen, R. & McGehee, M. D. Minimal long-term intrinsic degradation observed in a polymer solar cell illuminated in an oxygen-free environment. *Chemistry of Materials* **27**, 404–407 (2015).
- [84] Søndergaard, R., Hösel, M., Angmo, D., Larsen-Olsen, T. T. & Krebs, F. C. Roll-to-roll fabrication of polymer solar cells. *Materials today* **15**, 36–49 (2012).
- [85] Gu, X. *et al.* Roll-to-roll printed large-area all-polymer solar cells with 5% efficiency based on a low crystallinity conjugated polymer blend. *Advanced Energy Materials* **7**, 1602742 (2017).

- [86] Qu, B. & Forrest, S. R. Continuous roll-to-roll fabrication of organic photovoltaic cells via interconnected high-vacuum and low-pressure organic vapor phase deposition systems. *Applied Physics Letters* **113**, 053302 (2018).
- [87] van der Wiel, B., Egelhaaf, H.-J., Issa, H., Roos, M. & Henze, N. Market readiness of organic photovoltaics for building integration. *MRS Online Proceedings Library Archive* **1639** (2014).
- [88] Loo, Y.-L. L. Making smart windows smarter (conference presentation). In *Organic, Hybrid, and Perovskite Photovoltaics XIX*, vol. 10737, 1073702 (International Society for Optics and Photonics, 2018).
- [89] Peumans, P., Uchida, S. & Forrest, S. Efficient bulk heterojunction photovoltaic cells using small-molecular-weight organic thin films. *Nature* **425**, 158 (2003).
- [90] Yang, F. & Forrest, S. R. Photocurrent generation in nanostructured organic solar cells. *ACS nano* **2**, 1022–1032 (2008).
- [91] Valsakumar, M. *et al.* Crystal structure and disorder in solid  $c_{70}$ . *Physical Review B* **48**, 9080 (1993).
- [92] Scherrer, P. Estimation of the size and internal structure of colloidal particles by means of röntgen. *Nachr. Ges. Wiss. Göttingen* **2**, 96–100 (1918).
- [93] Lassiter, B. E., Zimmerman, J. D., Panda, A., Xiao, X. & Forrest, S. R. Tandem organic photovoltaics using both solution and vacuum deposited small molecules. *Applied Physics Letters* **101**, 063303 (2012).
- [94] Piersimoni, F. *et al.* Influence of fullerene ordering on the energy of the charge-transfer state and open-circuit voltage in polymer: fullerene solar cells. *The Journal of Physical Chemistry C* **115**, 10873–10880 (2011).
- [95] Fujita, T. Compound for organic electroluminescence and organic electroluminescent device (2010). US Patent 7,727,642.
- [96] Pandey, R. & Holmes, R. J. Characterizing the charge collection efficiency in bulk heterojunction organic photovoltaic cells. *Applied Physics Letters* **100**, 52 (2012).
- [97] Frisch, M. *et al.* Gaussian09. revision e. 01. gaussian inc., wallingford, ct, usa (2009).
- [98] Savoie, B. M. *et al.* Unequal partnership: asymmetric roles of polymeric donor and fullerene acceptor in generating free charge. *Journal of the American Chemical Society* **136**, 2876–2884 (2014).
- [99] Madigan, C. F. & Bulović, V. Solid state solvation in amorphous organic thin films. *Physical review letters* **91**, 247403 (2003).

- [100] Griffith, O. L. *et al.* Charge transport and exciton dissociation in organic solar cells consisting of dipolar donors mixed with  $c_{70}$ . *Physical Review B* **92**, 085404 (2015).
- [101] Lunt, R. R., Benziger, J. B. & Forrest, S. R. Relationship between crystalline order and exciton diffusion length in molecular organic semiconductors. *Advanced Materials* **22**, 1233–1236 (2010).
- [102] Deotare, P. *et al.* Nanoscale transport of charge-transfer states in organic donor–acceptor blends. *Nature materials* **14**, 1130 (2015).
- [103] Knupfer, M. Exciton binding energies in organic semiconductors. *Applied Physics A* **77**, 623–626 (2003).
- [104] Li, H.-W. *et al.* On the study of exciton binding energy with direct charge generation in photovoltaic polymers. *Advanced Electronic Materials* **2**, 1600200 (2016).
- [105] Leblebici, S. Y., Chen, T. L., Olalde-Velasco, P., Yang, W. & Ma, B. Reducing exciton binding energy by increasing thin film permittivity: an effective approach to enhance exciton separation efficiency in organic solar cells. *ACS applied materials & interfaces* **5**, 10105–10110 (2013).
- [106] Kraner, S., Scholz, R., Koerner, C. & Leo, K. Design proposals for organic materials exhibiting a low exciton binding energy. *The Journal of Physical Chemistry C* **119**, 22820–22825 (2015).
- [107] Menke, S. M., Ran, N. A., Bazan, G. C. & Friend, R. H. Understanding energy loss in organic solar cells: toward a new efficiency regime. *Joule* (2017).
- [108] Zhao, W. *et al.* Fullerene-free polymer solar cells with over 11% efficiency and excellent thermal stability. *Advanced materials* **28**, 4734–4739 (2016).
- [109] Chen, W. & Zhang, Q. Recent progress in non-fullerene small molecule acceptors in organic solar cells (oscs). *Journal of Materials Chemistry C* **5**, 1275–1302 (2017).
- [110] Li, Y. *et al.* A near-infrared non-fullerene electron acceptor for high performance polymer solar cells. *Energy & Environmental Science* **10**, 1610–1620 (2017).
- [111] Li, Y. *et al.* Non-fullerene acceptor with low energy loss and high external quantum efficiency: towards high performance polymer solar cells. *Journal of Materials Chemistry A* **4**, 5890–5897 (2016).
- [112] Nielsen, C. B., Holliday, S., Chen, H.-Y., Cryer, S. J. & McCulloch, I. Non-fullerene electron acceptors for use in organic solar cells. *Accounts of chemical research* **48**, 2803–2812 (2015).

- [113] Yao, Z. *et al.* Dithienopicenocarbazole-based acceptors for efficient organic solar cells with optoelectronic response over 1000 nm and an extremely low energy loss. *Journal of the American Chemical Society* **140**, 2054–2057 (2018).
- [114] Baran, D. *et al.* Reduced voltage losses yield 10% efficient fullerene free organic solar cells with  $> 1$  v open circuit voltages. *Energy & environmental science* **9**, 3783–3793 (2016).
- [115] He, B. *et al.* Molecular engineering for large open-circuit voltage and low energy loss in around 10% non-fullerene organic photovoltaics. *ACS Energy Letters* **3**, 1028–1035 (2018).
- [116] Rand, B. P., Burk, D. P. & Forrest, S. R. Offset energies at organic semiconductor heterojunctions and their influence on the open-circuit voltage of thin-film solar cells. *Physical Review B* **75**, 115327 (2007).
- [117] Coffey, D. C. *et al.* An optimal driving force for converting excitons into free carriers in excitonic solar cells. *The Journal of Physical Chemistry C* **116**, 8916–8923 (2012).
- [118] Ward, A. J. *et al.* The impact of driving force on electron transfer rates in photovoltaic donor–acceptor blends. *Advanced Materials* **27**, 2496–2500 (2015).
- [119] Petrus, M. L. *et al.* Capturing the sun: a review of the challenges and perspectives of perovskite solar cells. *Advanced Energy Materials* **7**, 1700264 (2017).
- [120] Benduhn, J. *et al.* Intrinsic non-radiative voltage losses in fullerene-based organic solar cells. *Nature Energy* **2**, 17053 (2017).
- [121] Azzouzi, M. *et al.* Nonradiative energy losses in bulk-heterojunction organic photovoltaics. *Physical Review X* **8**, 031055 (2018).
- [122] Rau, U. Reciprocity relation between photovoltaic quantum efficiency and electroluminescent emission of solar cells. *Physical Review B* **76**, 085303 (2007).
- [123] Englman, R. & Jortner, J. The energy gap law for radiationless transitions in large molecules. *Molecular Physics* **18**, 145–164 (1970).
- [124] Alamoudi, M. A. *et al.* Impact of nonfullerene acceptor core structure on the photophysics and efficiency of polymer solar cells. *ACS Energy Letters* **3**, 802–811 (2018).
- [125] Borioni, J. L., Puiatti, M., Vera, D. M. A. & Pierini, A. B. In search of the best dft functional for dealing with organic anionic species. *Physical Chemistry Chemical Physics* **19**, 9189–9198 (2017).
- [126] Lopez, S. A., Sanchez-Lengeling, B., de Goes Soares, J. & Aspuru-Guzik, A. Design principles and top non-fullerene acceptor candidates for organic photovoltaics. *Joule* **1**, 857–870 (2017).

- [127] Tomasi, J., Mennucci, B. & Cammi, R. Quantum mechanical continuum solvation models. *Chemical reviews* **105**, 2999–3094 (2005).
- [128] Yong Lee, J., Jin Mhin, B., Mukamel, S. & Kim, K. S. Size scaling of intramolecular charge transfer driven optical properties of substituted polyenes and polyynes. *The Journal of chemical physics* **119**, 7519–7524 (2003).
- [129] Slama-Schwok, A., Blanchard-Desce, M. & Lehn, J. Intramolecular charge transfer in donor-acceptor molecules. *Journal of Physical Chemistry* **94**, 3894–3902 (1990).
- [130] Rissler, J. Effective conjugation length of  $\pi$ -conjugated systems. *Chemical physics letters* **395**, 92–96 (2004).
- [131] Van Dyck, C., Marks, T. J. & Ratner, M. A. Chain length dependence of the dielectric constant and polarizability in conjugated organic thin films. *ACS nano* **11**, 5970–5981 (2017).
- [132] Chopra, P., Carlucci, L., King, H. F. & Prasad, P. N. Ab initio calculations of polarizabilities and second hyperpolarizabilities in organic molecules with extended  $\pi$ -electron conjugation. *The Journal of Physical Chemistry* **93**, 7120–7130 (1989).
- [133] Atahan-Evrenk, Ş. & Aspuru-Guzik, A. Prediction and theoretical characterization of p-type organic semiconductor crystals for field-effect transistor applications. In *Prediction and Calculation of Crystal Structures*, 95–138 (Springer, 2014).
- [134] de Jong, M., Seijo, L., Meijerink, A. & Rabouw, F. T. Resolving the ambiguity in the relation between stokes shift and huang–rhys parameter. *Physical Chemistry Chemical Physics* **17**, 16959–16969 (2015).
- [135] Gao, G. *et al.* Spiro-fused perylene diimide arrays. *Journal of the American Chemical Society* **139**, 15914–15920 (2017).
- [136] Zhang, Y. & Forrest, S. R. Existence of continuous-wave threshold for organic semiconductor lasers. *Physical Review B* **84**, 241301 (2011).
- [137] Sun, Y. *et al.* Management of singlet and triplet excitons for efficient white organic light-emitting devices. *Nature* **440**, 908 (2006).
- [138] Zhang, Y., Whited, M., Thompson, M. E. & Forrest, S. R. Singlet–triplet quenching in high intensity fluorescent organic light emitting diodes. *Chemical Physics Letters* **495**, 161–165 (2010).
- [139] Zhang, Y. & Forrest, S. R. Triplets contribute to both an increase and loss in fluorescent yield in organic light emitting diodes. *Physical review letters* **108**, 267404 (2012).

- [140] Zhang, Y., Lee, J. & Forrest, S. R. Tenfold increase in the lifetime of blue phosphorescent organic light-emitting diodes. *Nature communications* **5**, 5008 (2014).
- [141] Zhang, Y., Slightsky, M. & Forrest, S. R. Enhanced efficiency in high-brightness fluorescent organic light emitting diodes through triplet management. *Applied Physics Letters* **99**, 260 (2011).
- [142] Kozlov, V. *et al.* Study of lasing action based on Förster energy transfer in optically pumped organic semiconductor thin films. *Journal of applied physics* **84**, 4096–4108 (1998).
- [143] Lehnhardt, M., Riedl, T., Rabe, T. & Kowalsky, W. Room temperature lifetime of triplet excitons in fluorescent host/guest systems. *Organic electronics* **12**, 486–491 (2011).
- [144] Chandrasekhar, S. Stochastic problems in physics and astronomy. *Reviews of modern physics* **15**, 1 (1943).
- [145] Fishchuk, I. I. *et al.* Triplet energy transfer in conjugated polymers. ii. a polaron theory description addressing the influence of disorder. *Physical Review B* **78**, 045211 (2008).
- [146] Devi, L. S. *et al.* Triplet energy transfer in conjugated polymers. i. experimental investigation of a weakly disordered compound. *Physical Review B* **78**, 045210 (2008).
- [147] Richert, R. & Bässler, H. Dispersive triplet excitation transport in organic glasses. *The Journal of chemical physics* **84**, 3567–3572 (1986).
- [148] Movaghar, B., Grünwald, M., Ries, B., Bassler, H. & Würtz, D. Diffusion and relaxation of energy in disordered organic and inorganic materials. *Physical Review B* **33**, 5545 (1986).
- [149] Köhler, A. & Bässler, H. Triplet states in organic semiconductors. *Materials Science and Engineering: R: Reports* **66**, 71–109 (2009).
- [150] Mikhnenko, O. *et al.* Temperature dependence of exciton diffusion in conjugated polymers. *The Journal of Physical Chemistry B* **112**, 11601–11604 (2008).
- [151] Fishchuk, I., Kadashchuk, A., Bässler, H. & Nespurek, S. Nondispersive polaron transport in disordered organic solids. *Physical Review B* **67**, 224303 (2003).
- [152] Hertel, D., Bässler, H., Guentner, R. & Scherf, U. Triplet-triplet annihilation in a poly (fluorene)-derivative. *The Journal of Chemical Physics* **115**, 10007–10013 (2001).
- [153] Tang, C. W., VanSlyke, S. A. & Chen, C. Electroluminescence of doped organic thin films. *Journal of Applied Physics* **65**, 3610–3616 (1989).



- [154] Yokota, M. & Tanimoto, O. Effects of diffusion on energy transfer by resonance. *Journal of the physical society of Japan* **22**, 779–784 (1967).
- [155] Takahashi, Y. & Tomura, M. Diffusion of singlet excitons in anthracene crystals. *Journal of the Physical Society of Japan* **31**, 1100–1108 (1971).
- [156] Ern, V., Avakian, P. & Merrifield, R. Diffusion of triplet excitons in anthracene crystals. *Physical Review* **148**, 862 (1966).
- [157] Itskos, G. *et al.* Efficient dipole-dipole coupling of mott-wannier and frenkel excitons in (ga, in)n quantum well/polyfluorene semiconductor heterostructures. *Physical Review B* **76**, 035344 (2007).
- [158] Rindermann, J. J. *et al.* Dependence of resonance energy transfer on exciton dimensionality. *Physical review letters* **107**, 236805 (2011).
- [159] Heliotis, G. *et al.* Hybrid inorganic/organic semiconductor heterostructures with efficient non-radiative energy transfer. *Advanced Materials* **18**, 334–338 (2006).
- [160] Blumstengel, S., Sadofev, S. & Henneberger, F. Electronic coupling of optical excitations in organic/inorganic semiconductor hybrid structures. *New Journal of Physics* **10**, 065010 (2008).
- [161] Zhang, Q. *et al.* Highly efficient resonant coupling of optical excitations in hybrid organic/inorganic semiconductor nanostructures. *Nature nanotechnology* **2**, 555 (2007).
- [162] Holmes, R., Kéna-Cohen, S., Menon, V. & Forrest, S. Strong coupling and hybridization of frenkel and wannier-mott excitons in an organic-inorganic optical microcavity. *Physical Review B* **74**, 235211 (2006).
- [163] Agranovich, V., Gartstein, Y. N. & Litinskaya, M. Hybrid resonant organic–inorganic nanostructures for optoelectronic applications. *Chemical reviews* **111**, 5179–5214 (2011).
- [164] Slootsky, M., Liu, X., Menon, V. M. & Forrest, S. R. Room temperature frenkel-wannier-mott hybridization of degenerate excitons in a strongly coupled microcavity. *Physical review letters* **112**, 076401 (2014).
- [165] Grätzel, M. Dye-sensitized solar cells. *Journal of Photochemistry and Photobiology C: Photochemistry Reviews* **4**, 145–153 (2003).
- [166] Hagfeldt, A., Boschloo, G., Sun, L., Kloo, L. & Pettersson, H. Dye-sensitized solar cells. *Chemical reviews* **110**, 6595–6663 (2010).
- [167] So, F. F. & Forrest, S. R. Organic-on-inorganic semiconductor photodetector. *IEEE Transactions on Electron Devices* **36**, 66–69 (1989).

- [168] Forrest, S. Organic-on-organic semiconductor heterojunctions: building block for the next generation of optoelectronic devices. *IEEE Circuits and Devices Magazine* **5**, 33–37 (1989).
- [169] Forrest, S. R., Kaplan, M. & Schmidt, P. Organic-on-inorganic semiconductor contact barrier diodes. i. theory with applications to organic thin films and prototype devices. *Journal of applied physics* **55**, 1492–1507 (1984).
- [170] O’regan, B. & Grätzel, M. A low-cost, high-efficiency solar cell based on dye-sensitized colloidal tio<sub>2</sub> films. *nature* **353**, 737 (1991).
- [171] Coe-Sullivan, S., Woo, W.-K., Steckel, J. S., Bawendi, M. & Bulović, V. Tuning the performance of hybrid organic/inorganic quantum dot light-emitting devices. *Organic Electronics* **4**, 123–130 (2003).
- [172] Li, N., Lee, K., Renshaw, C. K., Xiao, X. & Forrest, S. R. Improved power conversion efficiency of inp solar cells using organic window layers. *Applied Physics Letters* **98**, 053504 (2011).
- [173] Zahn, D. R., Gavrilă, G. N. & Salvan, G. Electronic and vibrational spectroscopies applied to organic/inorganic interfaces. *Chemical reviews* **107**, 1161–1232 (2007).
- [174] Avasthi, S. *et al.* Silicon surface passivation by an organic overlayer of 9, 10-phenanthrenequinone. *Applied physics letters* **96**, 222109 (2010).
- [175] Lee, B. *et al.* Surface passivation of inp using an organic thin film. *Journal of Crystal Growth* (2018).
- [176] Sargent, E. H. Colloidal quantum dot solar cells. *Nature photonics* **6**, 133 (2012).
- [177] Malinkiewicz, O. *et al.* Perovskite solar cells employing organic charge-transport layers. *Nature Photonics* **8**, 128 (2014).
- [178] Wan, C. *et al.* Dielectric mismatch mediates carrier mobility in organic-intercalated layered tis<sub>2</sub>. *Nano letters* **15**, 6302–6308 (2015).
- [179] Renshaw, C. K. & Forrest, S. R. Excited state and charge dynamics of hybrid organic/inorganic heterojunctions. i. theory. *Physical Review B* **90**, 045302 (2014).
- [180] Panda, A., Renshaw, C. K., Oskooi, A., Lee, K. & Forrest, S. R. Excited state and charge dynamics of hybrid organic/inorganic heterojunctions. ii. experiment. *Physical Review B* **90**, 045303 (2014).
- [181] Panda, A. Exciton and charge dynamics at hybrid organic-inorganic semiconductor heterojunctions (2018).

- [182] Bansal, N. *et al.* Influence of crystallinity and energetics on charge separation in polymer–inorganic nanocomposite films for solar cells. *Scientific reports* **3**, 1531 (2013).
- [183] Panda, A., Ding, K., Liu, X. & Forrest, S. R. Free and trapped hybrid charge transfer excitons at a zno/small-molecule heterojunction. *Physical Review B* **94**, 125429 (2016).
- [184] Vaynzof, Y., Bakulin, A. A., Gélinas, S. & Friend, R. H. Direct observation of photoinduced bound charge-pair states at an organic-inorganic semiconductor interface. *Physical review letters* **108**, 246605 (2012).
- [185] Eyer, M., Sadofev, S., Puls, J. & Blumstengel, S. Charge transfer excitons at znmgo/p3ht heterojunctions: Relation to photovoltaic performance. *Applied Physics Letters* **107**, 221602 (2015).
- [186] Lim, H., Kwon, H., Kim, S. K. & Kim, J. W. Delayed triplet-state formation through hybrid charge transfer exciton at copper phthalocyanine/gaas heterojunction. *The journal of physical chemistry letters* **8**, 4763–4768 (2017).
- [187] Zhu, T. *et al.* Highly mobile charge-transfer excitons in two-dimensional ws<sub>2</sub>/tetracene heterostructures. *Science Advances* **4**, eaao3104 (2018).
- [188] Sokol, A. A. *et al.* Point defects in zno. *Faraday discussions* **134**, 267–282 (2007).
- [189] Novoselov, K. S. *et al.* Electric field effect in atomically thin carbon films. *science* **306**, 666–669 (2004).
- [190] Lee, C.-H. *et al.* Atomically thin p–n junctions with van der waals heterointerfaces. *Nature nanotechnology* **9**, 676 (2014).
- [191] Cheng, R. *et al.* Electroluminescence and photocurrent generation from atomically sharp wse<sub>2</sub>/mos<sub>2</sub> heterojunction p–n diodes. *Nano letters* **14**, 5590–5597 (2014).
- [192] Furchi, M. M., Pospischil, A., Libisch, F., Burgdörfer, J. & Mueller, T. Photovoltaic effect in an electrically tunable van der waals heterojunction. *Nano letters* **14**, 4785–4791 (2014).
- [193] Li, X. *et al.* Graphene and related two-dimensional materials: Structure-property relationships for electronics and optoelectronics. *Applied Physics Reviews* **4**, 021306 (2017).
- [194] Wang, Q. H., Kalantar-Zadeh, K., Kis, A., Coleman, J. N. & Strano, M. S. Electronics and optoelectronics of two-dimensional transition metal dichalcogenides. *Nature nanotechnology* **7**, 699 (2012).

- [195] Ding, Y. *et al.* First principles study of structural, vibrational and electronic properties of graphene-like  $mx_2$  ( $m = mo, nb, w, ta$ ;  $x = s, se, te$ ) monolayers. *Physica B: Condensed Matter* **406**, 2254–2260 (2011).
- [196] Sandoval, S. J., Yang, D., Frindt, R. & Irwin, J. Raman study and lattice dynamics of single molecular layers of  $mos_2$ . *Physical Review B* **44**, 3955 (1991).
- [197] Voiry, D. *et al.* Covalent functionalization of monolayered transition metal dichalcogenides by phase engineering. *Nature chemistry* **7**, 45 (2015).
- [198] Kang, Y. *et al.* Plasmonic hot electron induced structural phase transition in a  $mos_2$  monolayer. *Advanced Materials* **26**, 6467–6471 (2014).
- [199] Katagiri, Y. *et al.* Gate-tunable atomically thin lateral  $mos_2$  schottky junction patterned by electron beam. *Nano letters* **16**, 3788–3794 (2016).
- [200] Song, S. *et al.* Room temperature semiconductor–metal transition of  $mote_2$  thin films engineered by strain. *Nano letters* **16**, 188–193 (2015).
- [201] Kuc, A., Zibouche, N. & Heine, T. Influence of quantum confinement on the electronic structure of the transition metal sulfide  $ts_2$ . *Physical Review B* **83**, 245213 (2011).
- [202] Huang, Y. L. *et al.* Bandgap tunability at single-layer molybdenum disulphide grain boundaries. *Nature communications* **6**, 6298 (2015).
- [203] Cheiwchanchamnangij, T. & Lambrecht, W. R. Quasiparticle band structure calculation of monolayer, bilayer, and bulk  $mos_2$ . *Physical Review B* **85**, 205302 (2012).
- [204] Doolen, R., Laitinen, R., Parsapour, F. & Kelley, D. Trap state dynamics in  $mos_2$  nanoclusters. *The Journal of Physical Chemistry B* **102**, 3906–3911 (1998).
- [205] Carvalho, A., Ribeiro, R. & Neto, A. C. Band nesting and the optical response of two-dimensional semiconducting transition metal dichalcogenides. *Physical Review B* **88**, 115205 (2013).
- [206] Mayorov, A. S. *et al.* Micrometer-scale ballistic transport in encapsulated graphene at room temperature. *Nano letters* **11**, 2396–2399 (2011).
- [207] Radisavljevic, B. & Kis, A. Mobility engineering and a metal–insulator transition in monolayer  $mos_2$ . *Nature materials* **12**, 815 (2013).
- [208] Baugher, B. W., Churchill, H. O., Yang, Y. & Jarillo-Herrero, P. Intrinsic electronic transport properties of high-quality monolayer and bilayer  $mos_2$ . *Nano letters* **13**, 4212–4216 (2013).
- [209] Jariwala, D. *et al.* Band-like transport in high mobility unencapsulated single-layer  $mos_2$  transistors. *Applied Physics Letters* **102**, 173107 (2013).

- [210] Suzuki, R. *et al.* Valley-dependent spin polarization in bulk  $\text{mos}_2$  with broken inversion symmetry. *Nature nanotechnology* **9**, 611 (2014).
- [211] Wilson, J. A. & Yoffe, A. The transition metal dichalcogenides discussion and interpretation of the observed optical, electrical and structural properties. *Advances in Physics* **18**, 193–335 (1969).
- [212] Lv, R. *et al.* Transition metal dichalcogenides and beyond: synthesis, properties, and applications of single- and few-layer nanosheets. *Accounts of chemical research* **48**, 56–64 (2014).
- [213] Hernandez, Y. *et al.* High-yield production of graphene by liquid-phase exfoliation of graphite. *Nature nanotechnology* **3**, 563 (2008).
- [214] Gu, W. *et al.* Graphene sheets from worm-like exfoliated graphite. *Journal of Materials Chemistry* **19**, 3367–3369 (2009).
- [215] Zeng, Z. *et al.* Single-layer semiconducting nanosheets: High-yield preparation and device fabrication. *Angewandte Chemie* **123**, 11289–11293 (2011).
- [216] Coleman, J. N. *et al.* Two-dimensional nanosheets produced by liquid exfoliation of layered materials. *Science* **331**, 568–571 (2011).
- [217] Zheng, J. *et al.* High yield exfoliation of two-dimensional chalcogenides using sodium naphthalenide. *Nature communications* **5**, 2995 (2014).
- [218] Tung, V. C., Allen, M. J., Yang, Y. & Kaner, R. B. High-throughput solution processing of large-scale graphene. *Nature nanotechnology* **4**, 25 (2009).
- [219] Kim, K. S. *et al.* Large-scale pattern growth of graphene films for stretchable transparent electrodes. *nature* **457**, 706 (2009).
- [220] Lee, Y.-H. *et al.* Synthesis of large-area  $\text{mos}_2$  atomic layers with chemical vapor deposition. *Advanced materials* **24**, 2320–2325 (2012).
- [221] Najmaei, S. *et al.* Vapour phase growth and grain boundary structure of molybdenum disulphide atomic layers. *Nature materials* **12**, 754 (2013).
- [222] Elias, A. L. *et al.* Controlled synthesis and transfer of large-area  $\text{ws}_2$  sheets: from single layer to few layers. *ACS nano* **7**, 5235–5242 (2013).
- [223] Wang, X. *et al.* Chemical vapor deposition growth of crystalline monolayer  $\text{mose}_2$ . *ACS nano* **8**, 5125–5131 (2014).
- [224] Huang, J.-K. *et al.* Large-area synthesis of highly crystalline  $\text{wse}_2$  monolayers and device applications. *ACS nano* **8**, 923–930 (2013).
- [225] Bersch, B. M. *et al.* Selective-area growth and controlled substrate coupling of transition metal dichalcogenides. *2D Materials* **4**, 025083 (2017).

- [226] Ling, X. *et al.* Role of the seeding promoter in mos<sub>2</sub> growth by chemical vapor deposition. *Nano letters* **14**, 464–472 (2014).
- [227] Mak, K. F., Lee, C., Hone, J., Shan, J. & Heinz, T. F. Atomically thin mos<sub>2</sub>: a new direct-gap semiconductor. *Physical review letters* **105**, 136805 (2010).
- [228] Splendiani, A. *et al.* Emerging photoluminescence in monolayer mos<sub>2</sub>. *Nano letters* **10**, 1271–1275 (2010).
- [229] Britnell, L. *et al.* Strong light-matter interactions in heterostructures of atomically thin films. *Science* **340**, 1311–1314 (2013).
- [230] Huang, Y. L. *et al.* The organic–2d transition metal dichalcogenide heterointerface. *Chemical Society Reviews* **47**, 3241–3264 (2018).
- [231] Zheng, Y. J. *et al.* Heterointerface screening effects between organic monolayers and monolayer transition metal dichalcogenides. *ACS nano* **10**, 2476–2484 (2016).
- [232] Nicoara, N., Román, E., Gómez-Rodríguez, J. M., Martín-Gago, J. A. & Méndez, J. Scanning tunneling and photoemission spectroscopies at the ptcda/au (1 1 1) interface. *Organic electronics* **7**, 287–294 (2006).
- [233] Ludwig, C., Gompf, B., Petersen, J., Strohmaier, R. & Eisenmenger, W. Stm investigations of ptcda and ptedi on graphite and mos<sub>2</sub>. a systematic study of epitaxy and stm image contrast. *Zeitschrift für Physik B Condensed Matter* **93**, 365–373 (1994).
- [234] Yu, Z. *et al.* Towards intrinsic charge transport in monolayer molybdenum disulfide by defect and interface engineering. *Nature communications* **5**, 5290 (2014).
- [235] Tuxen, A. *et al.* Size threshold in the dibenzothiophene adsorption on mos<sub>2</sub> nanoclusters. *Acs Nano* **4**, 4677–4682 (2010).
- [236] Nguyen, E. P. *et al.* Electronic tuning of 2d mos<sub>2</sub> through surface functionalization. *Advanced Materials* **27**, 6225–6229 (2015).
- [237] Bettis Homan, S. *et al.* Ultrafast exciton dissociation and long-lived charge separation in a photovoltaic pentacene–mos<sub>2</sub> van der waals heterojunction. *Nano letters* **17**, 164–169 (2016).
- [238] Kim, J.-K. *et al.* Trap-mediated electronic transport properties of gate-tunable pentacene/mos<sub>2</sub> pn heterojunction diodes. *Scientific reports* **6**, 36775 (2016).
- [239] Song, Z. *et al.* Electronic properties of a 1d intrinsic/p-doped heterojunction in a 2d transition metal dichalcogenide semiconductor. *ACS nano* **11**, 9128–9135 (2017).

- [240] Mak, K. F. & Shan, J. Photonics and optoelectronics of 2d semiconductor transition metal dichalcogenides. *Nature Photonics* **10**, 216 (2016).
- [241] Shen, N. & Tao, G. Charge transfer and interface engineering of the pentacene and mos<sub>2</sub> monolayer complex. *Advanced Materials Interfaces* **4**, 1601083 (2017).
- [242] Jing, Y., Tan, X., Zhou, Z. & Shen, P. Tuning electronic and optical properties of mos<sub>2</sub> monolayer via molecular charge transfer. *Journal of Materials Chemistry A* **2**, 16892–16897 (2014).
- [243] Mouri, S., Miyauchi, Y. & Matsuda, K. Tunable photoluminescence of monolayer mos<sub>2</sub> via chemical doping. *Nano letters* **13**, 5944–5948 (2013).
- [244] Liu, X. *et al.* Photoresponse of an organic semiconductor/two-dimensional transition metal dichalcogenide heterojunction. *Nano letters* **17**, 3176–3181 (2017).
- [245] Huang, Y., Zheng, W., Qiu, Y. & Hu, P. Effects of organic molecules with different structures and absorption bandwidth on modulating photoresponse of mos<sub>2</sub> photodetector. *ACS applied materials & interfaces* **8**, 23362–23370 (2016).
- [246] Velusamy, D. B. *et al.* 2d organic–inorganic hybrid thin films for flexible uv–visible photodetectors. *Advanced Functional Materials* **27**, 1605554 (2017).
- [247] Shastry, T. A. *et al.* Mutual photoluminescence quenching and photovoltaic effect in large-area single-layer mos<sub>2</sub>–polymer heterojunctions. *ACS nano* **10**, 10573–10579 (2016).
- [248] Liu, F. *et al.* Van der waals p–n junction based on an organic–inorganic heterostructure. *Advanced Functional Materials* **25**, 5865–5871 (2015).
- [249] Jariwala, D. *et al.* Hybrid, gate-tunable, van der waals p–n heterojunctions from pentacene and mos<sub>2</sub>. *Nano letters* **16**, 497–503 (2015).
- [250] He, D. *et al.* A van der waals pn heterojunction with organic/inorganic semiconductors. *Applied physics letters* **107**, 183103 (2015).
- [251] Ren, Q. *et al.* High performance photoresponsive field-effect transistors based on mos<sub>2</sub>/pentacene heterojunction. *Organic Electronics* **51**, 142–148 (2017).
- [252] Ceballos, F., Bellus, M. Z., Chiu, H.-Y. & Zhao, H. Ultrafast charge separation and indirect exciton formation in a mos<sub>2</sub>–mose<sub>2</sub> van der waals heterostructure. *ACS nano* **8**, 12717–12724 (2014).
- [253] Rivera, P. *et al.* Observation of long-lived interlayer excitons in monolayer mose<sub>2</sub>–wse<sub>2</sub> heterostructures. *Nature communications* **6**, 6242 (2015).
- [254] Petoukhoff, C. E. *et al.* Ultrafast charge transfer and enhanced absorption in mos<sub>2</sub>–organic van der waals heterojunctions using plasmonic metasurfaces. *ACS nano* **10**, 9899–9908 (2016).

- [255] Schuller, J. A. *et al.* Orientation of luminescent excitons in layered nanomaterials. *Nature nanotechnology* **8**, 271 (2013).
- [256] Prins, F., Goodman, A. J. & Tisdale, W. A. Reduced dielectric screening and enhanced energy transfer in single- and few-layer  $\text{mos}_2$ . *Nano letters* **14**, 6087–6091 (2014).
- [257] Raja, A. *et al.* Energy transfer from quantum dots to graphene and  $\text{mos}_2$ : The role of absorption and screening in two-dimensional materials. *Nano letters* **16**, 2328–2333 (2016).
- [258] Goodfellow, K. M. *et al.* Distance-dependent energy transfer between cdse/cds quantum dots and a two-dimensional semiconductor. *Applied Physics Letters* **108**, 021101 (2016).
- [259] Zang, H. *et al.* Nonradiative energy transfer from individual cdse/zns quantum dots to single-layer and few-layer tin disulfide. *ACS nano* **10**, 4790–4796 (2016).
- [260] Gu, J. *et al.* Dipole-aligned energy transfer between excitons in two-dimensional transition metal dichalcogenide and organic semiconductor. *ACS Photonics* **5**, 100–104 (2017).
- [261] Castellanos-Gomez, A. *et al.* Deterministic transfer of two-dimensional materials by all-dry viscoelastic stamping. *2D Materials* **1**, 011002 (2014).
- [262] Lieb, M. A., Zavislan, J. M. & Novotny, L. Single-molecule orientations determined by direct emission pattern imaging. *JOSA B* **21**, 1210–1215 (2004).
- [263] Nollau, A., Hoffmann, M., Floreck, K., Fritz, T. & Leo, K. A simple measurement of the absolute internal quantum efficiency of thin organic films. *Journal of Applied Physics* **87**, 7802–7804 (2000).
- [264] Li, Y. *et al.* Measurement of the optical dielectric function of monolayer transition-metal dichalcogenides:  $\text{Mos}_2$ ,  $\text{mose}_2$ ,  $\text{ws}_2$ , and  $\text{wse}_2$ . *Physical Review B* **90**, 205422 (2014).
- [265] Friedrich, M. *et al.* Optical constants of 3, 4, 9, 10-perylenetetracarboxylic dianhydride films on silicon and gallium arsenide studied by spectroscopic ellipsometry. *Applied Physics A* **75**, 501–506 (2002).
- [266] Forrest, S., Burrows, P., Haskal, E. & So, F. Ultrahigh-vacuum quasiepitaxial growth of model van der waals thin films. ii. experiment. *Physical Review B* **49**, 11309 (1994).
- [267] Kang, J., Tongay, S., Zhou, J., Li, J. & Wu, J. Band offsets and heterostructures of two-dimensional semiconductors. *Applied Physics Letters* **102**, 012111 (2013).



- [268] Hill, I., Milliron, D., Schwartz, J. & Kahn, A. Organic semiconductor interfaces: electronic structure and transport properties. *Applied Surface Science* **166**, 354–362 (2000).
- [269] Zhu, X. *et al.* Charge transfer excitons at van der waals interfaces. *Journal of the American Chemical Society* **137**, 8313–8320 (2015).
- [270] Chen, H. *et al.* Ultrafast formation of interlayer hot excitons in atomically thin mos<sub>2</sub>/ws<sub>2</sub> heterostructures. *Nature communications* **7**, 12512 (2016).
- [271] Forrest, S., Kaplan, M. & Schmidt, P. Organic-on-inorganic semiconductor contact barrier diodes. ii. dependence on organic film and metal contact properties. *Journal of applied physics* **56**, 543–551 (1984).
- [272] Hoffmann, M. *et al.* The lowest energy frenkel and charge-transfer excitons in quasi-one-dimensional structures: application to meptcdi and ptcda crystals. *Chemical Physics* **258**, 73–96 (2000).
- [273] Scholz, R., Kobitski, A. Y., Zahn, D. R. & Schreiber, M. Investigation of molecular dimers in  $\alpha$ -ptcda by ab initio methods: Binding energies, gas-to-crystal shift, and self-trapped excitons. *Physical Review B* **72**, 245208 (2005).
- [274] Lunt, R. R., Giebink, N. C., Belak, A. A., Benziger, J. B. & Forrest, S. R. Exciton diffusion lengths of organic semiconductor thin films measured by spectrally resolved photoluminescence quenching. *Journal of Applied Physics* **105**, 053711 (2009).
- [275] Bergemann, K. J. & Forrest, S. R. Measurement of exciton diffusion lengths in optically thin organic films. *Applied Physics Letters* **99**, 274 (2011).
- [276] Reynaert, J., Arkhipov, V. I., Heremans, P. & Poortmans, J. Photomultiplication in disordered unipolar organic materials. *Advanced functional materials* **16**, 784–790 (2006).
- [277] Ma, D. *et al.* Repairing sulfur vacancies in the mos<sub>2</sub> monolayer by using co, no and no<sub>2</sub> molecules. *Journal of Materials Chemistry C* **4**, 7093–7101 (2016).
- [278] Addou, R. & Wallace, R. M. Surface analysis of wse<sub>2</sub> crystals: spatial and electronic variability. *ACS applied materials & interfaces* **8**, 26400–26406 (2016).
- [279] Amani, M. *et al.* Near-unity photoluminescence quantum yield in mos<sub>2</sub>. *Science* **350**, 1065–1068 (2015).
- [280] Li, Y. *et al.* Near-infrared ternary tandem solar cells. *Advanced Materials* 1804416 (2018).
- [281] Wang, C. *et al.* Ternary organic solar cells with minimum voltage losses. *Advanced Energy Materials* **7**, 1700390 (2017).

- [282] Cheng, P. *et al.* Alloy acceptor: superior alternative to pcbm toward efficient and stable organic solar cells. *Advanced Materials* **28**, 8021–8028 (2016).
- [283] Chen, Y. *et al.* Achieving high-performance ternary organic solar cells through tuning acceptor alloy. *Advanced Materials* **29**, 1603154 (2017).
- [284] Yang, Y. M. *et al.* High-performance multiple-donor bulk heterojunction solar cells. *Nature Photonics* **9**, 190 (2015).
- [285] Street, R. A., Davies, D., Khlyabich, P. P., Burkhart, B. & Thompson, B. C. Origin of the tunable open-circuit voltage in ternary blend bulk heterojunction organic solar cells. *Journal of the American Chemical Society* **135**, 986–989 (2013).
- [286] Cavallone, F. & Clementi, E. Electronic structure of ttf–tcnq complex. *The Journal of Chemical Physics* **63**, 4304–4307 (1975).
- [287] Goetz, K. P. *et al.* Charge-transfer complexes: new perspectives on an old class of compounds. *Journal of Materials Chemistry C* **2**, 3065–3076 (2014).
- [288] Ferraris, J., Cowan, D., Walatka, V. t. & Perlstein, J. Electron transfer in a new highly conducting donor-acceptor complex. *Journal of the American Chemical Society* **95**, 948–949 (1973).
- [289] Burlingame, Q. *et al.* Reliability of small molecule organic photovoltaics with electron-filtering compound buffer layers. *Advanced Energy Materials* **6**, 1601094 (2016).
- [290] Haigh, S. *et al.* Cross-sectional imaging of individual layers and buried interfaces of graphene-based heterostructures and superlattices. *Nature materials* **11**, 764 (2012).
- [291] Yu, W. J. *et al.* Vertically stacked multi-heterostructures of layered materials for logic transistors and complementary inverters. *Nature materials* **12**, 246 (2013).
- [292] Wang, C. *et al.* Monolayer atomic crystal molecular superlattices. *Nature* **555**, 231 (2018).
- [293] Paschos, G. *et al.* Hybrid organic-inorganic polariton laser. *Scientific Reports* **7**, 11377 (2017).
- [294] Flatten, L. C. *et al.* Electrically tunable organic–inorganic hybrid polaritons with monolayer  $\text{ws}_2$ . *Nature communications* **8**, 14097 (2017).